



# MARS 2020 INITIAL REPORTS

Crater Floor Campaign

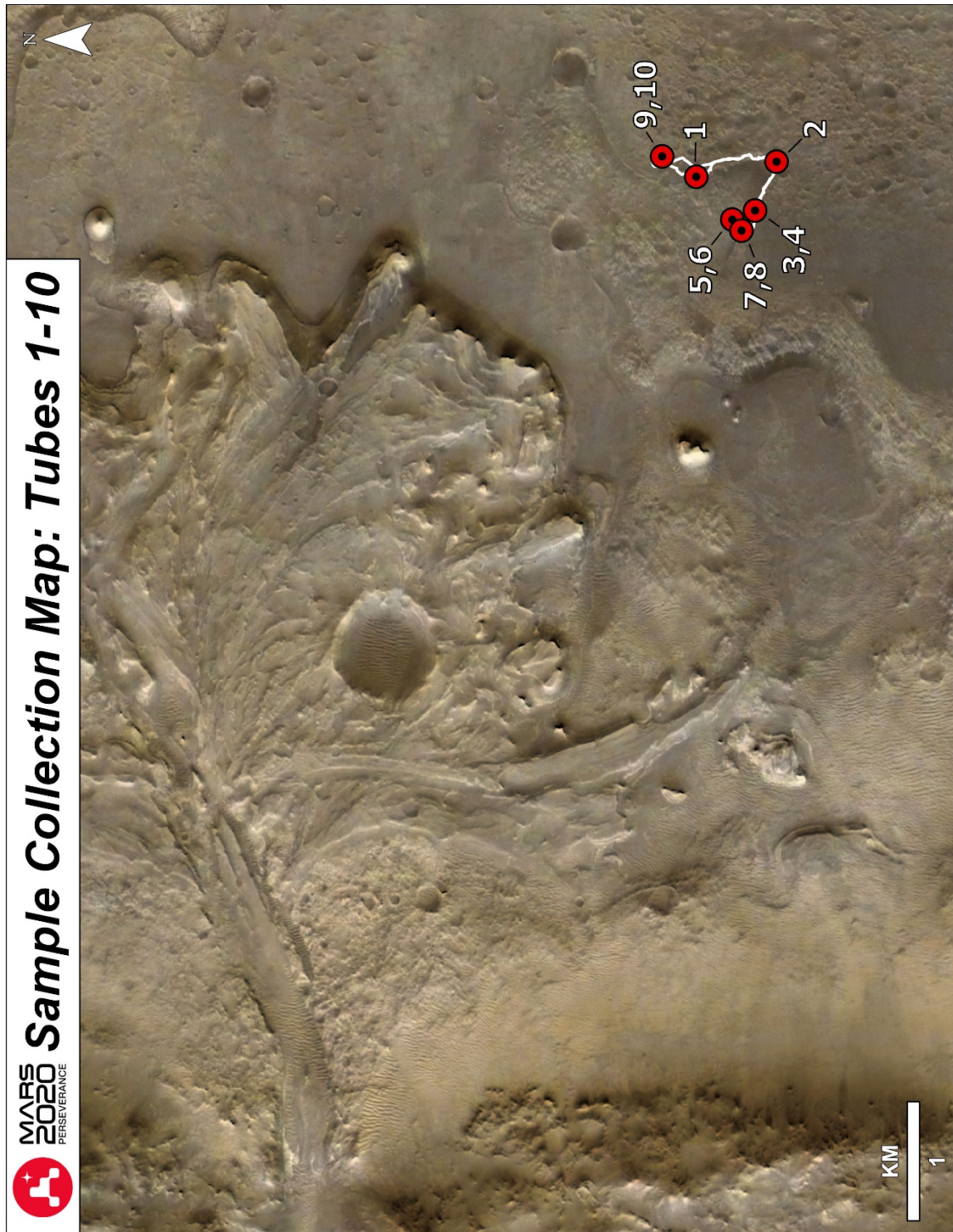
August 11, 2022

KEN FARLEY, MARS 2020 PROJECT SCIENTIST  
*CALIFORNIA INSTITUTE OF TECHNOLOGY*

KATIE STACK, MARS 2020 DEPUTY PROJECT SCIENTIST  
*JET PROPULSION LABORATORY  
CALIFORNIA INSTITUTE OF TECHNOLOGY*



# Frontispiece: Mars 2020 Sample Collection Map



# Contents

Frontispiece: Mars 2020 Sample Collection Map .....	i
Preface.....	iii
Mars 2020 Returned Sample Science Participating Scientists.....	iv
Explanatory Notes for Mars 2020 Initial Reports.....	v
Cite as, Revision History, Acknowledgements.....	xi
M2020-109-1 WB1.....	1-1
M2020-164-2 <i>Roubion</i> .....	2-1
M2020-190-3 <i>Montdenier</i> .....	3-1
M2020-196-4 <i>Montagnac</i> .....	4-1
M2020-262-5 <i>Salette</i> .....	5-1
M2020-271-6 <i>Coulettes</i> .....	6-1
M2020-298-7 <i>Robine</i> .....	7-1
M2020-337-8 <i>Malay</i> .....	8-1
M2020-371-9 <i>Hahonih</i> .....	9-1
M2020-377-10 <i>Atsah</i> .....	10-1

## Preface

A central goal of the Mars 2020 mission is collection of scientifically-selected martian rock, regolith, and atmosphere samples for possible return to Earth by future missions. This is an ambitious undertaking: *Perseverance* carries 38 sample tubes and 5 contamination-knowledge “witness tubes” to be filled over the course of the mission. Using the rover’s instruments, high priority outcrops must be identified, and the characteristics of each acquired sample and its surroundings investigated. With such a large number of samples to acquire and with an anticipated short interval between their acquisition, it is important to record in near real-time what the Mars 2020 Science Team has learned about each sample. The Mars 2020 Initial Reports series fills this need. A sample’s Initial Report is a set of field notes recording what is known about the sample and how it fits into its surroundings. The goal is to have each report *completed* within three weeks of sample acquisition, long enough to have downlinked, processed, and completed an initial high-level interpretation of the data, but short enough that the sample is still fresh in the team’s memory. Just like conventional field notes, the Initial Report is not updated after completion. The Initial Report is therefore preliminary, and the interpretations and even some of the underlying measurements will be revised and described more fully in detailed follow-on publications. The goal of the Initial Reports collection is to provide a timely, routine, systematic and preliminary narrative description of all the acquired samples in a single compendium. The Initial Reports complement the Sample Dossiers - a compilation of the digital records related to each sample. The Initial Reports series facilitates intercomparison among samples already collected as well as rocks under consideration for sampling over the course of the mission. It may also prove useful for prioritization of samples for Earth return and as a quick reference guide after samples arrive on Earth.

K.A. Farley, Project Scientist

K.M. Stack, Deputy Project Scientist

## Mars 2020 Returned Sample Science Participating Scientists

The Mars 2020 Science Team includes individuals selected by NASA to guide sample selection, interpretation, and documentation, including preparation of these Initial Reports. For the Prime Mission these individuals are:

Kathleen Benison, West Virginia University

Tanja Bosak, Massachusetts Institute of Technology

Barbara Cohen, NASA Goddard Space Flight Center

Andy Czaja, University of Cincinnati

Vinciane Debaille, FNRS-Université Libre de Bruxelles

Libby Hausrath, University of Nevada Las Vegas

Chris Herd, University of Alberta

Keyron Hickman-Lewis, Natural History Museum London

Lisa Mayhew, University of Colorado Boulder

Mark Sephton, Imperial College London

Davis Shuster, University of California Berkeley

Sandra Siljeström, RISE Research Institutes of Sweden

Justin Simon, NASA Johnson Space Center

Ben Weiss, Massachusetts Institute of Technology

Maria-Paz Zorzano, Centro de Astrobiología, Spain

# Explanatory Notes for Mars 2020 Initial Reports

## Sample Designation

The standardized format for sample designations is **M2020-sol-N name**. **M2020** refers to the mission that collected the sample, **sol** indicates the mission sol of sample tube sealing, **N** refers to the sequential number of the sample (or witness blank) acquisition, and *name* is the informal name applied to that sample and derived from the quadrangle in which the core was acquired. In the case of a witness blank acquisition, *name* is simply “WB” followed by the sequential number of the witness blank, starting with 1 and incrementing (e.g. WB1).

The same naming scheme is used for paired samples (i.e., two cores acquired with one associated STOP list execution; see below for definition of STOP list), except sol, N, and name all refer to the second member of the pair.

In typical usage the sample *name* alone is sufficient to uniquely identify a specific core. Because paired samples share a STOP list data set, when describing characteristics that refer to both members of paired samples, hyphenation of sample names will provide clarity: e.g., *name1-name2*.

## Date of Coring (or Exposure-Activation-Sealing)

This is the calendar date on which the corer was placed on the rock surface to begin acquisition. Ordinarily, coring is completed in one sol. In the case of a witness blank, the dates of initial exposure, activation (inner seal puncture), and sealing are indicated.

## Estimated Volume Recovered

The rock volume ( $V_{\text{rock}}$ ) estimate is derived from the penetration depth of the volume probe, a rod inserted into the tube after sample acquisition (in practice the tube is manipulated while the rod is fixed in place). Volume is computed from the implied length of sample multiplied by an assumed cylindrical cross section corresponding to the coring bit inner diameter  $d=13.4$  mm. The core itself has  $d=13$  mm; the 0.4 mm difference in diameter between the bit and the core is assumed to be filled by cuttings and so contributes to acquired rock volume. A full length core is typically 6 cm long, though shorter lengths can be commanded and will sometimes be all that is acquired. Note that void spaces between core fragments may exist, such that the true sample volume may be less than this estimate.

## Coring Bit Number

*Perseverance* carries 6 rock coring bits and 2 regolith bits. The bit number used here provides insight to usage history that may be relevant for contamination and cross-contamination assessment.

## Core Orientation

Three pieces of information are needed to orient the core in the Martian geographic frame (also known as the SITE frame) (Fig. 1). First, *two angles orient the core’s pointing vector*. Second, the *core’s roll* is noted by marking the pre-drilling WATSON image of the core face. The core orientation pointing vector is estimated as equal to the orientation of the coring drill after pre-loading on the core target.

The core pointing vector is quantified by the *azimuth* and *hade*. The azimuth is defined as the clockwise angle of the horizontal projection of the core y-axis, **cy**, from geographic north, **sx**, where the **cy**-axis lies in the martian geographic vertical plane. The hade is defined as the angle of the core face from martian geographic horizontal (**sx-sy** plane). These angles are obtained from coring drill and rover body ancillary orientation data at the time of pre-loading of the coring drill.

The core roll is quantified by an angle  $\alpha$ , defined as the clockwise angle from the WATSON y-axis (**wy**) to **cy** as viewed in the pre-coring WATSON images. WATSON 6-7-cm standoff images are typically used for this purpose.

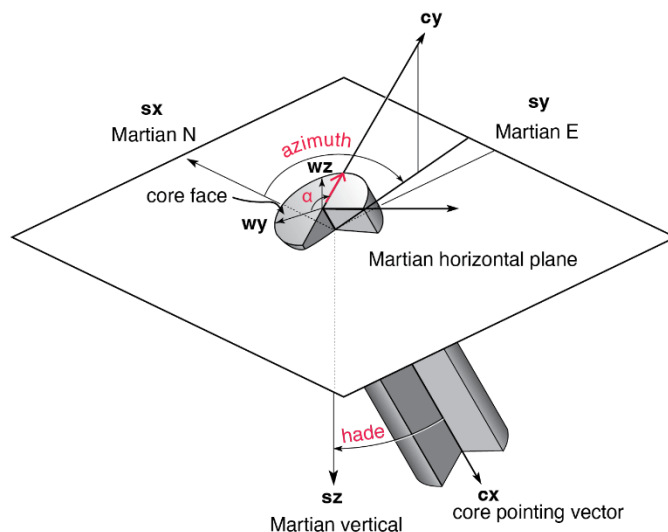


**Fig. 1.** Orientation system for cores collected by the Perseverance rover. Shaded cylinder is core with cutaway view in lower right quadrant. Martian geographic east, north, and down are the SITE axes, **sx**, **sy** and **sz**, respectively. The pointing vector, **cx**, points into outcrop and is normal to the core face and the **cy** axis lies in the vertical plane. The azimuth is the clockwise angle from geographic north of the projection of the **cy**-axis onto the Martian horizontal (**sx-sy**) plane. The hade is the angle of **cx** from vertical. The core roll,  $\alpha$ , is defined as the clockwise angle from the WATSON pre-coring image y-axis, **wy**, to **cy**; this direction is marked with an arrow on the WATSON image. Adapted from Butler (1992) *Paleomagnetism: Magnetic Domains to Geologic Terranes*, Blackwell Scientific, 319 pp.

### Sample Tube, Seal, and Ferrule Serial Numbers

Every sealed tube carries a unique set of serial numbers that will allow downstream identification. SN's are stamped into each tube, seal, and ferrule (the ferrule SN is commonly visible in Cachecam images).

### **ACA Temperature at Time of Sealing**

Sample tubes are sealed in the Adaptive Caching Assembly (ACA). Mechanisms in this subsystem are actively heated, so sealing occurs at temperatures higher than ambient conditions around the rover. The temperature recorded here is the average of the temperatures recorded on the Sealing Station and the Sample Handling Arm end effector. These temperatures are likely warmer than the sample and the associated head space gas.

### **Estimated Rover-Ambient Pressure and Temperature at Time of Sealing**

Atmospheric temperature and pressure are obtained from MEDA. When MEDA data was not acquired on the same sol as sample sealing (often the case given energy limitations), the average values of pressure and temperature are estimated from the closest sol or sols. The reported temperature is the minimum of MEDA ATS 4 and 5, the sensors located 0.84 m above the surface.

### **Estimated Amount of Martian Atmosphere Headspace Gas**

The estimated amount of headspace gas in moles ( $n_h$ ) is computed from the ideal gas law and assuming the rover ambient temperature (T) and pressure (P) described above.

$$n_h = P (V_{\text{tube}} - V_{\text{rock}}) / RT$$

where R is the gas constant.  $V_T$  is assumed to be 12 cm<sup>3</sup>. The actual temperature of the gas upon sealing is difficult to estimate because the Adaptive Caching Assembly (ACA) is substantially warmer than rover surroundings, typically by almost 100 K. For consistency we assume rover ambient temperature in this calculation, recognizing that it is an upper limit. A lower limit would be obtained by using the reported ACA temperature in the above equation.

### **Abrasion Patch Name and Depth**

To minimize possible degradation of the sample, much of the data associated with a given sample is acquired on a 5 cm diameter abrasion patch acquired within a few tens of cm of the coring site, and in the same lithology. This IR entry gives the name of that patch and its depth relative to the highest topographic feature in the 5 cm diameter circle that was abraded.

### **Anomalous Behavior**

This entry highlights noteworthy deviations from the standard sampling activities or their expected results.

**Additional Notes:****STOP List**

To expedite the sample collection and acquisition process, the Mars 2020 Team developed a minimum set of observations to be performed in association with each sample. This Standardized Observation Protocol, or STOP list, was encoded into an optimized sample sol path for efficient and repeatable execution. STOP list observations form the main data set for each sample's Initial Report. A standardized set of observations on each sample permits a templated Initial Report format. Although the STOP list is likely to evolve as the team learns what observations provide highest science value, it is the intention that the overall format be retained.

## **Instrument and Mission References**

- Allwood, Abigail C., Lawrence A. Wade, Marc C. Foote, William Timothy Elam, Joel A. Hurowitz, Steven Battel, Douglas E. Dawson, et al. "PIXL: Planetary Instrument for X-Ray Lithochemistry." *Space Science Reviews* 216, 134. <https://doi.org/10.1007/s11214-020-00767-7>.
- Balaram, J., MiMi Aung, and Matthew P. Golombek. "The Ingenuity Helicopter on the Perseverance Rover." *Space Science Reviews* 217, 56. <https://doi.org/10.1007/s11214-021-00815-w>.
- Bell, J. F., J. N. Maki, G. L. Mehall, M. A. Ravine, M. A. Caplinger, Z. J. Bailey, S. Brylow, et al. "The Mars 2020 Perseverance Rover Mast Camera Zoom (Mastcam-Z) Multispectral, Stereoscopic Imaging Investigation." *Space Science Reviews* 217, 24. <https://doi.org/10.1007/s11214-020-00755-x>.
- Bhartia, Rohit, Luther W. Beegle, Lauren DeFlores, William Abbey, Joseph Razzell Hollis, Kyle Uckert, Brian Monacelli, et al. "Perseverance's Scanning Habitable Environments with Raman and Luminescence for Organics and Chemicals (SHERLOC) Investigation." *Space Science Reviews* 217, 58. <https://doi.org/10.1007/s11214-021-00812-z>.
- Farley, Kenneth A., Kenneth H. Williford, Kathryn M. Stack, Rohit Bhartia, Al Chen, Manuel de la Torre, Kevin Hand, et al. "Mars 2020 Mission Overview." *Space Science Reviews* 216, 142. <https://doi.org/10.1007/s11214-020-00762-y>.
- Hamran, Svein-Erik, David A. Paige, Hans E. F. Amundsen, Tor Berger, Sverre Brovoll, Lynn Carter, Leif Damsgård, et al. "Radar Imager for Mars' Subsurface Experiment—RIMFAX." *Space Science Reviews* 216, 128. <https://doi.org/10.1007/s11214-020-00740-4>.
- Hayes, Alexander G., P. Corlies, C. Tate, M. Barrington, J. F. Bell, J. N. Maki, M. Caplinger, et al. "Pre-Flight Calibration of the Mars 2020 Rover Mastcam Zoom (Mastcam-Z) Multispectral, Stereoscopic Imager." *Space Science Reviews* 217, 29. <https://doi.org/10.1007/s11214-021-00795-x>.
- Hecht, M., J. Hoffman, D. Rapp, J. McClean, J. SooHoo, R. Schaefer, A. Aboobaker, et al. "Mars Oxygen ISRU Experiment (MOXIE)." *Space Science Reviews* 217, 9. <https://doi.org/10.1007/s11214-020-00782-8>.
- Kinch, K. M., M. B. Madsen, J. F. Bell, J. N. Maki, Z. J. Bailey, A. G. Hayes, O. B. Jensen, et al. "Radiometric Calibration Targets for the Mastcam-Z Camera on the Mars 2020 Rover Mission." *Space Science Reviews* 216, 141. <https://doi.org/10.1007/s11214-020-00774-8>.
- Maki, J. N., D. Gruel, C. McKinney, M. A. Ravine, M. Morales, D. Lee, R. Willson, et al. "The Mars 2020 Engineering Cameras and Microphone on the Perseverance Rover: A Next-Generation Imaging System for Mars Exploration." *Space Science Reviews* 216, 137. <https://doi.org/10.1007/s11214-020-00765-9>.
- Manrique, J. A., G. Lopez-Reyes, A. Cousin, F. Rull, S. Maurice, R. C. Wiens, M. B. Madsen, et al. "SuperCam Calibration Targets: Design and Development." *Space Science Reviews* 216, 138. <https://doi.org/10.1007/s11214-020-00764-w>.
- Maurice, S., R. C. Wiens, P. Bernardi, P. Caïs, S. Robinson, T. Nelson, O. Gasnault, et al. "The SuperCam Instrument Suite on the Mars 2020 Rover: Science Objectives and Mast-Unit Description." *Space Science Reviews* 217, 47. <https://doi.org/10.1007/s11214-021-00807-w>.
- Moeller, Robert C., Louise Jandura, Keith Rosette, Matt Robinson, Jessica Samuels, Milo Silverman, Kyle Brown, et al. "The Sampling and Caching Subsystem (SCS) for the Scientific Exploration of Jezero Crater by the Mars 2020 Perseverance Rover." *Space Science Reviews* 217, 5. <https://doi.org/10.1007/s11214-020-00783-7>.

Newman, C. E., M. de la Torre Juárez, J. Pla-García, R. J. Wilson, S. R. Lewis, L. Neary, M. A. Kahre, et al. "Multi-Model Meteorological and Aeolian Predictions for Mars 2020 and the Jezero Crater Region." *Space Science Reviews* 217, 20. <https://doi.org/10.1007/s11214-020-00788-2>.

Pla-García, Jorge, S. C. R. Rafkin, G. M. Martinez, Á. Vicente-Retortillo, C. E. Newman, H. Savijärvi, M. de la Torre, et al. "Meteorological Predictions for Mars 2020 Perseverance Rover Landing Site at Jezero Crater." *Space Science Reviews* 216, 148. <https://doi.org/10.1007/s11214-020-00763-x>.

Rodriguez-Manfredi, J. A., M. de la Torre Juárez, A. Alonso, V. Apéstigue, I. Arruego, T. Atienza, D. Banfield, et al. "The Mars Environmental Dynamics Analyzer, MEDA. A Suite of Environmental Sensors for the Mars 2020 Mission." *Space Science Reviews* 217, 48. <https://doi.org/10.1007/s11214-021-00816-9>.

Stack, Kathryn M., Nathan R. Williams, Fred Calef, Vivian Z. Sun, Kenneth H. Williford, Kenneth A. Farley, Sigurd Eide, et al. "Photogeologic Map of the Perseverance Rover Field Site in Jezero Crater Constructed by the Mars 2020 Science Team." *Space Science Reviews* 216, 127. <https://doi.org/10.1007/s11214-020-00739-x>.

Wiens, Roger C., Sylvestre Maurice, Scott H. Robinson, Anthony E. Nelson, Philippe Cais, Pernelle Bernardi, Raymond T. Newell, et al. "The SuperCam Instrument Suite on the NASA Mars 2020 Rover: Body Unit and Combined System Tests." *Space Science Reviews* 217, 4. <https://doi.org/10.1007/s11214-020-00777-5>.

Cite as:

K.A. Farley and K.M. Stack, Mars 2020 Initial Reports - Crater Floor Campaign, 2022. Include Digital Object Identifier (DOI) associated with this document on the NASA Planetary Data System.

Revision History:

This is Release 2 of the Mars 2020 Initial Reports series. Initial Reports 5-10 were added to an earlier release that included only Initial Reports 1-4. No changes were made to Initial Reports 1-4 in Release 2.

Acknowledgement:

This research was carried out at the Jet Propulsion Laboratory, California Institute of Technology, under a contract with the National Aeronautics and Space Administration (80NM0018D0004).

# INITIAL REPORT

## M2020-109-1 WB1

---

**Witness Tube Designation:** M2020-109-1 WB1

**Date of Initial Witness Exposure:** Pre-launch

**Date of Activation:** Pre-launch

**Date of Sealing:** 21-June-2021

**Mars Time of Witness Tube Sealing:** 16:25:55 LMST, Sol 120, Ls 61.4

**Latitude (N), Longitude (E), Elevation:** 18.43906919, 77.44940206, -2568.073

**Sample Serial Numbers:** Tube SN061; Seal SN147; Ferrule SN090

**ACA Temperature at Time of Sealing:** 40°C

**Estimated Rover-Ambient Pressure and Temperature at Time of Sealing:** 758 Pa, 245

**Estimated Amount of Martian Atmosphere Headspace Gas:**  $2.2 \times 10^{-6}$  mol

**Anomalous Behavior:** None

---

November 27, 2021

*K. A. Farley, Y. Goreva, R. Moeller and the Mars 2020 Science Team*

## **Summary Description**

*Perseverance* carries 5 Witness Tube Assemblies (WTA's) with which to document the evolving rover contamination environment over the course of the mission (Moeller et al., 2020). Four of these “witness tubes” are identical and are located in sheaths just like sample tubes within the ACA. The fifth witness tube, WB1, was handled differently. During final pre-launch activities, this witness tube was activated (the inner seal was punctured to begin accumulation) and placed in the Bit Carousel. This tube will therefore have accumulated contaminants for the entire duration of exposure from a few months before launch through cruise and EDL until it was sealed on the surface of Mars on Sol 120. This exposure is very unlike the sample tubes sheathed in the ACA. Sample tubes (and the four other witness tubes) are protected from particle accumulation by fluid mechanical particle barriers and are isolated from volatile organic molecules by a tortuous path of gettering surfaces (Moeller et al., 2020). Given its long exposure, it is likely that the inner surfaces of WB1 will be saturated with organic contaminants, i.e., they will be in adsorption equilibrium with their immediate surroundings in the rover (and or the entire spacecraft prior to landing). WB1 is therefore expected to have higher concentrations of contaminants, and potentially different contaminants, than the sample tubes.

## **Operations**

1. This witness tube was initially exposed and activated in the ultraclean ACA cleanroom at JPL just prior to being installed in its sheath in the Bit Carousel, after which the Bit Carousel doors were immediately closed.
2. The Bit Carousel doors were first re-opened, on Mars, on Sol 24.
3. Limited Bit Carousel motion occurred on sols 88, 90, and 92.
4. On Sol 118, WB1 was rotated to the lower Bit Carousel door.
5. WB1 was processed and sealed on sol 120. Note that this tube was not subjected to simulated sampling, i.e., it was not placed in the corer and moved in a fashion similar to rock core acquisition. In this sense it differs from the expected use case of the remaining four witness tubes.

**INITIAL REPORT****M2020-164-2 Roubion**

(no core recovered, atmospheric sample)

---

**Sample Designation:** M2020-164-2 Roubion

**Date of Coring:** 5-Aug-2021

**Mars Time of Sample Core Sealing:** 19:11:35 LMST, Sol 164, Ls 81.1

**Latitude (N), Longitude (E), Elevation:** 18.42769340, 77.45165066, -2584.96 m

**Campaign:** Crater Floor

**Region of Interest:** Séítah Thumb

**Lithology:** Fine- to medium-grained mafic and likely igneous rock, possibly basalt or microgabbro (alternatively, basaltic sandstone). Primary minerals are plagioclase and pyroxene, also possibly apatite and FeTi oxides. Weathering and/or aqueous alteration is indicated by pits and crevices in abraded surface and abundant secondary minerals including iron oxide (possibly hydrated), sulfates, perchlorate, and possibly phosphate and halite, usually in distinct patches.

**Estimated Volume Recovered:** ~0 cm<sup>3</sup> (some ~10 µm sized particles). No core recovery

**Coring Bit Number:** 5

**Core Orientation:** hade = 3.43°; azimuth = 208.74°; core roll = 289.35°

**Sample Serial Numbers:** Tube SN233; Seal SN025; Ferrule SN062

**ACA Temperature at Time of Sealing:** 40 C

**Estimated Rover-Ambient Pressure and Temperature at Time of Sealing:** 749 Pa, 221 K

**Estimated Amount of Martian Atmosphere Headspace Gas:** 4.9x10<sup>-6</sup> mol

**Abrasion Patch Name and Depth:** *Guillaumes*, 8 mm

**Anomalous Behavior:** Core disintegrated; no core acquired

---

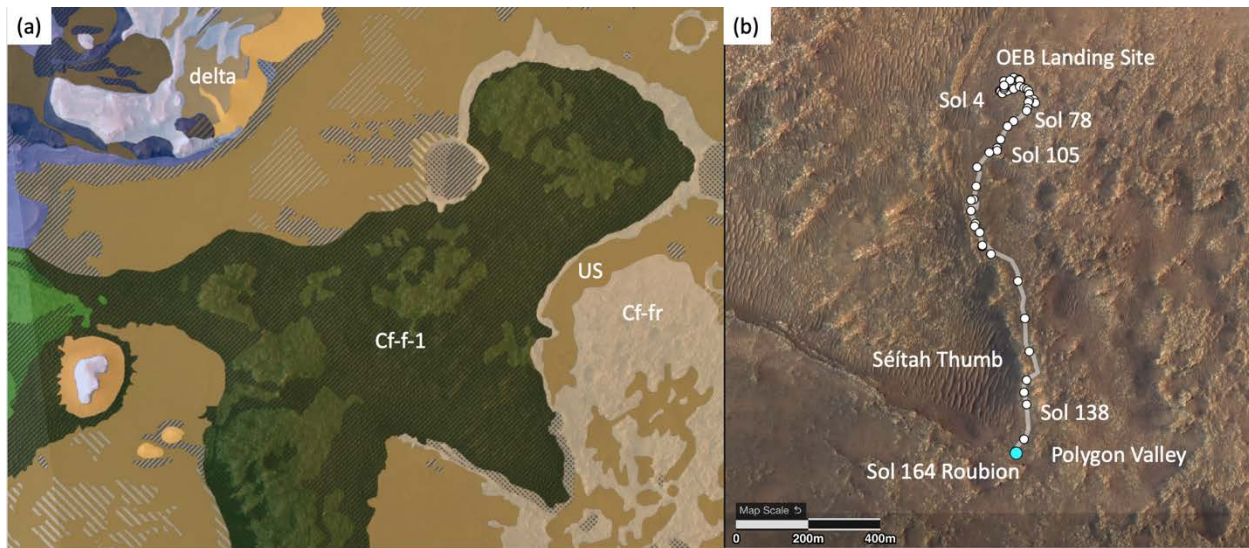
November 27, 2021

*J. I. Simon, K. A. Farley, D. L. Shuster, A. Udry, S. VanBommel, T. Bosak, S. McLennan, Y. Goreva, V. Sun, E. L. Scheller, E. L. Berger, A. D. Czaja, A. C. Fox, C. H. Lee, S. Sharma, J. Maki, J. Carsten, K. Edgett, L. W. Beegle, K. C. Benison, V. C. Debaille, L. Hausrath, C. Herd, J. Hurowitz, L. E. Mayhew, S. M. Siljestroem, M. Sylvestre, B. P. Weiss, R. Wiens, M.-P. Zorzano, and the Mars 2020 Science Team*

## Summary Description

Collection of *Roubion*, the first sample of the Mars2020 mission, was attempted in the *Séítah* Thumb region of the Jezero crater floor (**Figure 1**). Between Octavia E. Butler landing (OEB) and the sampling site, *Perseverance* traversed about 1 km southward over nearly continuous low-lying rocks typically forming meter-scale “paverstone” outcrops, with intervening regolith (**Figure 2**). In HiRISE orbital view, these rocks define a distinctive polygonal pattern, the lower lying of the several expressions of the Crater Floor Fractured Rough (Cf-fr) unit of Stack et al (2020).

**Figure 1 | Regional context.** (a) geologic map of Sun and Stack (2020) and units of Stack et al. 2020 and (b) HiRISE map with *Perseverance* traverse path leading to *Roubion*. Shown for reference are Octavia E. Buttler (OEB) landing site, *Séítah* Thumb area, Polygon Valley, *Mure*, and *Artuby* ridge.

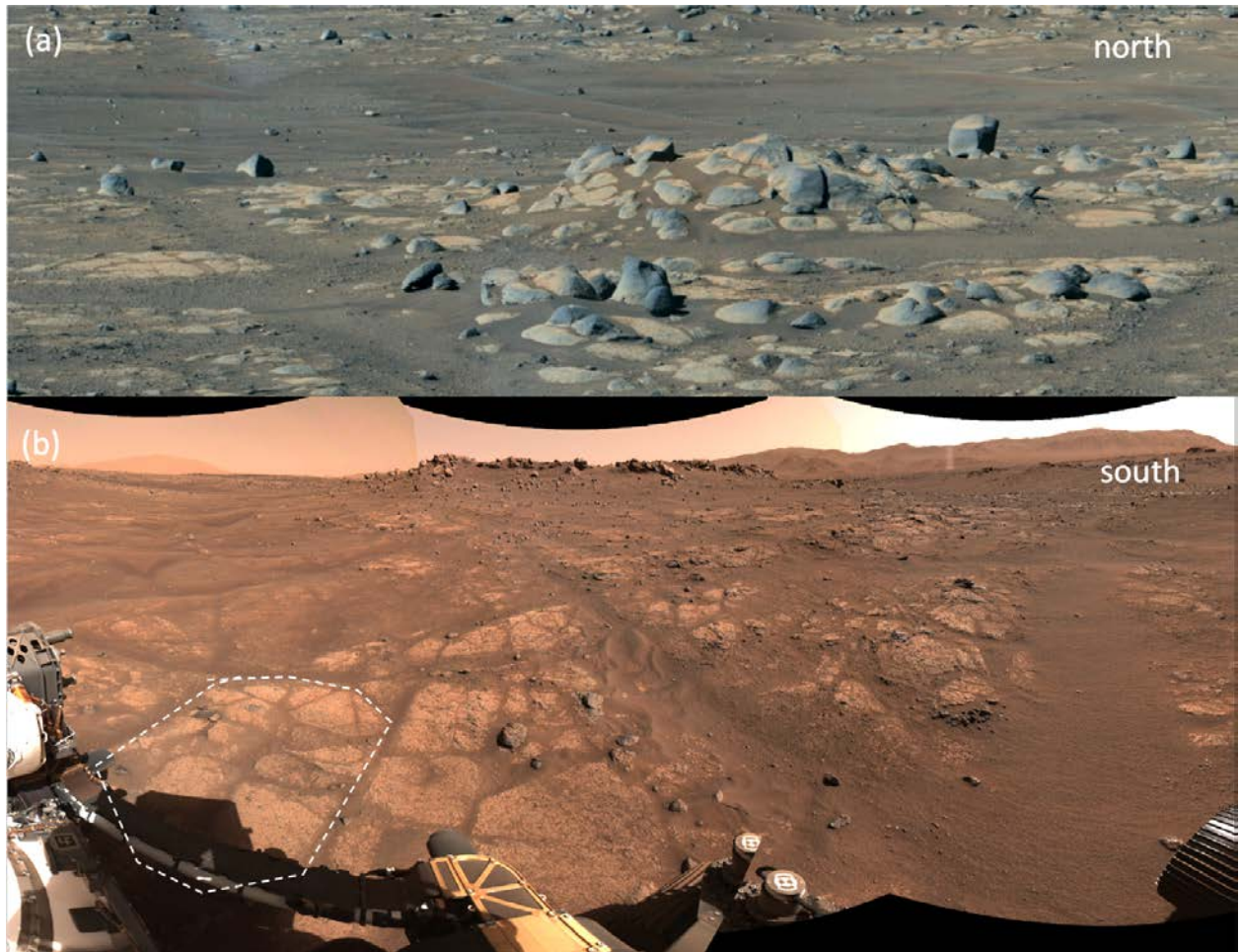


Prior to landing, the Cf-fr unit was variously interpreted to be igneous (lava or volcanoclastic) or sedimentary (fluviolacustrine or aeolian) in origin. Although the stratigraphic context of the fractured floor, and indeed the lithology itself, were unknown at the time of sampling, the Cf-fr unit was selected for sample acquisition because it is areally extensive and because it includes the most heavily cratered terrain to which the rover has access within Jezero crater. As such, a returned sample of this unit was thought to have high science value for understanding the geologic setting and timing of crater floor units, and possibly for calibration of the Mars crater chronology function.

As evidenced by the common whaleback morphology and surface polish and fluting, this expression of Cf-fr has been eroded to just above ground level by aeolian abrasion (**Figure 2**). Despite abundant outcrop, little or no visual evidence of sedimentary structure, clasts, or crystals were seen in natural exposures of these rocks. Supercam data on multiple outcrops along the traverse indicate an altered (hydrated, iron-oxide-bearing) mafic rock with crystal size large enough to create spot-to-spot variability in composition (i.e., > few hundred  $\mu\text{m}$  scale). These low-lying Cf-fr rocks are fairly homogenous in appearance and composition along the entire traverse from OEB to *Roubion*.

The *Roubion* coring attempt, and its companion *Guillaumes* abraded patch, were undertaken on a low relief rock at the tip of the *Séítah* Thumb region selected largely to meet first-time sampling requirements. *Roubion* is interpreted to be stratigraphically below several other expressions of Cf-fr, in particular the high-standing blocky, massive rocks to the east and north, and the layered rocks of *Mure* and *Artuby* ridge (Figures 2 and 3). *Roubion* is interpreted to be from a unit that overlies and therefore may be younger than the rocks of *Séítah* (Cf-f1 of Stack et al., 2020).

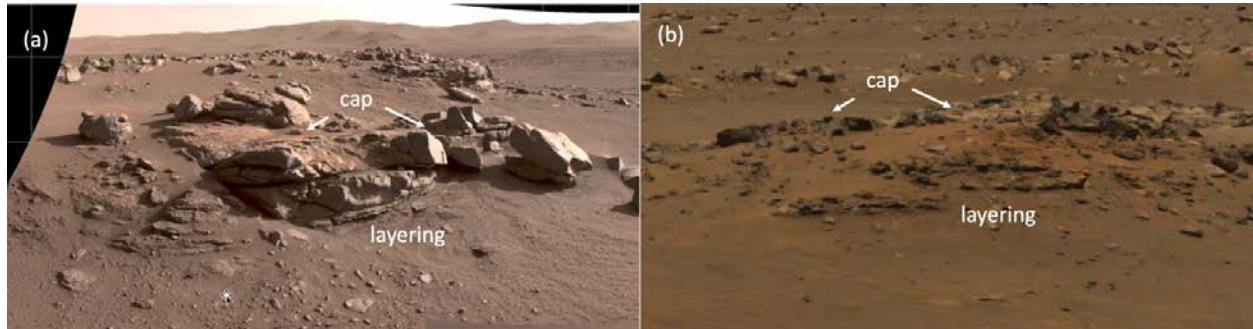
**Figure 2 | ZCAM images of distinct fractured crater floor surfaces. (a)** on Sol 58 that exhibit outcrops of less altered “whalebacks” and areas of rounded boulders, representative of early workspaces in the north near OEB. **(b)** on Sol 157 that exhibit flatter surfaces and more-polygonal outcrops where *Roubion* was sampled in the south near *Séítah* Thumb area.



The dominant mineralogy of the *Guillaumes* abraded surface appears to be ~mm-size pyroxene and plagioclase crystals, consistent in composition and texture with a relatively fine-grained gabbro or holocrystalline basalt. An igneous origin is preferred for this rock, but it is not currently possible to rule out the alternative interpretation that it is a basaltic sandstone. Extensive brown iron-rich patches are indicative of aqueous alteration, especially around several deep pits and crevices penetrating below the abraded surface. White patches containing secondary minerals (sulfate, perchlorate, and possibly halite and phosphate) provide additional evidence of aqueous interaction. SHERLOC fluorescence

spectroscopy identified two types of aromatic organic molecules within *Guillaumes*, one distributed widely across the abrasion patch and a second localized in a few specific regions. Chemical characteristics of the abraded patch are consistent with observations of this lithology all along the traverse, providing confidence that the sampled rock is reasonably representative of this expression of the Cf-fr unit. However, the rock appears more altered (more reddish, and appearing to be more granulated and/or flaky) than most other examples of this lithology (e.g., compare examples in **Figure 2**).

**Figure 3 | ZCAM images of crater floor stratigraphy near *Roubion*. (a) *Mure* Sol 168. (b) *Artubyridge* Sol 116.**



Coring produced a hole and cuttings pile of expected appearance, and the entire coring and sealing process completed nominally. However, the volume probe indicated no sample, a fact confirmed by a Cachecam image documenting an empty sample tube. **Thus, no core was recovered.** In the absence of core or core fragments on the ground, the most likely explanation for zero recovery is that the rock disaggregated during coring and wound up either in the cuttings pile or at the bottom of the hole. Further coring at this location was abandoned.

Although no rock was obtained, M2020-164-2 *Roubion* inadvertently provides a returnable sample of about 4.9  $\mu\text{mol}$  of martian atmosphere.

## **Stratigraphic and Geologic Context**

Coring of *Roubion* was attempted at a polygonal outcrop within a unit of the Jezero crater floor mapped in HiRISE orbital images as the “crater floor fractured rough” (Cf-fr) unit by the Mars 2020 Science Team (Stack et al., 2020). *Roubion* is positioned in a local topographic low, ~10 m downslope from blocky massive rocks to the ENE and resistant layered capping rocks of the *Mure* outcrop and *Artuby* ridge to the SSE and W, all of which were mapped as Cf-fr (**Figure 1**). *Roubion* is interpreted to be stratigraphically below these other expressions of Cf-fr, but the stratigraphic relationship between the higher-standing, blocky, massive rocks and the layered capping rocks is presently unknown.

*Roubion* is located ~80 m east of the inferred contact between Cf-fr and an extensive outcrop exposure called *Séítah*, included within a unit mapped by Stack et al. (2020) as the “crater floor fractured 1” (Cf-f-1). Although no exposed contact between these two units is observed in the immediate vicinity of *Roubion*, *Roubion* may be younger than the rocks of *Séítah* due to an apparent onlapping relationship

observed in orbital images, and topographic data and subsurface radargrams from the RIMFAX instrument. The age and stratigraphic relationship of *Roubion* relative to the rocks of the Jezero delta are less certain. Goudge et al. (2015) interpreted the unit containing *Roubion* to be younger than the Jezero delta, and the youngest in the crater, while Sun and Stack (2020), Stack et al. (2020), and Holm-Alwmark et al. (2021) proposed that the rocks of the Jezero crater floor, including *Roubion*, pre-date the currently exposed Jezero delta deposit.

## **Operations**

The desirability of sampling Cf-fr was apparent immediately after landing but abrading and sampling could not begin prior to completion of a series of hardware check-outs and first-time activities. The rover traverse and these preparatory activities were choreographed such that the first abrading and sampling effort would occur at the last obvious polygonal outcrops of Cf-fr along the planned southbound route, in the *Séítah* Thumb region (**Figure 1**).

Cf-fr in the OEB area occurs at an elevation of ~-2570 m. The elevation of this rock unit remained constant as *Perseverance* drove south, until Sol 131 (~650 linear m from OEB), when elevation started to decrease. By Sol 138, the elevation had decreased by 13 m to ~-2583 m in the *Séítah* Thumb area (1020 meters from OEB), the lowest elevation the rover is expected to visit on its entire mission.

Potentially sampleable polygonal outcrop was abundant in the *Séítah* Thumb area and ultimately the southernmost patch of outcrop was selected for sampling because it is adjacent to and can be directly related to a few-meter-high cliff of layered outcrop called *Mure* and its likely WNW continuation in *Artuby* ridge (**Figure 3a**). At this early stage of the mission, it was considered operationally prudent to target an outcrop with minimal surface roughness, thus limiting target options.

*Perseverance* arrived at the selected sampling target on Sol 156. Abrasion and sample collection were respectively conducted on Sols 160 and 164, as part of a single-core-sample STOP list sol path extending from Sol 157 to Sol 168. This was the first-time-activity for coring. In addition to the standardized STOP list observations, when it was recognized that no core was recovered, additional borehole imaging and inspection of the nearby surface was undertaken for anomaly resolution. On Sol 168 *Perseverance* executed its first drive towards and along *Artuby* ridge, leaving the *Séítah* Thumb region and the *Roubion* sampling site.

## **Sample-Related Observations**

### ***Workspace Images***

**Figure 4** shows the workspace in which both the *Guillaumes* abrasion patch and the *Roubion* coring attempt were undertaken. **Figure 4a** shows the southernmost cluster of Cf-fr polygons in the *Séítah* Thumb region in which these activities occurred. View is to the SSE. Note that the polygons appear to extend towards (and possibly beneath) the boulder-decorated hill named *Mure*. As evident in **Figure 3**, *Mure* is layered, distinct from Cf-fr pavestones as seen all along the traverse from OEB to *Séítah* Thumb. This layering also extends to the WNW in *Artuby* ridge (**Figures 1, 3**) indicating a notable transition in

surface appearance of rocks all mapped from orbit as Cf-fr. The transition appears to occur in or near the *Séítah* Thumb. Furthermore, in this area the polygons appear more granulated, flaky and flat, and less wind-polished, than the more typical whaleback morphology (e.g., as seen near OEB in **Figure 2a**).

**Figure 4 | ZCAM workspace images at *Roubion* sampling site. (a)** outcrop selected for abrasion and sample acquisition. **(b)** close up showing candidate target locations.

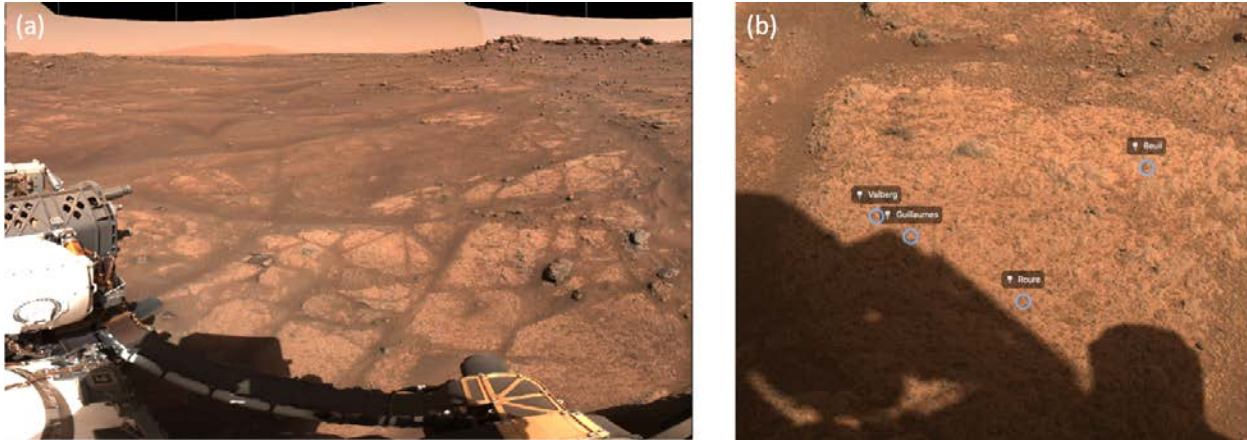


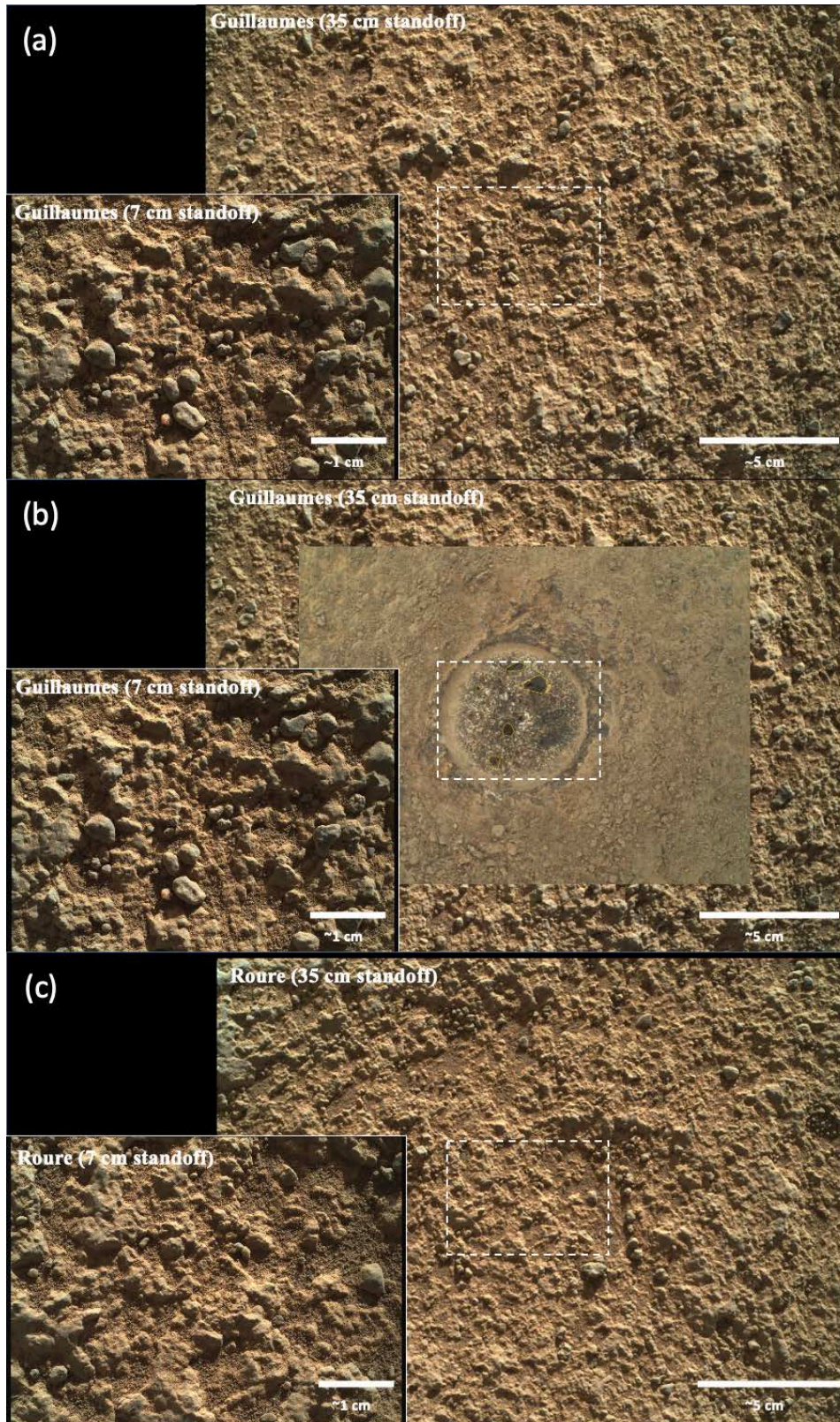
**Figure 4b**, a close-up of the sampled polygonal outcrop, further emphasizes the rather degraded appearance of the rocks in this area. Especially notable are the polygon edges, in which individual rock fragments appear to be falling or flaking out in a fashion like grus in a weathered granite. This figure shows the four locations considered for abrading and coring. Ultimately the location called *Guillaumes* was selected for abrasion and *Roure* was selected for coring (and the core was named *Roubion*). These target choices were largely dictated by engineering considerations (i.e., for minimum topographic relief to ensure safe instrument placement).

#### ***Images Pre and Post Coring/Abrasion***

**Figure 5a** provides WATSON images at two different standoffs prior to abrasion and coring. The rock surface appears stucco-like, with likely loose granules lying on a rather bumpy rock surface. Finer and likely loose grains (sand?) lie in low spots. The wind abrasion that is interpreted to have sculpted many examples of Cf-fr along the traverse is not evident here, rather the rock appears to be disaggregating faster than it is being abraded smooth. In contrast to the abraded patch (**Figure 5b**, and see below), these natural surfaces show no evidence of crystals/grains nor of holes penetrating into the rock; if holes are present, they have been filled with indistinct materials and totally obscured from view. Similarly, in these images there is no compelling evidence for the presence of the purple surface layer or coating which was observed on many rocks of Cf-fr along the traverse (but see post-abrasion discussion).

**Figure 5c** shows at high resolution the textural features of the natural surface before coring. These features were thought adequate for reconstruction of original core azimuthal orientation provided they survived coring. Dedicated orientation marking with SCAM LIBS points was not undertaken as it would not have substantially improved the likelihood of successful orientation of this core; indeed the LIBS pits

**Figure 5 | WATSON images. (a) pre-abrasion target surface. (b) post-abrasion (*Guillaumes*) target surface. (c) pre-coring (*Roubion*) target surface, here with its original target name, *Roure*.**

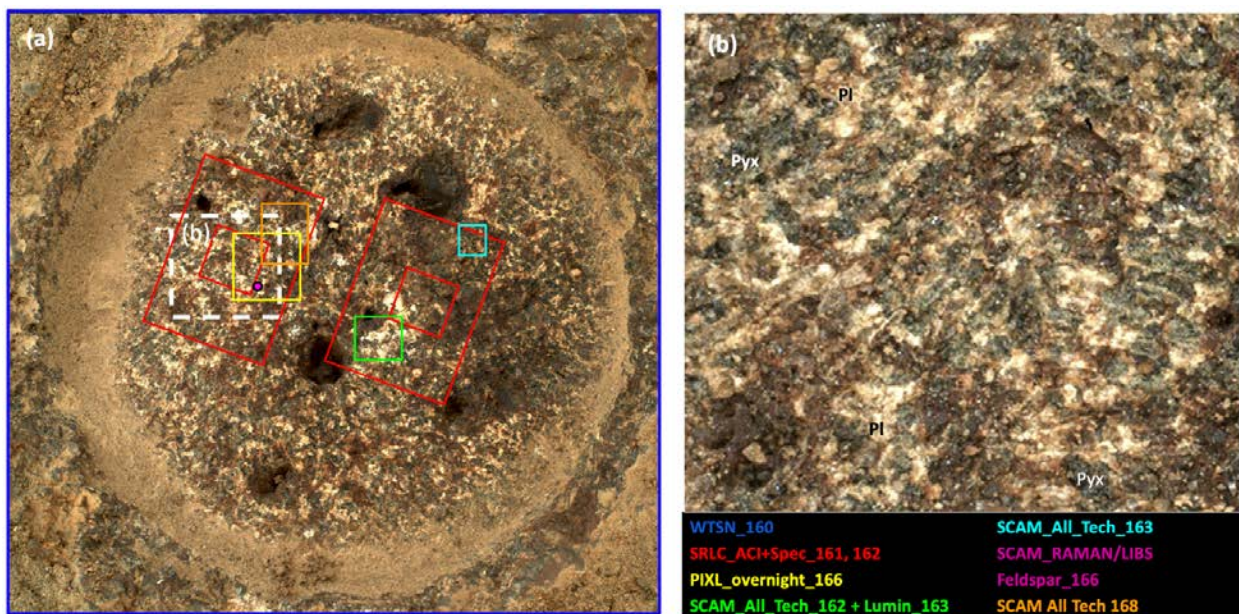


would likely be very difficult to locate in this surface, and in any case would be lost if the surface features were obliterated upon coring.

**Figure 6** shows WATSON images of *Guillaumes* after removal of abrasion cuttings using the gas dust removal tool (gDRT) at two different resolutions. Notable observations include:

a) mm-size light and dark grains or crystals comprise most of the abraded surface. White materials have at least two distinct morphologies and tones: some have angular shapes, including what may be elongated laths, others (especially those that are brightest white) have a more irregular outline. The latter suggests a secondary cavity-filling or replacement substance. Ignoring these patches as well as the brown material described in b, the light and dark grains appear roughly equal in grain size with no obvious spatial heterogeneity in relative abundance. In some cases, for example in parts of **Figure 6b**, the grains may be interlocking as if crystallized from a magma. Taken together these observations are reminiscent of the appearance of a fine-grained gabbro or holocrystalline basalt.

**Figure 6 | WATSON images of abrasion surface. (a)** ~25 cm standoff, showing SCAM, SHERLOC, and PIXL instrument placement footprints; abrasion patch is 5 cm diameter. Inset **(b)** ~7 cm standoff, showing holocrystalline rock texture.



b) some parts of the abraded surface are smooth and dark brown in color with less-evident grain boundaries, suggesting an (Fe-rich?) stain or coating. This material is heterogeneously distributed and is preferentially found in topographic lows of the abraded surface.

c) several irregularly shaped ~5 mm diameter pits and crevices penetrate below the abrasion patch and seem to share the dark brown color and texture noted in b. These pits are at least a few mm deep. Note that the abrasion removed 8 mm of surficial material (from original topographic peak to abraded surface); if these pits extended to the pre-abrasion surface they would have been 1.3 cm deep, possibly more. However, as noted above, pits were not visible on the natural surface. These pits do not have the typical appearance/distribution of vesicles in basalt and seem more likely to indicate mass removal by

some form of weathering that may have occurred prior to the formation of the current rock surface seen in **Figure 5c**.

d) while the abrasion patch rim is generally ragged in appearance, in some places the distinctive purple coating can be seen near or on the original surface, presumably now revealed by the gDRT. It is reasonable to expect the surface of the intact *Roubion* core would have captured this material.

### Elemental Geochemistry - PIXL

X-ray fluorescence mapping by PIXL was undertaken in a single region in the *Guillaumes* abrasion patch (**Figure 7**; observation footprint in **Figure 6**). A bulk sum analysis of the Sol 167 scanned abrasion surface is shown in **Table 1**. Note this analysis includes a mixture of what may be igneous mineral grains along with the white and brown patches suggestive of aqueous alteration. *Guillaumes* is clearly a silicate rock; compared to a typical basalt, it is low in  $\text{SiO}_2$ ,  $\text{Al}_2\text{O}_3$  and  $\text{MgO}$ , and rich in  $\text{FeO}$ ,  $\text{Na}_2\text{O}$ ,  $\text{SO}_3$ , and  $\text{Cl}$ .

The right-hand column of **Table 1** documents large point-to-point heterogeneity in elemental composition; the heterogeneity is much larger than analytical uncertainty, as is expected from a rock containing chemically distinct minerals of a size comparable to and/or larger than the  $120\ \mu\text{m}$  X-ray beam size. This point is further evident in elemental maps (**Figure 10a-d**): there are distinct  $\sim 500\ \mu\text{m}$  size regions rich in  $\text{FeO}$ , or  $\text{Al}_2\text{O}_3$ , or  $\text{CaO}$ . Further work is necessary to fully characterize these compositions and map them to the WATSON images, but a tentative interpretation is that the calcic regions correspond to the dark minerals and are pyroxene (augite), the aluminous phase is light colored and tabular and corresponds to plagioclase, and the Fe-rich material is the brownish coating(?) and could be an iron oxide or iron silicate. FeTi oxides and sodium and chlorine rich patches (halite? Na perchlorate?) are also apparent.

Table 1. PIXL Bulk Sum Composition

Guillaumes bulk sum (00167)				
Oxide	wt%	wt% err	std	std%
Na2O	5.55	0.28	3.10	55.8%
MgO	2.64	0.56	1.08	41.0%
Al2O3	7.56	0.38	3.02	40.0%
SiO2	38.29	1.92	7.12	18.6%
P2O5	1.65	0.46	1.41	85.4%
SO3	2.69	0.56	2.90	108.0%
Cl	3.40	0.54	4.14	121.8%
K2O	0.75	0.26	0.47	62.4%
CaO	7.77	0.39	3.86	49.6%
TiO2	1.47	0.43	2.27	154.8%
Cr2O3	0.03	0.06	0.07	246.9%
MnO	0.46	0.20	0.37	81.5%
FeO-T	18.72	0.94	10.94	58.5%
Ni	0.00	0.00	0.03	N/A
Zn	0.02	0.03	0.06	411.3%
Br	0.01	0.03	0.05	313.5%
Zr	0.02	0.03	0.03	122.7%

**Figure 7 | PIXL X-ray element maps. (a)  $\text{MgO}-\text{Al}_2\text{O}_3-\text{CaO}$ . (b)  $\text{SiO}_2-\text{FeO}_{\text{total}}-\text{TiO}_2$ . (c)  $\text{FeO}_{\text{total}}-\text{Al}_2\text{O}_3-\text{CaO}$ . (d)  $\text{MgO}-\text{Na}_2\text{O}-\text{Cl}$  in Sol 167 analysis of *Guillaumes*. Refer to Figure 6 for scale and region investigated.**

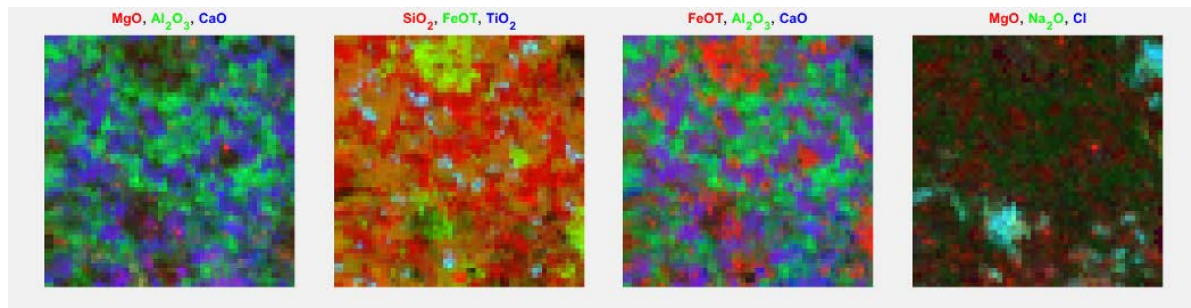
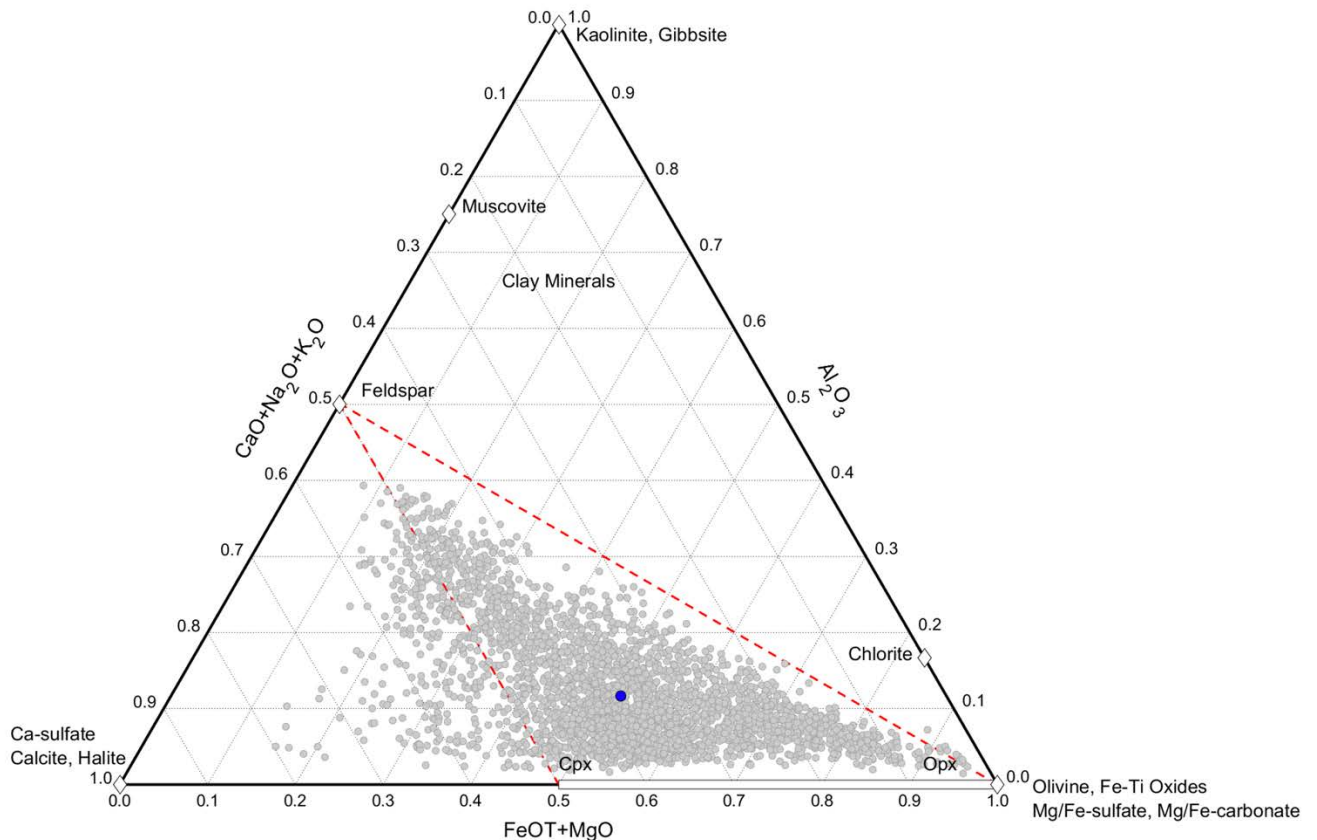


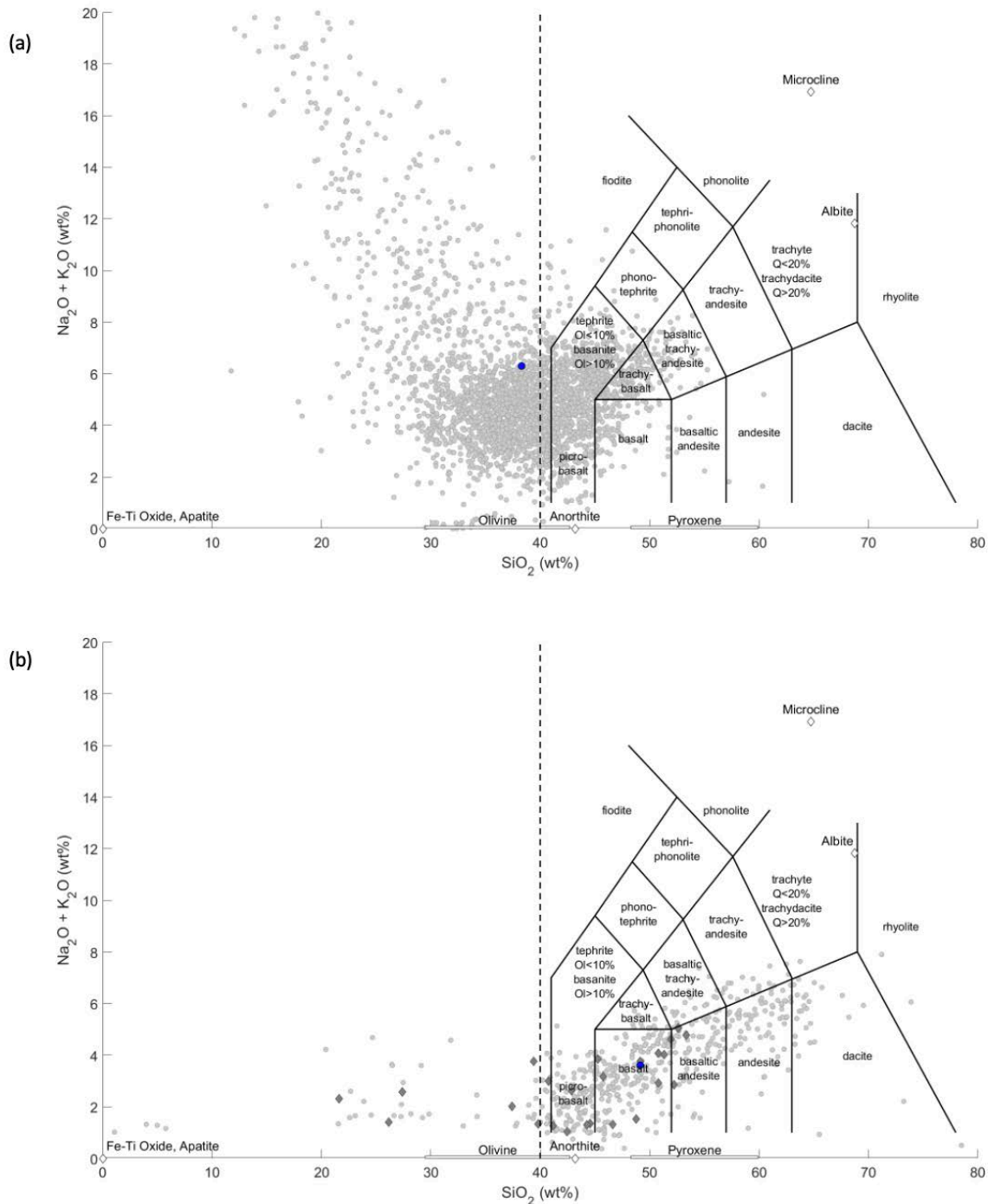
**Figure 8** is a ternary diagram of elemental compositions ( $\text{Al}_2\text{O}_3\text{-CaO+Na}_2\text{O+K}_2\text{O-FeO+MgO}$ ) for all the individual PIXL points and the bulk sum spectrum. Common mineral compositions are also plotted on the diagram. Most *Guillaumes* points lie in a triangle defined by minerals typical of mafic rocks (feldspar, pyroxenes, olivine). While there is little evidence of aluminum enrichment expected from open-system leaching and formation of aluminous clay minerals, there is a clear trend towards unidentified secondary phases which includes carbonates, halides, and sulfates. This plot supports the general conclusion that the analyzed rock is an aqueously altered but not intensely weathered basalt, gabbro, or basaltic sandstone.

**Figure 8 | *Guillaumes* sol 167 PIXL data.** Individual analysis points (grey) and bulk sum composition (blue) on a ternary diagram of molar abundances  $\text{Al}_2\text{O}_3\text{-(CaO+Na}_2\text{O+K}_2\text{O)-(FeO}_T\text{+MgO)}$ . Common igneous minerals (olivine, pyroxene, feldspar, Fe-Ti-oxides) are typically found within the red triangle whereas common clay minerals fall above this triangle.



The PIXL point measurements and bulk sum spectra are plotted on a total alkali versus silica igneous classification diagram in **Figure 9**. While this diagram can be useful for naming specific igneous lithologies, the high abundance of alteration phases complicates such usage. For that reason, no igneous lithology is assigned here. Of additional note on this diagram is the prominent array of points trending towards high alkalis and very low  $\text{SiO}_2$ ; this observation suggests the presence of alkali-rich salts such as NaCl or Na-perchlorate.

**Figure 9 | Total alkalis vs silica plots for *Guillaumes* and Cf-fr. (a) PIXL of *Guillaumes* (b) SCAM LIBS of all analyzed Cf-fr rocks through sol 168 (light symbols) and for *Guillaumes* (dark). The individual data points likely represent a mixture of one or more primary and/or secondary minerals. Bulk sum composition of PIXL data and average value of SCAM data shown by blue circles. Endmember igneous mineral compositions are shown for reference. The underlying igneous classification scheme does not apply to individual data points but provides a frame of reference.**

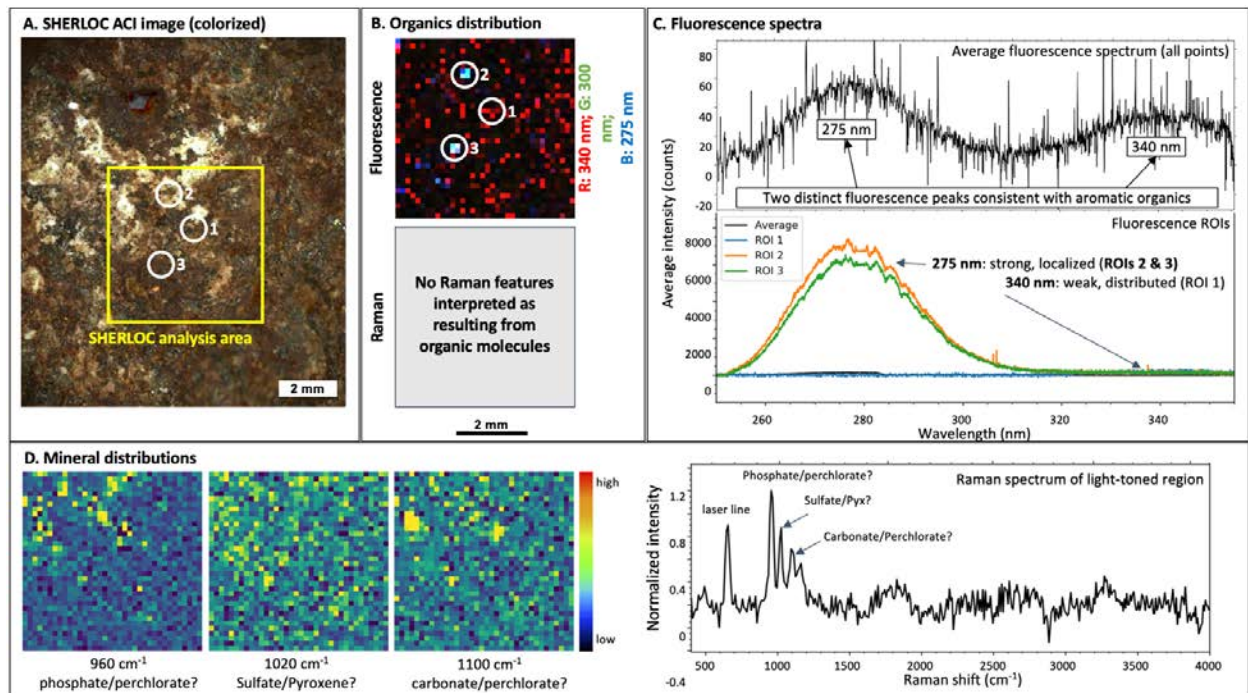


### Mineralogy and Organics-SHERLOC

A SHERLOC UV Raman and fluorescence survey scan was obtained on Sol 162. An additional SHERLOC scan, not discussed here, was obtained on Sol 161. The analysis footprints are indicated in **Figure 6**.

As shown in **Figure 10** and **Table 2**, SHERLOC Raman spectra indicate the likely presence of Ca-sulfate, Na-perchlorate, and possibly minor phosphate associated with the light-toned regions of *Guillaumes* (**Figure 10d**). An amorphous silicate phase widely distributed across the sample is also tentatively identified. These data are consistent with the multiple lines of evidence indicating aqueous alteration phases, especially concentrated in the bright white patches.

**Figure 10 | SHERLOC Spectral-textural correlations. (a)** SHERLOC ACI image. **(b)** Fluorescence and Raman maps of organic distribution. **(c)** Fluorescence spectra. **(d)** Raman mineral distribution and spectra



The average fluorescence spectrum indicates two peaks, one at 275 nm and the other at 340 nm (**Figure 10c**). Both are likely attributable to aromatic organic compounds in fairly low average abundance. The 275 nm peak is highly localized in a small number of spots (**Figure 10b**), but at the time of this writing it is not possible to link these hotspots to specific mineralogical or textural features of the rock. The 340 nm peak is more widely distributed across the analyzed region, suggesting it is a spatially dispersed organic constituent. Unlike fluorescence, there is no evidence from Raman spectroscopy for organic molecules in *Guillaumes*.

**Table 2 SHERLOC Mineral Identifications in *Guillaumes***

Sample	Certain	Almost certain (currently working to confirm)	Possible (not confirmed)	No detections found in the primary lithology
<i>Guillaumes</i>	Ca-sulfate (minor phase, occurs in white patches secondary to primary lithology)	Na-perchlorate (main phase, occurs in white patches secondary to primary lithology)	Phosphate (minor phase)  Observations where Ca-sulfate and perchlorate or phosphate were found in the same spot (main phase in white patches)  Amorphous silicate (potentially major phase covering whole target)	Pyroxene, olivine

### **Elemental Geochemistry and Mineralogy - Supercam**

SCAM LIBS and VISIR measurements of the pre- and post-abrasion surface, borehole, and borehole cuttings for the *Roubion* sample target are shown in **Figure 11**, a series of Harker oxide diagrams, supplemented with LIBS results from many Cf-fr rocks analyzed along the traverse from OEB to *Roubion* through sol 168. There are no striking differences among the *Roubion* borehole walls and cuttings and various *Guillaumes* abrasion patch LIBS datasets for MgO, Al<sub>2</sub>O<sub>3</sub>, and K<sub>2</sub>O. Although considerable scatter exists, the borehole appears to show higher FeO<sub>T</sub> and lower Na<sub>2</sub>O. This heterogeneity in composition within the cored and abraded rock is possible evidence for a greater concentration of salts near the rock surface. It is unclear whether FeO<sub>T</sub> may have been removed from the surface or enriched at depth. Despite these abrasion surface-borehole differences, the compositional trends from the abraded/cored rock are mostly in-family with those measured for the many Cf-fr rocks analyzed along the traverse. The main exception is the fact that the abrasion patch exhibits little evidence for SiO<sub>2</sub> concentrations higher than ~ 60 wt%, whereas such values are occasionally seen in other (unabraded) Cf-fr rocks. Such high SiO<sub>2</sub> concentrations may be restricted to natural rock surfaces. High MgO values like those of *Entrevaux* and *Alguines* (**Figure 11**, targets in the topographic low between *Artuby* ridge and *Séítah*) are absent in the abraded surface and are rare in Cf-fr rock analyses (the latter may reflect olivine regolith grains/sand on top of or trapped in Cf-fr paverstone rock crevices).

Many of the trends observed in these diagrams are reasonably attributed to mixing among igneous minerals, e.g. pyroxene and plagioclase. The 250 µm LIBS spots commonly interrogates more than one specific mineral (typical *Guillaumes* grain size is ~ 1 mm as described above).

To complement the PIXL data, the LIBS results from Cf-fr and from *Guillaumes* are also plotted on a total alkali vs. silica igneous classification diagram (**Figure 9b**). It is notable that within *Guillaumes*, PIXL picks up a strong trend towards high alkali and low silica (likely secondary salts) not seen by SCAM. Similarly SCAM LIBS of Cf-fr appears to yield more points with high SiO<sub>2</sub> concentrations (>50 wt %) than are observed by PIXL in *Guillaumes*. Both observations likely represent compositional heterogeneity among the different regions/rocks being analyzed.

SCAM VISIR spectra from the *Guillaumes* abraded patch have notable absorption features at 1.43 and 1.94 µm, attributable to hydration (**Figure 12**), a feature common to many of the Cf-fr rocks investigated

along the OEB to *Roubion* traverse. Interestingly, these features are not evident or are less pronounced in the *Roubion* borehole walls and in the *Roubion* cuttings. This observation may indicate preferential hydration of the upper surface of the investigated rock. A 2.28  $\mu\text{m}$  absorption feature observed in the abrasion patch may indicate Fe-bearing clay.

**Figure 11 | Harker oxide diagram.** SCAM LIBS spot compositions of natural rock surfaces of fractured crater floor (Cf-fr), *Guillaumes*, and borehole + borehole cuttings of *Roubion*. Distribution reflects individual laser spots ( $\sim 250$   $\mu\text{m}$ ) that represent mixtures of one or more primary and secondary mineral. Theoretical pyroxene, feldspar, and olivine compositions shown for reference.

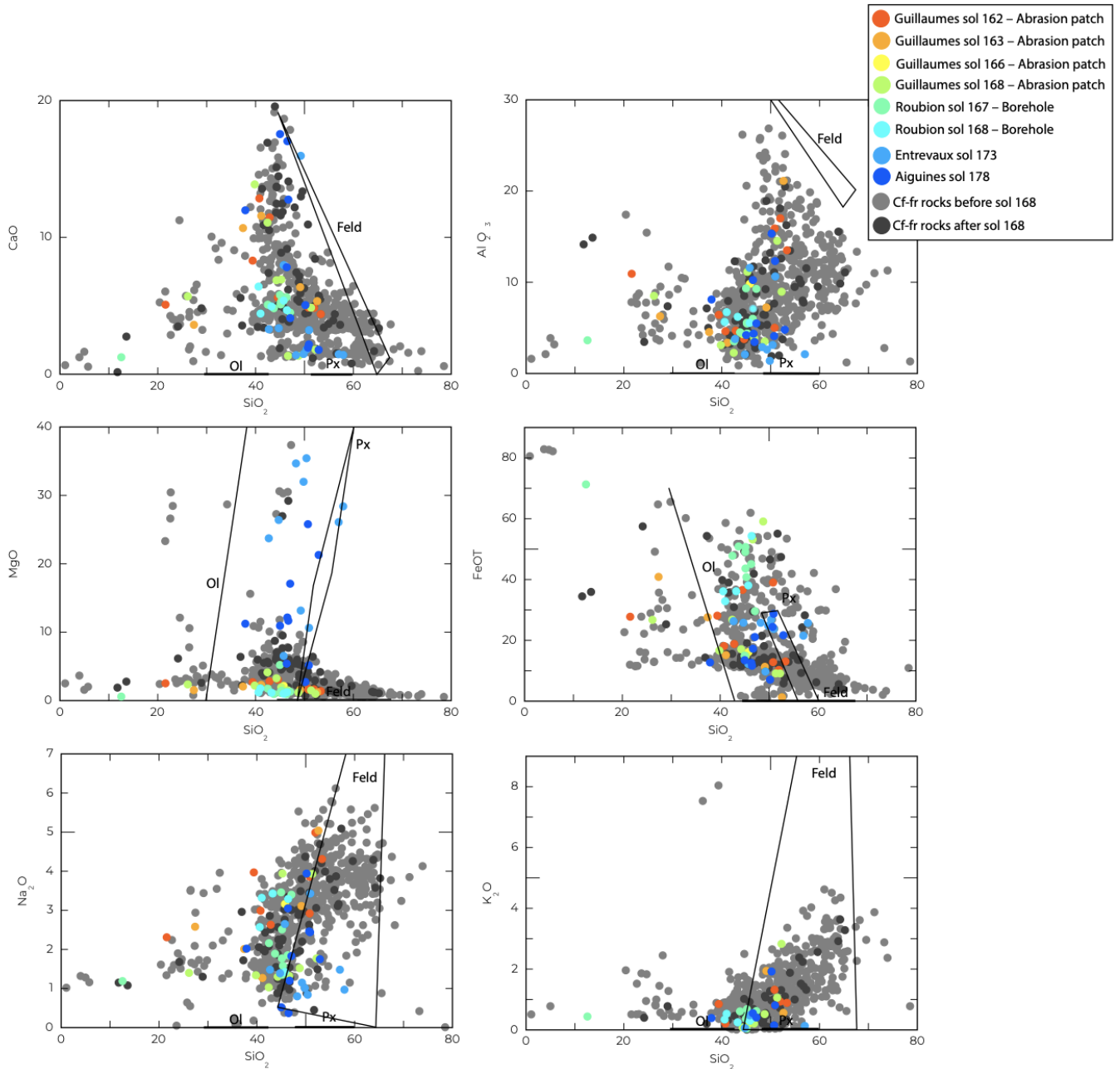
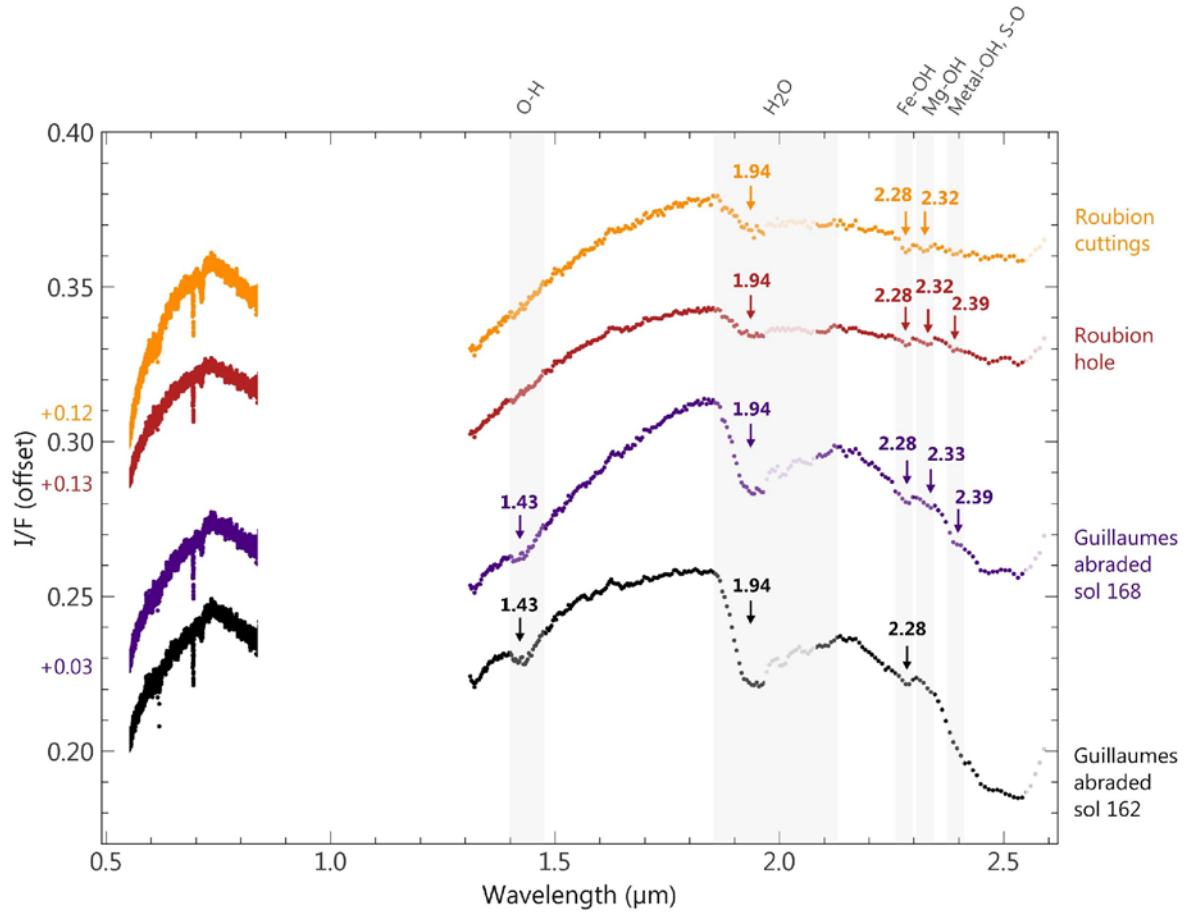


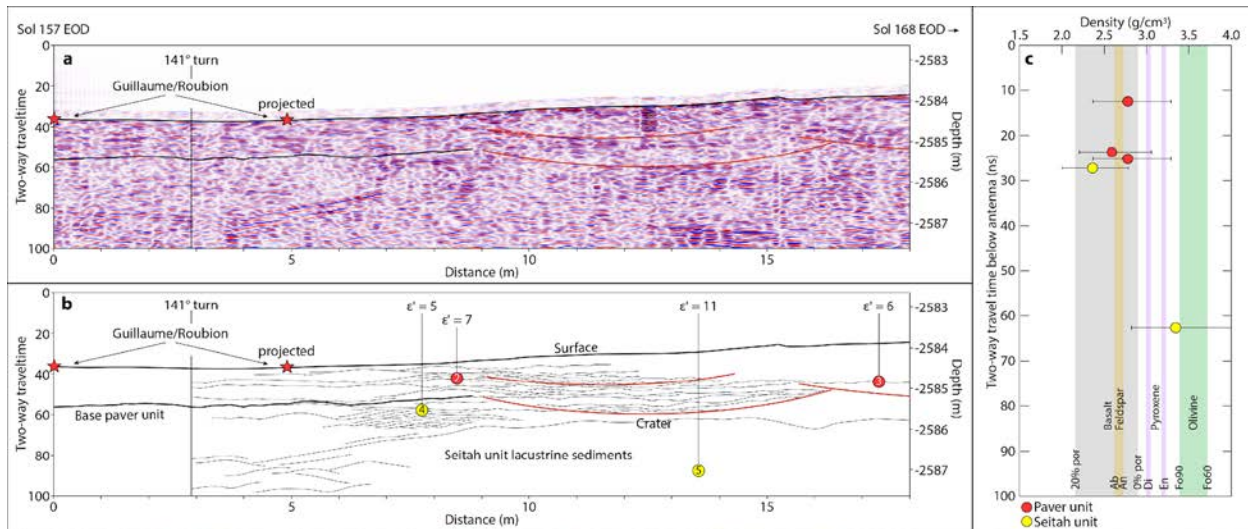
**Figure 12 | *Guillaumes* SCAM VISIR.** Abrasion surface shows absorptions at ~1.43 and 1.93  $\mu\text{m}$  that indicate hydration. These features are weaker in the borehole wall and borehole cuttings of *Roubion*.



## Subsurface Structure

The RIMFAX radargram for the sol 157-168 traverse path, including interpreted subsurface stratigraphy and densities from estimated permittivity values, are shown in **Figure 13**. Inferred densities are similar to basaltic material. The radargram shows surface-parallel reflectors and fine-scale layering below the paver-like morphology down to a burial depth of about a meter. Arcuate structures may be small, buried impact craters. Deeper reflectors (>3 m subsurface) appear to dip southward and may be associated with rocks of *Séitah*.

**Figure 13 | RIMFAX results from near *Guillaumes/Roubion*.** (a) Radargram for the sol 168 traverse including 3 m drive NE from the *Guillaumes/Roubion* site on sol 157 end of drive (EOD) followed by a 141° southward turn where the rover passes the target area at <2 m distance (“projected”). Base of the surface paver rock inferred to occur at ~1 m burial depth is denoted with a black line, and red lines denote curved reflector geometries that may be remnant impact craters. (b) Geological interpretation of reflector geometries in (a) illustrating subsurface stratigraphy with an ~1 m thick paver unit with decimeter scale surface-parallel layering overlaying south-dipping *Séitah* (?) reflectors. Location of permittivity measurements ( $\epsilon'$ ) from diffraction hyperbolae are denoted with red and yellow circles. (c) Densities derived from permittivity measurements annotated in (b) plotted vs depth given as two-way signal travel time below the antenna. Densities for basaltic rocks with zero to 20% porosity, feldspar, pyroxenes and olivine are shown for comparison. Paver unit densities are similar to basaltic rocks.



## Core orientation

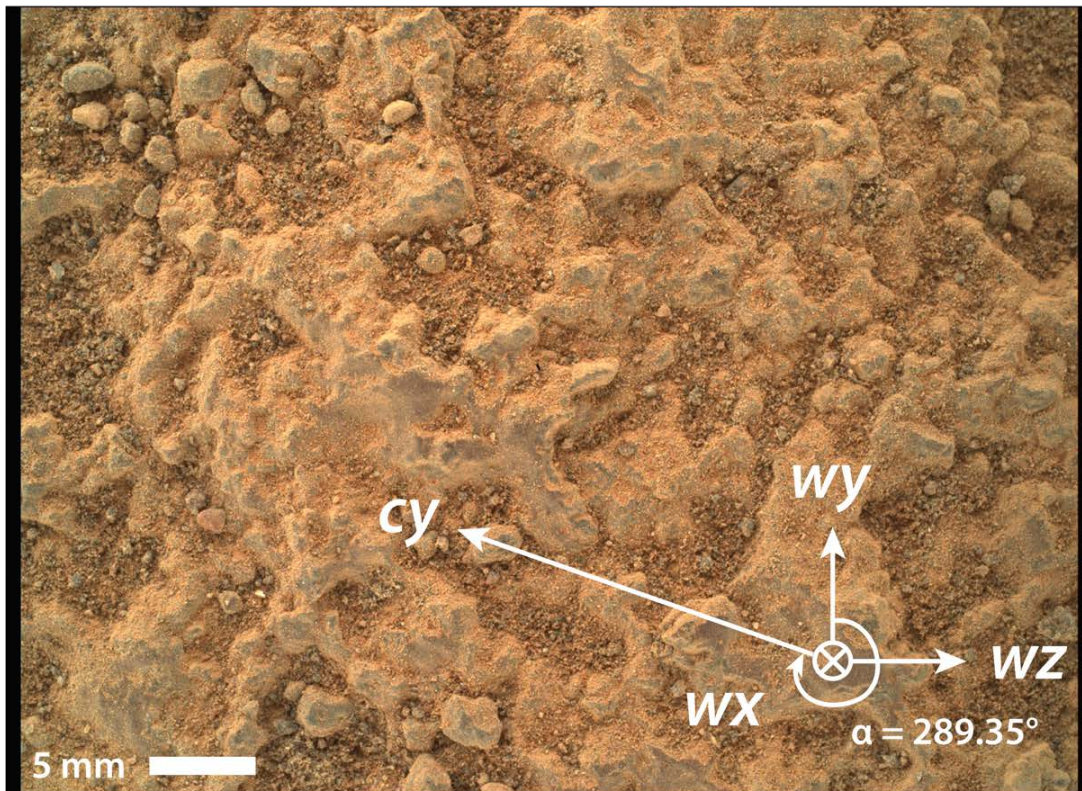
At the time of drilling and 7-cm pre-drilling WATSON imaging, the rover, corer, WATSON, and coring target (called “Roubion\_162.PSC.0668”), had the following characteristics:

1. Coring target normal (RMECH frame):  $\mathbf{uvw}_{\text{RMECH}} = (-0.005, -0.024, -1.000)$
2. Rover orientation quaternion at time of drilling (transferring from RMECH to SITE frame):  $\mathbf{bQII1} = (0.332886, 0.0174924, -0.00616092, 0.942785)$
3. Gravity vector (RMECH frame):  $\mathbf{g}_{\text{RMECH}} = (-0.0356277, -0.00190381, 0.999363)$
4. Coring Drill orientation quaternion (transferring from CD to RMECH frame):  $\mathbf{cdQb} = (0.665264, 0.233161, -0.661495, 0.255898)$

5. Rover orientation quaternion at time of acquisition of WATSON image  
SIF\_0161\_0681240940\_632FDR\_N0060000SRLC00702\_0000LMJ01: (transferring from RMECH to SITE frame):  $\mathbf{bQII2} = (0.332934, -0.0148229, -0.00733084, 0.942805)$
6. WATSON orientation quaternion at time of acquisition of WATSON image  
SIF\_0161\_0681240940\_632FDR\_N0060000SRLC00702\_0000LMJ01: (transferring from WATSON to RMECH frame):  $\mathbf{wQb} = (0.667723, 0.237418, -0.658963, 0.252084)$

Items 1 and 2 give a coring drill pointing vector estimate of (Hade = 3.33°; Azimuth = 195.47°). Item 3 gives an alternate coring drill hade estimate of (Hade = 2.76°). Items 2 and 4 gives a coring drill pointing vector estimate of (**Hade = 3.43°; Azimuth = 208.74°**). We report this as the final coring drill orientation estimate since it was estimated for the drill after preloading. Items 5 and 6 give an estimate of the angle between the WATSON y-axis and the up-dip direction in SITE coordinates of (Fig 14) (**core roll,  $\alpha = 289.35^\circ$** )

**Fig 14.** 7-cm standoff WATSON image of Roubion core target on sol 161. WATSON image SIF\_0161\_0681240940\_632FDR\_N0060000SRLC00702\_0000LMJ01 Image scale is  $31.1 \mu\text{m pixel}^{-1}$ . Orientation compass gives WATSON frame ( $\mathbf{wx}, \mathbf{wy}, \mathbf{wz}$ ). Core roll is clockwise angle of core y-axis,  $\mathbf{cy}$ , from  $\mathbf{wy}$ , given by  $\alpha = 289.35^\circ$ .



## **Preliminary Scientific Assessment**

### **Synthetic sample description and preliminary interpretation**

Sample type: **basaltic lava flow or microgabbro (or possibly basaltic sandstone)**

#### **1. Relationship with surrounding rocks**

- a. *Roubion* appears to be in family with the Cf-fr paverstone rocks investigated all along the traverse from OEB in terms of composition and texture. It is therefore considered representative of the low-lying morphology of Cf-fr.
- b. Within Cf-fr rocks, *Roubion* lies below both the high standing blocky and cratered expression to the E and N, and also the layered expression of *Artuby* ridge and *Mure*.
- c. *Roubion* is structurally higher than rocks of the *Séítah* region (Cf-f1) and is therefore younger, unless it is an intrusive.
- d. Although difficult to prove owing to partial burial, the sampled rock is thought to be in place or very nearly so.

#### **2. Texture and fabric**

- a. Grain size: approximately 0.5 to 1 mm (plagioclase, pyroxene, and alteration products).
- b. No obvious igneous flow banding or sedimentary structures were seen.
- c. Pits and crevices occur in the abraded patch but are not evident in the rock surface. They do not have the appearance of typical vesicles. These features may be voids created by some type of weathering.
- d. There is evidence for interlocking grain texture, suggesting crystallization from a magma.
- e. There is no compelling evidence of intergranular porosity or cements, common to many sedimentary rocks.

#### **3. Mineralogy and chemistry**

- a. Minerals present include pyroxene, feldspar, and FeTi-oxides, and secondary iron oxides or silicates, sulfates, Na-Cl salts (halite? Na-perchlorate), and possibly phosphate. The phosphate could alternatively be primary.
- b. The bulk composition is consistent with a basalt modified by aqueous alteration. The alteration is sufficiently intense that it is not possible to assign a specific igneous lithologic name without further analysis to isolate the least altered portions of the rock.
- c. Low concentrations of aromatic organics are present.

#### **4. Alteration/secondary characteristics**

- a. There is significant textural and mineralogical evidence in the abraded patch for interaction of the rock with aqueous fluids, alteration, and mineral hydration.
- b. Secondary mineralogy remains speculative, but likely includes Ca-sulfates, Na-perchlorates, Ca-phosphates, and halite.
- c. The absence of Al-rich phases argues for low water/rock ratios and little cation leaching.

## **Returned Sample Science Considerations**

Outcrop morphology and texture, as well as the appearance, composition and mineralogy of the abraded patch suggest that *Roubion* represents a fine- to medium-grained mafic lithology, possibly a basaltic lava flow or a microgabbro. An alternative interpretation of this unit is volcanoclastic sandstone derived from basaltic rocks of the Jezero watershed. The striking absence of sedimentary textures in the well-exposed Cf-fr rocks from OEB to *Roubion* disfavors the latter interpretation and would constrain potential sedimentary depositional mechanisms if this were indeed a sedimentary rock. The crystallization age of volcanic rocks (or volcanic minerals in a sandstone) can be readily determined by radiometric methods undertaken on returned samples. If the timing of this rock's deposition can be obtained (e.g., if *Roubion* is a lava flow), this age would quantitatively constrain the ages of other crater floor units: *Séítah* is older, and the layered rocks of *Artuby* ridge and *Mure* are younger. The latter presumes that *Roubion* is not an intrusive rock. The composition of igneous rocks and/or mafic minerals in this rock would provide a geochemical probe that would reveal the geophysical and geochemical nature of the planet's interior at the time of eruption. Furthermore, if *Roubion* can be confidently related to the heavily cratered portions of Cf-fr (e.g., to the east of the traverse), and the surface exposure history of Cf-fr can be understood, then geochronology of a returned sample of this lithology may provide a test of (or calibration for) crater chronology models. However, we are not yet confident in tying *Roubion* to the heavily cratered part of Cf-fr.

Patches of water-soluble salts compellingly document aqueous alteration in this rock. There is no strong evidence for clay minerals in *Guillaumes*, suggesting that chemical weathering (i.e., open system behavior in which cation leaching yields clay minerals) is limited. There is no doubt this rock has experienced interaction with one or more aqueous fluids, possibly groundwater that may or may not be related to Jezero lake. Soluble salts (e.g., halite or perchlorate) almost by definition document the final aqueous interaction experienced by this rock. It is likely these water-rock interactions occurred in a habitable subsurface environment recorded in the alteration mineral assemblage. Analysis of the secondary minerals may be used to study the chemistry and conditions (e.g., pH, temperature, salinity, age) of aqueous fluids. Similar salts on Earth are known to contain organic molecules and even fossilized microscopic life.

For these reasons a returned sample of this unit has high science value for astrobiology, as a point in the geochemical/geophysical evolution of the martian interior and surface environment, and for understanding the geologic setting and timing of Jezero floor units.

The core sample was not recovered. The sealed tube includes martian atmosphere and a few tiny *Roubion* particles that are most likely fragments of the failed core. Thus, the sample tube could be used to study martian atmosphere. Alternatively (or perhaps in addition) the tube may provide a sample processing contamination blank.

## **References**

- Stack et al. (2020) Photogeologic Map of the Perseverance Rover Field Site in Jezero Crater Constructed by the Mars 2020 Science Team, *Space Sci Rev* 216:127, <https://doi.org/10.1007/s11214-020-00739-x>
- Goudge, T.A., Mustard, J.F., Head, J.W., Fassett, C.I., & Wiseman, S.M. (2015). Assessing the mineralogy of the watershed and fan deposits of the Jezero crater paleolake system, *Mars. Journal of Geophysical Research: Planets*, 120, 775-808, doi:10.1002/2014JE004782.
- Stack, K.M. et al. (2020). Photogeologic Map of the Perseverance Rover Field Site in Jezero Crater Constructed by the Mars 2020 Science Team. *Space Science Reviews*, 216, 127, doi:10.1007/s11214-020-00739-x.
- Sun, V.Z. & Stack, K.M. (2020). Geologic Map of Jezero Crater and the Nili Planum Region, Mars. USGS Scientific Investigations Map 3464, pamphlet 14 p., scale 1:75,0000, doi:10.3133/sim3464.
- Holm-Alwmark, S., Kinch, K.M., Hansen, M.D., Shahrzad, S., Svennevig, K., Abbey, W.J., Anderson, R.B., Calef, F.J., Gupta, S., Hauber, E., Horgan, B.H.N., Kah, L.C., Knade, J., Miklusicak, N.B., Stack, K.M., Sun, V.Z., Tarnas, J.D., Quantin-Nataf, C. (2021). Stratigraphic Relationships in Jezero Crater, Mars: Constraints on the Timing of Fluvial-Lacustrine Activity from Orbital Observations. *Journal of Geophysical Research: Planets*, 126, 7, doi:10.1029/2021JE006840

# INITIAL REPORT

## M2020-190-3 Montdenier

---

**Sample Designation:** M2020-190-3 Montdenier

**Date of Coring:** 31-Aug-2021

**Mars Time of Sample Core Sealing:** 16:53:19 LMST, Sol 194, Ls 92.5

**Latitude (N), Longitude (E), Elevation:** 18.43074132, 77.44436502, -2574.553 m

**Campaign:** Crater Floor

**Region of Interest:** Artubyridge

**Lithology:** Fine-grained mafic and likely igneous rock, possibly basalt (alternatively, basaltic sandstone). Primary minerals are plagioclase, pyroxene, and FeTi oxides. Aqueous alteration is indicated by abundant secondary minerals including iron oxide, Ca-sulfates (occasionally hydrated), phosphate, and minor carbonate.

**Estimated Volume Recovered:** 8.4 cm<sup>3</sup>

**Coring Bit Number:** 5

**Core Orientation:** hade = 9.42°; azimuth = 219.27°; core roll = 191.24°

**Sample Serial Numbers:** Tube SN266; Seal SN170; Ferrule SN099

**ACA Temperature at Time of Sealing:** 37 C

**Estimated Rover-Ambient Pressure and Temperature at Time of Sealing:** 702 Pa, 245 K

**Estimated Amount of Martian Atmosphere Headspace Gas:** 1.2x10<sup>-6</sup> mol

**Abrasion Patch Name and Depth:** Bellegarde, 8 mm

**Anomalous Behavior:** Multiple sols between coring and sealing

---

November 30, 2021

*J. I. Simon, K. A. Farley, T. Bosak, A. Udry, S. VanBommel, S. McLennan, L. Mandon, Y. Goreva, R. C. Moeller, V. Sun, E. L. Berger, A. D. Czaja, A. C. Fox, C. H. Lee, E. L. Scheller, S. Sharma, S. Siljeström, H. E. F. Amundsen, S.-E. Hamran, T. M. Casademont, L. W. Beegle, K. C. Benison, V. C. Debaille, L. Hausrath, C. Herd, J. Hurowitz, L. E. Mayhew, D. L. Shuster, K.M. Stack, M. Sylvestre, B. P. Weiss, P. A. Willis, R. Wiens, M.-P. Zorzano, and the Mars 2020 Team*

## **Summary Description**

Collection of *Montdenier* and *Montagnac*, the pair of rock cores from the second sample target of the Mars 2020 mission, was conducted in the *Citadelle* area, a relatively high-standing outcrop within the “crater floor fractured rough” orbital unit (Cf-fr of Stack et al., 2020; **Figure 1**). *Citadelle* sits on the crest of *Artuby*, an ~1 km long NW-SE trending linear ridge exposing on its NE side a several meter high cliff of the crater floor stratigraphy. *Artuby* ridge borders the southern edge of an exposure of rocks called *Séítah* (Cf-f-1 of Stack et al., 2020). After an unsuccessful first attempt to collect a core from low-lying outcrops at *Roubion*, *Perseverance* traversed about 450 m NW along the base of *Artuby* ridge, in a regolith-covered topographic low that defines the boundary between *Séítah* and Cf-fr. *Perseverance* traversed to *Citadelle* to access and sample crater floor rocks that were prominently exposed on the ridgeline (**Figure 2**) on the supposition that such rocks would be more resistant to disaggregation than *Roubion*.

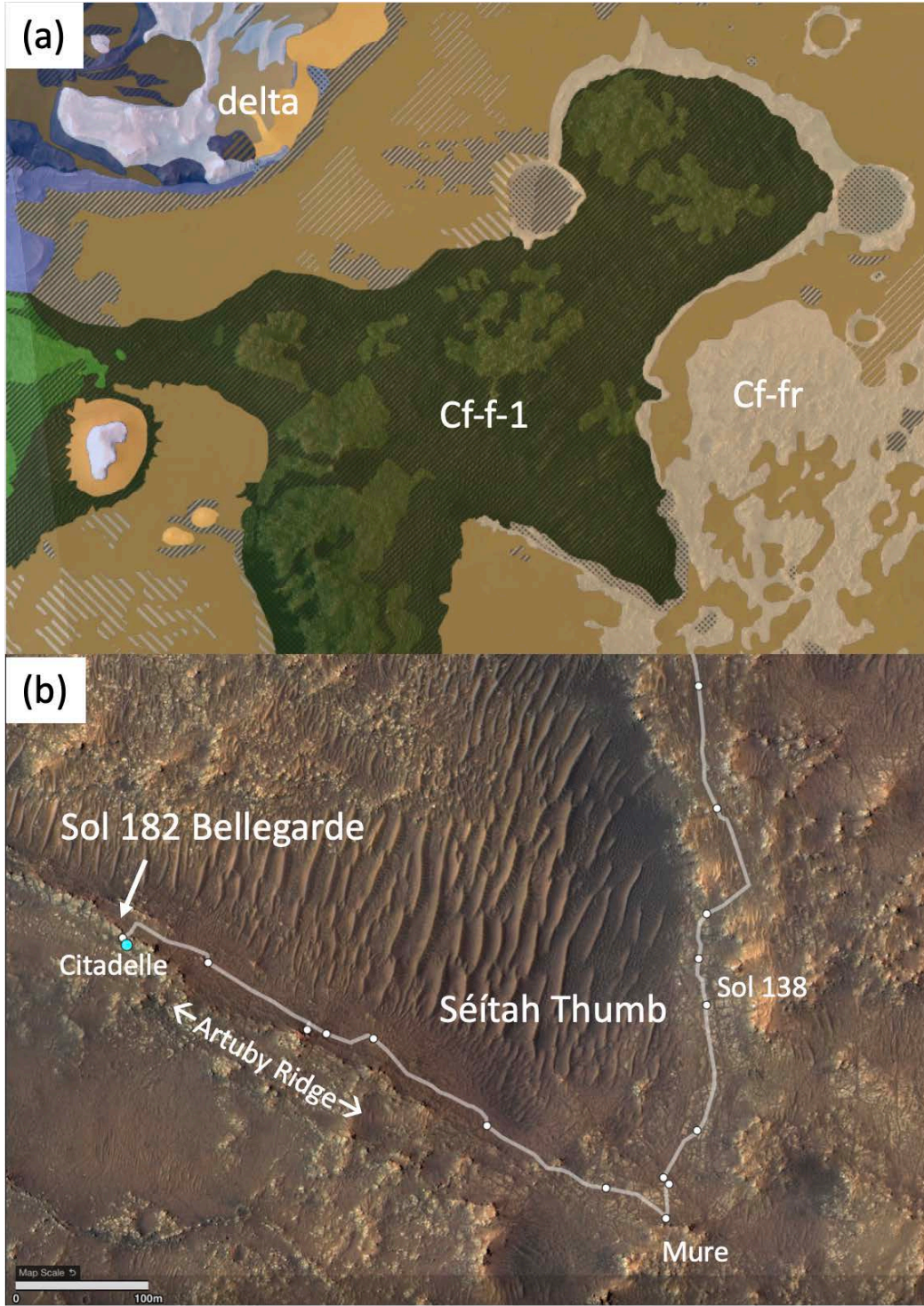
Prior to landing, the Cf-fr unit was variously interpreted to be igneous (a lava flow or a volcanoclastic deposit) or sedimentary (fluviolacustrine or aeolian). The lithology of Cf-fr remains uncertain, though evidence from *Roubion* suggests that at least part of Cf-fr is igneous. Unlike outcrops of Cf-fr observed between the Octavia E. Butler (OEB) landing site and *Roubion*, rocks of *Artuby* ridge display fine and coarse semi-continuous layers and a distinctive knobby texture (**Figure 3**). Despite excellent exposure, there is no compelling evidence for sedimentary structures formed via traction transport, nor were clasts observed. Supercam data collected on these rocks reveal an altered (hydrated, iron-oxide-bearing) mafic composition with distinct crystals greater than the ~200 µm size of the LIBS shots.

The *Montdenier* and *Montagnac* cores, and their companion *Bellegarde* abrasion patch, were acquired on a small tabular boulder (*Rochette*, ~40 cm across) that is a member of a NW-SE-trending band of boulders or outcrop on the SW side of the *Artuby* ridge crest. These rocks are morphologically consistent with a degraded lava flow or layer (**Figure 2b**). *Rochette* moved slightly during coring, suggesting it is not currently anchored in-place. Although *Rochette* may have been displaced from its original location, the similarity and abundance of blocks near *Rochette* suggest displacement is likely small. *Rochette* was selected for coring primarily for its accessibility by the rover, limited relief, and perceived resistance to disaggregation during coring. Additionally, its position high on *Artuby* ridge places it stratigraphically above and potentially younger than other studied rocks including *Roubion* and Cf-f-1 rocks outcropping in *Séítah*.

The *Bellegarde* abrasion patch is dominated by 0.2-0.5 mm pyroxene and plagioclase crystals, and is consistent in composition and texture with an aphanitic holocrystalline basalt (or microgabbro). The interlocking crystal texture and the lack of fine-grained matrix or intergranular cement suggest an igneous origin. Extensive iron-rich brown patches are indicative of aqueous alteration, especially evident around white patches that may reflect cavities filled by secondary minerals such as Ca-sulfate (occasionally hydrated) and phosphate. Carbonate and amorphous silicates were tentatively identified within *Bellegarde* by SHERLOC, as were three types of aromatic organic signals, one distributed widely across the abrasion patch and two localized in a few specific regions. Chemical characteristics of the abraded patch are generally consistent with other Cf-fr rocks observed along the traverse from OEB to *Roubion*, and along *Artuby* ridge from *Roubion* to *Bellegarde*, providing high confidence that the sampled rock is reasonably representative of the Cf-fr unit. The abraded rock appears less altered (has

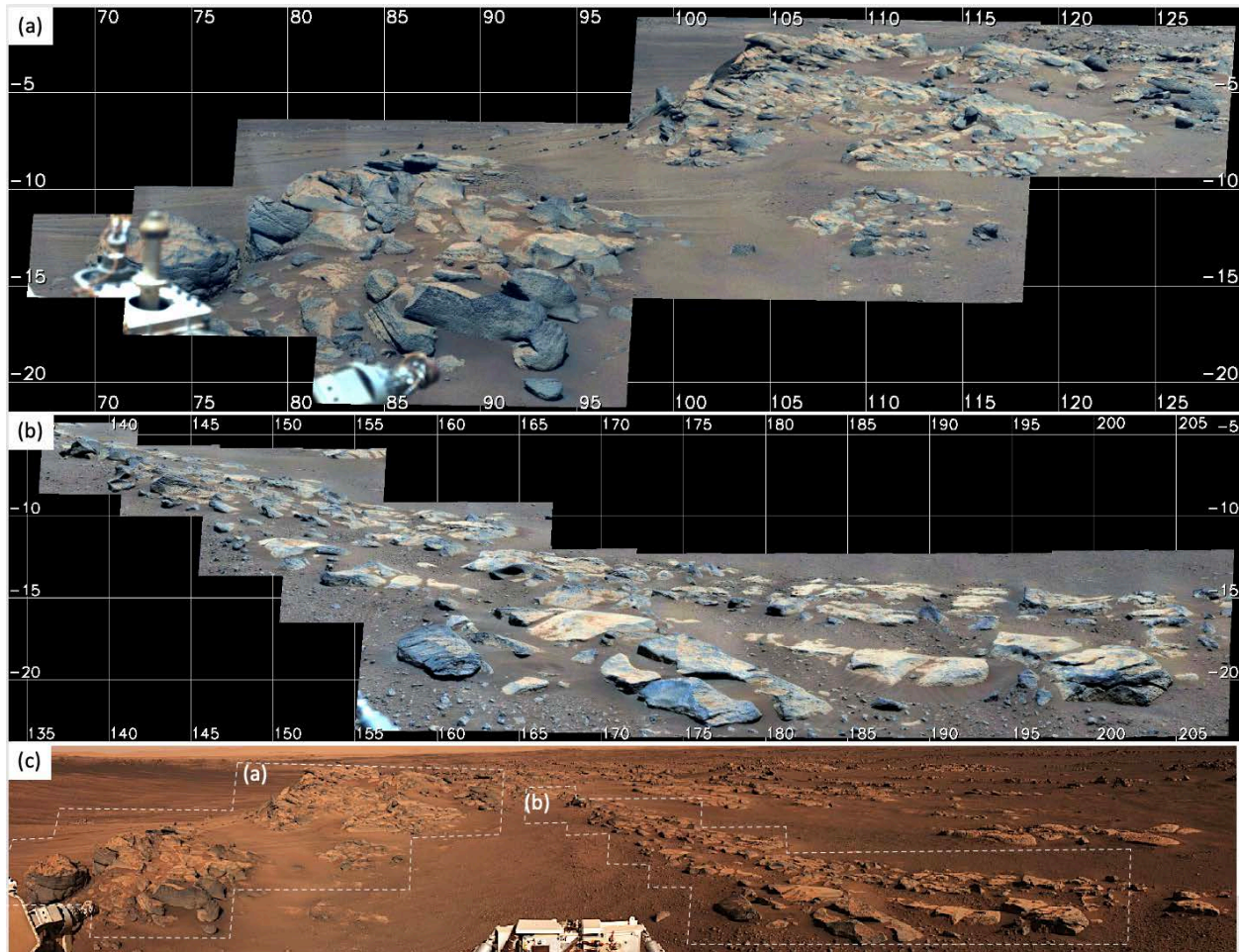
no obvious pits or crevices, has less abundant secondary mineralization, is less reddish, and overall appears more intact) than *Roubion*, and therefore better represents the primary lithology.

**Figure 1 | Regional context.** (a) geologic map, Stack et al. 2020. (b) HIRISE map with *Perseverance* traverse leading to *Bellegarde*.



Given the failure to acquire core at *Roubion*, coring of *Montdenier* included a special step to confirm sample-in-the-tube with ZCAM images prior to tube sealing. This added four sols to the period between coring and sealing; in that period the sample was held in the drill, external to the rover. Coring of both *Montdenier* and *Montagnac* produced a hole and tailings pile of expected appearance, the ZCAM image of *Montdenier* revealed core in the tube, and the sealing process of both tubes completed nominally. The volume probe indicated full length cores (i.e., ~60 mm or ~8.5 cm<sup>3</sup>) were acquired in both cases.

**Figure 2 | ZCAM and NCAM images of *Citadelle* area. (a)** caprock of crater floor stratigraphy defining the crest of *Artuby* ridge **(b)** surface unit from which sample cores *Montdenier* and *Montagnac* were collected. **(c)** overview of (a) and (b) showing how the dip of the strata shallows from about 10° to near horizontal to the south away from *Séitah*.



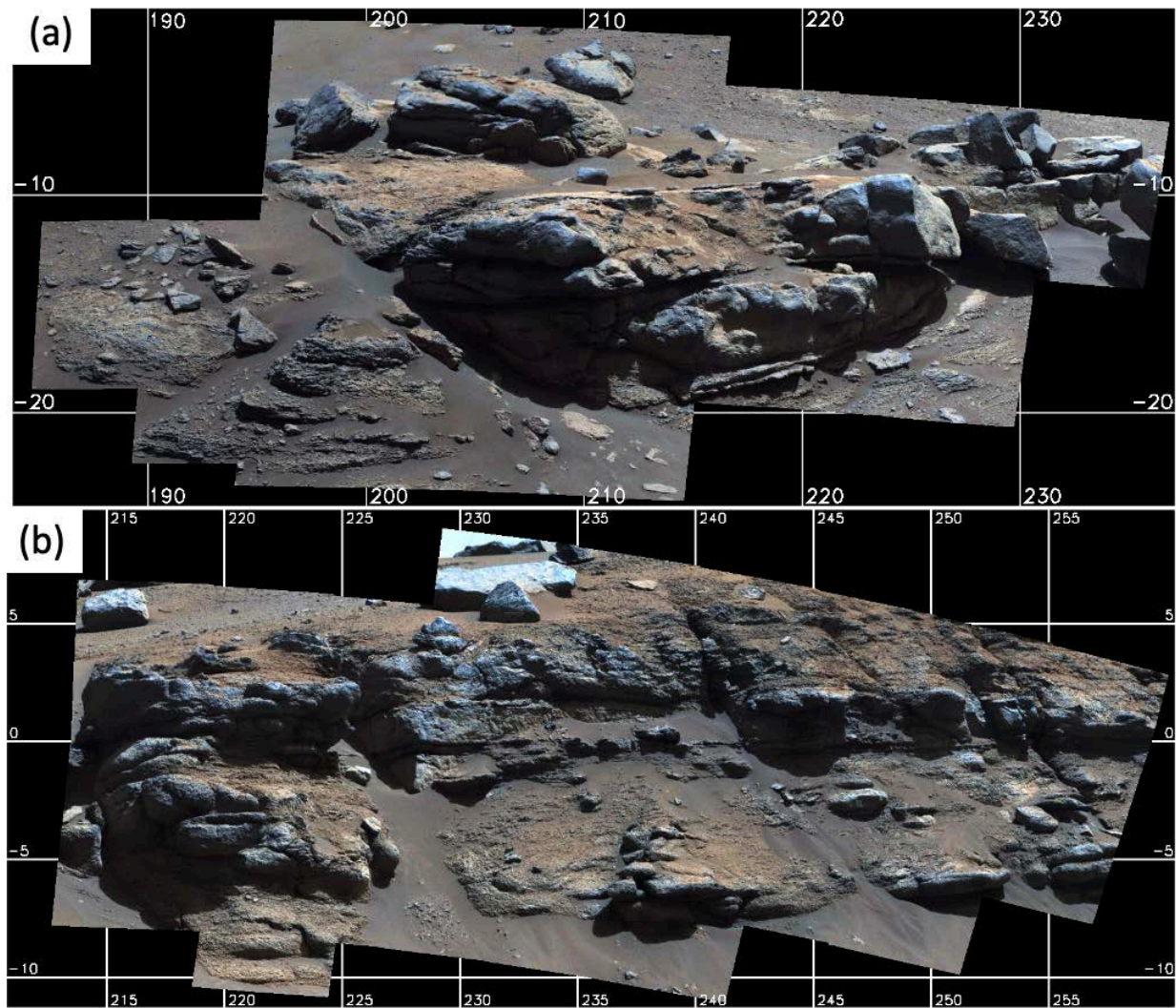
## **Stratigraphic and Geologic Context**

The *Montdenier* and *Montagnac* cores and *Bellegarde* abrasion patch were collected from *Rochette*, a ~40 cm wide tabular boulder that is part of an elongated exposure of similar rocks on the SW side of the *Artuby* ridge crest (**Figure 2**). *Rochette* and the boulders in its immediate vicinity are inferred to be part of a single degraded rock layer forming part of the caprock of *Artuby* ridge based on the similar alignment of boulder long axes, their similar thickness, and their nearly interlocking shapes. The strata

exposed by the *Artuby* scarp appear to be dipping  $\sim 10^\circ$  to the southwest, roughly perpendicular to the strike of *Artuby* ridge. This dip appears to flatten out within tens of meters southwest of the ridge crest (**Figure 2c**). The dip and exposures are such that the rock layer containing *Rochette* may be a few tens of cm higher in the stratigraphy than rocks on the crest of *Artuby* ridge.

The contact between Cf-fr and Cf-f-1 locally coincides with *Artuby* ridge (**Figure 1a**). Cf-fr is distinguished from other units on the crater floor by its relatively high crater density, curvilinear margins, and lack of the strong olivine absorption characteristic of Cf-f-1 (Goudge et al., 2015). Rocks thus far examined along *Artuby* ridge, including *Rochette*, lack evidence for abundant olivine, suggesting the exposed rocks of the ridge are all part of the Cf-fr unit. Unlike the apparently structureless Cf-fr rocks from OEB to *Roubion*, the rocks forming *Artuby* ridge are clearly layered, with layers varying in thickness from a few cm to several tens of cm (**Figure 3**). The Cf-fr - Cf-f-1 contact is inferred to lie in a topographic low at the base of the ridge, where it is obscured by regolith.

**Figure 3 | ZCAM images of layering of Cf-fr rocks exposed in near-vertical outcrop. (a)  $\sim 2$  m cliff at *Mure* Sol 169. (b)  $\sim 2$ -3 m cliff at *Artuby* Sol 177.**



*Rochette* is stratigraphically higher than rocks of *Séítah* and may therefore be younger. The relationship between the *Artuby* cap rocks and those observed at *Mure*, OEB, and north and east of OEB is presently unknown given the discontinuity of outcrop exposure and local disruption by impact craters, but these caprocks share morphological and compositional similarities suggesting they may be correlative. The age and stratigraphic relationship of *Artuby* caprocks relative to the rocks of the Jezero delta is also uncertain. Goudge et al. (2015) interpreted the unit containing *Rochette* to be younger than the Jezero delta, and the youngest in the crater, while Sun and Stack (2020), Stack et al. (2020), and Holm-Alwmark et al. (2021) proposed that the rocks of the Jezero crater floor, including *Rochette* and *Roubion*, pre-date the currently exposed Jezero delta deposit.

## **Operations**

After failing to recover sample at *Roubion* (see Initial Report for M2020-164-2 *Roubion*), the mission team prioritized a sampling attempt on a rock more likely to resist disaggregation. Boulders of the upper layers of *Artuby* ridge were considered likely to have survived eons of exposure to wind abrasion, suggesting less friability than the low-lying degraded-appearing outcrop at *Roubion*. Accordingly, a traverse to the first location where such rocks were accessible along the rover's strategically planned traverse, at a site named *Citadelle*, was undertaken.

On Sol 168 *Perseverance* executed its first drive NW along *Artuby* ridge, leaving the *Roubion* sampling site and gradually regaining about 10 meters of elevation along the base of the ridge. On Sol 178 *Perseverance* executed an autonomous drive that included a sharp turn up the NE-facing slope of *Artuby* ridge, concluding at *Citadelle* (**Figure 1 and 2**). After selecting *Rochette* as the preferred sampling target, abrasion at *Bellegarde* and collection of the first core *Montdenier* were respectively conducted on Sols 182 and 190. A paired-core, strategically developed sampling sol path was executed between Sols 180 and 196. Because visual proof of core acquisition was desired before ingesting the sample tube inside the rover, sealing of the *Montdenier* tube was delayed until Sol 194. In the intervening 4-sol period, the sample was exposed to the martian environment. This exposure is a notable deviation from expected practice in which a tube is sealed autonomously within hours of coring. The paired core *Montagnac* was collected and sealed on Sol 196 following the normal automated procedure and without visual confirmation prior to sealing.

On Sol 197, after successful collection of two cores, *Perseverance* executed its next drive NW along *Artuby* ridge, heading towards the planned entry point into *Séítah*.

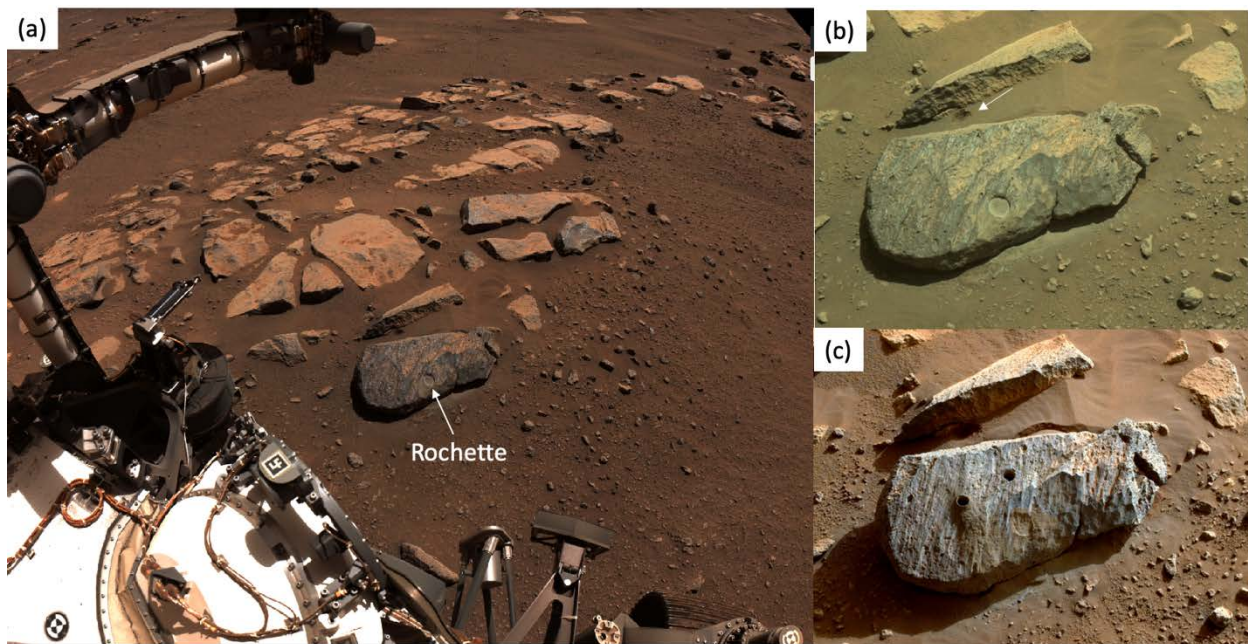
## Sample-Related Observations

### *Workspace Images*

**Figure 4** shows the workspace in which both the *Bellegarde* abrasion patch and the *Montdenier* and *Montagnac* coring were undertaken. **Figure 4a** shows the tabular boulder *Rochette* and its alignment with, and spacing from, other blocks near where these activities occurred. *Rochette* appears darker in tone than nearby blocks, likely because its surface is less dusty. The *Rochette* block is smooth, with sharp angular edges, abundant mm- to cm-scale pits, and parallel fluting suggesting wind abrasion. It stands ~20 cm higher than the surrounding surface, and on several sides overhangs the surrounding regolith. *Rochette* has a mottled grey and purple appearance. There is no evidence for layering or any other substantial heterogeneity across the boulder. *Rochette* appears to have broken off of, and is slightly displaced from, the triangular shaped rock behind it (**Figure 4**).

**Figure 4b and 4c** show *Rochette* after abrasion of the *Bellegarde* patch and after the acquisition of the two cores, respectively. All three targets (*Bellegarde*, *Montdenier*, and *Montagnac*) seem to have been acquired in compositionally similar material. Tailings slid off the rock during abrading and coring, and appear grey on the reddish brown regolith in front of *Rochette*. Behind *Rochette*, localized regolith subsidence and a steep crevice formed during abrasion. These features were further developed during coring.

**Figure 4 | NCAM workspace images. (a)** flat-lying outcrop containing resistant target rock *Rochette*. **(b)** Close-up of *Rochette* showing a abraded surface *Bellegarde*. The act of abrading *Rochette* resulted in localized subsidence of regolith (arrow), and **(c)** *Rochette* with boreholes from a acquisition of sample cores *Montdenier* (right hole) and *Montagnac* (left hole). *Rochette* is ~40 cm across.



### Pre and Post Coring/Abrasion Images

WATSON images at two different standoffs prior to abrasion and coring are shown in **Figures 5 and 6**. At high resolution the rock surface appears very smooth and fairly free of dust except where it has collected along the edges of subtle sculpted surfaces and within rare pits. In contrast to the abraded patch (**Figure 5b**, and see below), these natural surfaces show no evidence of crystals or grains. A heterogeneous purple surface layer or coating is evident in these images (see post-abrasion discussion). A similar coating appears on many rocks along the traverse from OEB to *Roubion*.

**Figure 5 | WATSON images. (a) pre-abrasion target surface. (b) post-abrasion target surface.**

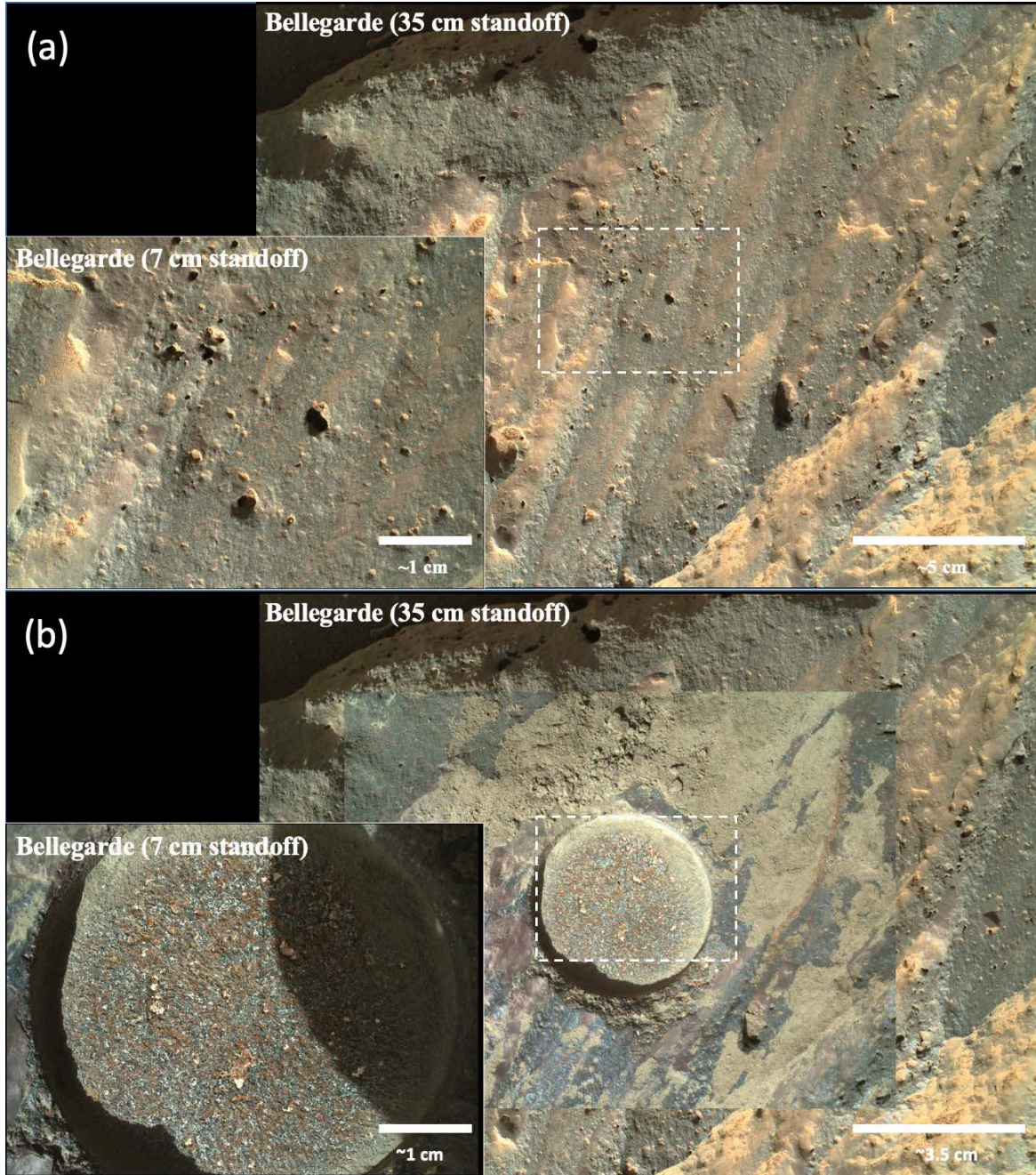
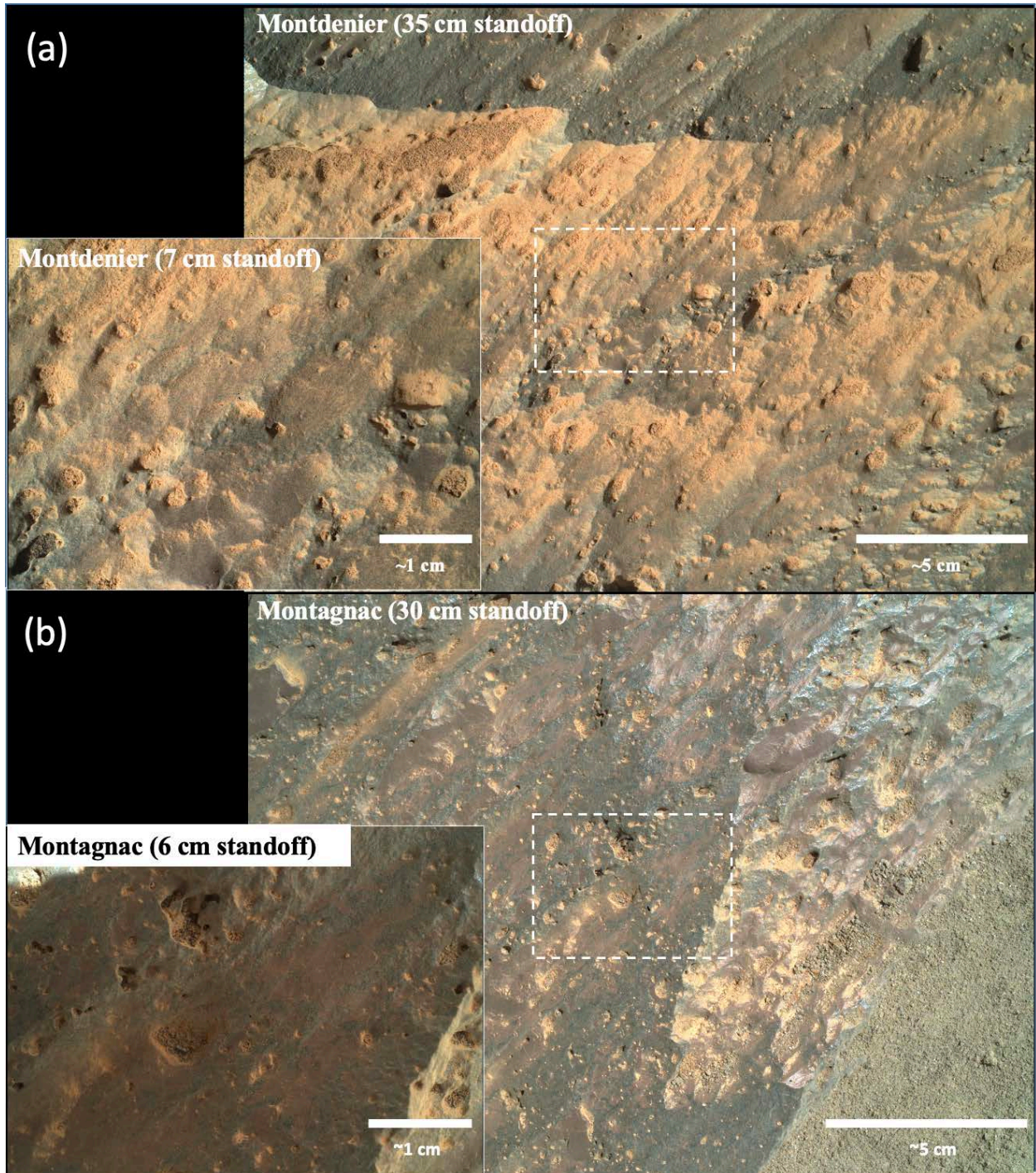
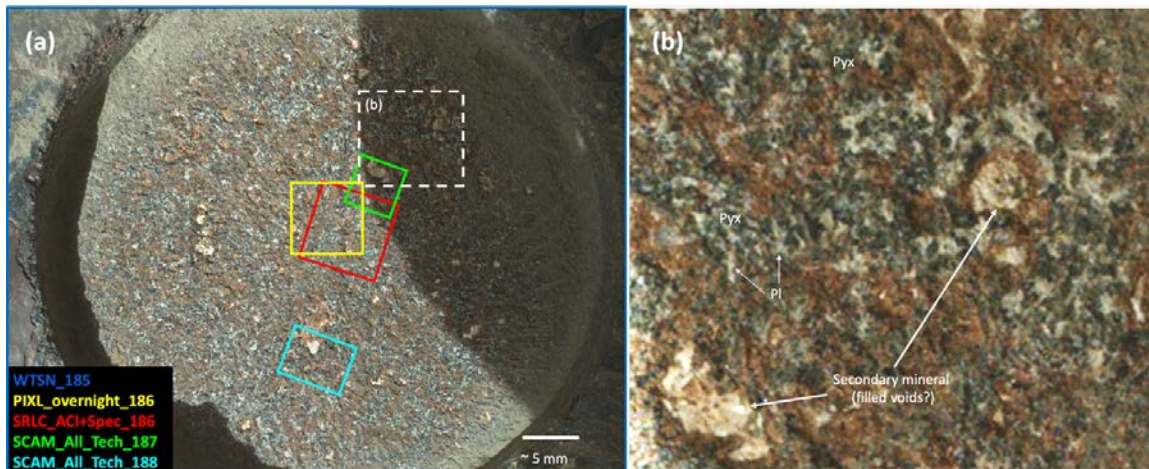


Figure 6 | WATSON images. (a) pre-coring target surface Montdenier. (b) pre-coring target surface Montagnac.



**Figure 7 | WATSON images of abrasion surface. (a)** ~25 cm standoff, showing PIXL, SHERLOC, and SCAM instrument placement. Abrasion patch is 5 cm across. Inset **(b)** holocrystalline rock texture with regions of less altered intergrown plagioclase and pyroxene and secondary minerals potentially filling voids.



**Figure 7** shows a WATSON image of the gDRT-cleared abraded patch *Bellegarde*. Notable observations include:

a) 0.2-0.5 mm-size dark and light grains or crystals comprise most of the abraded surface. White materials have at least two distinct morphologies and tones: some have angular shapes, others (especially those that are brightest white) have a more irregular outline. The latter suggests a secondary cavity-filling or replacement substance. Ignoring these patches as well as the brown material described in b, the dark and light grains appear roughly equal in grain size with no obvious spatial heterogeneity in relative abundance. In some cases, for example in parts of **Figure 7b**, the grains may be interlocking as if crystallized from a magma. Taken together these observations are consistent with the appearance of a holocrystalline basalt.

b) Some parts of the abraded surface are reddish brown in color with more diffuse boundaries, suggesting an (Fe-rich?) stain or coating. In some cases, this apparent staining is seen as haloes and in association with (or even partially covering) the irregular-shaped white phases that appear to fill cavities. This association can also be seen in Cachecam images showing the bottom of both the *Montdenier* and *Montagnac* cores (**Figure 8**). The *Montagnac* core has one especially large white patch in its Cachecam image, measuring more than 3 mm across and accounting for about 10% of the entire exposed surface of the bottom of the core.

c) The surface of *Rochette* and associated boulders appear to have a purple to tan coating (**Figure 5b**). This coating is particularly common on what appear to be wind abraded and likely older surfaces. The coating is less obvious, possibly thinner to absent, on fractured (younger) dark gray surfaces. These rough fractured surfaces also tend to exhibit more pitting.

d) Unlike the ragged appearance of the edge of the *Guillaumes* abrasion patch (*Roubion* sample), that of *Bellegarde* is sharp and angular. In some places the previously noted purple material can be seen near or on the original surface (**Figure 9**). It is reasonable to expect that the *Montdenier* and *Montagnac* cores contain some of this purple material.

**Figure 8 | Cachecam images of the bottom of sample cores. (a) Montdenier on Sol 194. (b) Montagnac on Sol 196.** Core diameter is ~1.3 cm. Note reddish haloes around secondary minerals potentially filling voids.

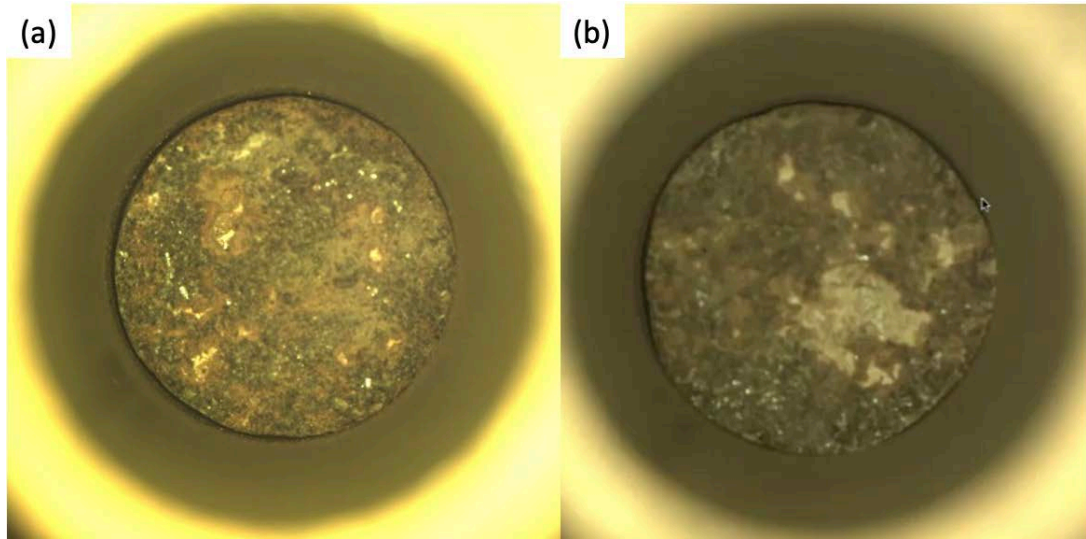
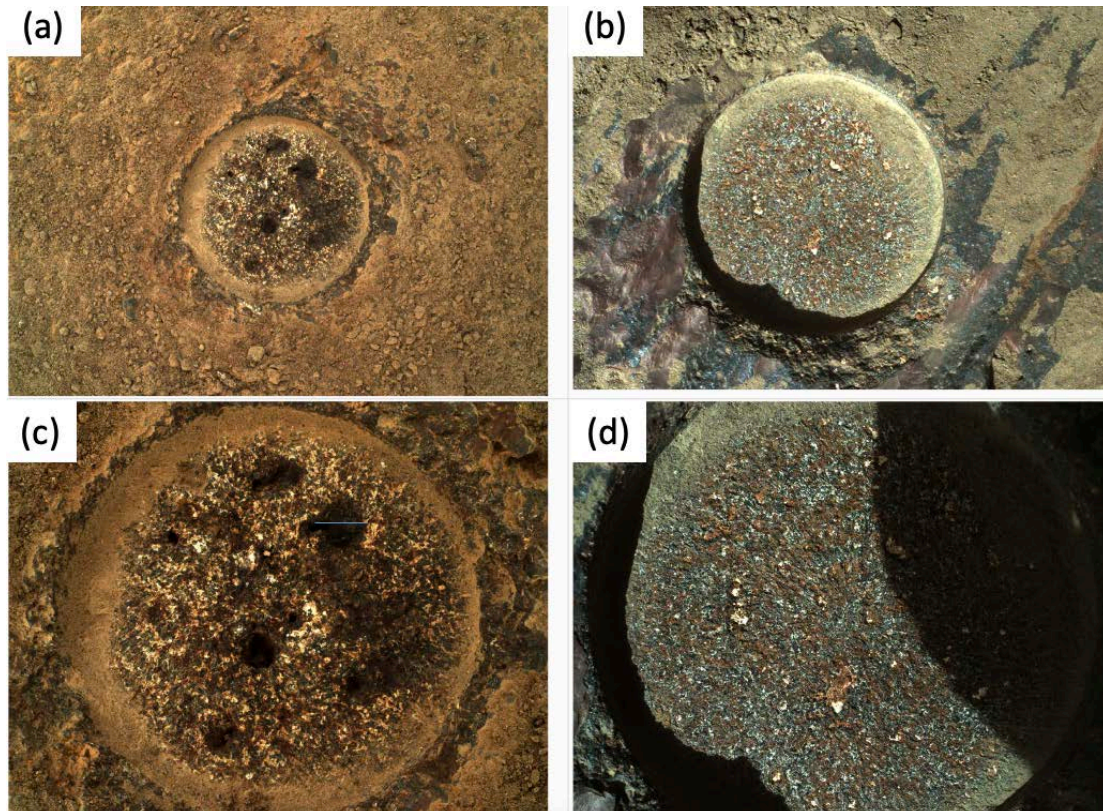


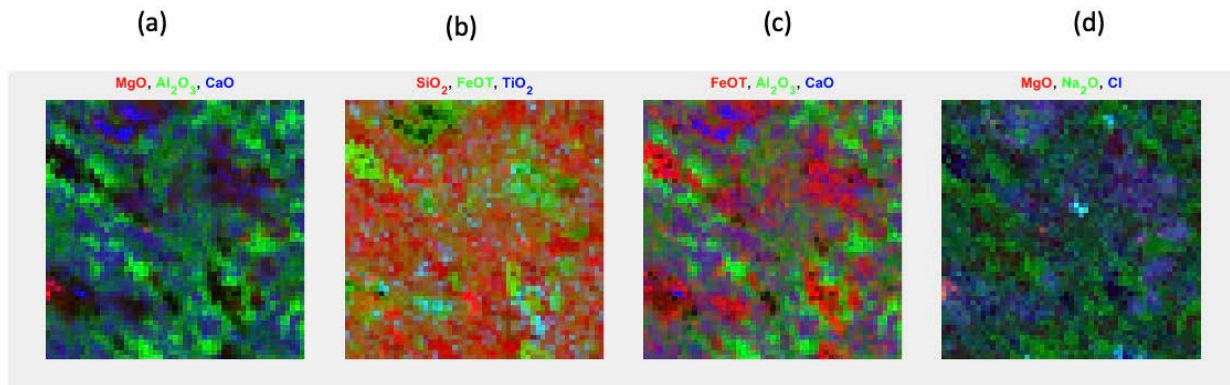
**Figure 9 | WATSON images of abraded crater floor surfaces. (a) Large (up to ~7 mm) pits and ~1.0 mm crystals in Guillaumes were exposed on Sol 160 in the lower Cf-fr pavement surface. (b) the presence of a few, possibly filled pits and smaller ~0.2-0.5 mm crystals in Bellegarde were exposed on Sol 186 from the surface unit at the top of Artuby ridge. (c) close up of Guillaumes. (d) close up of Bellegarde.** Degree of alteration appears less in Bellegarde.



### Elemental Geochemistry - PIXL

X-ray fluorescence mapping by PIXL was performed on the *Bellegarde* abrasion patch (**Figure 10**; observation footprint in **Figure 7**). A bulk sum analysis of the scanned abrasion surface is shown in **Table 1**. Note this analysis includes a mixture of what are believed to be primary silicates (pyroxene and plagioclase) along with the bright white and reddish brown patches suggestive of aqueous alteration. *Bellegarde* is clearly a silicate rock; compared to a typical basalt, it is low in  $\text{SiO}_2$ ,  $\text{Al}_2\text{O}_3$  and  $\text{MgO}$ , and rich in  $\text{FeO}$ ,  $\text{Na}_2\text{O}$ ,  $\text{SO}_3$ , and  $\text{Cl}$ .

**Figure 10 | PIXL X-ray element maps. (a)  $\text{MgO-Al}_2\text{O}_3\text{-CaO}$ . (b)  $\text{SiO}_2\text{-FeO}_{\text{total}}\text{-TiO}_2$ . (c)  $\text{FeO}_{\text{total}}\text{-Al}_2\text{O}_3\text{-CaO}$ . (d)  $\text{MgO-Na}_2\text{O-Cl}$  in *Bellegarde*.** The bulk sum composition of this scan area is included as Table 1. See Figure 7 for scale and location.



Chemically distinct minerals of a size comparable to and/or larger than the  $120\ \mu\text{m}$  X-ray beam size can be seen in elemental maps (**Figure 10a-d**) where there are distinct regions up to  $\sim 500\ \mu\text{m}$  in size rich in  $\text{FeO}$ , or  $\text{Al}_2\text{O}_3$ , or  $\text{CaO}$ . Further work is necessary to fully characterize these compositions and map them to the WATSON images, but a tentative interpretation is that the calcic regions correspond to the dark minerals and are pyroxene (augite), some iron and silicon bearing dark minerals may be an Fe-rich, Ca-poor pyroxene, the aluminous phase is tabular and light colored (bone white as opposed to the bright white secondary sulfate) and corresponds to plagioclase, and the Fe-rich material is the brownish coating(?) and could be an iron oxide or iron silicate. Apatite and FeTi oxides are also apparent in the PIXL data.

Table 1. PIXL Bulk Sum Composition

Bellegarde bulk sum (00187)				
Oxide	wt%	wt% err	std	std%
Na <sub>2</sub> O	4.67	0.34	1.59	34.0%
MgO	2.21	0.54	1.16	52.6%
Al <sub>2</sub> O <sub>3</sub>	6.97	0.35	3.62	52.0%
SiO <sub>2</sub>	43.79	2.19	10.65	24.3%
P <sub>2</sub> O <sub>5</sub>	2.76	0.56	2.46	89.1%
SO <sub>3</sub>	3.21	0.56	5.84	181.9%
Cl	1.48	0.43	0.84	56.8%
K <sub>2</sub> O	1.06	0.34	0.76	71.4%
CaO	7.62	0.38	4.34	57.0%
TiO <sub>2</sub>	2.49	0.55	2.18	87.4%
Cr <sub>2</sub> O <sub>3</sub>	0.01	0.03	0.02	183.3%
MnO	0.44	0.21	0.21	47.9%
FeO-T	23.23	1.16	11.27	48.5%
Ni	0.00	0.00	0.01	N/A
Zn	0.01	0.03	0.04	260.4%
Br	0.00	0.01	0.03	742.6%
Zr	0.02	0.03	0.04	213.1%

**Figure 11** is a ternary diagram of molar compositions  $\text{Al}_2\text{O}_3\text{-(CaO+Na}_2\text{O+K}_2\text{O)-(FeO}_T\text{+MgO)}$  for all of the individual PIXL points and the bulk sum spectrum. Idealized common mineral compositions are also plotted on the diagram. Most *Bellegarde* points lie in a triangle defined by typical mafic rock minerals (e.g., feldspar, pyroxene, olivine). While there is some evidence for unidentified secondary phases, there is little evidence of aluminum enrichment expected from open-system leaching (e.g., chemical

weathering) and formation of aluminous clay minerals. This plot supports the general conclusion that the analyzed rock is weakly altered by interaction with water.

The PIXL point measurements and bulk sum spectra are also plotted on a total alkali versus silica igneous classification diagram (**Figure 12**). While this diagram can be useful for naming specific igneous lithologies, the high abundance of secondary and/or alteration phases in *Rochette* complicates such usage. For that reason, no specific igneous name is assigned here. Of additional note on this diagram is the prominent array of points trending towards very low  $\text{SiO}_2$ ; this observation is consistent with the presence of sulfates or carbonates.

**Figure 11 | Bellegarde PIXL data.** Plotted as individual points (grey) and as bulk sum composition (blue circle) on a ternary diagram of molar abundances  $\text{Al}_2\text{O}_3$ – $(\text{CaO}+\text{Na}_2\text{O}+\text{K}_2\text{O})$ – $(\text{FeO}_{\text{Total}}+\text{MgO})$ . Common igneous minerals (olivine, pyroxene, feldspar, Fe-Ti-oxides) are typically found within the dashed red triangle whereas common clay minerals fall above the upper red dashed line. Several additional secondary minerals (e.g., Fe-Mg-Ca-sulfates/carbonates, halite) are also plotted.

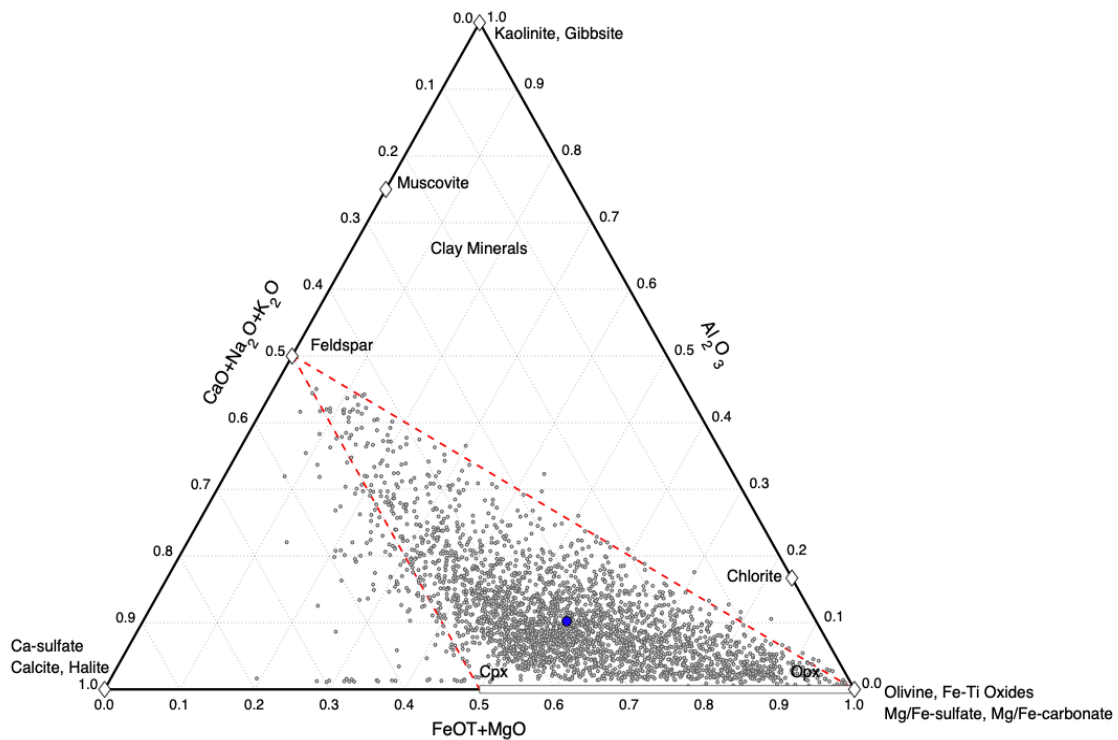
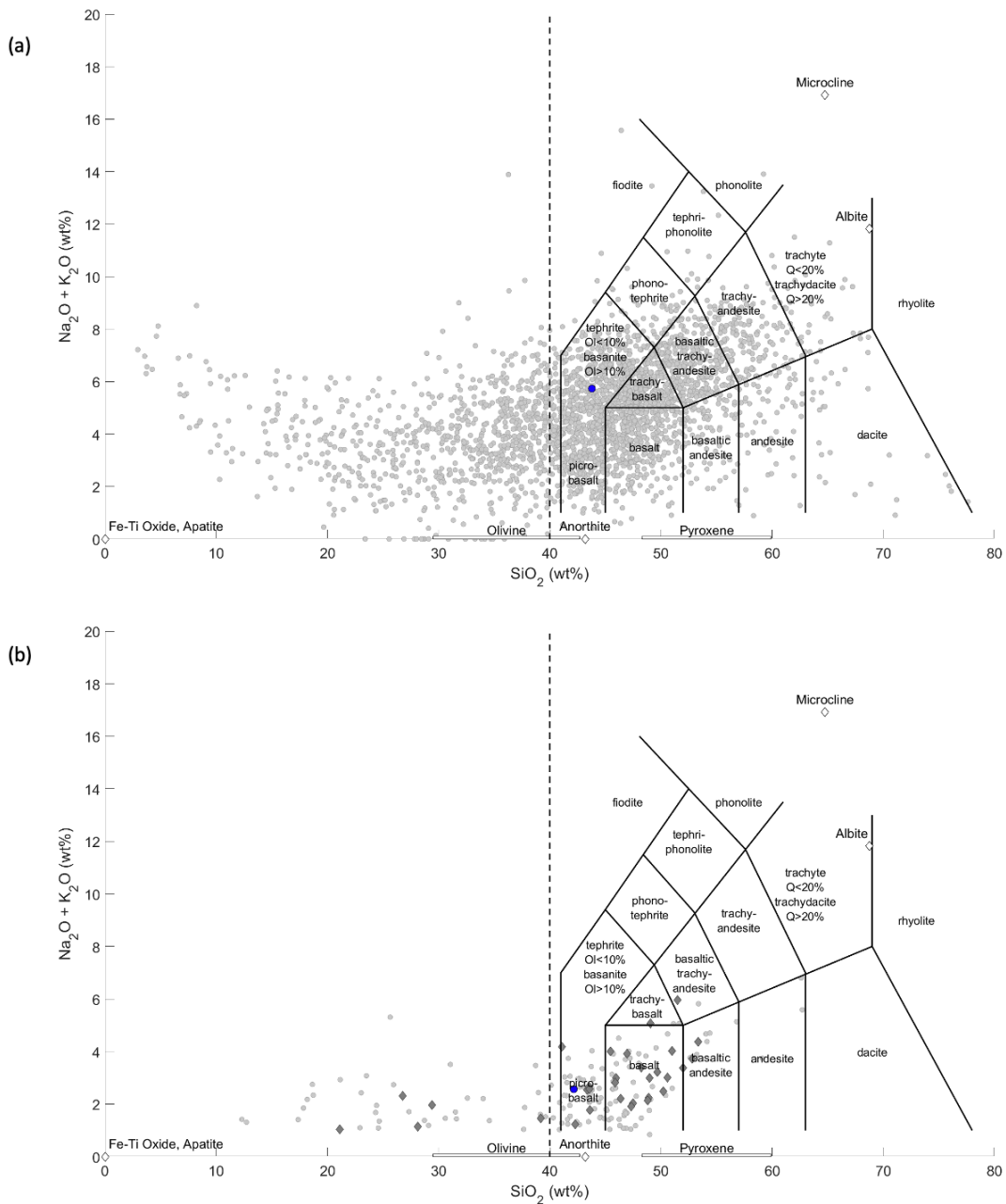


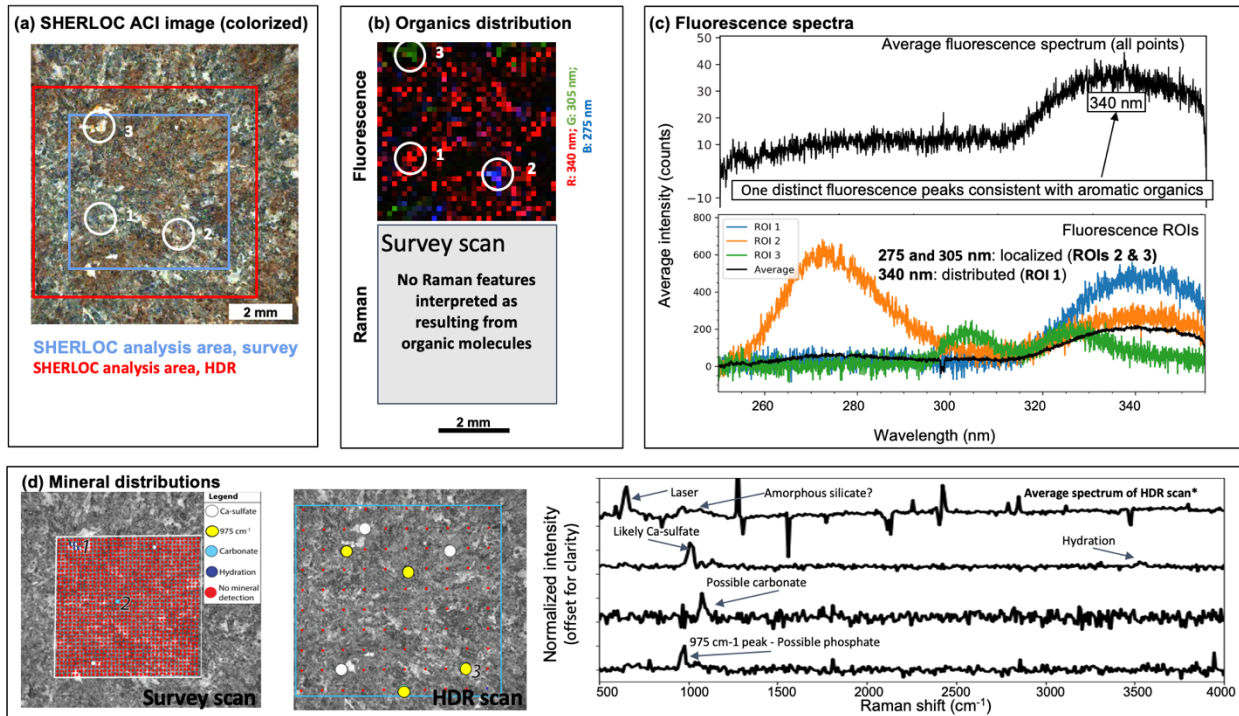
**Figure 12 | Total alkalis versus silica plots. (a)** PIXL data from scan of a braded surface *Bellegarde*. **(b)** SCAM LIBS laser spot data from abraded surface *Bellegarde* and from Cf-fr rocks obtained from sols 170 through 205. The individual data points represent small regions of the abraded surface (~100  $\mu\text{m}$  for PIXL; ~250  $\mu\text{m}$  for SCAM) and therefore represent a mixture of one or more primary and/or secondary minerals. Bulk sum composition of PIXL data and average value of SCAM data shown by blue circles. Endmember igneous mineral compositions shown as diamonds and lines for those with solid solution for reference. The underlying igneous classification scheme does not apply to the individual data points and simply provides a frame of reference for comparing samples.



## Mineralogy and Organics-SHERLOC

A SHERLOC UV Raman and fluorescence survey scan was obtained on Sol 186. The analysis footprint is shown in **Figure 7**. As shown in **Figure 13** and **Table 2**, SHERLOC Raman spectra indicate the likely presence of Ca-sulfate (occasionally hydrated) that appears to fill voids and/or replace primary mineral(s). SHERLOC also detected an unknown amorphous silicate, and minor carbonate and phosphate phases. These data are consistent with the multiple lines of evidence indicating that secondary phases are concentrated in the bright white patches (**Figure 10d**). Where PIXL observations overlap the SHERLOC scan area, they corroborate these secondary mineral identifications.

**Figure 13 | SHERLOC fluorescence and Raman spectral results for Bellegarde.** Spectra were collected with an HDR scan (7x7 mm, 100 points, 780  $\mu\text{m}$ , and 500) and a survey scan (5x5 mm, 1296 points, 144  $\mu\text{m}$  spacing, 15 pulses per point). **(a)** Colorized ACI image rectangles indicating scan areas: red=HDR, blue=survey, and white circles indicating ROIs highlighted in b and c. **(b)** Possible presence of organics. RGB map showing main regions of organic fluorescence (275, 305, and 340 nm). Note the 340 nm peak is distributed throughout, but the 275 and 305 nm peaks are found mainly in two ROIs (see panel a). No Raman features indicative of organics were detected. **(c)** Fluorescence spectra. The upper panel is the average fluorescence spectrum for the whole analysis area. The lower panel includes spectra from ROIs. **(d)** Mineral distributions. The left and middle panels show the results of the Raman survey and HDR scans, respectively. In each, the grid of red circles indicates the points analyzed, and the blue, white, and blue/white circles indicate locations of mineral detections, corresponding largely to lighter-toned features in ACI image. The legend in the survey scan panel applies to that of the HDR scan as well. The right panel includes selected Raman spectra from the two scans. The upper spectrum is the average spectrum of the HDR scan. The majority of features are caused by cosmic rays, but there is a possible detection of amorphous silicates based on a broad band centered near 1000  $\text{cm}^{-1}$ . The spectra labeled No. 1, 2, and 3 correspond to the points in the map panels with the same numbers and are representative of spectra assigned to Ca-sulfate (1050  $\text{cm}^{-1}$ ), carbonate (1100  $\text{cm}^{-1}$ ), and (possibly) phosphate ( $\sim 975 \text{ cm}^{-1}$ ), respectively. The spectrum labeled No. 1 also contains a possible peak for hydration at  $\sim 3550 \text{ cm}^{-1}$ . Scale in panel a also applies to panel d.



The average fluorescence spectrum of the scanned area contains one major peak at 340 nm. Two other peaks at 275 nm and 305 nm are observed in the spectra from the selected region of interest (**Figure 10c**). All these peaks can likely be attributed to aromatic organic compounds. The relatively low intensity of fluorescence at all wavelengths and absence of Raman organics signature suggests that, if there are indeed organic materials present, they are in low abundance and generally dispersed with some localized hotspots.

Table 2. SHERLOC Raman Spectra Mineral ID\*

Sample	Certain	Possible (not confirmed)	No detections found in the primary lithology
Bellegarde	Ca-sulfate, occasionally hydrated (occurs in white void fills or crystals, secondary to primary lithology)	Carbonate (very minor phase, only detected in a single spot)  Amorphous silicate (potentially major phase covering whole target)  Phosphate (minor phase)	Pyroxene, olivine  We looked for these, but cannot find them

#### Elemental Geochemistry and Mineralogy - SuperCam

SCAM LIBS and VISIR measurements of the pre- and post-abrasion surfaces, boreholes, and borehole tailings for the *Montdenier* and *Montagnac* sample targets are shown in **Figure 14**. These data are supplemented with LIBS results from many Cf-fr rocks acquired along the traverse, divided for clarity between those from OEB to *Roubion* (up until sol 168) and from *Roubion* to *Citadelle*. The *Montdenier* and *Montagnac* borehole walls and tailings and *Bellegarde* abrasion patch compositions are broadly similar. The compositional trends from the abraded/cored rock are consistent with those measured for the many Cf-fr rocks along the traverses. One notable distinction is that while SiO<sub>2</sub> values >55% are fairly common in Cf-fr targets, they are absent in the abraded and cored materials. The high SiO<sub>2</sub> values may thus be restricted to natural surfaces, possibly suggesting an association with a surficial coating. High MgO values comparable to those of *Entrevaux* and *Aiguines* (rocks at the base of *Artuby* ridge and likely exposures of *Séítah*) are absent in the abraded surface and are only present in regolith grains inadvertently analyzed in the Cf-fr targets. The ~250 µm LIBS spot most commonly interrogates more than one specific mineral. Given that the typical *Bellegarde* grain size is 0.2-0.5 mm, as described above, many of the trends observed in **Figure 14** are reasonably attributed to a mixing among igneous minerals such as pyroxene and plagioclase.

To complement the PIXL data, the LIBS results from *Bellegarde* are also plotted on the total alkali vs. silica diagram (**Figure 12b**). PIXL detects more points rich in alkali elements and low in silica (tentatively interpreted as secondary salts) than are detected by SCAM. Similarly, no SCAM points exhibit SiO<sub>2</sub> values higher than ~55 wt % despite many such points detected by PIXL. These differences as well as distinct PIXL and SCAM bulk mean values (blue circles in **Figure 12**) could be related to different analysis regions on *Bellegarde*, but might also be related to the difference in spot size of the two measurement techniques.

SCAM VISIR spectra of the *Bellegarde* abraded patch have notable absorption features at 1.42 and 1.93  $\mu\text{m}$ , attributable to hydration (**Figure 15**), a feature common to many of the Cf-fr rocks investigated along the OEB to *Roubion* traverse. These features are not evident or are less pronounced in the *Montdenier* borehole walls and in the *Montdenier* and *Montagnac* tailings. This observation may indicate preferential hydration of the upper surface of the investigated rock or may arise from the different grain size of the tailings compared to the original rock. Absorption features in spectra at 2.28  $\mu\text{m}$  could reflect carbonate and/or may indicate an Fe-bearing smectite clay.

**Figure 14 | Harker oxide diagram.** SCAM LIBS spot compositions of natural rock surfaces of fractured crater floor (Cf-fr), abraded surface *Bellegarde* sols 187-188, vertical borehole scan of *Montdenier*, two vertical borehole scans of *Montagnac*, and borehole tailings of *Montdenier*.

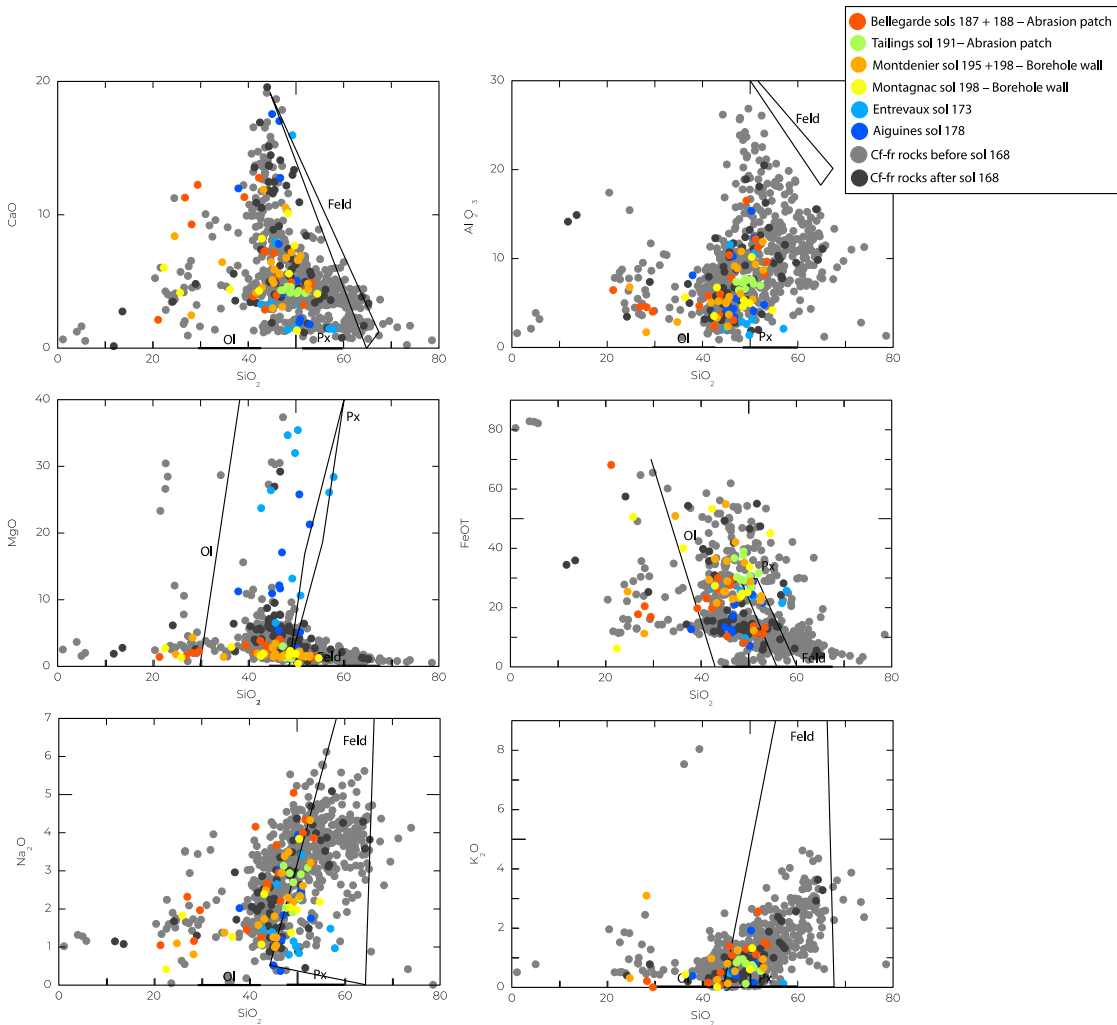
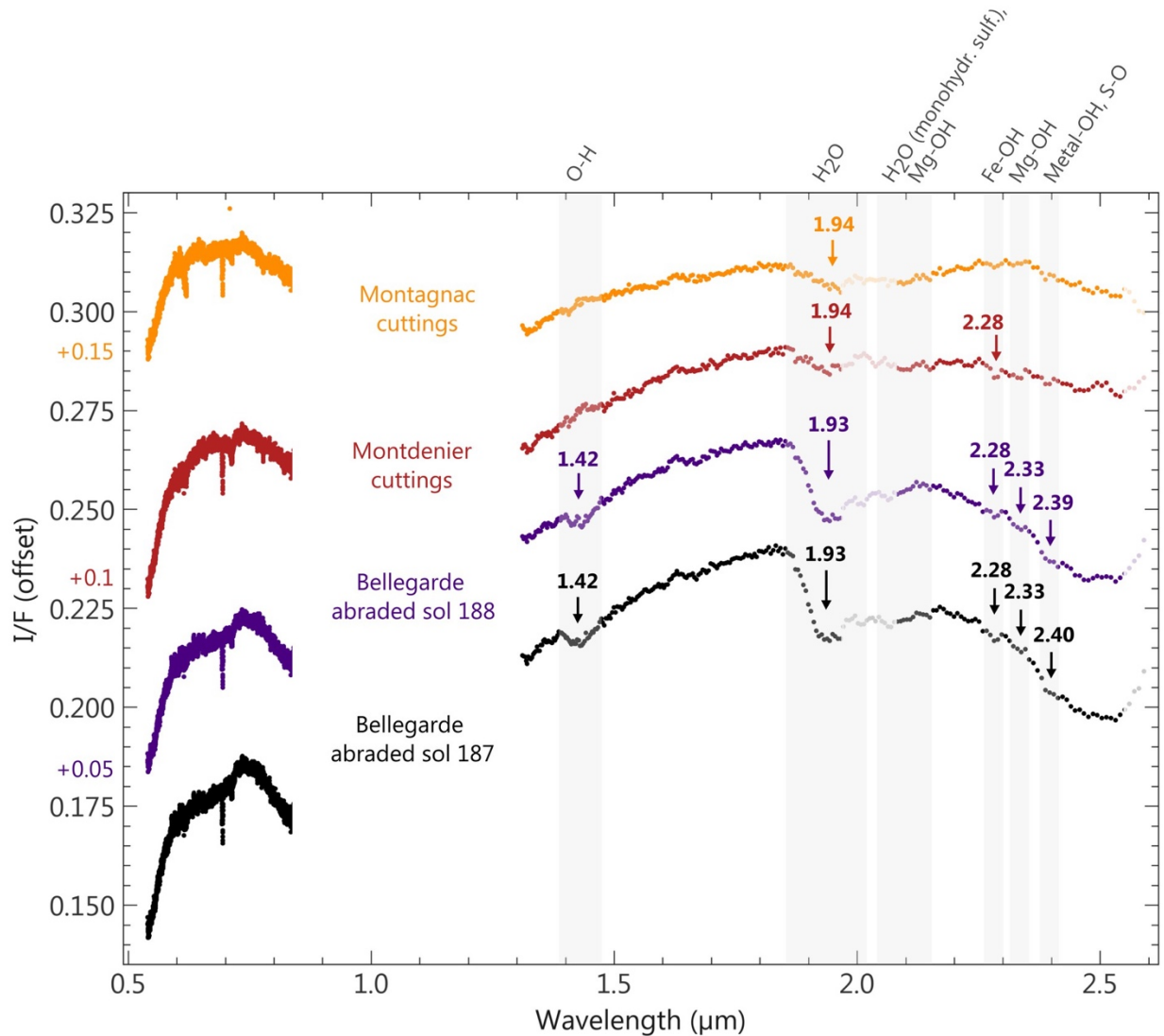


**Figure 15 | Bellegarde SCAM VISIR.** Abrasion surface shows evidence of hydration at  $\sim 1.42$  and  $1.93$   $\mu\text{m}$ . These absorptions are much weaker in borehole tailings.

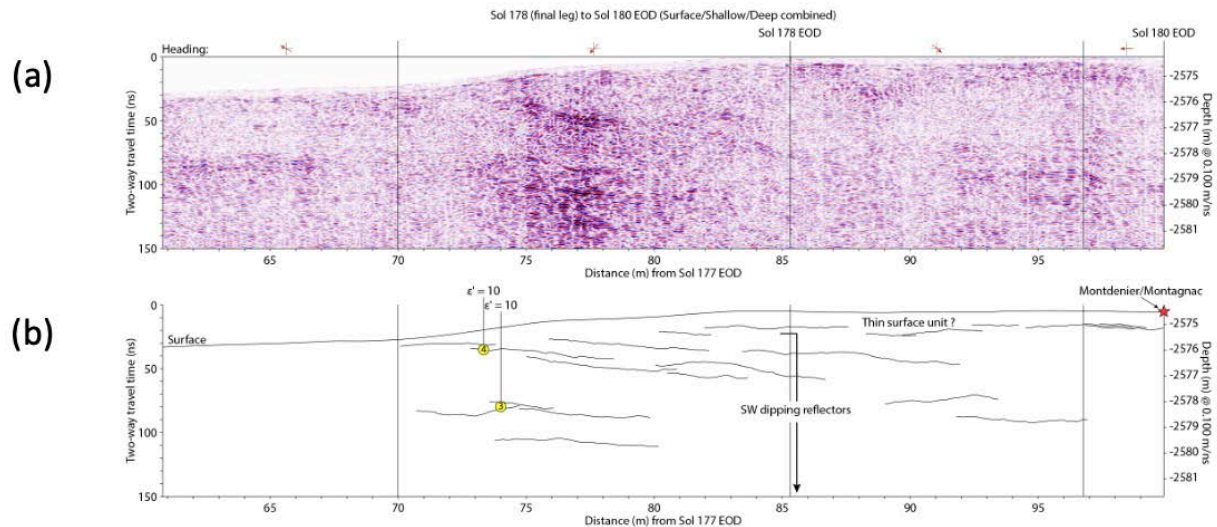


### Subsurface Structure

The RIMFAX radargram acquired on sols 177-180, during the rover's drive along *Artuby* ridge (177), ascent of *Artuby* ridge and arrival at *Citadelle* (178), and short bump to *Rochette* (180), can be seen in **Figure 16**. From left to right, the four panels in **Figure 16** present results along a rover path that 1) begins NW, parallel to the NW-SE strike of *Artuby* ridge, then 2) turns left to cross the ridge, then 3) runs NW parallel to the ridge again, and 4) finishes with a nearly 180-degree turn. **Figure 16** also includes an interpreted subsurface stratigraphy and rock densities based on permittivity. While driving along the base of *Artuby* ridge, RIMFAX observed a sequence of SW dipping reflectors that dominate the stratigraphy from approximately surface levels to  $>10$  m burial depth. Starting on sol 178, the radargram shows a relatively thin horizontal capping layer, consistent with the *Rochette* outcrop at the surface. The estimated permittivity suggests that the horizontal, near surface layers are similar in density to basaltic

material and those at depth exhibit greater density, consistent with an olivine-rich lithology (see **Figure 16** caption for details).

**Figure 16 | Geological context for Citadelle area of Artubyridge including subsurface stratigraphy and permittivity. (a)** RIMFAX radargram for the sol 178 to 180 traverse. **(b)** Geological interpretation of reflector geometries in (a) with the *Montdenier-Montagnac* target indicated with a red star. A capping surface unit with decimeter-scale sub-horizontal layering appears to be present from ~ 80 m distance to the end of the sol 180 drive. A sequence with SW dipping reflectors dominates the stratigraphy from near surface levels to >10 m burial depth. Location of permittivity measurements ( $\epsilon'$ ) from diffraction hyperbolae are denoted with yellow circles. These and additional nearby permittivity measurements within sol 178 and 199 radargrams range between 7-8 and 10-14, translating to rock densities around 3.0-3.2 and 3.5-4.0 g/cm<sup>3</sup>, with the latter group suggesting olivine-rich lithologies (possibly *Séitah*).



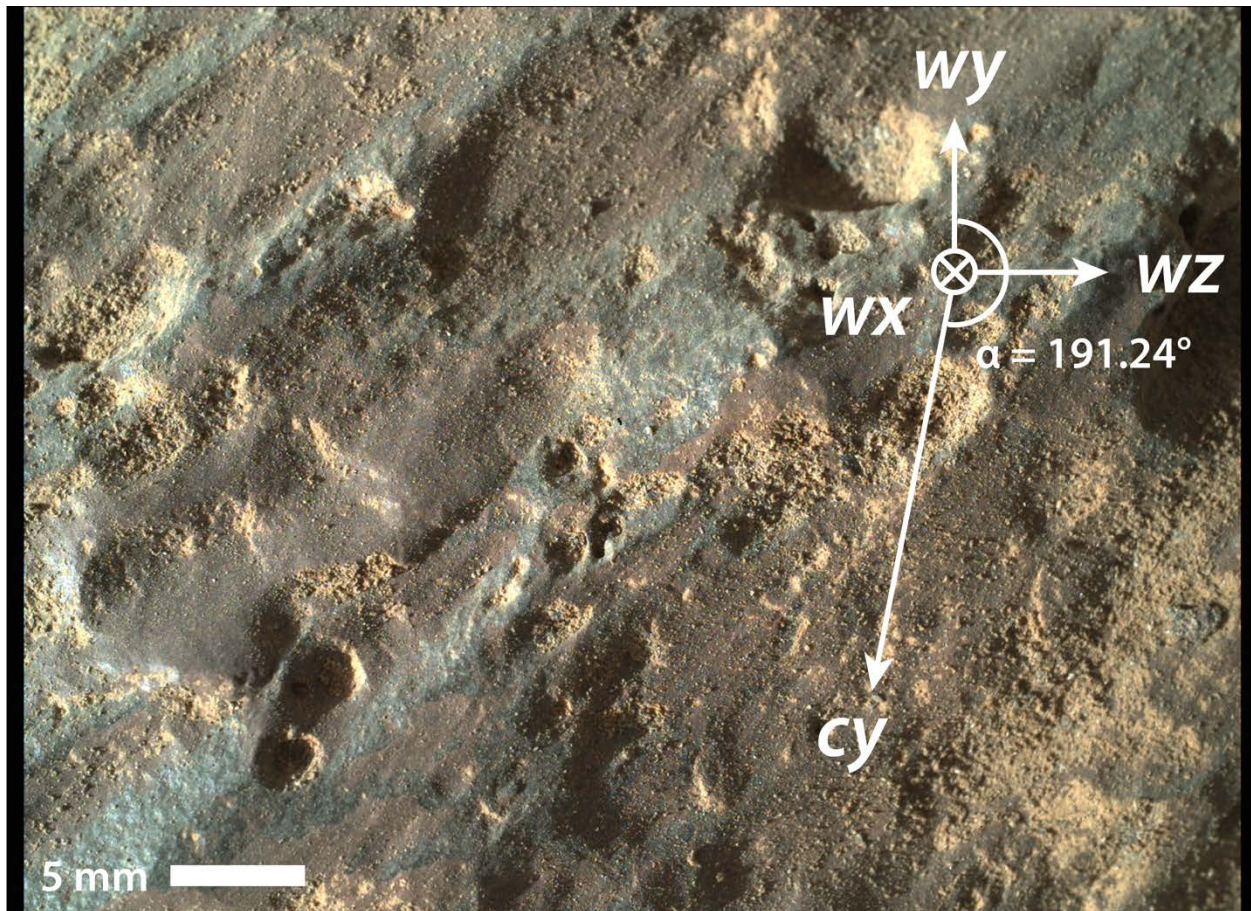
### Core orientation

At the time of drilling and 6-cm pre-drilling WATSON imaging, the rover, coring drill, WATSON, and coring target (called "Montdenier\_188.PSC.0.0638"), had the following characteristics:

- Coring target normal (RMECH frame):  $\mathbf{uvw}_{\text{RMECH}} = (-0.089, 0.104, -0.991)$
- Rover orientation quaternion at time of drilling (transferring from RMECH to SITE frame):  $\mathbf{bQII1} = (0.696481, 0.0183586, -0.00168854, -0.717339)$
- Gravity vector (RMECH frame):  $\mathbf{g}_{\text{RMECH}} = (-0.028215, -0.0211681, 0.999378)$
- Coring Drill orientation quaternion (transferring from CORING DRILL to RMECH frame):  $\mathbf{cdQb} = (0.705714, 0.20918, -0.664503, 0.129009)$
- Rover orientation quaternion at time of acquisition of WATSON image  
SIF\_0188\_0683643364\_351FDR\_N0070000SRLC00678\_0000LMJ01: (transferring from RMECH to SITE frame):  $\mathbf{bQII2} = (0.696524, 0.0163777, -0.00351771, -0.717338)$
- WATSON orientation quaternion at time of acquisition of WATSON image  
SIF\_0188\_0683643364\_351FDR\_N0070000SRLC00678\_0000LMJ01: (transferring from WATSON to RMECH frame):  $\mathbf{wQb} = (0.706087, 0.213611, -0.663116, 0.126843)$

Items (a) and (b) gives a coring drill pointing vector estimate of (Hade =  $9.98^\circ$ ; Azimuth =  $218.87^\circ$ ). Item (c) gives an alternate coring drill hade estimate of (Hade =  $8.24^\circ$ ). Items (b) and (d) gives a coring drill pointing vector estimate of (**hade =  $9.42^\circ$ ; azimuth =  $219.27^\circ$** ). We report this as the final coring drill orientation estimate since it was estimated for the drill after preloading. Items (e) and (f) give an estimate of the angle between the WATSON y-axis and the up-dip direction in SITE coordinates of **Figure 17: (core roll,  $\alpha = 191.24^\circ$ )**

**Figure 17 | Core orientation.** 6-cm standoff WATSON image of *Montdenier* on sol 188. WATSON image SIF\_0188\_0683643364\_351FDR\_N0070000SRLC00678\_0000LMJ01. Image scale is  $27.8 \mu\text{m pixel}^{-1}$ . Orientation compass gives WATSON frame (**wx, wy, wz**). Core roll is clockwise angle of core y-axis, **cy**, from **wy**, given by  $\alpha = 191.24^\circ$ .



## **Preliminary Scientific Assessment**

### **Synthetic sample description and preliminary interpretation**

Sample type: **Basalt (or possibly basaltic sandstone)**

#### **1. Relationship with surrounding rocks**

- a. *Montdenier-Montagnac* are part of the layered caprock of *Artuby* ridge, appearing to be in family, morphologically and compositionally, with caprocks investigated along the traverse from *Roubion* to *Citadelle* in terms of composition and texture. These cores are therefore considered representative of the Cf-fr unit.
- b. Within Cf-fr rocks, *Montdenier-Montagnac* probably lie below the high standing blocky and cratered expression to the east and north, and clearly above the granular rocks exposed at *Roubion* and along the NE-facing slope of *Artuby* ridge.
- c. *Montdenier-Montagnac* are stratigraphically higher than and therefore probably younger than rocks of the *Séítah* region (Cf-f1).
- d. Although dislodged from the flat-lying outcrop at *Citadelle*, *Rochette*, the rock from which *Montdenier-Montagnac* were cored, is generally thought to be very close to its original outcrop location.

#### **2. Texture and fabric**

- a. Grain size: ~0.2-0.5 mm (plagioclase, pyroxene). Alteration products exhibit a greater size range appearing to fill void space (~primary minerals up to ~3 mm in size).
- b. The surface of *Rochette* is pitted. These pits could be the result of aeolian abrasion, volcanic vesicles enhanced by aeolian abrasion, or voids created by some type of chemical weathering or alteration. In the abraded surface, there are no obvious holes, although sulfate-filled voids are observed.
- c. There is evidence for interlocking grains, suggesting crystallization from a magma. But there is also evidence for more equigranular textures, and possible rounded grains.
- d. There is no compelling evidence of intergranular porosity or cements, common to many sedimentary rocks.

#### **3. Mineralogy and chemistry**

- a. Minerals present include pyroxene, feldspar, and FeTi-oxides, and secondary iron oxides or silicates, sulfates, and phosphate. The phosphate may be primary, secondary or both.
- b. The bulk composition is consistent with a basalt modified by aqueous alteration. Unlike *Roubion*, the alteration was not sufficiently intense to move it out of the basalt compositional field.
- c. Low concentrations of aromatic organics are present, both localized and distributed in the rock.

#### **4. Alteration/secondary characteristics**

- a. There is textural and mineralogical evidence in the abraded patch for interaction of the rock with aqueous fluids, resulting in chemical alteration and mineral hydration.
- b. Secondary mineralogy remains speculative, but likely includes Ca-sulfates and Ca-phosphates.

#### **5. Core orientation**

- a. Sample cores were absolutely oriented to  $\sim 1^\circ$  in martian geographic coordinates, although *Rochette* may have been differentially tilted with respect to the underlying bedrock.

### **Returned Sample Science Considerations**

Outcrop morphology and texture, as well as the appearance, composition and mineralogy observed in the *Bellegarde* abrasion patch, suggest that *Rochette* is a fine-grained mafic igneous rock, possibly a member of a sequence of lava flows. An alternative interpretation is that it is a volcanoclastic sandstone derived from basaltic rocks of the Jezero watershed. The absence of sedimentary textures in the Cf-fr rocks exposed in cliffs at *Mure* and *Artuby* and the texture of *Rochette* disfavor the latter interpretation.

*Geochronology:* The timing of volcanic rock crystallization (and volcanic minerals preserved in a sandstone) will be quantifiable using laboratory-based, radio-isotopic geochronology of returned samples. Likewise, with knowledge of cosmogenic nuclide production rates in specific minerals on Mars, quantitative constraints on the sample's surface exposure age may also be possible. The timing of *Rochette's* deposition will constrain the emplacement ages of other crater floor units, e.g., *Séítah* is likely older, as is the stratigraphically lower *Roubion*. Furthermore, if *Rochette's* lithology represents the heavily cratered surfaces of Cf-fr (e.g., to the east and north of the OEB), and the surface exposure and exhumation history of Cf-fr can be understood, then geochronology of returned samples may document the duration of crater accumulation and retention of the exposed Jezero floor. Such information could then be used to test, and potentially improve, the fundamental parameters assumed in the Mars crater chronology functions.

*Geochemistry:* The chemical composition and mineralogical properties of this igneous rock (or detrital igneous minerals, if sedimentary) will provide information on the geophysical and geochemical conditions of the rock's source (i.e., at depth, within the martian crust or mantle) at the time of its primary eruption or intrusion. In addition, water-soluble salts, apparently filling holes, suggests aqueous alteration and/or addition of secondary phases at some point after deposition. Thus, this rock has likely experienced interaction with one or more aqueous fluids, possibly groundwater that may or may not be related to Jezero lake. The extent of alteration appears to be less than observed in *Roubion*. These water-rock interactions may have occurred in a habitable subsurface environment. Laboratory analyses of the secondary minerals will provide information on the chemistry and environmental conditions (e.g., pH, temperature, salinity, timing) during aqueous activity. However, at the time of writing, there is no strong chemical evidence for clay minerals in *Rochette*, indicating that any open system conditions (i.e., cation leaching yielding clay minerals) was limited. It is also unclear whether the observed phosphates are secondary or primary phases in the rock. Organic molecules within *Rochette* would provide information on the martian carbon cycle and organic preservation.

For these reasons, a returned sample of this unit has high science value for astrobiology, global evolution of Mars (interior and near surface environments), and for understanding the geologic setting and timing of Jezero floor units.

**References**

- Carrier W.D. III, Olhoeft, G.R., Mendell, W. (1991) Physical Properties of the Lunar Surface. Lunar Sourcebook, A User's Guide to the Moon, ISBN 0521334446, Cambridge University Press, 475-594.
- Goudge, T.A., Mustard, J.F., Head, J.W., Fassett, C.I., & Wiseman, S.M. (2015). Assessing the mineralogy of the watershed and fan deposits of the Jezero crater paleolake system, Mars. *Journal of Geophysical Research: Planets*, 120, 775-808, doi:10.1002/2014JE004782.
- Holm-Alwmark, S., Kinch, K.M., Hansen, M.D., Shahrzad, S., Svennevig, K., Abbey, W.J., Anderson, R.B., Calef, F.J., Gupta, S., Hauber, E., Horgan, B.H.N., Kah, L.C., Knade, J., Miklusick, N.B., Stack, K.M., Sun, V.Z., Tarnas, J.D., Quantin-Nataf, C. (2021). Stratigraphic Relationships in Jezero Crater, Mars: Constraints on the Timing of Fluvial-Lacustrine Activity from Orbital Observations. *Journal of Geophysical Research: Planets*, 126, 7, doi:10.1029/2021JE006840.
- Stack, K.M. et al. (2020). Photogeologic Map of the Perseverance Rover Field Site in Jezero Crater Constructed by the Mars 2020 Science Team. *Space Science Reviews*, 216, 127, doi:10.1007/s11214-020-00739-x.
- Sun, V.Z. & Stack, K.M. (2020). Geologic Map of Jezero Crater and the Nili Planum Region, Mars. USGS Scientific Investigations Map 3464, pamphlet 14 p., scale 1:75,000, doi:10.3133/sim3464.

# INITIAL REPORT

## M2020-196-4 Montagnac

---

**Sample Designation:** M2020-196-4 Montagnac

**Date of Coring:** 7-Sept-2021

**Mars Time of Sample Core Sealing:** 20:35:07 LMST, Sol 196, Ls 95.6

**Latitude (N), Longitude (E), Elevation:** 18.43074132, 77.44436502, -2574.553 m

**Campaign:** Crater Floor

**Region of Interest:** Artuby Ridge

**Lithology:** Fine-grained mafic and likely igneous rock, possibly basalt (alternatively, basaltic sandstone). Primary minerals are plagioclase, pyroxene, and FeTi oxides. Aqueous alteration is indicated by abundant secondary minerals including iron oxide, Ca-sulfates (occasionally hydrated), phosphate, and minor carbonate.

**Estimated Volume Recovered:** 8.7 cm<sup>3</sup>

**Coring Bit Number:** 5

**Core Orientation:** hade = 17.0°; azimuth = 225.96°; core roll = 197.25°

**Sample Serial Numbers:** Tube SN267; Seal SN170, Ferrule SN074

**ACA Temperature at Time of Sealing:** 35 C

**Estimated Rover-Ambient Pressure and Temperature at Time of Sealing:** 707 Pa, 215 K

**Estimated Amount of Martian Atmosphere Headspace Gas:** 1.3x10<sup>-6</sup> mol

**Abrasion Patch Name and Depth:** Bellegarde, 8 mm

**Anomalous Behavior:** None

---

December 3, 2021

*J. I. Simon, K. A. Farley, T. Bosak, A. Udry, S. VanBommel, S. McLennan, L. Mandon, Y. Goreva, R. C. Moeller, V. Sun, E. L. Berger, A. D. Czaja, A. C. Fox, C. H. Lee, E. L. Scheller, S. Sharma, S. Siljeström, H. E. F. Amundsen, S.-E. Hamran, T. M. Casademont, L. W. Beegle, K. C. Benison, V. C. Debaille, L. Hausrath, C. Herd, J. Hurowitz, L. E. Mayhew, D. L. Shuster, K.M. Stack, M. Sylvestre, B. P. Weiss, P. A. Willis, R. Wiens, M.-P. Zorzano, and Mars 2020 Team*

This sample is paired with M2020-190-3 *Montdenier*. See section 3 (M2020-190-3 Montdenier) for details of this paired sampling. Only the core orientation for *Montagnac* is described below.

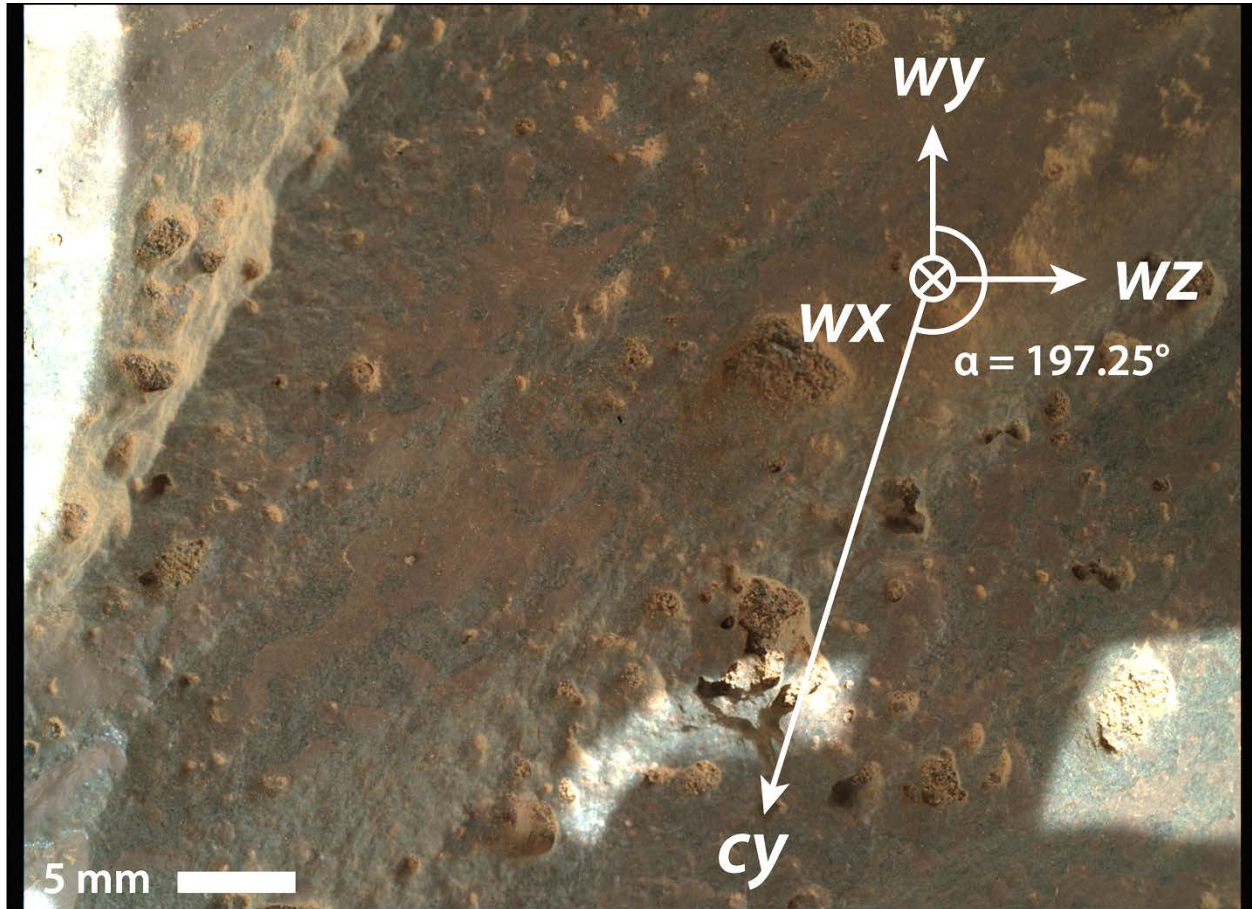
### **Core orientation**

At the time of drilling and 7-cm pre-drilling WATSON imaging, the rover, coring drill, WATSON, and coring target (called “Montagnac\_RP.PSC.0.0691”), had the following characteristics:

- a) Coring target normal (RMECH frame):  $\mathbf{uvw}_{\text{RMECH}} = (-0.205, 0.182, -0.962)$
- b) Rover orientation quaternion at time of drilling (transferring from RMECH to SITE frame):  $\mathbf{bQII1} = (0.696493, 0.0181555, -0.0019524, -0.717331)$
- c) Gravity vector (RMECH frame):  $\mathbf{g}_{\text{RMECH}} = (-0.028215, -0.0211681, 0.999378)$
- d) Coring Drill orientation quaternion (transferring from CORING DRILL to RMECH frame):  $\mathbf{cdQb} = (0.730214, 0.260758, -0.623407, 0.100777)$
- e) Rover orientation quaternion at time of acquisition of WATSON image SIF\_0195\_0684255577\_390FDR\_N0070000SRLC00701\_0000LMJ01: (transferring from RMECH to SITE frame):  $\mathbf{bQII2} = (0.696528, 0.0164346, -0.00334345, -0.717334)$
- f) WATSON orientation quaternion at time of acquisition of WATSON image SIF\_0195\_0684255577\_390FDR\_N0070000SRLC00701\_0000LMJ01: (transferring from WATSON to RMECH frame):  $\mathbf{wQb} = (0.729438, 0.26773, -0.620981, 0.103072)$

Items (a) and (b) gives a coring drill pointing vector estimate of (Hade = 17.98°, Azimuth = 225.73°). Item (c) gives an alternate coring drill hade estimate of (Hade = 16.43°). Items (b) and (d) gives a coring drill pointing vector estimate of (**hade = 17.70°, azimuth = 225.96°**). We report this as the final coring drill orientation estimate since it was estimated for the drill after preloading. Items (e) and (f) give an estimate of the angle between the WATSON y-axis and the up-dip direction in SITE coordinates of **Figure 1: (core roll,  $\alpha = 197.25^\circ$ )**

**Figure 1 | Core orientation.** 7-cm standoff WATSON image of Montagnac core target on sol 195. WATSON image SIF\_0195\_0684255577\_390FDR\_N0070000SRLC00701\_0000LMJ01. Image scale is  $32.0 \mu\text{m pixel}^{-1}$ . Orientation compass gives WATSON frame ( $w_x$ ,  $w_y$ ,  $w_z$ ). Core roll is clockwise angle of core y-axis,  $c_y$ , from  $w_y$ , given by  $\alpha = 197.25^\circ$ .



# INITIAL REPORT

## M2020-262-5 Salette

---

**Sample Designation:** M2020-262-5 Salette

**Date of Coring:** 15-November-2021

**Mars Time of Sample Core Sealing:** 20:22 LMST, Sol 262, Ls 127.5

**Latitude (N), Longitude (E), Elevation:** 18.43397°, 77.44301°, -2569.2 m

**Campaign:** Crater Floor

**Region of Interest:** *Séítah South*

**Lithology:** Medium- to coarse-grained poikilitic olivine cumulate rock. Primary minerals are olivine and pyroxene. Aqueous alteration phases include sulfates, carbonates and hydrated phases. Organic matter was detected.

**Estimated Volume Recovered:** 8.9 cm<sup>3</sup>

**Coring Bit Number:** 5

**Core Orientation:** hade = 17.78°; azimuth = 81.51°; core roll = 253.58°

**Sample Serial Numbers:** Tube SN246; Seal SN194; Ferrule SN107

**ACA Temperature at Time of Sealing:** 40°C

**Estimated Rover-Ambient Pressure and Temperature at Time of Sealing:** 643 Pa, 221 K

**Estimated Amount of Martian Atmosphere Headspace Gas:** 1.1 x10<sup>-6</sup> mol

**Anomalous Behavior:** None

**Abrasion Patch Name and Depth:** *Dourbes*, 8 mm

---

January 27, 2022

*K. Hickman-Lewis, K. A. Farley, J. I. Simon, J. R. Johnson, B. Horgan, M. Rice, J. Bell, J. Rice, T. Bosak, L. Mandon, A. Udry, S. VanBommel, S. M. McLennan, Y. Goreva, R. C. Moeller, V. Sun, K.P. Hand, E. L. Berger, F. Calef, A. D. Czaja, C. H. Lee, A. C. Fox E. L. Scheller, S. Sharma, S. Siljeström, H. E. F. Amundsen, L. W. Beegle, B. P. Weiss, E. N. Mansbach, D. L. Shuster, C. D. K. Herd, R. C. Wiens, S. Le Mouélic, G. Caravaca, O. Gasnault, S. Maurice, A. Treiman, M. P. Zorzano and the Mars 2020 Team.*

## **Summary Description**

*Salette* and *Coulettes*, the pair of rock cores representing the third sample target of the Mars 2020 mission, were collected in the *South Séítah* region from *Brac*, a low-lying layered outcrop in the *Caille* locality at the easternmost end of the rover's traverse into *Séítah*. *Brac* lies within a group of blocky outcrops near the crest of one of the NE-SW trending ridges that are common in *Séítah*, ~130 meters from the *Máaz-Séítah* contact at the base of *Artuby* ridge (**Figures 1 and 2**). *Brac* is likely to be in-place.

*Séítah* makes up the stratigraphically lowest rocks exposed on the floor of Jezero crater. In orbital mapping, *Séítah* corresponds to a light-toned olivine-bearing unit referred to as Crater floor-fractured-1 (Cf-f-1) by Stack et al., 2020. This unit may be correlated with a regional olivine-bearing unit exposed between Syrtis Major and Nili Fossae. The mineralogy, micro-texture, color and spectral characteristics of *Brac* and other outcrops observed throughout *Séítah* suggest that the Cf-f-1 unit is mostly or entirely an igneous olivine cumulate. The horizontal to gently dipping layers observed in *Séítah* may represent primary igneous layering as seen in layered igneous bodies, though no layer-bounding mineralogical or grain-size variations were observed.

The *Dourbes* abrasion patch, acquired on *Brac*, revealed abundant ~3–5 mm euhedral to subhedral olivine grains surrounded by clinopyroxene in a poikilitic texture with minor feldspars, magnetite, and phosphates. The rock is therefore interpreted to be an igneous olivine cumulate formed by the settling of olivine in a magma body such as a sill or thick lava flow. No evidence was obtained that could distinguish between intrusive and extrusive origins. Alteration phases include sulfates (most likely Ca- or Mg-dominated), which fill voids and are thus secondary to the igneous mineralogy. Carbonate, most likely Fe/Mg-carbonate, and amorphous/nanocrystalline material may also be present, and hydrated phases were detected. Organic matter is present in low abundance, dispersed throughout the rock matrix and concentrated in a few spots.

The returned sample science objectives of these cores include geochronology, paleomagnetism, geochemistry, and the past history of water and water–rock interactions in Jezero crater. This core pair is geochemically similar and likely genetically related to the other *Séítah* samples in the cache (*Robine* and *Malay*). Together with cores of the *Máaz* formation (*Montdenier*, *Montagnac*, *Atsah*, *Hahonih*), these samples constitute the entirely igneous Crater Floor Campaign sample suite.

## **Stratigraphic and Geologic Context**

*Salette* and paired core *Coulettes* were collected from the *Brac* outcrop near the top of a local topographic high point in a region of the Jezero crater floor informally named *Séítah*, mapped in HiRISE images as the Cf-f-1 unit by the Mars 2020 Science Team (Stack et al., 2020; **Figure 1**). Prior to landing, the Cf-f-1 unit was interpreted to be either igneous or sedimentary. Several origin hypotheses have been suggested, including a pre-Isidis impact melt (Mustard et al., 2007), a pre-Isidis intrusive complex (Hoefen et al., 2003), basalt flows (Hamilton and Christensen, 2005; Tornabene et al., 2008), volcanic ash (Kremer et al. 2019), pyroclastic deposits (Mandon et al., 2020), and detrital sedimentary rocks (Rogers et al., 2018). *Séítah* has been correlated with a regional olivine-bearing unit exposed between Syrtis Major and Nili Fossae (Mandon et al., 2020).

Orbital mapping suggests that *Séitah* rocks are the stratigraphically lowest exposed rock unit on the crater floor and are overlain by both the *Máaz* formation and the delta. Rover observations confirm that *Séitah* lies below *Máaz*. Perseverance has not yet explored the relationship of the crater floor units to the delta. Consistent with its lower position in the stratigraphy, *Séitah* may be older than *Máaz*. However, because *Séitah* could be intrusive, the inverse is also possible.

## **Operations**

**Figure 2** shows the local context of *Perseverance* rover operations leading up to the sampling of *Salette* and *Coulettes*. Prior to approaching *Brac*, we conducted abrasion and proximity science of the nearby layered outcrop *Bastide*; however, we were unable to execute the full STOP list on *Bastide* and its *Garde* abrasion patch, thus the decision was made to seek another nearby rock for STOP list execution and sampling.

On Sol 248, we arrived at the *Brac* workspace and started the sampling sol path. On Sol 250, we selected four targets for abrasion (*Lane*, *Traverses*, *Pont du Loup* and *Laupon*) and acquired WATSON images of each. *Pont de Loup* was favored as the abrasion target because it appeared to cross multiple layers of the outcrop and because it may have offered a possibility to study later alteration phenomena in cross-cutting(?) veins. We attempted abrasion on *Pont du Loup* on Sol 251, but this operation faulted due to slip of the abrasion bit across the rock surface. Following recovery, we attempted abrasion on a new target, *Dourbes*, on sol 253. This target was chosen for its proximity to *Pont du Loup* and its potential to answer many of the same science questions as *Pont du Loup*. On Sol 255, we successfully abraded at *Dourbes*. PIXL and SHERLOC data were acquired on *Dourbes* on sol 257. We acquired the *Salette* core on sol 262.

After sampling *Salette*, we encountered a fault while picking up the abrading bit on sol 263; this precluded subsequent remote sensing and proximity science on the borehole. After performing a recovery on sol 267, we planned borehole proximity science on *Salette*, and pre-coring WATSON images on *Coulettes*, the second locality from which a core sample was to be obtained. The *Coulettes* core was acquired on sol 271.

We drove away from the *Brac* workspace on sol 277, heading in the direction of the *Issole* workspace.

**Figure 1 | Regional context of Perseverance rover operations.** (a) geologic map showing Jezero crater floor units defined by Stack et al. 2020. The light green shaded overlay indicates the location of the Jezero Crater Floor campaign. (b) Geological map showing the crater floor Cf-fr and Cf-f-1 units. Adapted from Stack et al. (2020).

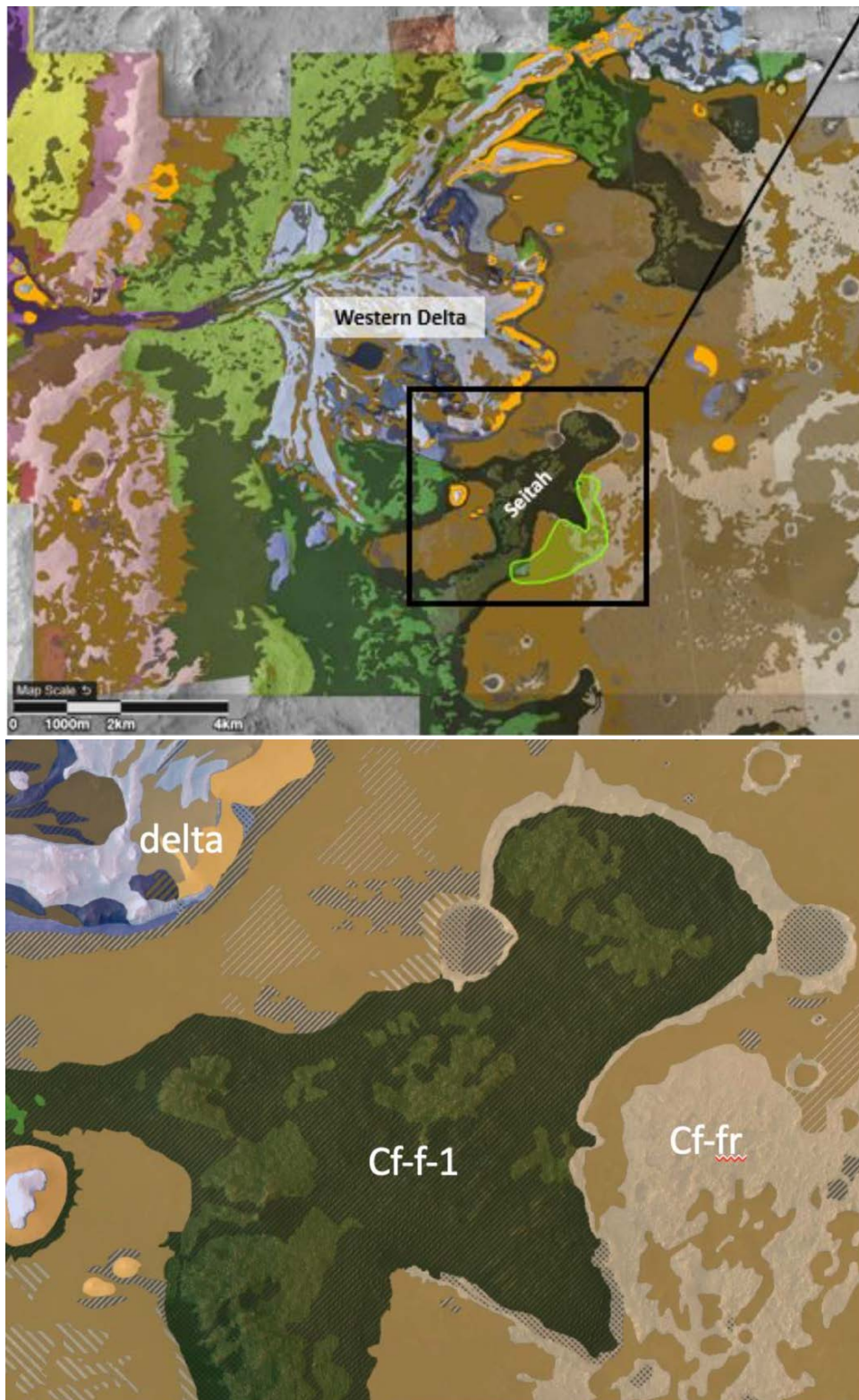
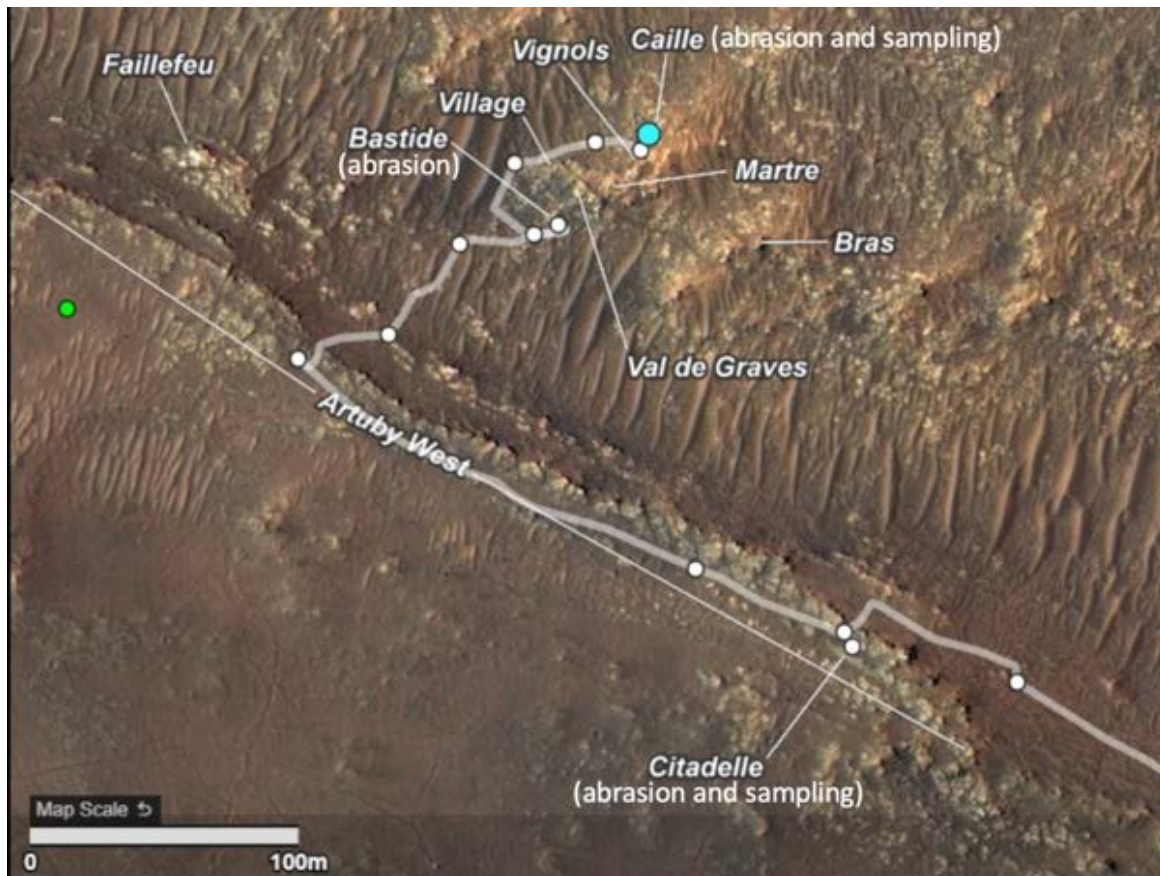


**Figure 2 | Local context of Perseverance rover operations during Salette and Coulettes sampling.** HIRISE map showing the locations of sample collection together with other notable outcrops investigated during the sol path leading to *Brac*. Location of *Brac* is indicated with a blue circle.

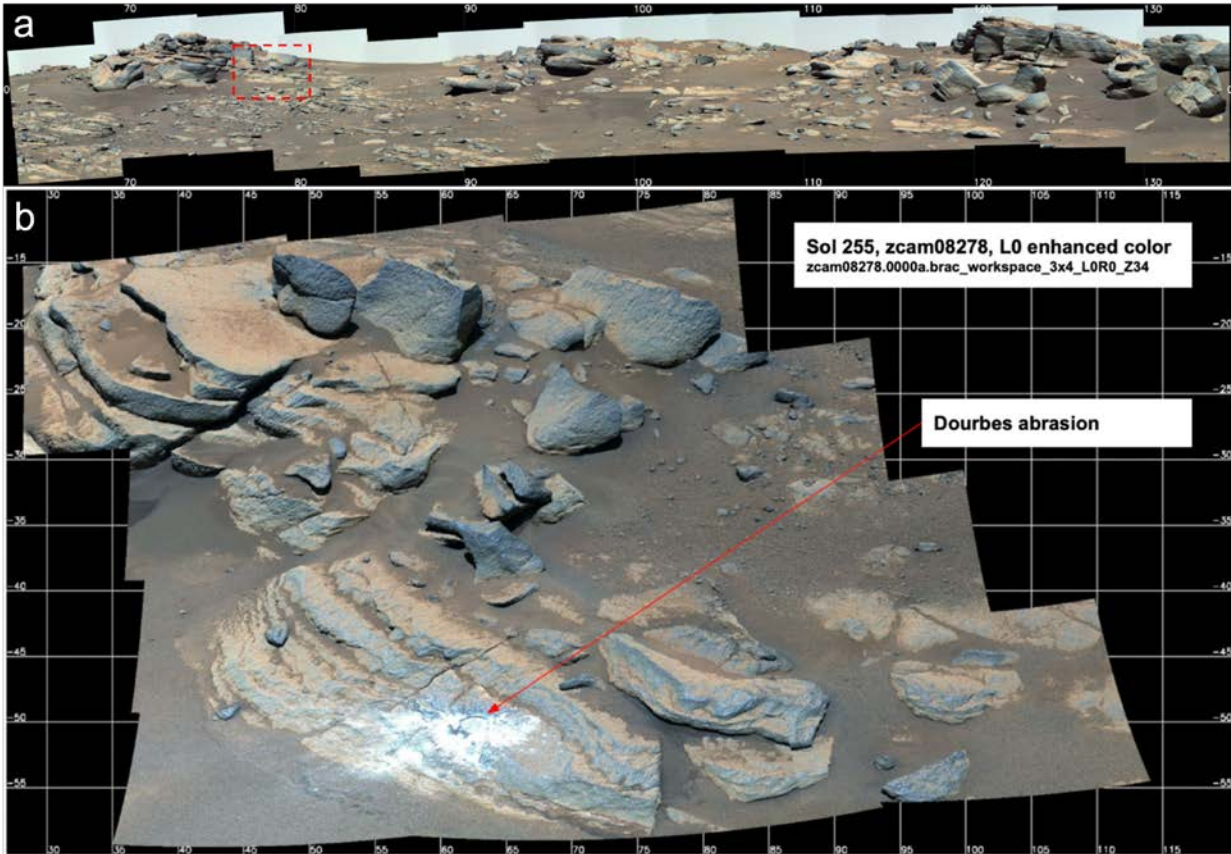


## Sample-Related Observations

### *Workspace Images*

**Figure 3a** shows a Mastcam-Z mosaic of the *Brac* outcrop in its local context (view is to the SE). **Figure 3b** shows the Mastcam-Z image of the workspace after the *Dourbes* abrasion patch and before *Salette* and *Coulettes* were sampled. To the upper left of *Brac* in **Figure 3b** the outcrop transitions into apparently massive blocks and thickly layered outcrop. *Brac* and surrounding outcrop feature both smooth and sharper angular edges, surficial depressions, and some evidence for parallel fluting arising from wind erosion (*cf.* **Figure 4–6**). Although the natural surface of *Brac* is fairly free of dust, dust accumulations at the boundaries between layers obscure the layer–layer contacts (**Figure 4**). During workspace observations, the team proposed two scales of layering in *Brac*: i) layers several centimeters to tens of centimeters in thickness, delineated by dust-covered, recessively weathered contact; and ii) less distinct, thinner layers distinguished by ridges, parallel to the thicker layers, across the outcrop. No compelling evidence for layering was observed in the abrasion patch or the borehole.

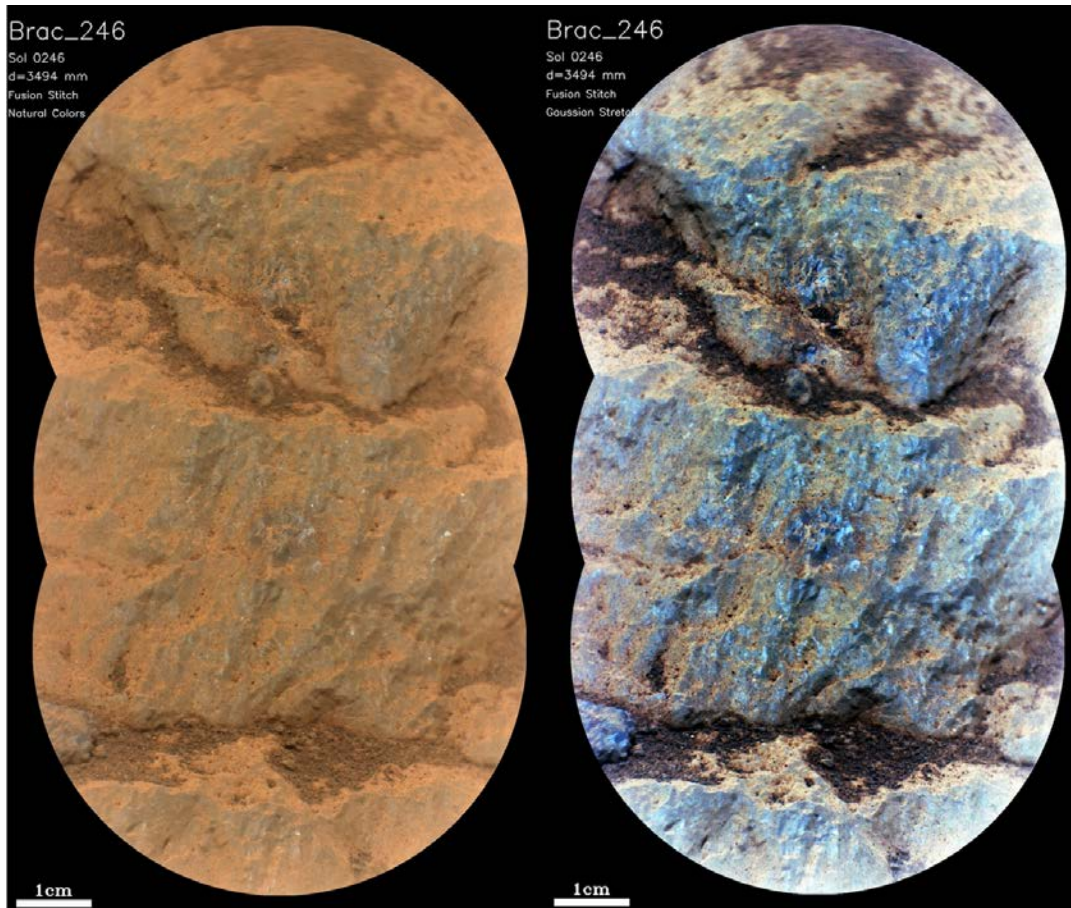
**Figure 3 | Geology near the *Brac* outcrop.** a) *Caille* locality; red rectangle indicates the location of the *Brac* outcrop. *Brac* is ~70 cm in length and located below the red rectangle. b) Post-abrasion Mastcam-Z image of the *Brac* outcrop and workspace. Location of the *Dourbes* abrasion patch is indicated by the red arrow. The abrasion patch is 5 cm in diameter. File: zcam08261.0000a.caille\_vignols\_baleine\_scam\_rmi\_visir\_P28\_LOR0\_Z110.



RMI images of the outcrop (**Figure 4**) show large (0.1–0.4 cm), dark grey, angular minerals surrounded by a pale brown interstitial phase similar to that observed on relatively fresh surfaces at *Bastide* (e.g. the RMI target *Cine*). These observations are consistent with those undertaken on the *Dourbes* abrasion patch (see below). The interstitial phase may represent the dark brown phase between minerals observed in the *Dourbes* abrasion patch, dust trapped between grains, or a combination of the two.

*Brac* is surrounded by regolith and conceivably may have moved downhill slightly as evidenced by the regolith-filled crevice to the left of the outcrop and a lack of layer continuity with other adjacent outcrops. However, it is more likely that *Brac* is in-place because its layering has the same apparent orientation as the surrounding outcrops throughout this portion of *South Séítah*. Subsurface data confirm that *Brac* is not significantly out of place (if at all) and as such it is confidently interpreted to be bedrock. Regolith settled into the subvertical fracture to the immediate left of *Dourbes* after abrasion, but no motion of the outcrop was observed.

**Figure 4 | SuperCam RMI mosaic of the *Brac* outcrop** showing large gray grains surrounded by pale white-brown phases visible on less dusty surfaces. Natural color (a) and Gaussian stretch (b) images of the same region are shown. Regolith and loose grains have accumulated in depressions at the outcrop surface.



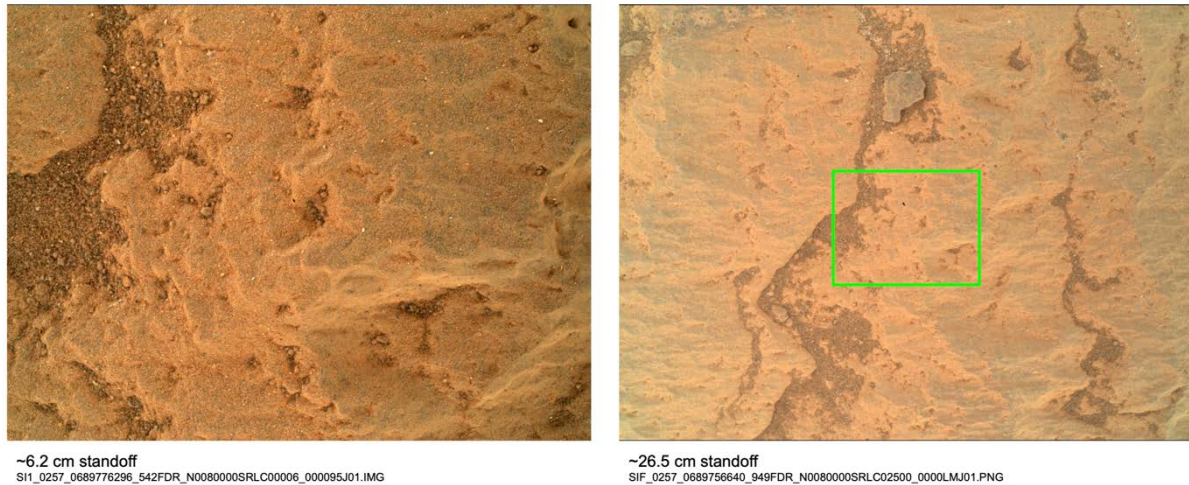
#### ***Pre and Post Coring/Abrasion Images***

**Figure 5** shows the natural surface of *Brac* prior to coring of *Salette*. **Figure 6a** shows the WATSON pre-coring image of the natural surface of *Dourbes*, **Figure 6b** shows a WATSON image of the gDRT-cleared abraded patch and **Figures 6c–d** show the corresponding WATSON ACI images.

Notable observations of high-resolution pre- and post-coring images include:

a) The natural weathered surface of *Brac* is generally smooth but has numerous small depressions that are filled with dust and other fine-grained, likely wind-blown, materials. There is some evidence of fluting caused by wind erosion. Few, if any, individual grains are visible in the natural surface images (**Figures 5–6**), but abundant grains were noted in RMIs of less-dusty surfaces (**Figure 4**).

**Figure 5 | WATSON pre-coring images of the Salette core target area at two standoff distances.** Green box in 26.5 cm standoff images shows location of 6.2 cm standoff image.



b) 0.1–0.3 mm pale brown–white sub-angular phases dominate the *Dourbes* abrasion patch (**Figure 6b**). Other major constituents are 0.2–0.8 mm mid-brown crystals with sub-angular to angular morphologies, 0.1–0.4 mm grey–green crystals with angular and elongate morphologies, <0.1 mm white crystals and a single white crystal with a triangular cross-section. The pale brown–white, mid-brown, grey–green and white minerals are distributed throughout the abrasion patch with no obvious spatial heterogeneity in their relative abundances.

c) Most minerals within the abrasion patch are surrounded by mid-brown inter-crystal boundaries, suggesting a pervasive Fe-rich influence. Pale reddish rims also surround many olivine crystals. This apparent Fe staining is particularly strong in association with the pale brown–white phases that dominate much of the abrasion patch. This association is especially visible in the ACI images where its interstitial nature is obvious.

WATSON post-coring images were acquired on the *Coulettes* sampling site (**Figure 7**). Note the well-formed conical mound of tailings, and, on the underlying rock, the purple-hued coating frequently seen on crater floor rocks.

CacheCam images of the acquired samples in their sample tubes are shown in **Figure 8**. Although the *Coulettes* core end is slightly out of focus because the core was not full length, the image of the full length *Salette* core shows the core end to be very similar in color and texture to the *Dourbes* abrasion patch, suggesting little lithologic change to a depth of ~ 6 cm in *Brac*.

**Figure 6 | WATSON images of the *Dourbes* abrasion surface (sol 257).** (a) Pre-abrasion WATSON 8 cm standoff image showing the natural surface of *Dourbes*. (b) WATSON image of the entire abrasion target. (c-d) ACl images, grayscale and colorized, of a region of interest within the *Dourbes* abrasion patch. Note that the WATSON images are rotated with respect to the images obtained by the remote sensing mast.

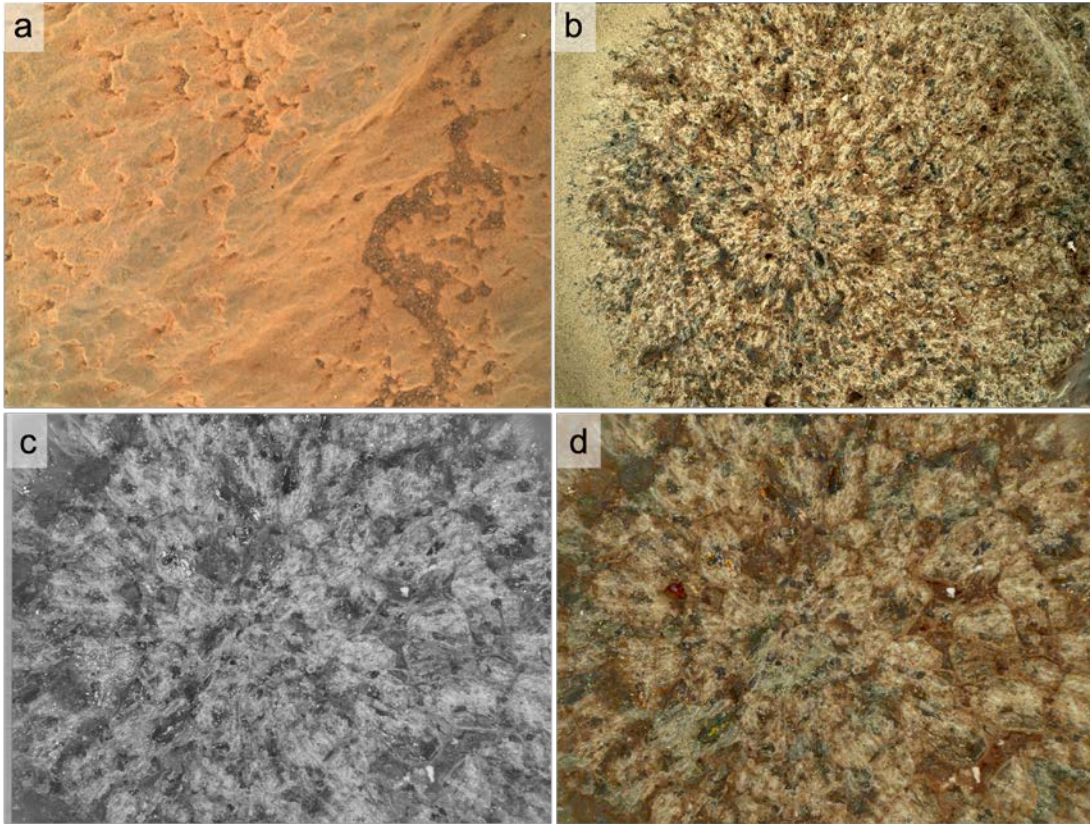
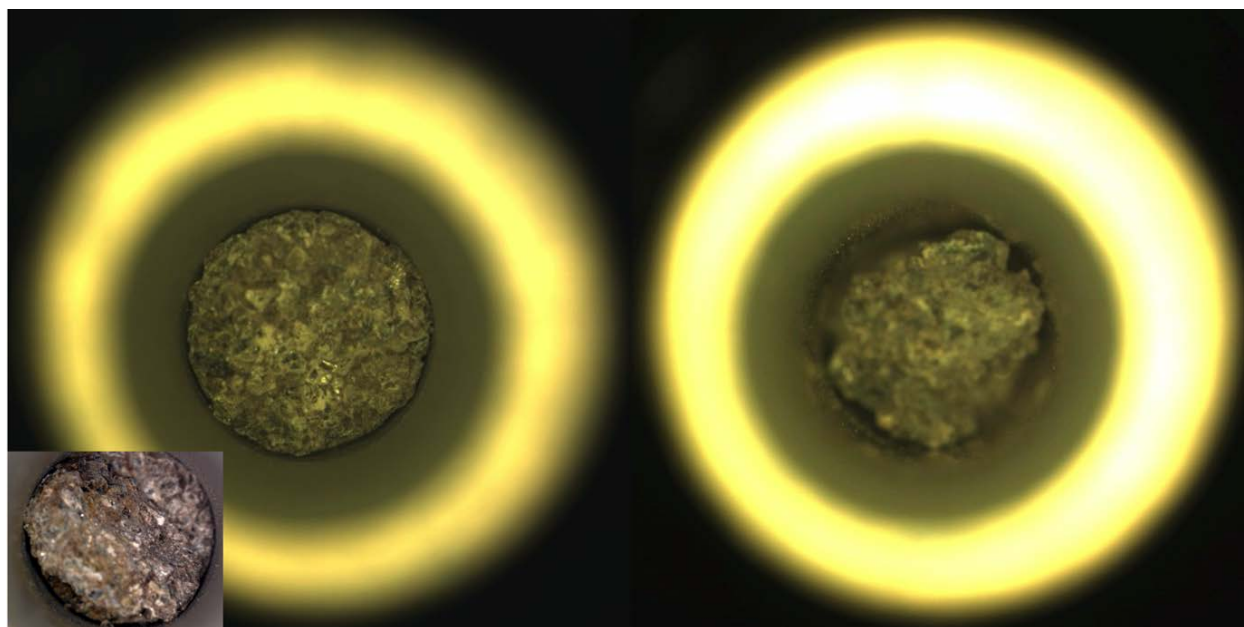


**Figure 7 | Post-coring WATSON image of the *Salette* borehole.**



**Figure 8 |** CacheCam images of the *Salette* (left) and *Coulettes* (right) samples. Inset is a high-resolution montage of CacheCam frames of *Salette*.



### **Elemental Geochemistry - PIXL**

Elemental geochemistry was determined using X-ray fluorescence (XRF) mapping by the PIXL instrument on the *Dourbes* abrasion patch. XRF rasters were acquired on sols 257 and 270 (**Figure 9**). This report includes only limited data from the sol 270 raster. Based on texture, bulk chemistry, and mineral chemistry, *Brac/Dourbes* is inferred to be a cumulate igneous rock formed by settling of olivine crystals and subsequent crystallization of interstitial basaltic magma.

The bulk sum analysis for the sol 257 raster, i.e. the average chemical composition, is given in **Table 2**. *Brac* is clearly a silicate rock, and high abundances of MgO, FeO, and Al<sub>2</sub>O<sub>3</sub> suggest an igneous basaltic parentage. Compared to a typical basalt (terrestrial or martian), it is low in SiO<sub>2</sub>, Al<sub>2</sub>O<sub>3</sub> and MgO, and rich in FeO, Na<sub>2</sub>O, SO<sub>3</sub> and Cl. Note that this bulk sum represents a mixture of what are believed to be anhydrous primary silicate minerals (olivine, pyroxene and plagioclase) and secondary (aqueous alteration) volatile-bearing minerals. In addition to the tabulated values, the bulk composition contains 550±200 (1s) ppm Ni; all other minor and trace elements are below detection limits.

On a total alkali versus silica (TAS) plot, **Figure 10**, PIXL analyses are distributed across the fields of olivine, picobasalt, and basalt. Some points also fall within the basaltic andesite field and a few points follow the trachybasalt–trachyte trend (a few points have SiO<sub>2</sub>>55 wt%). Several also plot near the Fe-Ti oxide and apatite positions. The bulk sum of the PIXL analysis raster falls within the olivine–basalt field. **Figure 11** shows a ternary diagram of molar compositions Al<sub>2</sub>O<sub>3</sub> – (CaO+Na<sub>2</sub>O+K<sub>2</sub>O) – (FeO<sub>T</sub>+MgO) for every individual PIXL point in the sol 257 raster and the bulk sum. Idealized common mineral compositions are also plotted on the diagram. The majority of points fall inside the triangle defined by typical mafic

minerals (e.g., olivine, Ca-rich pyroxene, feldspar), and so are consistent with being mixtures of those minerals. PIXL data points along the olivine–clinopyroxene and olivine–feldspar lines represent binary mixtures of these minerals, arising because their analytical volumes included both minerals. Almost no points fall above the feldspar–olivine line, i.e. enriched in  $\text{Al}_2\text{O}_3$  as would be expected for a weathered rock. Overall, this plot indicates that *Dourbes* is neither strongly aqueously altered nor intensely weathered.

**Figure 9 | PIXL raster scans on *Dourbes*.** Approximate locations of PIXL XRF scans on the *Dourbes* abrasion patch (field of view = ~5 cm across), annotated with the corresponding sol. Sol 0257 scan is 12.5 x 4 mm; sol 0270 scan is 7 x 5 mm. Olivine grains are pale buff, augite is greenish-black, and poorly diffracting Fe-Mg-poor silicate material is brown. Locations are overlain on WATSON image SIF\_0257\_0689757397\_902FDR\_N0080000SRLC00672\_0000LMJ01, rotated 90° clockwise from its original orientation.

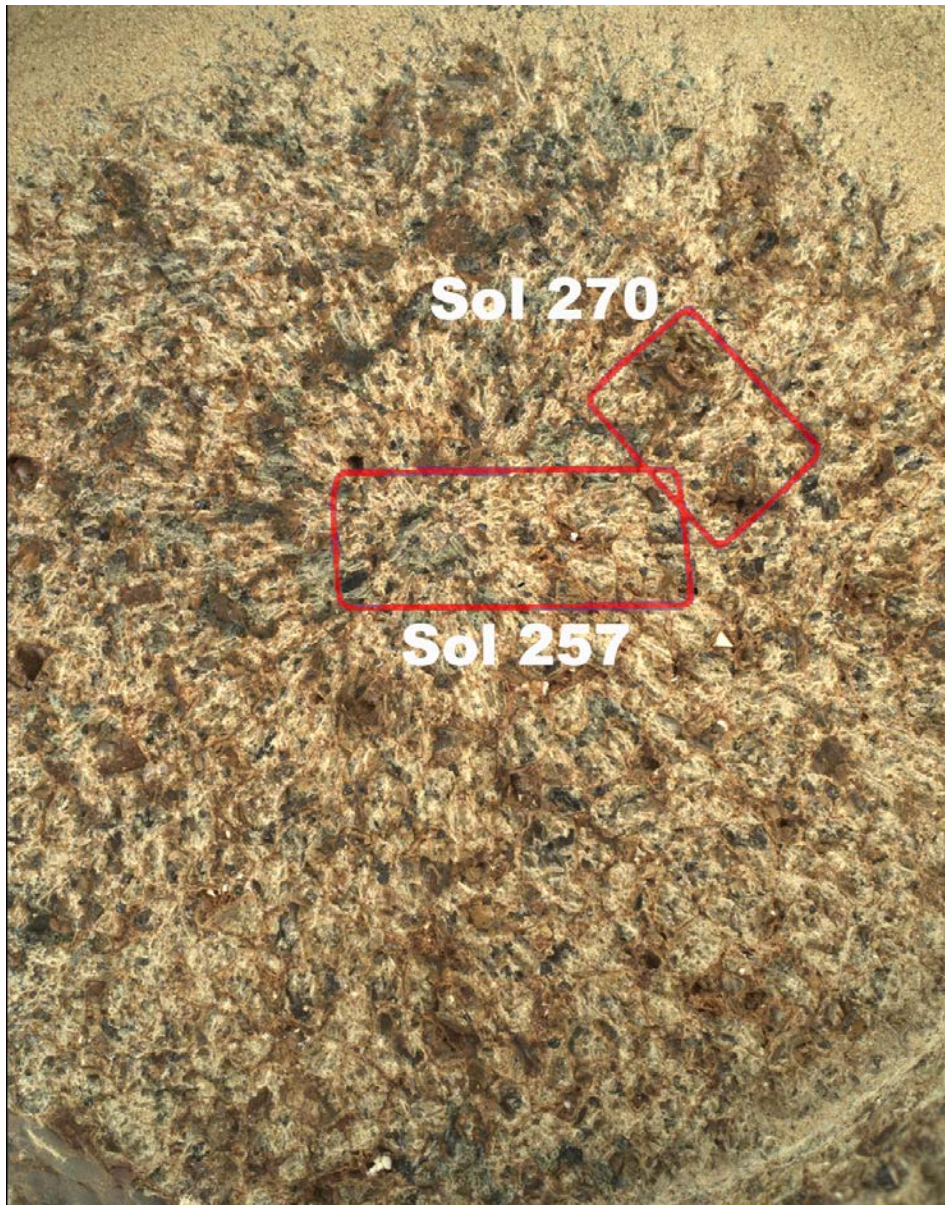


**Table 1. Chemical compositions by PIXL XRF.**

Wt %	Bulk rasters 257&270		Olivine salt-free		Augite salt-free	
	N=5670	Err 1 $\sigma$	N=33	Err 1 $\sigma$	N=28	Err 1 $\sigma$
Na <sub>2</sub> O	1.93	0.70	0.38	0.53	0.58	0.53
MgO	19.24	0.97	25.03	0.79	15.33	1.01
Al <sub>2</sub> O <sub>3</sub>	2.42	0.55	0.18	0.17	0.89	0.22
SiO <sub>2</sub>	39.42	1.98	35.52	0.74	51.12	3.07
P <sub>2</sub> O <sub>5</sub>	0.48	0.23	0.06	0.07	0.06	0.09
SO <sub>3</sub>	0.78	0.27	0.02	0.02	0.00	0.00
Cl	0.66	0.23	0.00	0.00	0.00	0.00
TiO <sub>2</sub>	0.37	0.25	0.00	0.00	0.00	0.00
CaO	2.94	0.56	0.23	0.05	16.76	1.57
K <sub>2</sub> O	0.18	0.19	0.00	0.00	0.26	0.06
Cr <sub>2</sub> O <sub>3</sub>	0.26	0.23	0.00	0.00	0.27	0.06
MnO	0.69	0.29	0.62	0.02	0.33	0.09
FeO-T	30.05	1.50	36.60	0.42	12.92	1.65
Sum %	99.4		98.68		98.5	
Mg#	54		55		68	

N indicates the number of analyses averaged. Err is uncertainty (1 $\sigma$ ) from calibration and counting statistics. Mg# is molar Mg/(Mg+Fe), in percent.

PIXL multi-elemental maps show abundant euhedral to subhedral olivine grains (~Fo<sub>55</sub>) varying in size between 1 and 3.5 mm, together with anhedral augite (<8 mm). Olivine is the most abundant mineral, accounting for more than 60 vol% of the mafic material in the *Dourbes* abrasion patch (**Figure 12**). Olivine grains are partially enclosed by augite in a poikilitic texture commonly seen in igneous rocks on Earth, as well as in the chassignite Martian meteorites. Average chemical compositions of olivine and augite are given in **Table 2**. Back-reflection diffracted x-rays detected from augite regions indicate that they are monocrystalline and crystallographically oriented across non-contiguous areas separated by olivine in the abrasion patch. This feature is characteristic of pyroxenes in many olivine cumulate rocks. Other components identified in PIXL scans include mesostasis material among the olivine and augite, and secondary phases. The mesostasis consists of a mixture of Na-rich feldspar (<1 mm), Fe-Cr-Ti magnetite ( $\leq 0.25$  mm), K-rich feldspar (<0.125 mm) and Ca-phosphates (<0.125 mm). Secondary phases include poorly diffracting (or very fine grained) silicate(s) with low Fe and Mg, Fe-Mg carbonate, Ca-sulfate, Mg-sulfate (likely MgSO<sub>4</sub>·4H<sub>2</sub>O), and Na chloride and/or perchlorate. These secondary materials, interpreted to be products of post-igneous aqueous alteration, occur in light-toned patches (primarily salt minerals) and in reddish brown patches (low Fe-Mg silicates) surrounding and invading anhydrous minerals, especially olivine.

PIXL Micro-Context Camera (MMC) images of the *Dourbes* abrasion patch (**Figure 13**) show more of the abrasion area than the XRF scans (**Figure 13a**) and are used to extrapolate phase proportions from those of the XRF scan areas to nearly the whole abrasion patch. The MMC image of NIR-G-B (**Figure 13b**) is analogous to WATSON visible images, and the G/NIR ratio image shows a clear distinction among the olivine, augite, and mesostasis phases (**Figure 13c**). These visible & qualitative relationships are quantified

in a graph of *G* versus NIR reflectances (**Figure 13d**), which allows extraction of the proportions of these phases in the whole MMC image area.

**Figure 10 | Total alkali versus silica (TAS) plot for the *Dourbes* abrasion, PIXL raster of sol 257.** Individual data points represent regions of the abraded surface (~100  $\mu\text{m}$ ) and therefore a mixture of one or more primary and/or secondary minerals. The bulk sum composition of PIXL data (**Table 2**) is shown by the blue circle. Reference end-member igneous mineral compositions are shown as diamonds and lines for those with solid solution series. The underlying igneous classification scheme does not apply to the individual data points and simply provides a frame of reference for comparing samples.

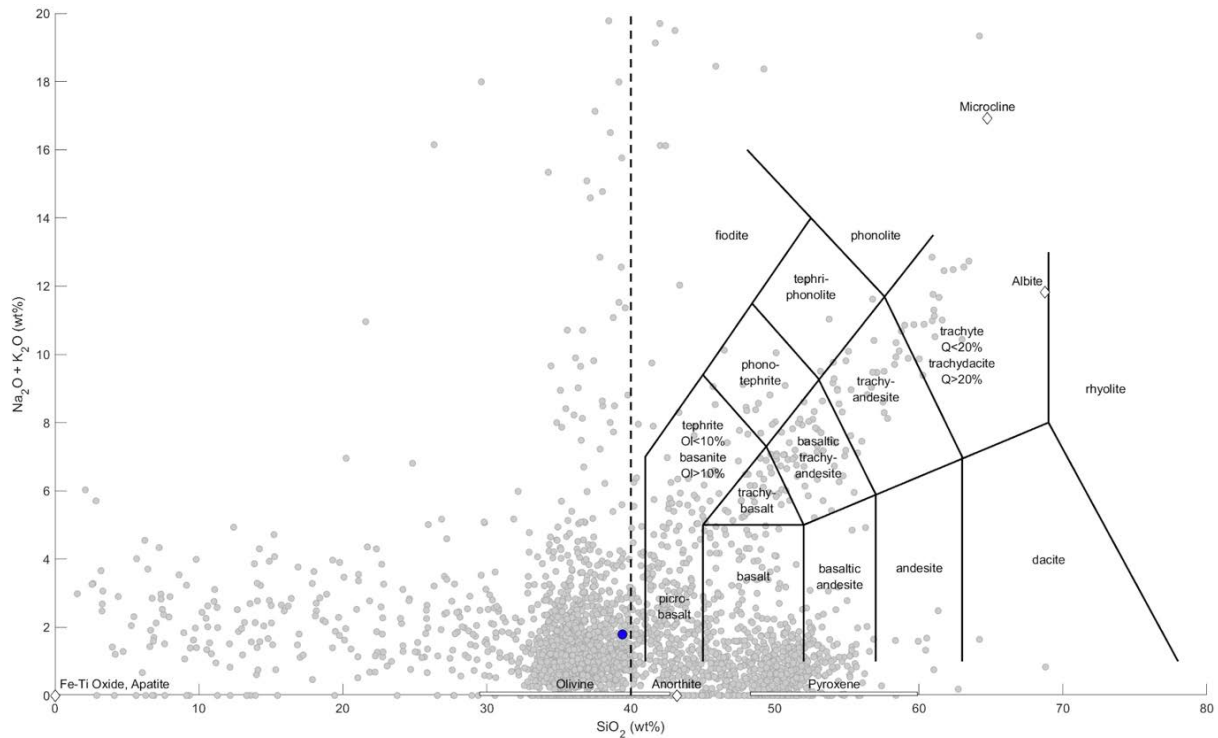


**Figure 11 | Mineralogical interpretation of the *Dourbes* abrasion, PIXL raster of sol 257.** Data are plotted by pixel and as bulk sum composition (blue circle, **Table 1**) on ternary diagrams of molar abundances of  $\text{Al}_2\text{O}_3$ – $(\text{CaO}+\text{Na}_2\text{O}+\text{K}_2\text{O})$ – $(\text{FeO}_T+\text{MgO})$ . Common pure mineral compositions are shown (opx = Ca-poor pyroxene, i.e. orthopyroxene; cpx = calcic pyroxene, i.e. augite). Most of the individual PIXL analysis points are consistent with being either pure minerals (olivine, cpx) or binary mixtures of olivine–cpx or olivine–feldspar, or ternary mixtures of olivine–cpx–feldspar. Aluminous alteration minerals, including common clay minerals, fall above the upper red dashed line. Several other secondary minerals (e.g., Fe–Mg–Ca-sulfates/carbonates, halite) are also plotted.

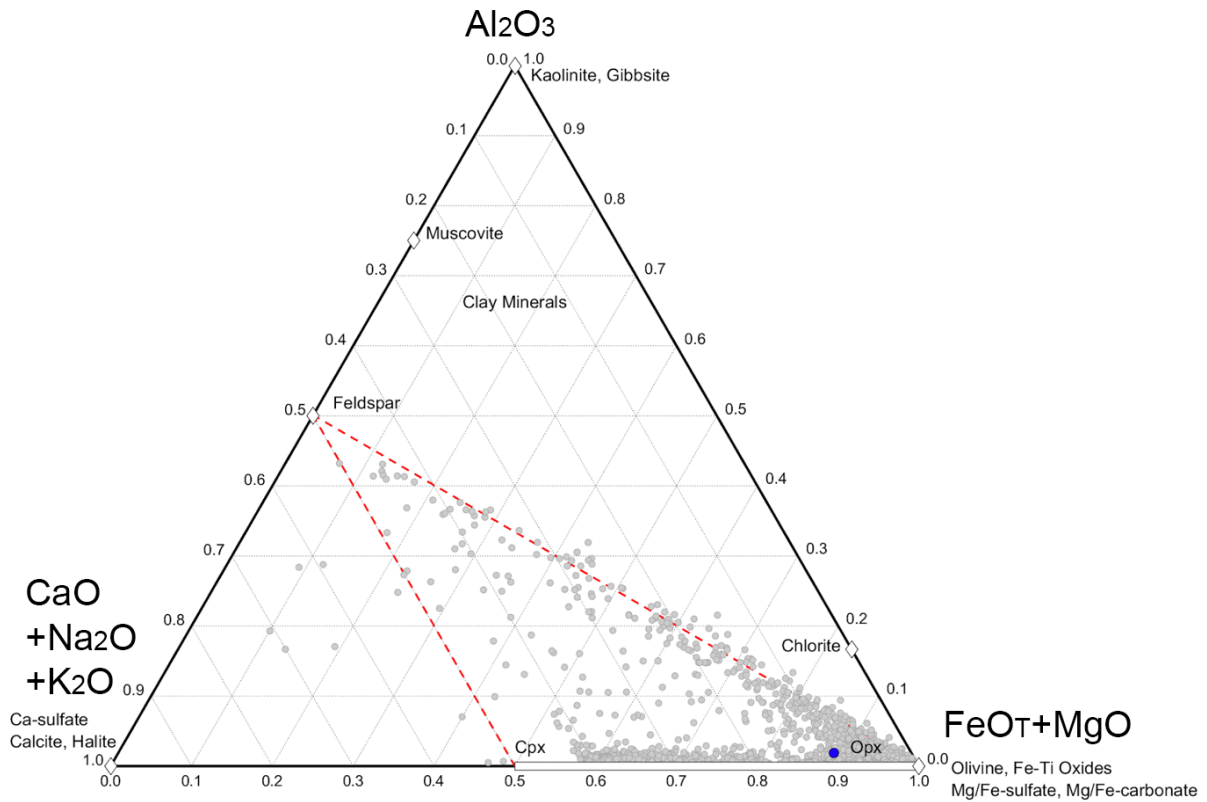


**Figure 12 | PIXL X-ray multi-element maps for the Dourbes abrasion patch, PIXL raster sol 257; raster is 12.5 x 4 mm.** (a) Red=MgO, Green=Al<sub>2</sub>O<sub>3</sub>, Blue=CaO. (b) Red=CaO, Green=Na<sub>2</sub>O, Blue=K<sub>2</sub>O. (c) Red=MgO, Green=Na<sub>2</sub>O, Blue=Cl. (d) Red=FeO<sub>T</sub>, Green=TiO<sub>2</sub>, Blue=Cr<sub>2</sub>O<sub>3</sub>. Olivine is the most abundant material (red in panel a.). Augite pyroxene is purple in panel a, and red in panel b. Feldspars are green in panel a. Salt is green in panel b, and white in panel c. Panel d shows Fe oxide minerals: Ti-rich oxides are yellow, Cr-rich oxides are purple.

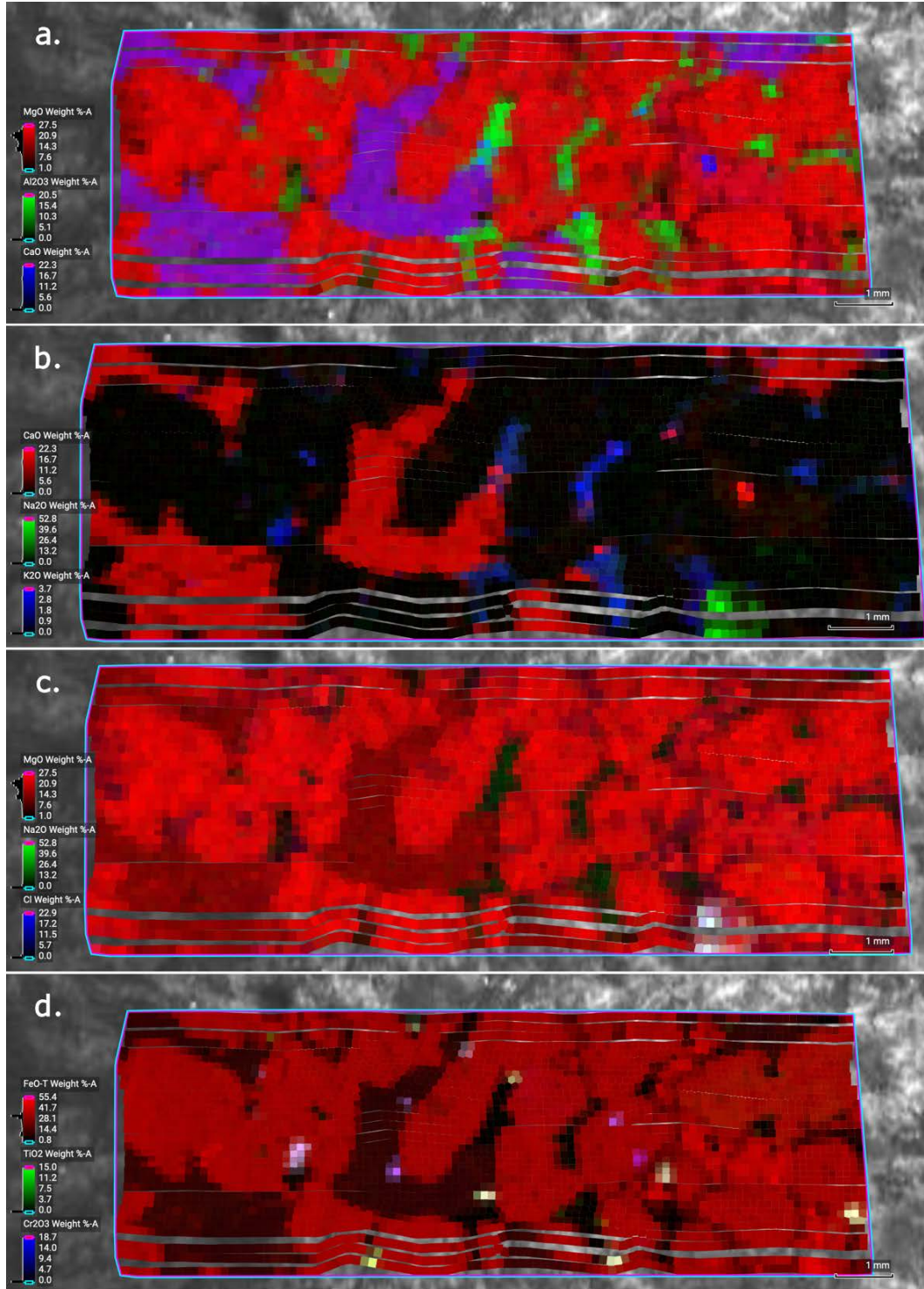
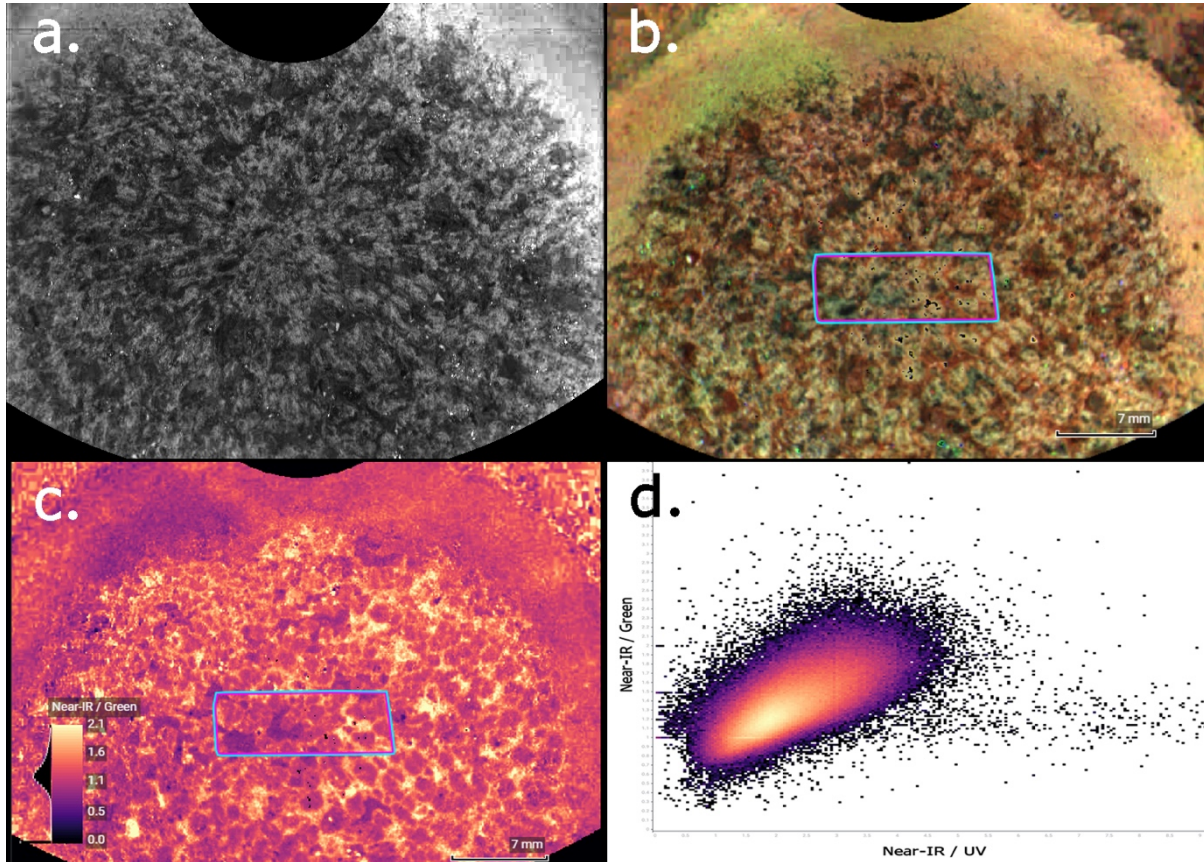


**Figure 13 | PIXL MCC (Micro-context camera) data for the *Dourbes* abrasion, sol 257.** (a) MMC grayscale image showing a portion of the *Dourbes* abrasion. (b) MMC false color of a abrasion area; Red = MMC Near-IR; Green = MMC Green; Blue = MMC Blue. Location of the PIXL XRF scan is shown. (c) MMC ratio image Near-IR/Green reflectances. Augite, A, is darkest; olivine, O, is mid-toned, and mesostasis and alteration materials have the lightest tone. Location of PIXL XRF scan shown. (d) MMC reflectance ratios.



### **Mineralogy and Organics-SHERLOC**

SHERLOC Raman and fluorescence scans were performed on *Dourbes* on sols 257 (HDR and survey scans; **Figure 14**) and 269 (survey scan and three detail scans; **Figure 15**). The analytical footprints are shown in the corresponding figures.

In the sol 257 scans, Raman data show spectra with peaks assigned to Ca/Mg-sulfate ( $\sim 1050\text{ cm}^{-1}$ ), carbonate ( $\sim 1090\text{ cm}^{-1}$ ) and olivine ( $\sim 840\text{ cm}^{-1}$ ). Some spectra contain a possible hydration peak at  $\sim 3450\text{ cm}^{-1}$  and a broader peak at  $\sim 997\text{ cm}^{-1}$  assigned to pyroxene or sulphate. Fluorescence features at 290 and 330–340 nm are consistent with single and double ring aromatic organic molecules, respectively. The relatively low intensity of fluorescence at all wavelengths and absence of Raman organic signatures suggests that, if organics are present, they occur with low abundances and are generally dispersed with the exception of some localized hot spots.

In the sol 269 scans, Raman spectra show features assigned to Ca- and/or Mg-sulfate ( $1020\text{ cm}^{-1}$ ) and Ca/Mg(/Fe)-carbonate ( $1100\text{ cm}^{-1}$ ). Some spectra also exhibit a peak for hydration at  $\sim 3450\text{ cm}^{-1}$ . Detail scan 3 shows a possible detection of olivine based on a broad band centered near  $840\text{ cm}^{-1}$ . The fluorescence feature at 330–340 nm is consistent with double ring aromatic organic molecules. As in the sol 257 scan, the relatively low intensity of fluorescence at all wavelengths and absence of Raman organic signatures suggests that any organics present have low abundance and/or a dispersed distribution. SHERLOC-based mineral identifications are shown in **Table 2**.

**Table 2. SHERLOC mineral identifications in *Dourbes* abrasion patch.**

Sample	Certain	Possible (not confirmed)	We looked for these, but cannot find them
Dourbes	Sulfate (most likely Ca or Mg), occasionally hydrated <i>(occurs in white void fills or crystals, secondary to primary lithology)</i>	Olivine (major phase, low Fo#) occurs sometimes associated with darker grains.  Carbonate (major phase, most likely Ca/Mg/Fe)  Amorphous/microcrystalline silicate  Pyroxene	

**Figure 15 | SHERLOC fluorescence and Raman spectral results for *Dourbes*.** Spectra were collected with an HDR scan (7x7 mm, 100 points, 780  $\mu\text{m}$  spacing, 500 pulses per point) and a survey scan on sol 257 (5x5 mm, 1296 points, 144  $\mu\text{m}$  spacing, 15 pulses per point, not shown). A) Colorized ACI image of *Dourbes*; blue rectangle indicates the HDR scan area (sol 257) and white circles indicate regions of interest (ROIs) correlating to the fluorescence data presented in B and C. B) HDR scan maps showing the possible presence of organics. Upper panel shows an RGB map indicating the main regions of organic fluorescence (290 and 330–340 nm). Both doublet peaks at 290 and 330 nm (ROI1) and the 330–340 nm peak (ROI 2) are localized primarily within two ROIs (see panel A). The lower panel is blank because no Raman features consistent with organic materials were detected. C) Fluorescence spectra. The upper panel shows the average fluorescence spectrum for the whole area of analysis and the lower panel includes spectra from selected fluorescence “regions of interest” (see A). D) Map showing the results of the Raman HDR scan. The grid of red unfilled circles indicates the points analyzed (*cf.* A), while blue, yellow, green, brown and purple filled circles indicate mineral detections. The right panel includes selected Raman spectra from the HDR scan. The upper spectrum is the average spectrum of the HDR scan. With the exception of cosmic ray artifacts, features within are rather weak, but do match some of the features in the spectra below. The spectra labeled Pts. 2, 1, and 18 correspond to the points in the map panels with the same numbers and are representative of spectra assigned to (Ca)/Mg-sulfate ( $\sim 1050\text{ cm}^{-1}$ ), carbonate ( $\sim 1090\text{ cm}^{-1}$ ) and olivine ( $\sim 840\text{ cm}^{-1}$ ), respectively. The spectrum labeled Pt. 2 also contains a possible hydration peak at  $\sim 3450\text{ cm}^{-1}$ . The lowermost spectrum includes a broader peak at  $\sim 997\text{ cm}^{-1}$  assigned to potential pyroxene or sulfate (consistent with hydrated  $\text{MgSO}_4$ ). The detection of pyroxene in this region by PIXL gives confidence to this interpretation, but given the broadness of the peak and absence of secondary peaks at lower wavenumber (not detectable with SHERLOC), sulfate is also a possibility. The scale in panel A also applies to the maps in panel D.

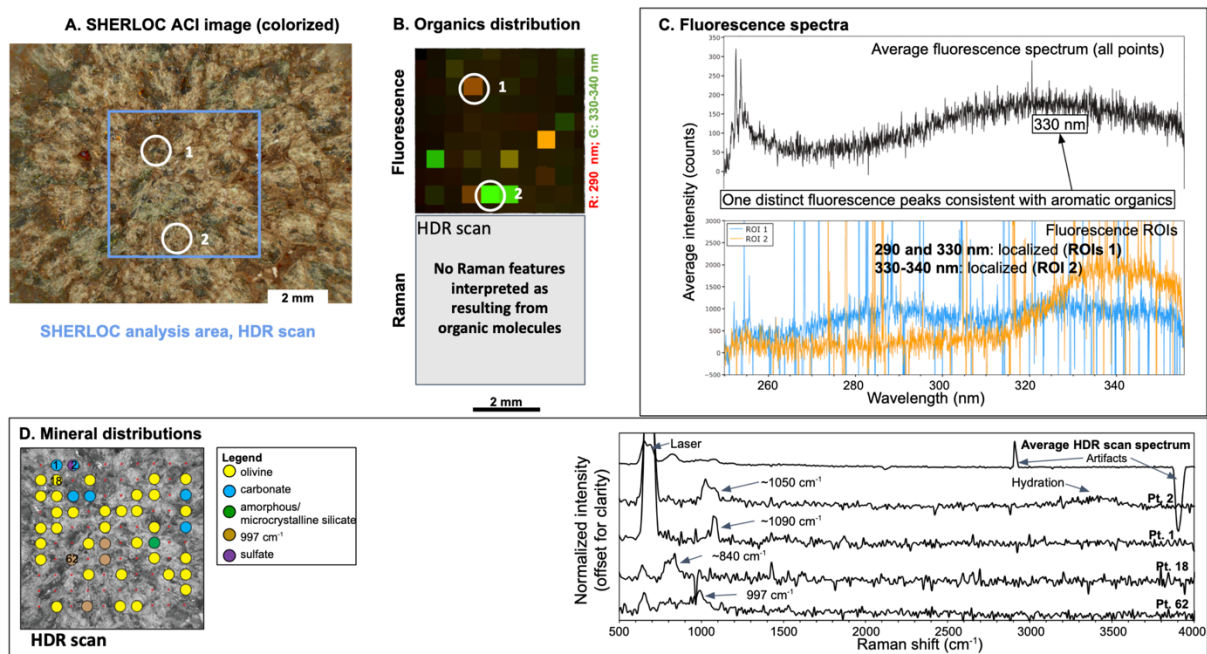
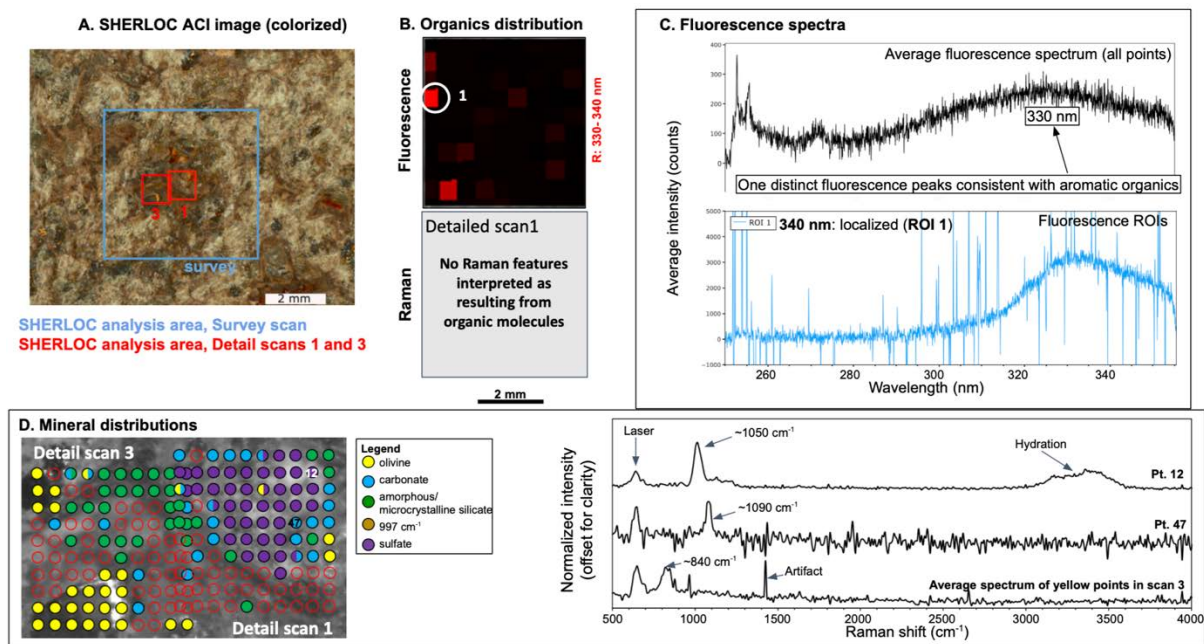


**Figure 16 | SHERLOC fluorescence and Raman spectral results for *Dourbes*.** Spectra were collected with a survey scan (5x5 mm, 1296 points, 144  $\mu\text{m}$  spacing, 15 pulses per point, not shown) and three detail scans (1x1 mm, 100 points, 144  $\mu\text{m}$  spacing, 500 pulses per point) on sl 269. A) Colorized ACI image of the abraded patch; blue rectangle indicates the survey scan area and red squares indicate detail scans 1 and 3. B) Detail scan 1 map showing the possible presence of organics. The upper panel shows an RGB map indicating the main regions of organic fluorescence (330–340 nm). The 330–340 nm peak (ROI 1) is localized mainly in “regions of interests” (ROI). The lower panel is blank because no Raman features consistent with organic materials were detected. C) Fluorescence spectra. The upper panel shows the average fluorescence spectrum for the whole analysis area and the lower panel includes spectra of selected fluorescence from ROI 1 (see A). D) Maps showing the results of the Raman detail scans 1 and 3. In each, the grid of red unfilled circles indicates the points analyzed (cf. A), and the blue, yellow, green, brown and purple filled circles indicate mineral detections. The right panel includes selected Raman spectra from the two scans. The spectra labeled Pts. 12 and 47 correspond to the points in the map panels with the same numbers and are representative of spectra assigned to Ca or Mg-sulfate ( $1050\text{ cm}^{-1}$ ) and Ca/Mg-carbonate ( $1100\text{ cm}^{-1}$ ). The spectrum labeled Pt. 12 also exhibits a peak for hydration at  $\sim 3450\text{ cm}^{-1}$ . The lower spectrum is the average spectrum of the points labeled with yellow circles in detail scan 3, which are interpreted to represent possible detections of olivine based on a broadband centered near  $840\text{ cm}^{-1}$ . The scale in panel A also applies to the maps in panel D.



### Elemental Geochemistry and Mineralogy - SuperCam

SCAM LIBS data from *Brac* and other *Séítah* targets, when plotted on the total alkalis versus silica (TAS) diagram (**Figure 17**), are scattered within the picrobasalt and basalt fields, and to a lesser extent within the olivine and basaltic andesite fields. The SCAM LIBS analyses targeted primarily natural surfaces, with only a small subset targeting the abraded patch. Olivine is the dominant detection and bulk sum average in the PIXL data obtained on the abraded patch, but the SCAM LIBS data differ, likely owing to natural variability in *Séítah*. Nonetheless, SCAM data are consistent with PIXL data in observing few points above  $\text{SiO}_2=55$  wt%.

Harker oxide diagrams of SCAM measurements of *Brac* are plotted against a background of all *Séítah* points in **Figure 18**. These diagrams show that *Brac* is generally representative of *Séítah*; potentially with lower  $\text{CaO}$ ,  $\text{Al}_2\text{O}_3$  and  $\text{Na}_2\text{O}$  contents.

Note that the  $\sim 250$   $\mu\text{m}$  LIBS spot most commonly interrogates more than one mineral grain. Given that the typical *Dourbes* grain size is 0.2–0.5 mm, as described above, many of the trends observed in the diagrams shown in **Figures 18** and **19** can be reasonably attributed to mixing among mafic minerals, e.g., olivine and low-Ca pyroxene.

**Figure 17 | TAS plot of SCAM LIBS data.** Average value of all data is shown as a blue circle. All *Séítah* analyses, i.e., including those not from the *Brac* outcrop, are plotted as grey points.

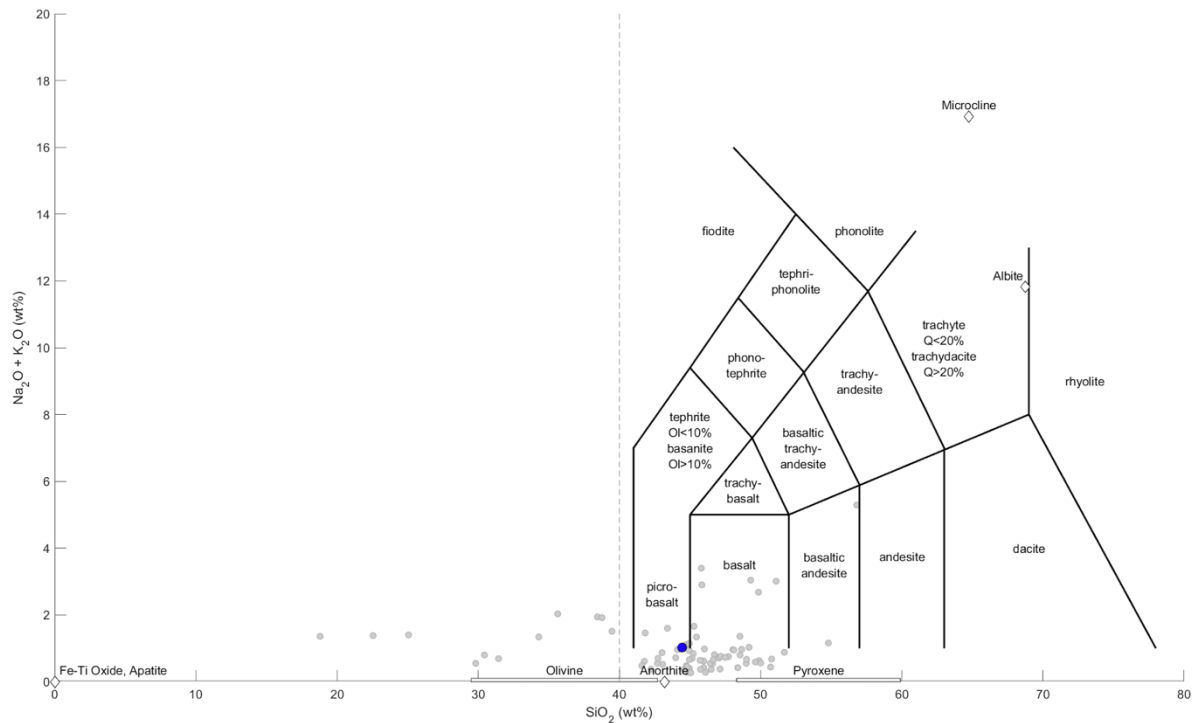


**Figure 18 | Harker oxide diagrams of SCAM data from *Séitah*.** Data from the *Brac* outcrop are shown as colored points. All *Séitah* points, including those not from *Brac*, are shown as black points.

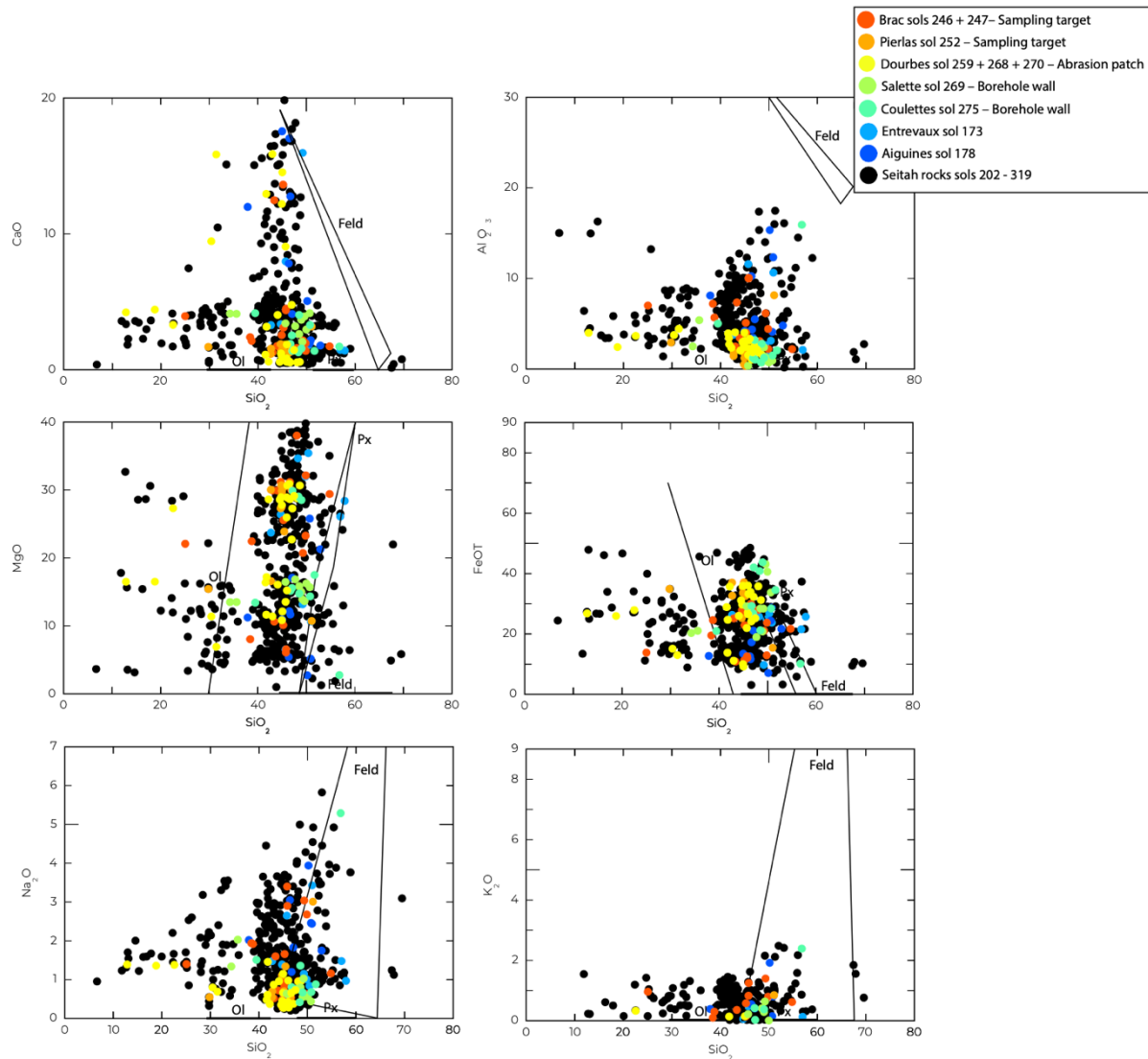
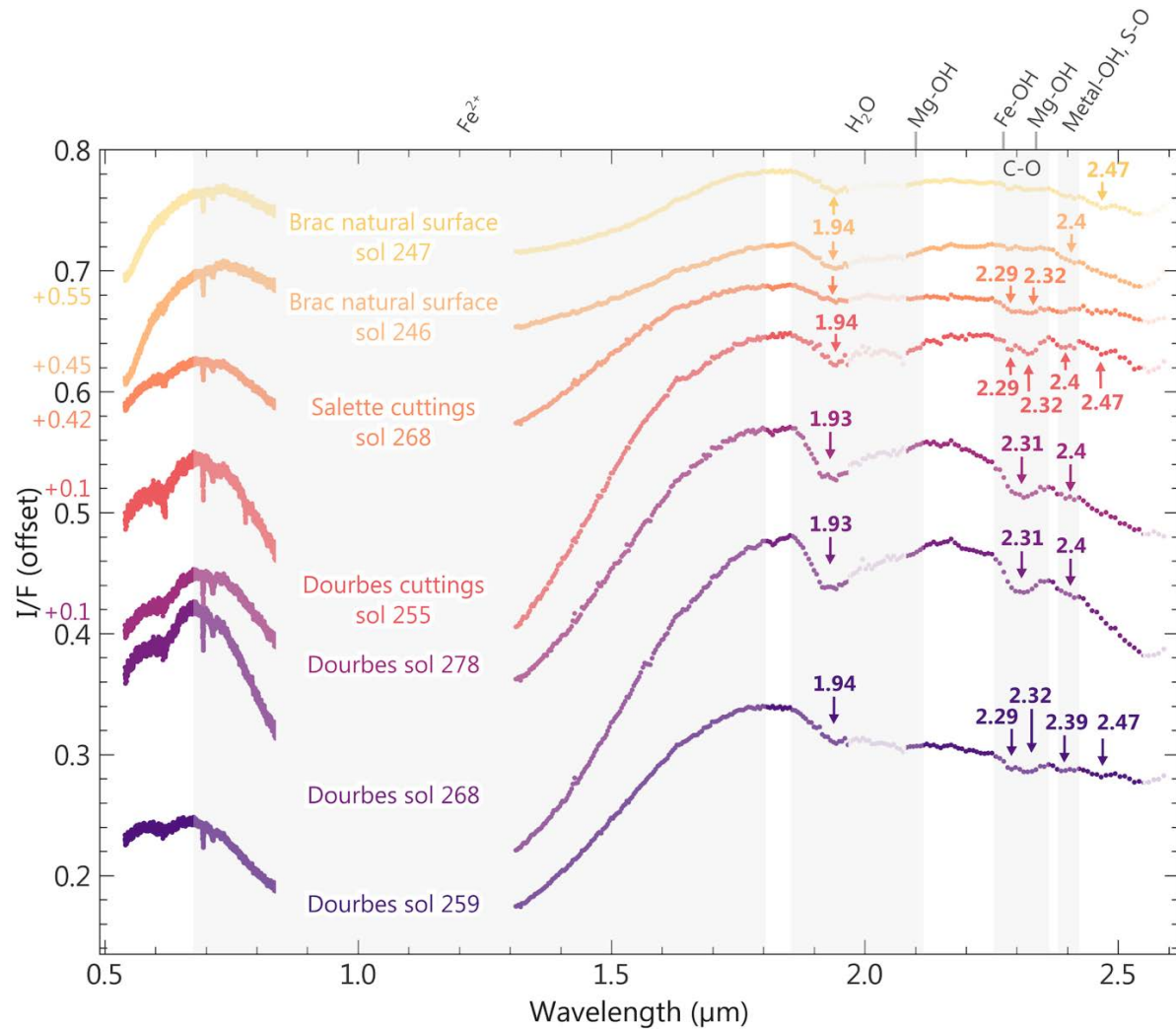


**Figure 19** shows mean VISIR spectra of the natural surface, the *Dourbes* abraded patch, and the tailings of the *Dourbes* abrasion and *Salette* coring acquired between sols 247 and 278. The broad absorption at 0.8–1.8  $\mu\text{m}$  denotes olivine in all observations. This signal is stronger in the abraded surface measurements relative to the natural surface. This is consistent with the stronger evidence for olivine in the PIXL abraded patch data relative to the SCAM LIBS natural surface data. The broad slope at 2.2–2.5  $\mu\text{m}$  denotes the presence of hydrated minerals. Specifically, the absorption at 2.28–2.29  $\mu\text{m}$  likely indicates Fe-bearing phyllosilicate, the absorption at 2.32  $\mu\text{m}$  likely indicates Mg-phyllosilicate, and the broad absorption centered around 2.3  $\mu\text{m}$  is consistent with Ca/Mg/Fe-carbonates and/or Fe/Mg-phyllosilicates.

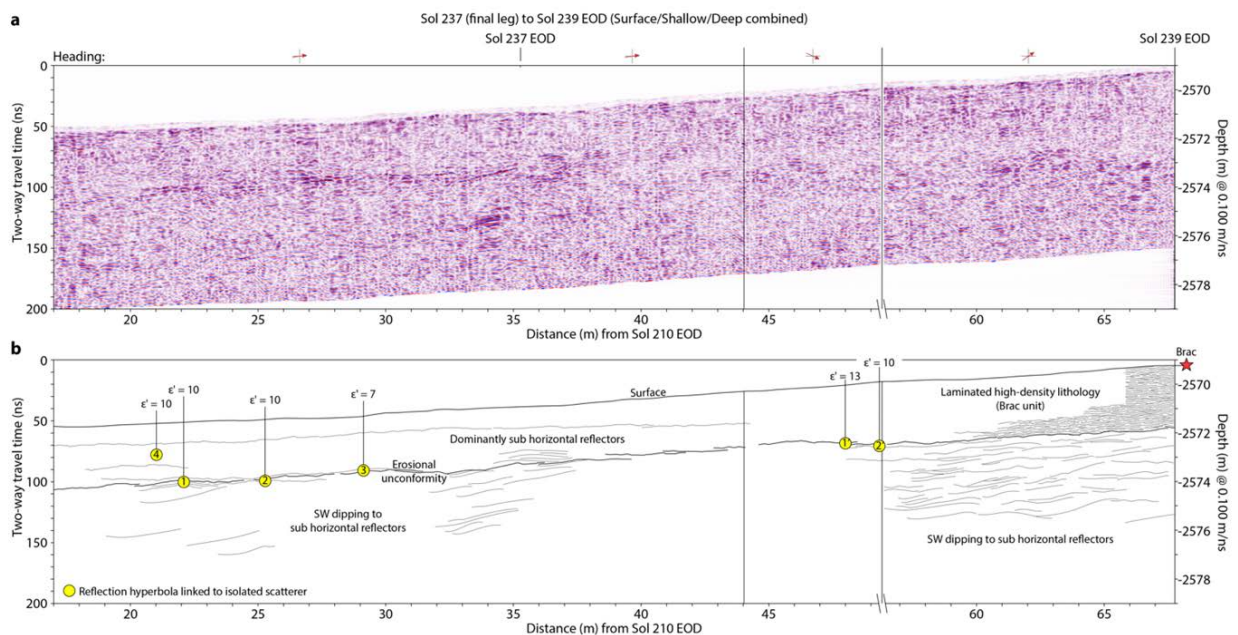
**Figure 19 | Mean VISIR spectra of the natural surface of *Brac*, the abraded patch *Dourbes*, the tailings of the *Salette* core and the tailings of the *Dourbes* abraded patch rasters.** The broad slope between 2.2 and 2.5  $\mu\text{m}$  is consistent with the presence of hydrated minerals. The broad absorption between 0.8 and 1.8  $\mu\text{m}$  indicates olivine in all observations; the signal is stronger in the abraded surface relative to the natural surface. The absorption at 2.28–2.29  $\mu\text{m}$  likely indicates Fe-bearing phyllosilicates, the absorption at 2.32  $\mu\text{m}$  likely indicates Mg-phyllosilicates, and the broad absorption centered around 2.3  $\mu\text{m}$  is consistent with Fe/Mg-phyllosilicates. Note that owing to temperature sensitivities in the IRS instrument, the calibration is uncertain for wavelengths longer than  $\sim 2.5$   $\mu\text{m}$ .



## Subsurface Structure

Subsurface structure in the vicinity of the *Brac* outcrop was characterized by RIMFAX radargrams acquired on sols 237–239 during the rover’s drive across *Séítah* on a mostly easterly traverse heading toward *Brac* (**Figure 20**). From left to right, the three panels in **Figure 20a** present results along the rover path that 1) begins ENE past the *Village* region, 2) turns ESE toward *Vignols*, then turns NE toward *Caille* and the *Brac* outcrop. The interpreted subsurface stratigraphy and rock density is shown in **Figure 20b**. Throughout this traverse, the data indicate SW-dipping to sub-horizontal reflectors that dominate the stratigraphy at ~3–8 m below the surface, which is interpreted to represent an extension of the SW-dipping reflector unit extending NE from *Artuby* Ridge (see the Initial Report for samples *Montdenier* and *Montagnac* from the *Rochette* locality). Above this unit is a 2–3 m thick laminated sequence with dominantly sub-horizontal reflectors (the unit containing *Brac*). A particularly intense reflector may be an erosional unconformity between these two packages of reflectors. Permittivity measurements of the upper laminated sequence indicate rock densities of approximately 3.5 g/cm<sup>3</sup>, consistent with the olivine-rich lithology observed in the *Brac* outcrop.

**Figure 20 | Geological context of the *Brac* outcrop from RIMFAX** a) Radargram for the sol 237–239 traverse. b) Geological interpretation of reflector geometries in panel a with *Brac* at sol 240 EOD (annotated with red star). The stratigraphy is identified by SW-dipping to sub-horizontal reflectors in the lower unit, sub-horizontal reflectors in the upper unit (including *Brac*), and scattered reflection hyperbolae in between. The locations of permittivity measurements ( $\epsilon'$ ) from reflection hyperbolae are denoted with yellow circles. Reflection hyperbolae 1–4 are from sol 237 and 1' and 2' are from sol 280. These and additional nearby permittivity measurements within the sol 237–280 radargrams cluster around  $\epsilon' = 10$ . Reflection hyperbolae record the average permittivity within the overlying strata. Permittivity–density relationships are determined after Carrier III et al. (1991).



### Core orientation

At the time of drilling and 6.6 cm pre-drilling WATSON imaging, the rover, coring drill, WATSON, and coring target (“Salette.PSC.0.0679”), had the following characteristics:

1. Rover orientation quaternion just after drilling but before unloading the stabilizers (transferring from RMECH to SITE frame):  $\mathbf{bQII1} = (0.8161970, -0.0570105, 0.0018349, 0.5749510)$ ;
2. Coring Drill orientation quaternion just after drilling but before unloading the stabilizers (transferring from CORING DRILL to RMECH frame):  $\mathbf{cdQb} = (0.7611450, 0.1932350, -0.6043060, 0.1346610)$ ;
3. Rover orientation quaternion at time of acquisition of WATSON image SIF\_0195\_0684255577\_390FDR\_N0070000SRLC00701\_0000LMJ01: (transferring from RMECH to SITE frame):  $\mathbf{bQII2} = (0.816367, -0.0553839, -0.000861533, 0.574871)$ ;
4. WATSON orientation quaternion at time of acquisition of WATSON image SIF\_0195\_0684255577\_390FDR\_N0070000SRLC00701\_0000LMJ01: (transferring from WATSON to RMECH frame):  $\mathbf{wQb} = (0.761644, 0.197503, -0.60257, 0.133416)$ .

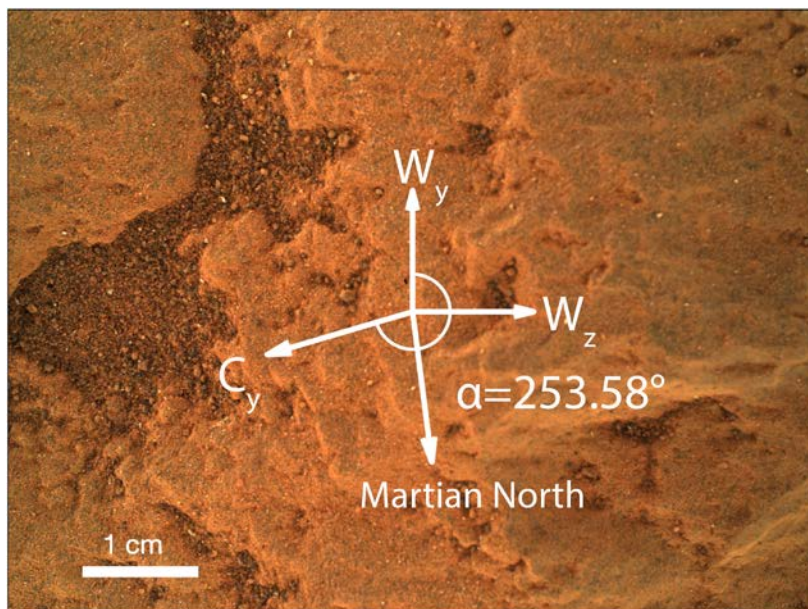
Items 1 and 2 give a coring drill pointing vector estimate of

$$\begin{aligned} \text{hade} &= 17.78^\circ \\ \text{azimuth} &= 81.51^\circ \end{aligned}$$

Items 3 and 4 give an estimate of the angle between the WATSON y-axis and the up-dip direction in SITE coordinates (**Figure 21**) of

$$\text{core roll, } \alpha = 253.58^\circ$$

**Figure 21** | 6.6-cm standoff WATSON image of Salette core target on sol 262. Image is  $30.9 \mu\text{m pixel}^{-1}$ . Orientation compass gives WATSON frame ( $\mathbf{w}_x, \mathbf{w}_y, \mathbf{w}_z$ ). Core roll is clockwise angle of core y-axis,  $\mathbf{c}_y$ , from  $\mathbf{w}_y$ , given by  $\alpha = 253.58^\circ$ . Projection of Martian geographic north onto WATSON image plane is noted. WATSON image SIF\_0195\_0684255577\_390FDR\_N0070000SRLC00701\_0000LMJ01.



## **Preliminary Scientific Assessment**

### **Synthetic sample description and preliminary interpretation**

Sample type: **Olivine cumulate**

#### **1. Relationship with surrounding rocks**

- a. *Salette* and *Coulettes* were obtained from a position high in the accessible stratigraphy of *Séítah*, near the location of overlying pitted rocks (e.g. the *Hôtel* rock).
- b. Based on its appearance, concordance with surrounding outcrops, and estimated dip consistent with that of the wider *Séítah* region, the *Brac* outcrop is interpreted to be an in-place portion of the *Séítah* bedrock.

#### **2. Texture and fabric**

- a. Grain size: <0.1–4 mm
- b. Rock fabric (natural surface): large olivine grains surrounded by interstitial pale materials exposed on relatively fresh surfaces, but minimal observations of grains on natural weathered surfaces.
- c. Rock fabric (abrasion patch): no obvious textural heterogeneity, main constituents include 0.1–0.3 mm pale brown–white sub-angular phases, 0.2–0.8 mm mid-brown sub-angular to angular crystals, 0.1–4 mm grey–green angular and elongate crystals, <0.1 mm white crystals.
- d. There is no compelling evidence of intergranular porosity or cements common to many sedimentary rocks.

#### **3. Mineralogy and chemistry**

- a. Minerals present: dominant olivine and low-Ca pyroxene (augite, potential ferrosilite). Mesostasis consists of a mixture of Na-rich feldspar (<1 mm), Fe-Cr-Ti magnetite ( $\leq 0.25$  mm), K-rich feldspar (<0.125 mm) and Ca-phosphates (<0.125 mm). Secondary phases include poorly diffracting (or very fine grained) silicate(s) with low Fe and Mg, Fe-Mg carbonate, Ca-sulfate, Mg-sulfate (likely  $\text{MgSO}_4 \cdot 4\text{H}_2\text{O}$ ), and Na chloride and/or perchlorate. Aromatic organic materials are present, but in low abundance and dispersed throughout the rock matrix except for a few hot spots.
- b. The bulk composition is consistent with a mafic rock modified by a low degree of aqueous alteration and weathering. Point analyses by SCAM and PIXL plot mostly within the olivine, picobasalt and basalt regions of the TAS diagram.

#### **4. Alteration/secondary characteristics**

- a. Interactions with aqueous fluids, alteration, and mineral hydration: some, e.g. carbonate and sulfate signatures.
- b. Secondary mineralogy: see point 3a above.

## **Returned Sample Science Considerations**

Observations of olivine surrounded by clinopyroxene in a poikilitic texture within the *Dourbes* abrasion patch, along with remote observations of the mineralogy, texture, and spectral characteristics of *Brac* and other *Séítah* outcrops, suggest that the *Salette* (and *Coulettes*) core and much or all of *Séítah* are best interpreted as an igneous olivine cumulate. As such, the return of samples from *Brac* is expected to address a number of RSS themes of significance to the Mars 2020 mission:

*Geochronology*: The timing of volcanic rock crystallization can be quantified using laboratory-based, radiometric dating of returned samples. Likewise, assuming cosmogenic nuclide production rates in specific mineral on Mars can be established, quantitative constraints on the sample's surface exposure age and/or erosion rate may also be obtained. Quantifying the timing of crystallization of *Brac* will also constrain the emplacement ages of other crater floor units, given their stratigraphic relationships (e.g. *Séítah* is likely older than *Máaz* from which the *Montdenier* and *Montagnac* samples were collected).

*Paleomagnetism*: The igneous lithologies of the *Salette/Coulettes* samples may enable absolute measurements of the paleointensity of the ancient Martian magnetic field at the time of crystallization. The orientations of the samples, combined with paleohorizontal indicators from outcrop foliation, may enable measurements of the absolute paleodirection of the ancient field. Paleomagnetic investigations of secondary ferromagnetic minerals if present could constrain the field at the time of aqueous alteration. Combined with measurements from other samples, these data could test the hypothesis that Martian atmospheric loss was driven by the cessation of an early dynamo, constrain the dynamo's secular variation, and determine if the dynamo exhibited polarity reversals. Paleomagnetic analyses could also test whether *Séítah* rocks have experienced regional or global-scale tectonic tilting and displacements. Comparison of paleomagnetic directions with *Máaz* rocks (*Montdenier/Montagnac* and *Atsah/Hahonih*) could distinguish between the hypotheses that *Máaz* and *Séítah* form a single layered intrusion versus *Máaz* being an overlying lava flow deposited on *Séítah*.

*Geochemistry*: With a hypothesized origin as an olivine cumulate, understanding the petrogenesis of the *Salette* and *Coulettes* samples will place constraints on the nature of igneous processes on early Mars. These constraints can be applied to the origins of the extensive "Cf-f-1" unit that has been correlated with a regional olivine-bearing unit exposed between Syrtis Major and Nili Fossae. The diverse mineral assemblages of the obtained samples will be valuable for quantifying the conditions and timing of primary, high-temperature crystallization of igneous phases and later-stage alteration events. The bulk chemistry of the rock, as well as trace element and stable and radiogenic isotope geochemistry of the rock and its constituent igneous minerals, will enable comparisons with similar lithologies in the Martian meteorite suite, and insights into magmagenesis and mantle/crustal evolution more generally. The large grains observed in *Brac* may contain melt inclusions that are of sufficient size to track the petrogenesis of this material.

*Water-rock interactions and habitability*: Many hypotheses for the origins of olivine-carbonate rocks involve aqueous alteration of igneous rocks. The interaction of aqueous media with (ultra)mafic rocks produces secondary mineral phases that can be indicative of the temperature, redox state, and fluid chemistry. High resolution mineral identification and stable isotope measurements can place constraints on such aspects of the alteration history and environment and provide insights into the presence, distribution, and nature of water on Mars. Water/rock interactions could have occurred as result of

groundwater, possibly associated with Jezero lake, moving through these rocks and may have led to the establishment of microniches with water, energy, pH, nutrients and transition metals essential to life. Although likely a variable component in the history of these samples, the team has noted that low-temperature hydrothermal, serpentinizing and carbonation reactions may have sustained microbial life, particularly chemoautotrophs/chemolithotrophs that have been suggested as likely inhabitants of Martian biotopes. Although the fossil record of igneous rocks is highly variable and generally poor, the biosignature preservation potential of certain alteration phases associated with the *Brac* outcrop is higher, and it is possible that organic materials and/or biosignatures have been preserved within these phases.

## **References**

- Carrier W.D. III, Olhoeft, G.R., Mendell, W. (1991) Physical Properties of the Lunar Surface. Lunar Sourcebook, A User's Guide to the Moon, ISBN 0521334446, Cambridge University Press, 475-594.
- Hamilton V. E. and Christensen P. R. (2005) Evidence for extensive, olivine-rich bedrock on Mars. *Geology* **33**, 433–436.
- Hoefen T. M., Clark R. N., Bandfield J. L., Smith M. D., Pearl J. C., and Christensen P. R. (2003) Discovery of Olivine in the Nili Fossae Region of Mars. *Science* **302**, 627–630.
- Kremer C. H., Mustard J. F. and Bramble M. S. (2019) A widespread olivine-rich ash deposit on Mars. *Geology* **47**, 677–681.
- Mandon L., Quantin-Nataf C., Thollot P., Mangold N., Lozac'H L., Dromart G., Beck P., Dehouck E., Breton S., Millot C. and Volat M. (2020) Refining the age, emplacement and alteration scenarios of the olivine-rich unit in the Nili Fossae region, Mars. *Icarus* **336**, 113436.
- Rogers A. D., Warner N. H., Golombek M. P., Head III J. W. and Cowart J. C. (2018) A really Extensive Surface Bedrock Exposures on Mars: Many Are Clastic Rocks, Not Lavas. *Geophysical Research Letters* **45**, 1767–1777.
- Stack, K.M. et al. (2020). Photogeologic Map of the Perseverance Rover Field Site in Jezero Crater Constructed by the Mars 2020 Science Team. *Space Science Reviews*, 216, 127, doi:10.1007/s11214-020-00739-x.
- Tornabene L. L., Moersch J. E., McSween Jr. H. Y., Hamilton V. E., Piatek J. L. and Christensen P. R. (2008) Surface and crater-exposed lithologic units of the Isidis Basin as mapped by coanalysis of THEMIS and TES derived data products. *Journal of Geophysical Research: Planets* **113**.

# INITIAL REPORT

## M2020-271-6 Coulettes

---

**Sample Designation:** M2020-271-6 Coulettes

**Date of Coring:** 24-November-2021

**Mars Time of Sample Core Sealing:** 20:18 LMST, Sol 271, Ls = 132.0

**Latitude (N), Longitude (E), Elevation:** 18.43397°, 77.44301°, -2569.2 m

**Campaign:** Crater Floor

**Region of Interest:** *Séítah South*

**Lithology:** Medium- to coarse-grained poikilitic olivine cumulate rock. Primary minerals are olivine and pyroxene. Aqueous alteration phases include sulfates, carbonates and hydrated phases. Organic matter was detected.

**Estimated Volume Recovered:** 4.7 cm<sup>3</sup>

**Coring Bit Number:** 1

**Core Orientation:** hade = 14.50°; azimuth = 78.68°; core roll = 220.85°

**Sample Serial Numbers:** Tube SN284; Seal SN219; Ferrule SN189

**ACA Temperature at Time of Sealing:** 40°C

**Estimated Rover-Ambient Pressure and Temperature at Time of Sealing:** 636 Pa, 222 K

**Estimated Amount of Martian Atmosphere Headspace Gas:** 2.5 x10<sup>-6</sup> mol

**Anomalous Behavior:** None

**Abrasion Patch Name and Depth:** *Dourbes*, 8 mm

---

January 27, 2022

*K. Hickman-Lewis, K. A. Farley, J. I. Simon, J. R. Johnson, B. Horgan, M. Rice, J. Bell, J. Rice, T. Bosak, L. Mandon, A. Udry, S. VanBommel, S. M. McLennan, Y. Goreva, R. C. Moeller, V. Sun, K.P. Hand, E. L. Berger, F. Calef, A. D. Czaja, C. H. Lee, A. C. Fox E. L. Scheller, S. Sharma, S. Siljeström, H. E. F. Amundsen, L. W. Beegle, B. P. Weiss, E. N. Mansbach, D. L. Shuster, C. D. K. Herd, R. C. Wiens, S. Le Mouélic, G. Caravaca, O. Gasnault, S. Maurice, M. P. Zorzano and the Mars 2020 Team.*

## Summary Description

This sample is paired with M2020-262-5 *Salette*. Only the core orientation for *Coulettes* is described below. See the Initial Report for M2020-262-5 *Salette* for sample details.

### **Core orientation**

At the time of drilling and 6.6-cm pre-drilling WATSON imaging, the rover, Coring Drill, WATSON, and coring target (called “*Coulettes\_271.PSC.0.0656*”), had the following characteristics:

1. Rover orientation quaternion just after drilling but before unloading the stabilizers (transferring from RMECH to SITE frame): **bQII1** = (0.8161870000, -0.0570269000, 0.0016600700, 0.5749640000);
2. Coring Drill orientation quaternion just after drilling but before unloading the stabilizers (transferring from CORING DRILL to RMECH frame): **cdQb** = (0.6692760, 0.3774960, -0.5735080, 0.2839970);
3. Rover orientation quaternion at time of acquisition of WATSON image SIF\_0195\_0684255577\_390FDR\_N0070000SRLC00701\_0000LMJ01: (transferring from RMECH to SITE frame): **bQII2** = (0.816343, -0.0553775, -0.000576532, 0.574906);
4. WATSON orientation quaternion at time of acquisition of WATSON image SIF\_0195\_0684255577\_390FDR\_N0070000SRLC00701\_0000LMJ01: (transferring from WATSON to RMECH frame): **wQb** = (0.669666, 0.383208, -0.570312, 0.281855).

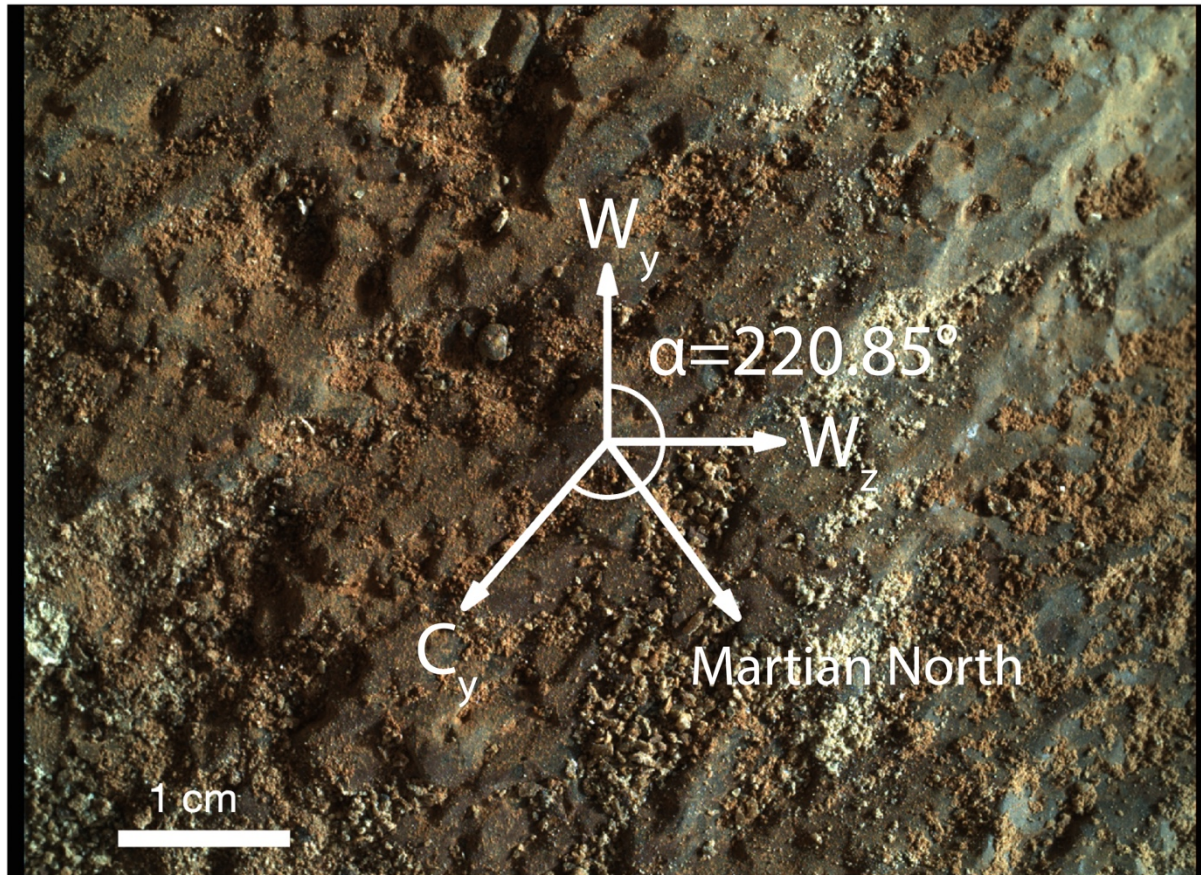
Items 1 and 2 give a coring drill pointing vector estimate of

**hade = 14.50°**  
**azimuth = 78.68°**

Items 3 and 4 give an estimate of the angle between the WATSON y-axis and the up-dip direction in SITE coordinates of (**Figure 1**):

**core roll,  $\alpha$  = 220.85°**

**Figure 1 | 6.6-cm standoff WATSON image of *Coulettes* core target on sol 271.** Image scale is  $30.7 \mu\text{m pixel}^{-1}$ . Orientation compass gives WATSON frame ( $w_x, w_y, w_z$ ). Core roll is clockwise angle of core y-axis,  $c_y$ , from  $w_y$ , given by  $\alpha = 220.85^\circ$ . Projection of Martian geographic north onto WATSON image plane is noted. WATSON image SIF\_0195\_0684255577\_390FDR\_N0070000SRLC00701\_0000LMJ01.



# INITIAL REPORT

## M2020-298-7 Robine

---

**Sample Designation:** M2020-298-7 Robine

**Date of Coring:** 18-December-2021

**Mars Time of Sample Core Sealing:** 17:22 LMST, Sol 298, Ls 143.4

**Latitude (N), Longitude (E), Elevation:** 18.43264°, 77.44133°, -2574.3 m

**Campaign:** Crater Floor

**Region of Interest:** *Séítah South*

**Lithology:** Medium- to coarse-grained poikilitic olivine cumulate rock. Primary minerals are olivine and pyroxene. Limited secondary aqueous alteration, including carbonate, hydrated sulfate, and other hydrated phases. Organic material is present, at least partially associated with sulfate phase(s).

**Estimated Volume Recovered:** 8.6 cm<sup>3</sup>

**Coring Bit Number:** 2

**Core Orientation:** hade = 5.36°; azimuth = 225.58°; core roll = 231.60°

**Sample Serial Numbers:** Tube SN206; Seal SN184; Ferrule SN064

**ACA Temperature at Time of Sealing:** 40°C

**Estimated Rover-Ambient Pressure and Temperature at Time of Sealing:** 608 Pa, 246 K

**Estimated Amount of Martian Atmosphere Headspace Gas:** 1.0 x10<sup>-6</sup> mol

**Anomalous Behavior:** Three sols between coring and sealing.

**Abrasion Patch Name and Depth:** *Quartier*, 8 mm

---

January 27, 2022

*K. Hickman-Lewis, K. A. Farley, J. I. Simon, J. R. Johnson, B. Horgan, M. Rice, J. Bell, J. Rice, T. Bosak, L. Mandon, A. Udry, S. VanBommel, McLennan, S.M., Y. Goreva, R. C. Moeller, V. Sun, K.P. Hand, E. L. Berger, F. Calef, A. D. Czaja, C. H. Lee, A.C. Fox E. L. Scheller, S. Sharma, S. Siljeström, H. E. F. Amundsen, L. W. Beegle, B. P. Weiss, D.L. Shuster, C.D.K. Herd, M. P. Zorzano, K. Benison, J.I. Núñez, R. C. Wiens, S. Le Mouélic, G. Caravaca, O. Gasnault, S. Maurice, A. Treiman, and the Mars 2020 Team.*

## Summary Description

*Robine* and *Malay*, the pair of rock cores representing the fourth sample target of the Mars 2020 *Perseverance* rover mission, were collected in the *South Séítah* region on sols 295–298 and 337, respectively (**Figures 1–2**). Both samples were acquired from an outcrop named *Issole*, a ~5-20 cm high NE–SW-trending ridge of layered bedrock within the *Séítah* formation that parallels the larger ~2 m high *Artuby* ridge of the *Máaz* formation. *Issole* was collected in part because it was the *Séítah* outcrop closest to the *Máaz* contact along the *South Séítah* traverse.

*Séítah* is mapped as part of the olivine-bearing Crater Floor Fractured 1 unit defined from orbital observations (Cf-f-1 of Stack et al., 2020). The *Séítah* formation includes the stratigraphically lowest rocks exposed on the floor of Jezero crater, including a distinct light-toned olivine-bearing unit. This unit has been correlated with a regional olivine-bearing unit exposed between Syrtis Major and Nili Fossae.

The natural surface of *Issole* features large olivine grains and chemically-distinct purple patches. The *Quartier* abrasion patch contains abundant 1-4 mm size olivine crystals surrounded by augite, as well as feldspars, magnetite, and Ca-phosphates. *Issole* is interpreted to be an olivine cumulate formed either in a thick lava flow or in a sill. It is thus unclear whether *Issole* represents an extrusive or intrusive igneous rock. *Issole* shows evidence of limited aqueous alteration in the form of sulfates, carbonates, and chlorides or perchlorates. Organic compounds are present, especially in association with sulfates, but in low abundance.

*Issole* is interpreted to be in-place. Rover observations have shown conclusively that the *Séítah* formation, and in particular the reflector that outcrops at *Issole*, dip below the *Máaz* formation along *Artuby* ridge. Despite this relationship, the relative ages of *Máaz* and *Séítah* depend on whether the olivine cumulate is an intrusive or extrusive lithology.

*Issole* is located about 120 meters SW of *Brac*, a geochemically and mineralogically similar *Séítah* outcrop that yielded the *Salette* and *Coulettes* cores. Although we interpret both sets of samples to derive from a single olivine cumulate body, compared to the *Brac* cores, *Robine* and *Malay* appear to be less mafic and to have experienced a greater degree of aqueous alteration.

Sample processing and sealing of *Robine* occurred 3 sols after coring. *Malay* was acquired in a single sol.

The returned sample science objectives of this core pair are similar to those of *Salette* and *Coulettes*, and include geochronology, paleomagnetism, igneous geochemistry, and the past history of water and water–rock interactions in Jezero crater. Together with cores of the *Máaz* formation (*Montdenier*, *Montagnac*, *Atsah*, *Hahonih*), the four *Séítah* cores constitute the entirely igneous Crater Floor Campaign sample suite.

**Figure 1 | Regional context of *Perseverance* rover operations during acquisition of *Robine* and *Malay*.** (a) geological map showing Jezero crater floor units. Light green shading indicates the location of the Jezero Crater Floor campaign. (b) Geological map showing the crater floor Cf-fr and Cf-f-1 units. Adapted from Stack et al. (2020).



**Figure 2 | Local context of *Perseverance* rover operations during sampling of *Robine* and *Malay*.** HIRISE map showing the locations of sample collection together with other notable outcrops observed or analyzed in the sols leading up to *Issole*. Rover position at *Issole* is highlighted by a blue circle. *Issole* is located along a ridge near the NW–SE-trending boundary with the *Máz* formation (Cf-fr in Stack et al., 2020) along the ridge labelled *Artuby West*.



## **Stratigraphic and Geologic Context**

The *Robine* core (and paired core *Malay*) were collected from the *Issole* outcrop, the second *Séítah* sampling locality. The *Issole* outcrop is located near the boundary between the *Séítah* (Cf-f-1) and *Máz* (Cf-fr) formations in the south *Séítah* region (**Figure 1**; Stack et al. 2020). The formation boundary is covered by regolith but its location is known to within a few meters from outcrop lithology.

Orbital mapping suggests that *Séítah* rocks are the stratigraphically lowest exposed rock unit on the crater floor and are overlain by both the *Máz* formation and the delta. Rover observations confirm that *Séítah* lies below *Máz*. When this sample pair was collected, *Perseverance* had not yet explored the relationship of the crater floor units to the delta. Consistent with its lower position in the stratigraphy, *Séítah* may be older than *Máz*. However, because *Séítah* could be intrusive, the inverse is also possible. For more details of *Séítah* context see Initial Report for M2020-262-5 *Salette*.

The *Robine* and *Malay* samples were cored from the *Issole* outcrop approximately 120 meters SW and about 5 meters lower than the *Séítah* formation cores *Salette* and *Coulettes* acquired from the *Brac*

outcrop. Based on the dip of what is likely igneous layering, *Issole* may be stratigraphically higher than *Brac* by a few meters. However this is less apparent in subsurface observations (see Subsurface Structure section). *Issole* is approximately 200 meters northwest of, and at the same elevation as, *Rochette*, from which the *Máz* formation cores *Montdenier* and *Montagnac* were acquired.

## **Operations**

**Figure 2** shows the local context of *Perseverance* rover operations leading up to the sampling of *Robine* and *Malay*. To reach *Issole* after sampling *Salette* and *Coulettes* at the locality labeled *Caille* in **Figure 2**, the rover retraced its route through a narrow traversable corridor of South *Séítah*, returning to an outcrop (*Issole*) that had previously been imaged and analyzed remotely on sol 202 during the drive to *Bastide* and *Brac*.

On Sol 286, *Perseverance* arrived at the *Issole* workspace and started the sampling sol path. On Sol 287 WATSON imaging of abrasion and sampling candidates was acquired on the *Quartier*, *Pauls*, *Robine*, and *Soberro* targets. The *Quartier* abrasion patch was made on Sol 292. On Sol 293 post-abrasion WATSON and SHERLOC/PIXL scans were acquired on the *Quartier* abrasion patch, as well as pre-coring WATSON images on *Robine* and *Pauls*, our two coring candidates. On Sol 294, we completed the post-abrasion proximity science and performed other remote sensing activities to satisfy the requirements of the STOP list. Around this time, we also decided to split the sampling sol (nominally 1 sol) into 2 sols (similar to *Montdenier*), based on concerns from outcrop images and the abrasion patch that the *Issole* rock might be susceptible to fragmentation/disaggregation. By including imaging and a ground-in-the-loop assessment, we were able to verify that core was acquired before proceeding to seal the sample tube. Also, as a precaution, on this sol we acquired WATSON images of the *Malay* target located on a more resistant part of the rock, with the intention that if the first sampling attempt on *Robine* was not successful, we would try again on a potentially more resistant part of the rock at *Malay*. Successful core acquisition of *Robine* occurred on Sol 295, and sample processing and sealing on Sol 298.

On Sol 306, we attempted sampling of *Pauls* in a single sol, since we now had confidence that we could acquire an intact sample at this location. Although we successfully acquired the *Pauls* core, a fragment of the core slipped out of the sample tube during docking with the bit carousel, and prevented mating of drill to bit carousel. On Sol 322, we dumped the *Pauls* sample on to the ground to aid in the fault recovery process. Recovery activities ensued until sol 332.

On Sol 337, we successfully sampled *Malay*, our second *Issole* core, using the same (now-empty) sample tube used for the *Pauls* sampling attempt.

On sol 340 we drove away from the *Issole* workspace.

## **Sample-Related Observations**

### ***Workspace Images***

**Figure 3a** shows a Mastcam-Z mosaic of the *Issole* outcrop in its local context and **Figure 3b** shows the Mastcam-Z image of the workspace in which the *Quartier* abrasion patch and the *Robine* and *Malay* cores were acquired. All abrasion and sampling was conducted on the same block and on the same surface (**Figure 4**). *Issole* features shallowly dipping layers, generally 1–5 cm, but up to several tens of centimeters, in thickness. These layers have a rough texture with sharp, angular edges, apparent recessive weathering beneath ledges, and surficial depressions. Although *Issole* appears layered at the outcrop scale, no layering was observed in the abrasion patch or borehole observations.

The continuity of the several tens of meters long ridge on which *Issole* is located and the similarity between the dip of *Issole* and that of nearby outcrops suggest that *Issole* is in-situ bedrock. WATSON images show that the natural surface of *Issole* is well-exposed, although dust and wind-blown sediment have accumulated in surficial depressions and beneath overhangs (**Figures 5–7**). Wind polishing and fluting are present on the higher relief parts of *Issole*, whereas the lower relief portions of the outcrop have an abundance of small pits partly filled with sand (**Figure 3b**). RMI images of *Issole* (**Figure 4**) show dark gray grains, mostly around 0.1–0.5 cm, and abundant smooth brown coatings. Where not dust covered, mineral faces are visible. The surface appearance of *Issole* is similar to that observed on *Bastide* and on *Brac*.

**Figure 3 | Local and outcrop images of *Issole*.** a) *Issole* locality; location of the sampled block within the outcrop is indicated. b) Post-abrasion and coring Mastcam-Z image of the *Issole* outcrop and workspace. The abrasion patch is 5 cm in diameter and the *Robine* borehole is 2.7 cm in diameter.

Sol 285 zcam08306 Z110 enhanced color  
zcam08306.0000a.lombards\_issle\_pdi\_P56\_L0R0\_Z110

This block where Quartier/Robine/Pauls  
occurs is ~70 cm across

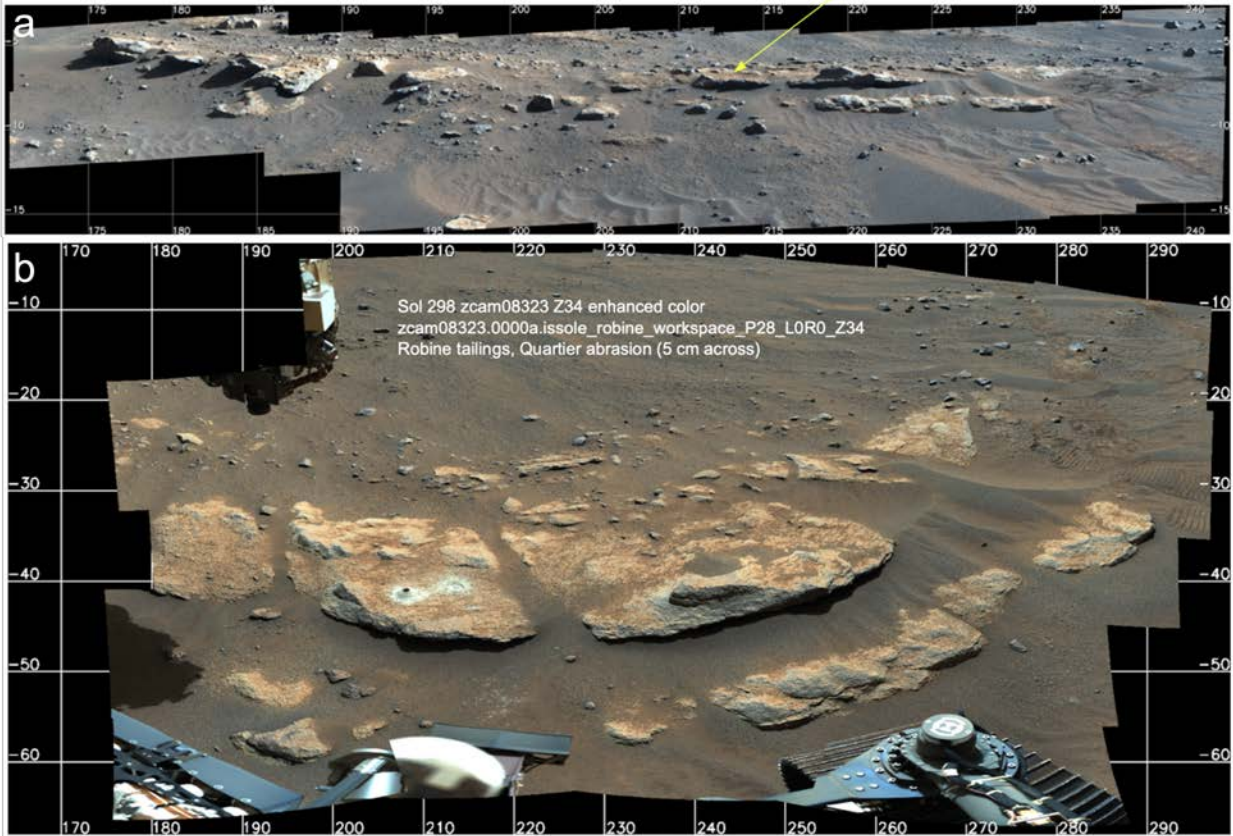


**Figure 4 | RMIs of the *Issole* outcrop.** Gaussian stretch RMIs of two different targets from *Issole* illustrate a) the presence of coarse-grained textures with a dusty surface (*Castiglione* target) and b) smooth brownish coatings (*Gacia* target).

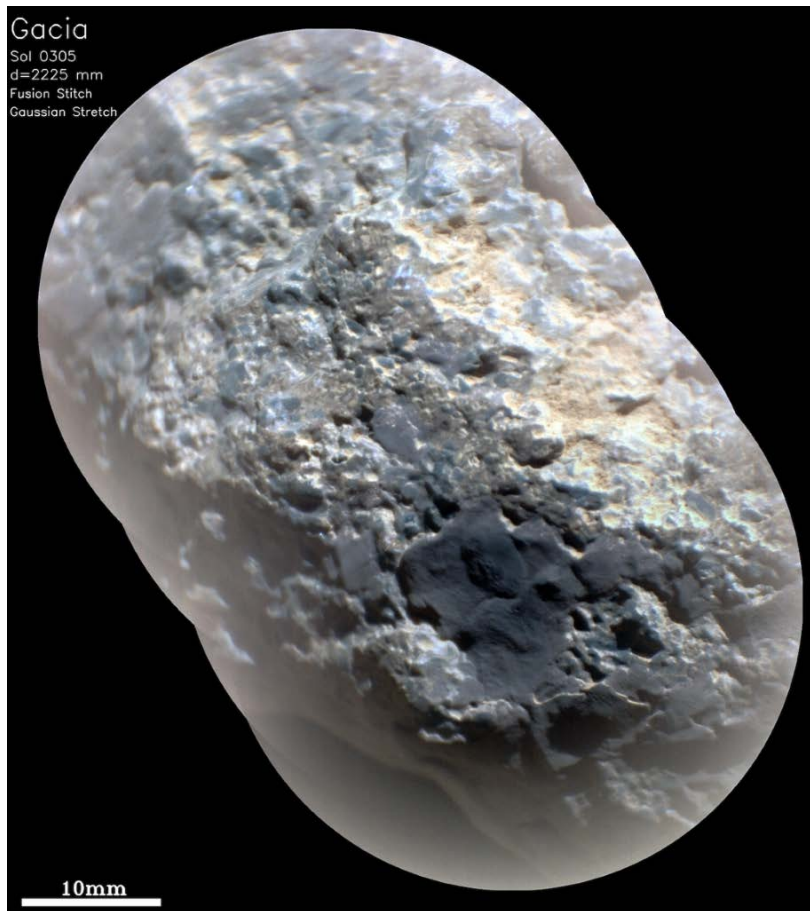
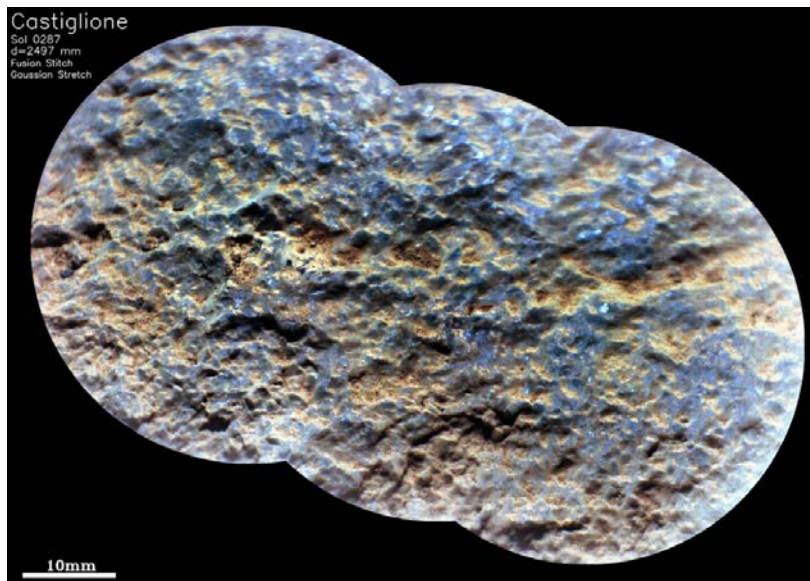


**Figure 5 | WATSON pre-coring images of the *Robine* target at ~7 and 35 cm standoff distances.**

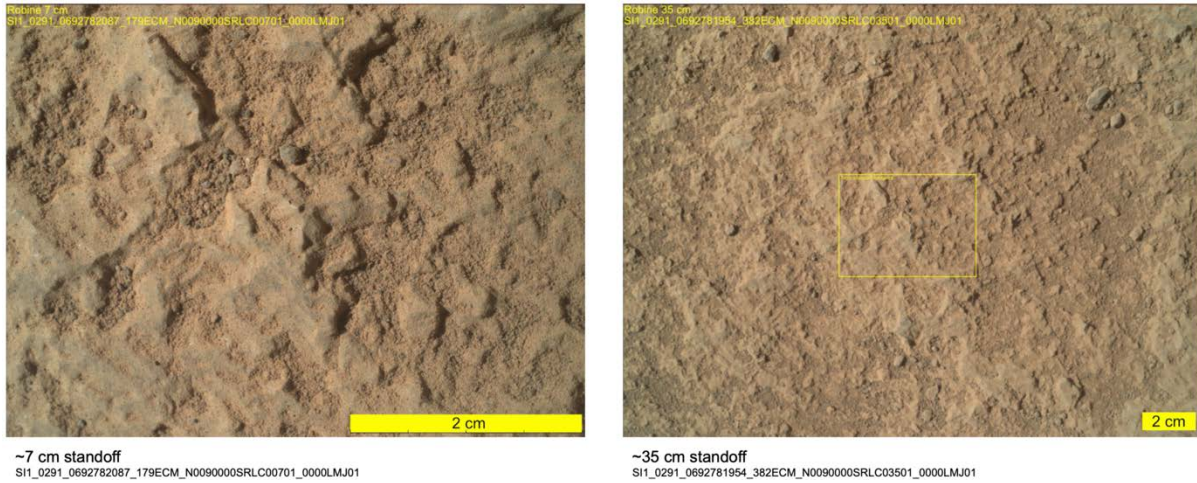
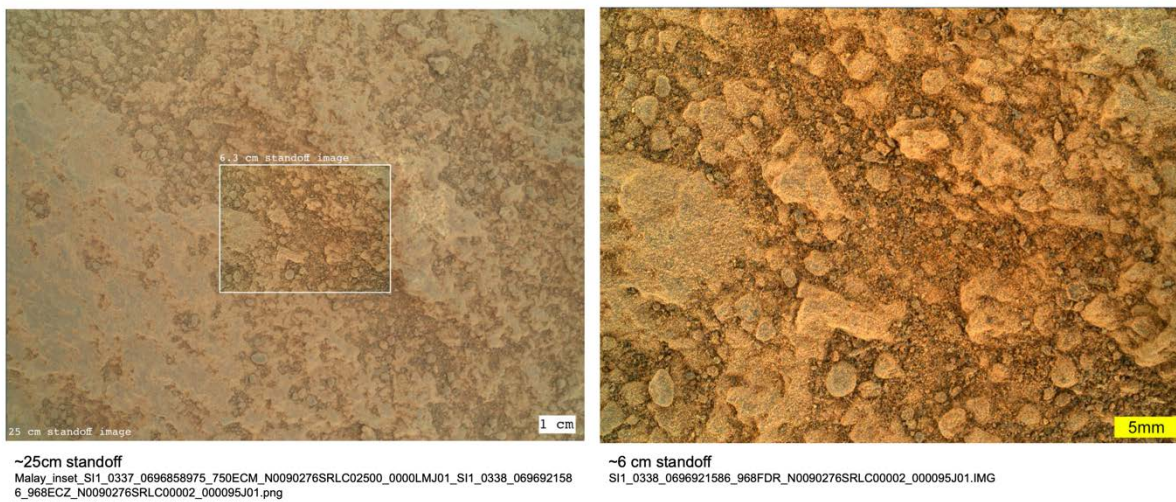


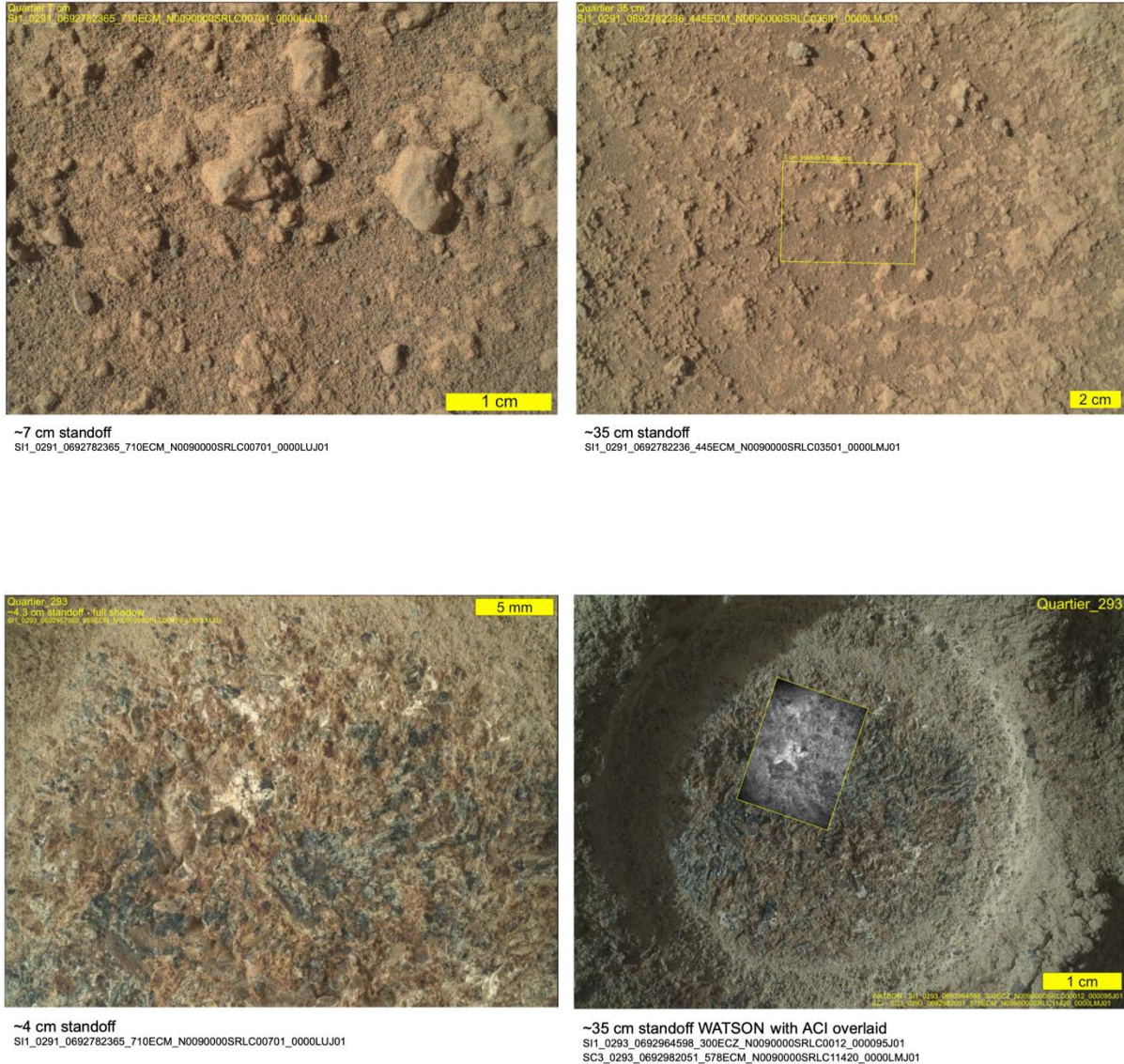
**Figure 6 | WATSON pre-coring images of the *Malay* target at ~6 and 25 cm standoff distances.**



***Pre- and Post-Coring/Abrasion Images***

Pre- and post-abrasion WATSON and ACI images of the *Quartier* abrasion patch are shown in **Figures 7**. **Figure 7A–B** shows WATSON pre-abrasion images of the natural surface of *Quartier*, **Figure 7C** shows a WATSON image of the gDRT-cleared abraded patch and **Figure 7D** shows a greyscale ACI image superimposed onto the abraded patch. The ACI image corresponds to the locations of SHERLOC scans shown in subsequent figures. Notable observations from RMI, WATSON and ACI images include:

**Figure 7 | WATSON images of the *Quartier* abrasion surface (sol 257).** (a-b) Pre-abrasion WATSON ~7 and 35 cm standoff images showing the natural surface of *Quartier*. (c) WATSON image of the entire abrasion target. (d) WATSON image of the abrasion patch overlain with greyscale ACI image. Note that the WATSON images are rotated with respect to the images obtained by the remote sensing mast.



a) The natural weathered surface has numerous large and small protuberances, grains and pebbles (between 0.1 and 1.5 cm), as well as small depressions that are filled with dust and other fine-grained, wind-blown materials. Few, if any, individual grains are visible in the WATSON pre-coring natural surface images, but note that abundant grains are visible in the RMIs of relatively dust-free surfaces.

b) 0.2–3 mm pale brown–white sub-angular phases comprise most of the abraded surface. Other major constituents are 0.2–0.8 mm mid-brown crystals with sub-angular to angular morphologies, 1–4 mm grey–

green crystals with angular and elongate, <0.1 mm white crystals. The pale brown–white, mid-brown, gray–green and white minerals are distributed irregularly throughout the abraded patch with no obvious spatial heterogeneity in their relative abundances.

c) Some minerals within the abraded surface are surrounded by mid-brown and grey inter-crystal boundaries, potentially suggesting Fe-rich alteration phenomena. Pale reddish rims also surround or are spatially associated with many grey–green crystals.

WATSON and Mastcam-Z post-coring images of the *Robine* and *Malay* sampling sites are shown in **Figures 8-9**. The location of the unsuccessful *Pauls* sampling attempt, and the dumped core fragments, are also visible in **Figure 9**. Mastcam-Z and CacheCam images of the samples within the coring bit and secured within their sample tubes are shown in **Figures 10-11**. The Mastcam-Z images of the three *Issole* cores (*Robine*, *Pauls* and *Malay*) show clear visual similarities, confirming that *Malay* was an appropriate substitute for the disaggregated *Pauls* core.

**Figure 8 | Post-coring WATSON image of the *Robine* borehole.**



~6 cm standoff

0303\_borehole\_psd\_merge\_SI3\_0303\_0693866609\_718ECM\_N0090000SRLC08025\_0000LMJ01\_SI3\_0303\_0693866372\_687ECM\_N0090000SRLC08025\_0000LMJ01.jpg

**Figure 9 | Mastcam-Z images showing the *Issole* outcrop before (left) and after (right) drilling of the *Malay* core;** images taken on Sol 335 and 337, respectively. Within the field of view, the *Quartier* abrasion patch (5 cm diameter) is visible in the lower middle of the image, the *Robine* borehole is to the right, the *Pauls* borehole is in the middle, and the *Malay* borehole is to the left in the right-hand image (boreholes = 2.7 cm diameter). In the lower right quadrant of the image, some fragments of the discarded *Pauls* core are visible between the abrasion patch and boreholes.



**Figure 10 | Mastcam-Z images of *Robine* (left), *Pauls* (middle), and *Malay* (right) cores inside the drill bit,** taken on Sols 295, 306 and 337, respectively.

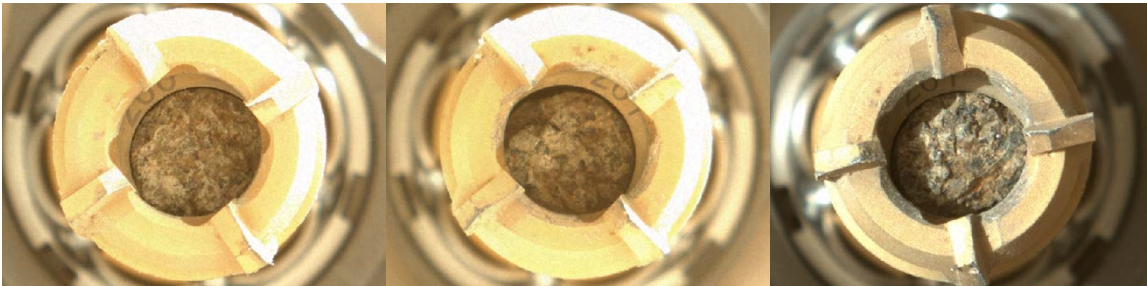
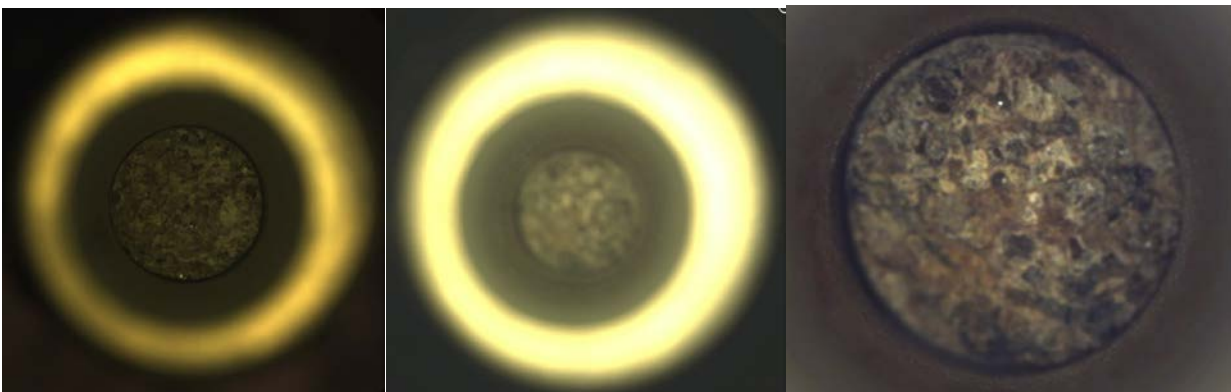


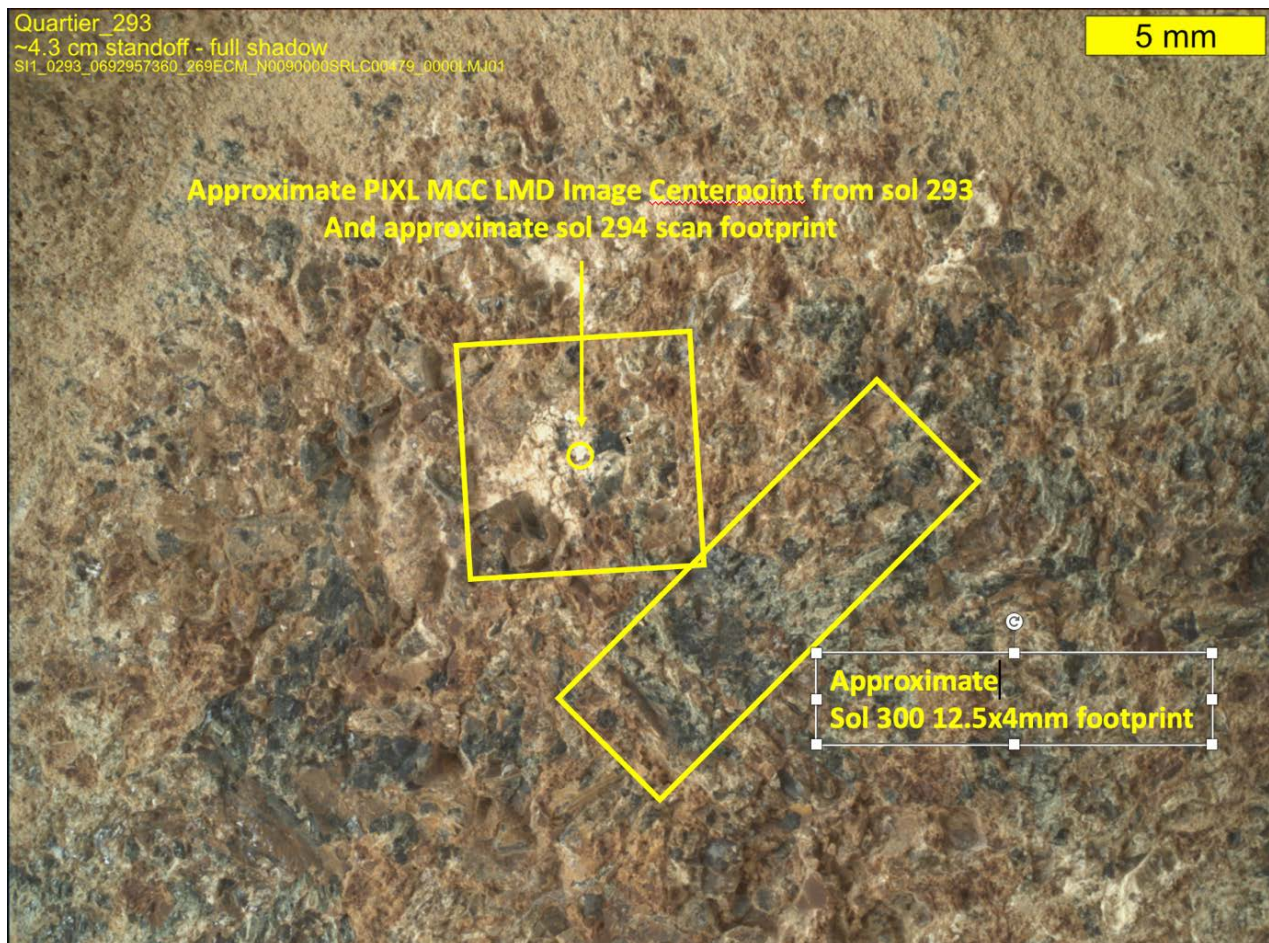
**Figure 11 | CacheCam images of the *Robine* and *Malay* cores.** Rightmost image shows a more in-focus image of *Malay*.



### Elemental Geochemistry - PIXL

Elemental geochemistry of the *Issole* rock was obtained by PIXL X-ray fluorescence (XRF) mapping on the *Quartier* abrasion patch. Two XRF rasters were acquired, on sols 292 and 300 (**Figure 12**). The sol 292 raster focused on a patch of white alteration material (informally called the ‘polar bear’), while the sol 300 raster emphasized silicate (igneous) mineralogy. *Issole* is inferred to be a cumulate igneous rock formed by accumulated olivine crystals with crystallized basaltic magma among the olivine grains; later alteration by one or more aqueous solutions deposited salt minerals and produced hydrous silicates and carbonates (see similar observations in the *Salette* and *Coulettes* Initial Reports).

**Figure 12 | PIXL raster scans on *Quartier*.** Approximate locations of PIXL XRF scans on the *Quartier* abrasion patch (~5 cm across), annotated as to scan sol. On this image, salt minerals are off-white, olivine grains are pale buff, augite is greenish-black, and poorly diffracting Fe-Mg-poor silicate material is brown. Locations overlain on WATSON image SIF\_0293\_0692957360\_269ECM\_N0090000SRLC00479\_0000LMJ01, rotated 90° clockwise from original orientation.



The average chemical composition for the sol 300 raster on *Quartier* is given in **Table 1**. *Quartier* has a silicate composition. Compared to a typical basalt (terrestrial or Martian), the *Quartier* sol 300 scan is low in SiO<sub>2</sub>, Al<sub>2</sub>O<sub>3</sub> and MgO, and rich in FeO and Na<sub>2</sub>O. Note that this bulk sum represents a mixture of igneous silicate minerals (olivine, pyroxene and plagioclase) and secondary salts, carbonates, and hydrous silicates. Besides the tabulated values, no minor or trace elements were detected.

**Table 1. Chemical compositions obtained using PIXL XRF.**

Wt %	Bulk Raster 0300		Olivine		Augite	
	N=3333	Err 1 $\sigma$	N=93	Err 1 $\sigma$	N=58	Err 1 $\sigma$
Na <sub>2</sub> O	1.87	0.50	0.53	0.53	0.8	0.8
MgO	12.8	0.6	17.86	0.79	12.6	0.7
Al <sub>2</sub> O <sub>3</sub>	2.36	0.55	0.92	0.17	1.2	0.4
SiO <sub>2</sub>	40.3	2.0	35.14	0.74	46.9	2.4
P <sub>2</sub> O <sub>5</sub>	0.28	0.23	0.08	0.07	0.1	0.1
SO <sub>3</sub>	1.66	0.47	0.68	0.02	1.1	0.3
Cl	0.94	0.3	0.38	0.00	0.4	0.2
K <sub>2</sub> O	0.20	0.19	0.01	0.00	0.0	0.0
CaO	2.94	0.56	0.61	0.05	17.1	1.57
TiO <sub>2</sub>	0.99	0.32	0.01	0.00	1.7	0.4
Cr <sub>2</sub> O <sub>3</sub>	0.29	0.23	0.00	0.00	0.2	0.2
MnO	0.58	0.21	0.62	0.02	0.3	0.2
FeO-T	25.7	1.3	41.20	0.42	14.8	0.7
Sum %	94.1		98.04		97.2	
Mg#	47		44		60	

N are number of analyses averaged. Err is uncertainty (1 $\sigma$ ) from calibration and counting statistics. Mg# is molar Mg/(Mg+Fe), in percent.

On total alkali *versus* silica (TAS) plots (**Figure 13**), the PIXL spot analyses for *Quartier* are distributed widely. For the sol 292 scan, which included abundant salt minerals, points spread toward the origin. These points represent mixtures of igneous silicates with non-silicate igneous minerals (Fe-Ti-Cr oxides, Ca-phosphates) and abundant salt minerals, including Fe-Mg-Ca carbonates, sulfates, and chlorides (or oxychlorine compounds). Points on that plot with low silica and moderate alkali contents likely represent alkali-bearing sulfates, chlorides, and/or oxychlorine compounds. A few spot analyses show high SiO<sub>2</sub> (>65%) and relatively low alkali content, suggesting that the alteration assemblage includes a silica-rich phase. Other points with SiO<sub>2</sub> > 40% likely represent diverse igneous phases (described below) and mixtures thereof. On the TAS diagram for the sol 300 raster the bulk composition lies within the olivine field, consistent with the interpretation of *Quartier* as an olivine cumulate igneous rock. Most analysis points are consistent with mixtures of olivine, augite pyroxene and alkali-rich feldspar. Several points

extend toward the origin and represent mixtures of olivine and other mafic minerals with non-silicate minerals (Fe-Ti-Cr oxides, Ca-phosphates) and/or salt minerals.

**Figure 13 | Total alkalis vs silica plots for the *Quartier* abrasion; data from PIXL.** Individual data points represent regions of the abraded surface (~125  $\mu\text{m}$ ) and most are mixtures of multiple minerals. Bulk sum compositions shown by blue circles. Reference end-member igneous mineral compositions are shown as diamonds and as lines for those with solid solution series. The underlying igneous classification scheme does not apply to the individual data points and simply provides a frame of reference for comparing samples. Upper panel) Scan of sol 292 (see also **Figures 15 and 17**), including the ‘polar bear.’ Points with  $>35\%$   $\text{SiO}_2$  likely represent anhydrous silicate minerals (olivine, augite, intermediate feldspar) or mixtures thereof, as well as hydrous silicate alteration materials. The points at  $\text{SiO}_2 < 35\%$  represent oxide and salt minerals, mostly sulfates and carbonates. Lower panel) Scan of sol 300 (see also **Figures 16 and 17**), focused on igneous silicate materials. Most individual points are consistent with olivine and/or augite compositions with some mixture of plagioclase and/or salts. Individual points at  $\text{SiO}_2 < 35\%$  represent oxide and salt minerals, mostly sulfates and carbonates.

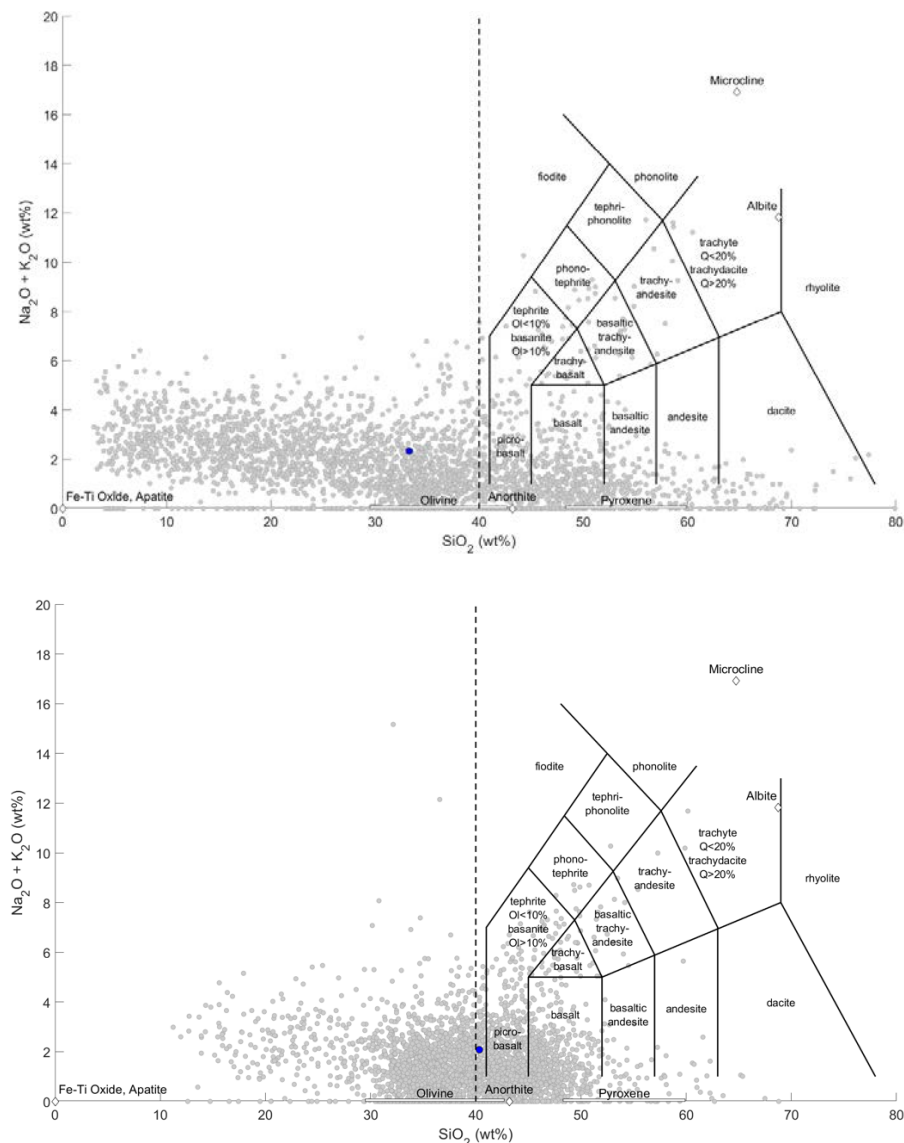


**Figure 14** shows ternary diagrams of molar compositions  $\text{Al}_2\text{O}_3 - (\text{CaO} + \text{Na}_2\text{O} + \text{K}_2\text{O}) - (\text{FeO}_T + \text{MgO})$  for PIXL spot analyses and scan averages. Idealized common mineral compositions are also plotted on the diagram. In this projection, the sol 292 (**Figure 14a**) and sol 300 (**Figure 14b**) plots appear very similar, with the vast majority of points near the (FeOT+MgO) apex. For the sol 292 scan, these points are rich in Fe-Mg bearing sulfates and carbonates. For the sol 300 scan, these points represent areas rich in olivine. Effectively all spot analyses for both scans fall in the triangle feldspar–augite–(FeOT+MgO), suggesting that *Issole/Quartier* experienced little loss of Ca+alkalis, i.e., no points are enriched in Al as would be expected through open-system weathering processes. Overall, this plot indicates that *Quartier* is neither heavily weathered nor altered, although it does contain a significant proportion of salt minerals and carbonate (**Figure 15**).

PIXL multi-elemental maps are shown in **Figures 15-16**. **Figure 15**, of the sol 292 raster, includes the sulfate-rich ‘polar bear’ area (see also **Figure 12**). The core of the ‘polar bear’ appears to be Na-bearing Mg-sulfate (orange in **Figure 15b**), it is surrounded by Mg-rich sulfate (**Figure 15a**). Fe-rich sulfate may be present, and Fe-Mg carbonate is inferred to be widespread outside the ‘polar bear’ because PIXL analytical totals are low. Chlorine is not commonly associated with Na, but rather with Mg (**Figure 15a–b**). Sodium is most commonly associated with Al in alkali feldspar (**Figure 15a–b**). Little Ca-bearing sulfate is apparent. These secondary materials, interpreted to be products of post-igneous aqueous alteration, occur in light-toned patches (primarily salt minerals) and in reddish brown patches (low Fe-Mg silicates) surrounding and invading anhydrous minerals, especially olivine.

**Figure 16** shows multi-element maps of the sol 300 PIXL scan, which targeted an area with a small amount of salt minerals. Olivine of intermediate Fe/Mg ratio (~Fo44) is the most abundant mineral, and occurs in euhedral to elongate subhedral to euhedral shapes (to ~5x2 mm). The olivines contain multi-mineral inclusions, possibly crystallized melt inclusions, along their midlines and elsewhere. Olivine grains are partially enclosed by anhedral augite grains in a poikilitic texture similar to that observed in the *Brac* rock, and as seen in some igneous rocks on Earth and the chassignite Martian meteorites. Augite grains are up to ~10 mm in size. Back-reflection diffracted X-rays from augite regions indicate that they are monocrystalline and crystallographically oriented across non-contiguous areas separated by olivine in the abrasion patch. Average chemical compositions of olivine and augite are given in **Table 1**. Other components identified in the sol 300 raster include mesostasis material among the olivine and augite and secondary phases. The mesostasis consists of alkali feldspar (rich in Na and K, <1 mm), Cr-rich and Ti-rich Fe oxides (≤0.25 mm), and Ca-phosphates (<0.125 mm). Secondary phases include poorly diffracting (or very fine grained) silicate(s) with low Fe and Mg, and salt minerals as described above.

**Figure 14 | Mineralogical interpretation for the *Quartier* abrasion; data from PIXL.** Data plotted by point and as bulk sum composition (blue circle, **Table 2**) on ternary diagrams of molar abundances of  $Al_2O_3$ – $(CaO+Na_2O+K_2O)$ – $(FeO_T+MgO)$ . Common pure mineral compositions are shown (opx = Ca-poor pyroxene, i.e. orthopyroxene; cpx = calcic pyroxene, i.e. augite). Most PIXL analysis points are consistent with pure minerals (olivine, cpx) or binary mixtures of olivine–cpx or olivine–feldspar, or ternary mixtures of olivine–cpx–feldspar. Aluminous alteration minerals, including common clay minerals, fall above the upper red dashed line. Several salt minerals (e.g., Fe-Mg-Ca-sulfates/carbonates, halite) are also plotted. a) Sol 292. In this projection, the Mg-bearing sulfate minerals of the ‘polar bear’ plot near the ‘FeOT+MgO’ corner of the triangle b) Sol 300. Most of the points are consistent (in this projection) with mixtures of olivine and cpx.

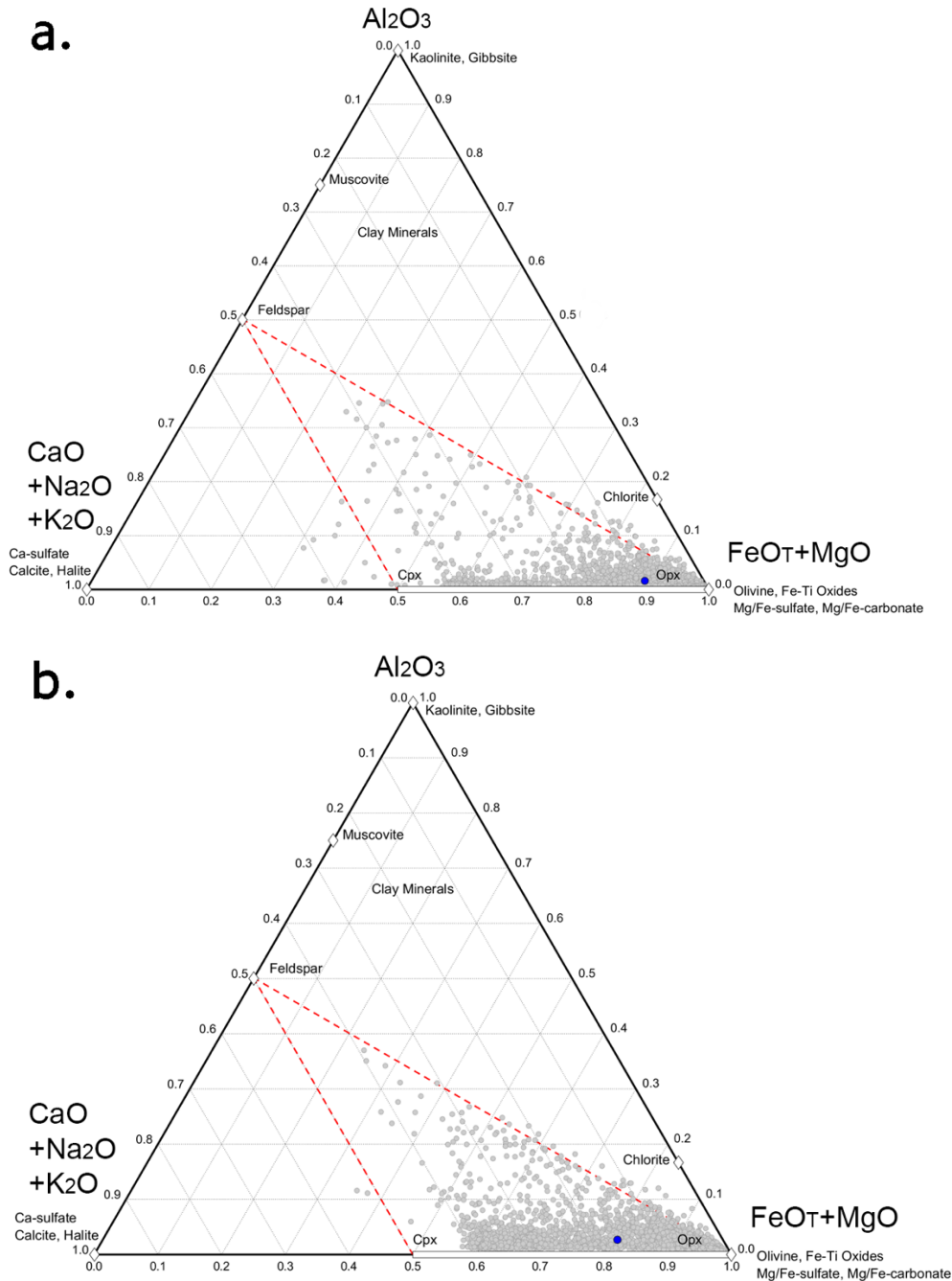


**Figure 15 | PIXL X-ray multi-element maps for the *Quartier* abrasion patch, sol 292.** Raster area is 7x5 mm. a) Red=MgO, Green=SO<sub>3</sub>, Blue=Cl. b) Red= SO<sub>3</sub>, Green=Na<sub>2</sub>O, Blue=Cl. c) Red=MgO, Green=Al<sub>2</sub>O<sub>3</sub>, Blue=CaO. d) Red=FeO<sub>T</sub>, Green=TiO<sub>2</sub>, Blue=Cr<sub>2</sub>O<sub>3</sub>. The ‘polar bear’ comprises mostly sulfate minerals (panels a, b) with little Ca (panel c); its rind is rich in Mg (orange in panel a), and its core contains Mg (panel c) and Na (orange, panel b), but little Ca (panel c). Chlorine-rich spots are scattered (panels a, b); most are not associated with Na (panel b). Most of the rock outside the ‘polar bear’ is olivine (red, panel c) with interstitial augite (purple, panel c) and feldspar (green, panel c). This area contains few oxide minerals: a grain of Fe-Ti-Cr oxide to the upper left, and a Cr-rich grain to the lower right.

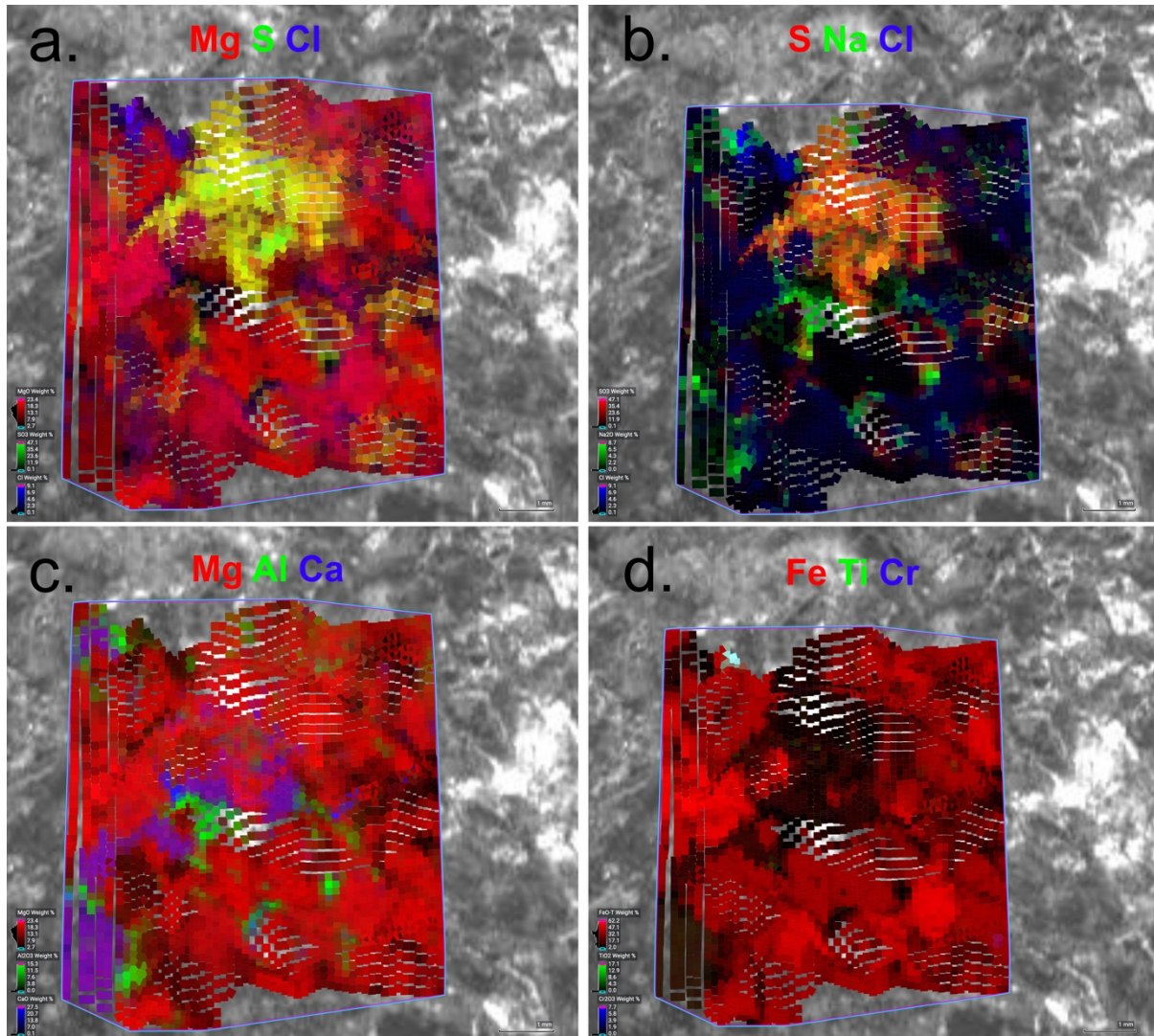
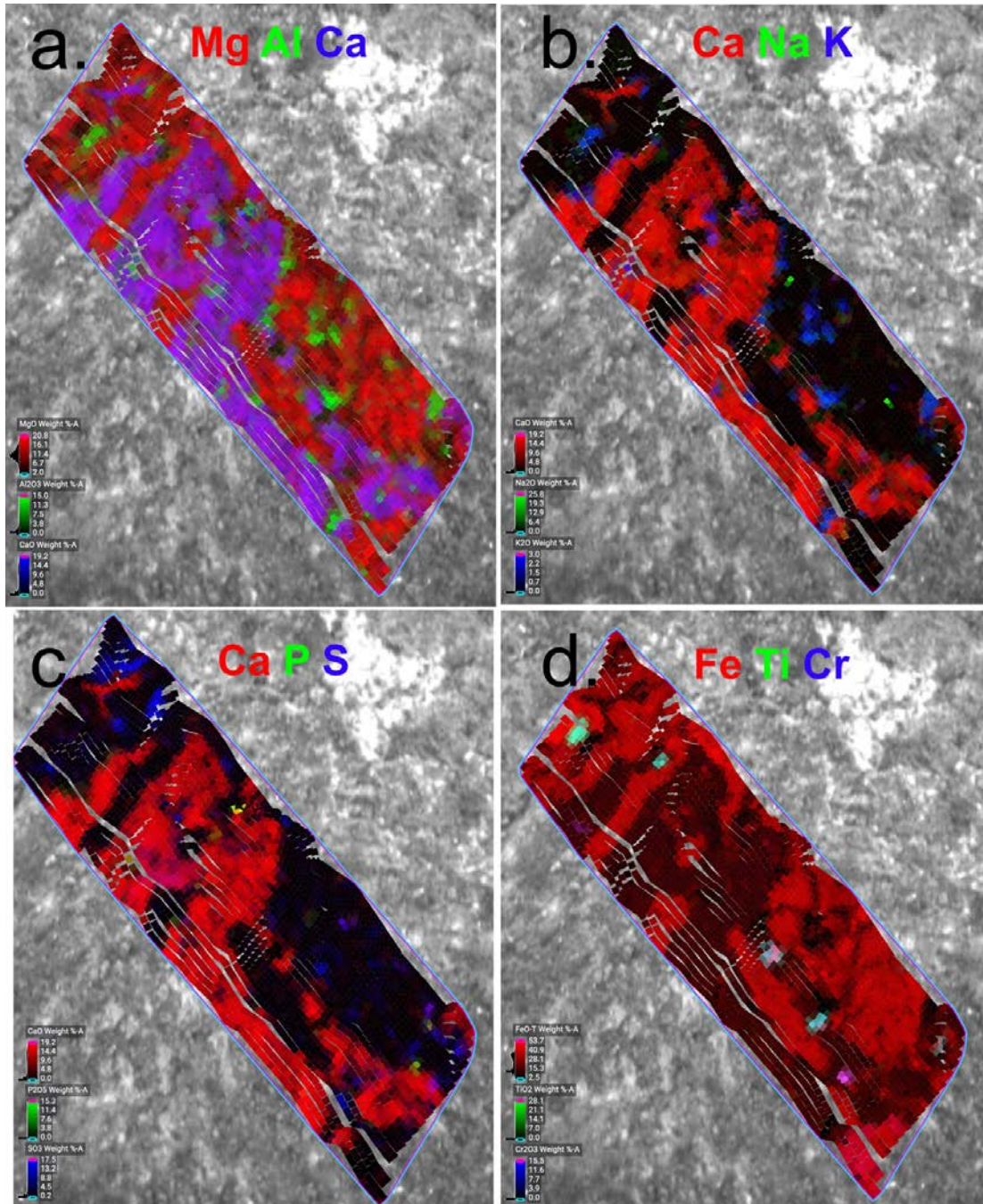
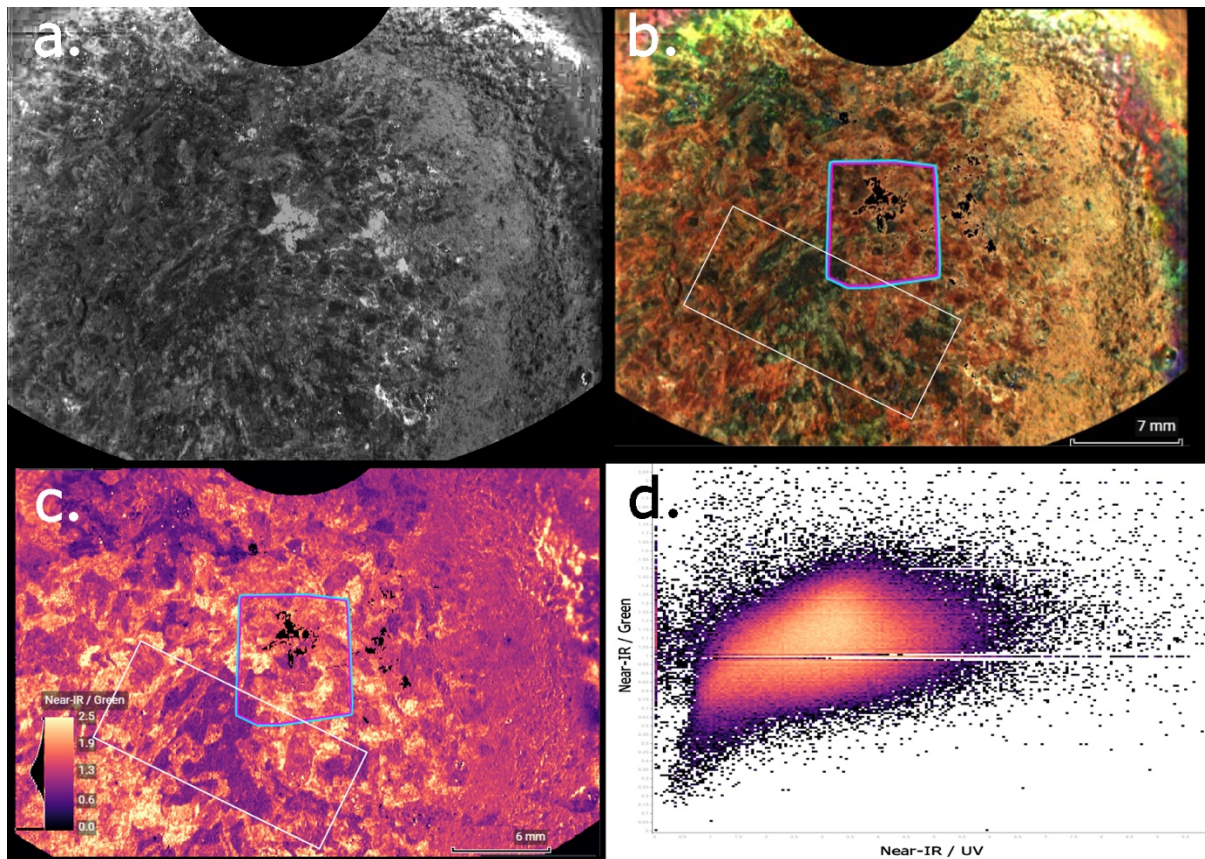


**Figure 16 | PIXL X-ray multi-element maps for the *Quartier* abrasion patch, sol 300.** Raster area is 12.5x4 mm. a) Red=MgO, Green=Al<sub>2</sub>O<sub>3</sub>, Blue=CaO. b) Red=CaO, Green=Na<sub>2</sub>O, Blue=K<sub>2</sub>O. c) Red=CaO, Green= P<sub>2</sub>O<sub>5</sub>, Blue=Cl. d) Red=FeO<sub>T</sub>, Green=TiO<sub>2</sub>, Blue=Cr<sub>2</sub>O<sub>3</sub>. Olivine is the most abundant material (red in panel a), with interstitial augite (purple in panel a) and plagioclase (green in panel a). Only one feldspar is present; panel b shows only one blue-green color correlated with the Al in panel a. A few salt grains (green in panel b) are present, as is a little Mg-Fe sulfate (blue in panel c), and a grain of phosphate (yellow in panel c). Panel d shows Fe oxide minerals: Ti-rich oxides are teal-green, and Cr-rich oxides are purple.



PIXL Micro-Context Camera (MMC) images of the *Quartier* abrasion patch (**Figure 17**) show more of the abrasion area than the XRF scans and may be used to extrapolate phase proportions from those of the XRF scan areas to nearly the whole abrasion patch. The MMC image of NIR-G-B (**Figure 17b**) is analogous to WATSON visible images, and the G/NIR ratio image shows a clear distinction among the olivine, augite, and mesostasis phases (**Figure 17c**). These visible and qualitative relationships are quantified in a graph of G versus NIR reflectance (**Figure 17d**), which allows extraction of the proportions of these phases over the whole MMC image area.

**Figure 17 | PIXL MCC (Micro-context camera) data for the Quartiers abrasion.** a) MMC grayscale image, a portion of the Quartiers abrasion. b) MMC false colour of a abrasion area; Red = MMC Near-IR; Green = MMC Green; Blue = MMC Blue. Location of PIXL XRF scans shown. c) MMC ratio image Near-IR/Green reflectances. Augite is darkest; olivine is next, and mesostasis and alteration materials are lightest tone. Location of PIXL XRF scan is shown. d) MMC reflectance ratios.



### Mineralogy and Organics-SHERLOC

SHERLOC Raman and fluorescence scans were obtained on sols 293 (survey and HDR scans; **Figure 18**) and 304 (detail scan; **Figure 19**). In the sol 293 and 304 scans, several mineral identifications were made (**Table 2**). Spectral features were assigned to carbonate ( $\sim 1090\text{ cm}^{-1}$ ), olivine ( $\sim 840\text{ cm}^{-1}$ ) and Mg/Ca/Fe-sulfate ( $\sim 1050\text{ cm}^{-1}$ ), the latter corresponding to the white material observed in the ACI image (**Figure 18A**). Possible hydration peaks between  $3100$  and  $3600\text{ cm}^{-1}$  were also observed in some spectra. Fluorescence features at  $303\text{ nm}$ ,  $325\text{ nm}$ , and  $330\text{--}340\text{ nm}$  are consistent with single- and double-ring aromatic organic molecules. The Raman peak at  $\sim 1664\text{ cm}^{-1}$  is consistent with the presence of aromatic organic carbon and is exclusively found in association with fluorescence features at  $303$  and  $330\text{ nm}$ . This signal is present in several spots associated with hydrated sulfate, but is not uniformly found throughout the sulfate detected in the scan regions. The only significant difference between the spectra obtained on sol 293 and 304 is in the hydration region between  $3100$  and  $3600\text{ cm}^{-1}$ . Differences in spectral structure might be caused by a change in hydration state during the eleven sols between analyses, during which the abrasion patch was exposed to the martian atmosphere potentially causing mineral dehydration.

**Table 2. SHERLOC mineral identifications in Quartier.**

Sample	Certain	Possible (not confirmed)	We looked for these, but cannot find them
Quartier	Sulfate (most likely Mg, Ca and/or Fe), virtually always hydrated <i>(occurs in white void fills or crystals, secondary to primary lithology)</i>	Olivine (low Fo#) occurs associated with one darker grain.  Carbonate (major phase, could be Mg/Ca/Fe)  Amorphous/microcrystalline silicate	Pyroxene

**Figure 17 | SHERLOC fluorescence and Raman spectral results for the *Quartier* abrasion surface.** Spectra were collected with a survey scan (5x5 mm, 1296 points, 144  $\mu\text{m}$  spacing, 15 pulses per point, not shown) and a HDR scan (7x7 mm, 100 points, 780  $\mu\text{m}$  spacing, 500 pulses per point) on sol 293. A) Colorized ACI image of the abraded patch in which the blue rectangle indicates the HDR scan area from sol 293, and the white circles indicate regions of interest (ROIs) that correlate with fluorescence data shown in B and C. B) HDR scan maps show the possible presence of organics. Upper panel is an RGB maps showing the main regions of organic fluorescence (303 and 330–340 nm). Both doublet peaks at 303 and 325 nm (ROI1) and the 330–340 nm peak (ROI 2) are localized to the ROIs in panel A. Lower panel shows Raman features at 1664  $\text{cm}^{-1}$  that indicate the presence of organic materials (see Raman data in D). C) Fluorescence spectra. Upper panel shows the average fluorescence spectrum for the whole analysis area; lower panel shows spectra from selected fluorescence ROIs (see panel A). D) Map showing the results of the Raman HDR scan. The colored circles correspond to mineral and organic detections. The right panel includes selected Raman spectra from the HDR scan, offset on the y-axis for clarity. The uppermost spectrum corresponds to Pt. 34 in the Raman map and is representative of spectra assigned to Mg/Ca/Fe-sulfate ( $\sim 1050 \text{ cm}^{-1}$ ), which corresponds to the white material in the ACI image. The second spectrum is also from Pt. 34, but the vertical scale has been exaggerated by 2000x to show the presence of peaks at 1664 and  $\sim 1400 \text{ cm}^{-1}$  that are assigned to organic carbon. These peaks were also observed in several points in the sol 304 SHERLOC map (see **Figure 18**). The third spectrum is an average of all spectra marked with light blue circles on the map in D and is assigned to carbonate ( $\sim 1090 \text{ cm}^{-1}$ ). The bottom spectrum is an average of those from Pts. 65 and 66 and is assigned to olivine ( $\sim 840 \text{ cm}^{-1}$ ). The spectrum from Pt. 34 (and all spectra marked with purple dots on the map) also contains possible hydration peaks between 3100 and 3600  $\text{cm}^{-1}$ . The scale in panel A also applies to D.

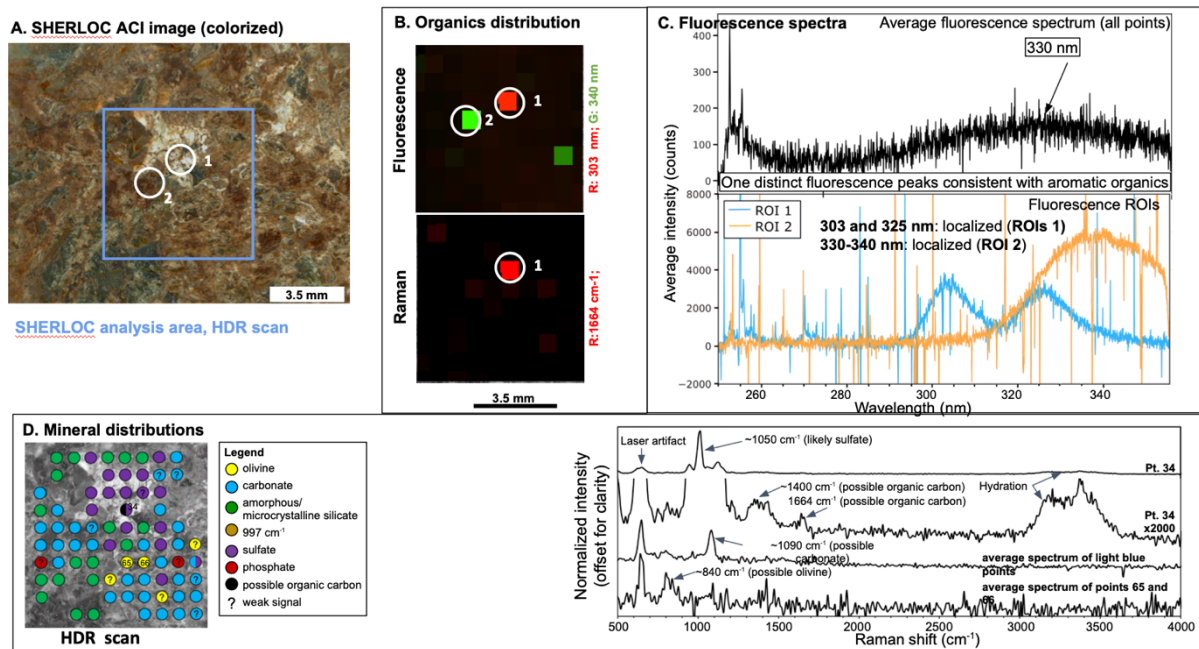
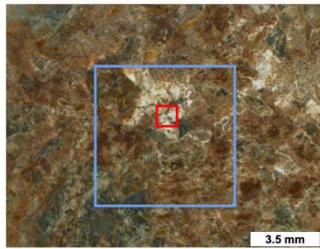


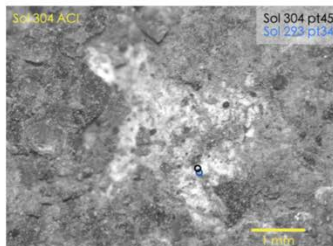
**Figure 18 | SHERLOC Raman spectral results for *Quartier* abrasion surface.** Spectra shown were collected with the HDR scan described in **Figure 17** (7x7 mm, 100 points, 780  $\mu\text{m}$  spacing, 500 pulses per point) on sol 293, and a detail scan (1x1 mm, 100 points, 144  $\mu\text{m}$  spacing, 500 pulses per point) on sol 304. A) Colored ACI image of the abraded patch where the blue box indicates the HDR scan area from sol 293 and the red box indicates the detail scan from sol 304. B) Sol 304 ACI image of the scanned region indicating the locations of point 34 from the 293 detail scan (blue circle) and point 45 from the sol 304 detail scan #1 (black circle). Note the overlap of analysis spots. C) Raman spectra from point 34 (sol 293 HDR scan; blue) and point 45 (sol 304 detail scan #1; black). Note the high degree of similarity between these two spectra, including the peaks at 1664 and  $\sim 1400\text{ cm}^{-1}$ , confirming the identification of organic carbon. The only significant difference between the two spectra is in the hydration region between 3100 and 3600  $\text{cm}^{-1}$ . This difference might be caused by a change in hydration state during the eleven sols between analyses.

A. SHERLOC ACI image (colorized)

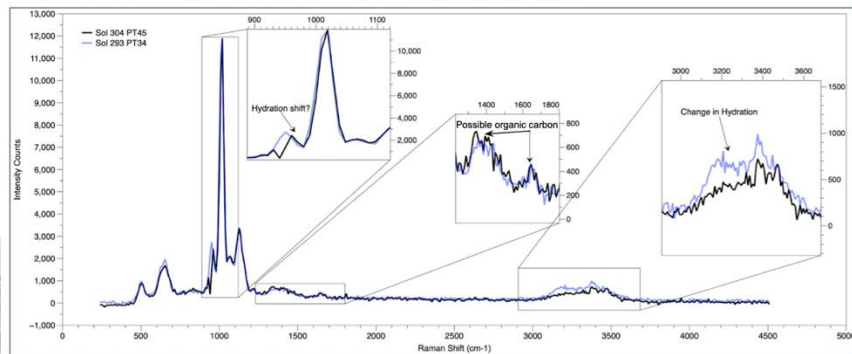


Analysis area, sol 293 HDR scan  
Analysis area, sol 304 Detail scan

B. Sol 304 ACI image with overlapping analysis points



C. Spectra from overlapping points from sols 293 and 304 SHERLOC analyses

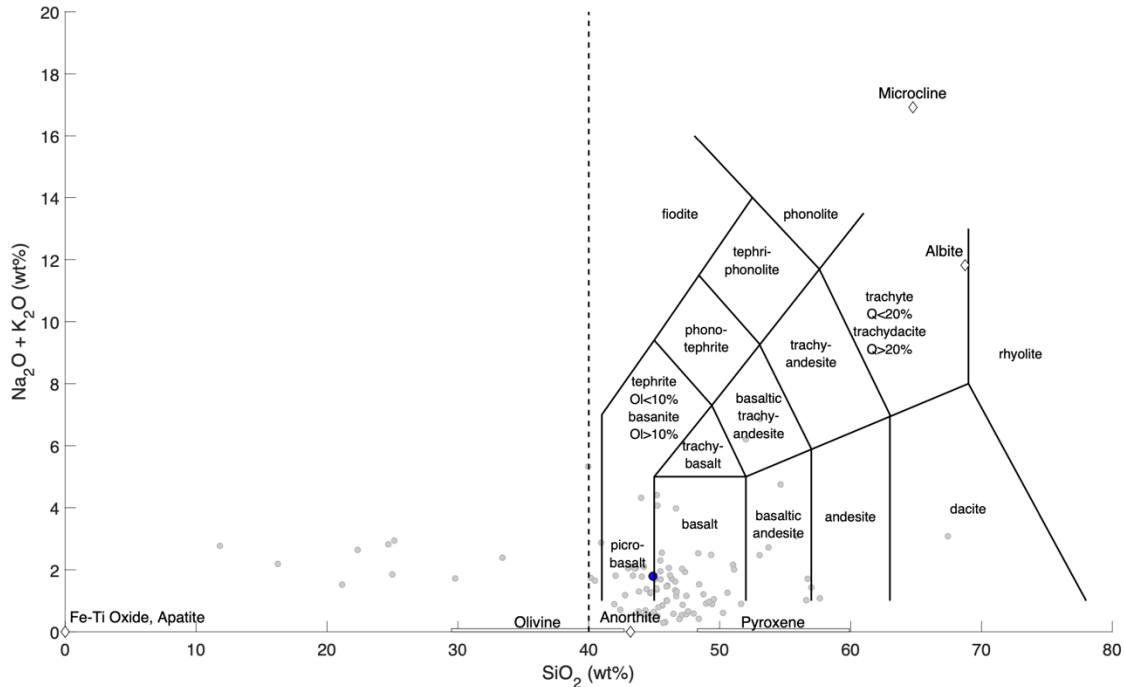


### Elemental Geochemistry and Mineralogy - SuperCam

SCAM LIBS data are shown plotted on a total alkalis vs silica diagram in **Figure 19**. Points are scattered within the microbasalt and basalt fields, and to a lesser extent within the olivine and basaltic andesite fields. The SCAM LIBS analyses targeted primarily natural surfaces in *Séítah*, with only a small subset targeting the abraded patch. Olivine is the dominant detection and bulk sum average in the PIXL data obtained on the abraded patch. SCAM LIBS data differ but are consistent with PIXL data in that both contain few points with  $\text{SiO}_2 > 50\text{ wt}\%$ .

Harker oxide diagrams of SCAM measurements of *Issole* are plotted against a background of all *Séítah* points in **Figure 20**. These diagrams show that *Issole* is generally representative of the wider *Séítah* region with potentially lower contents of CaO and MgO. Additionally, relatively few points in the borehole and abrasion tailings have  $\text{SiO}_2$  values below 40 wt%.

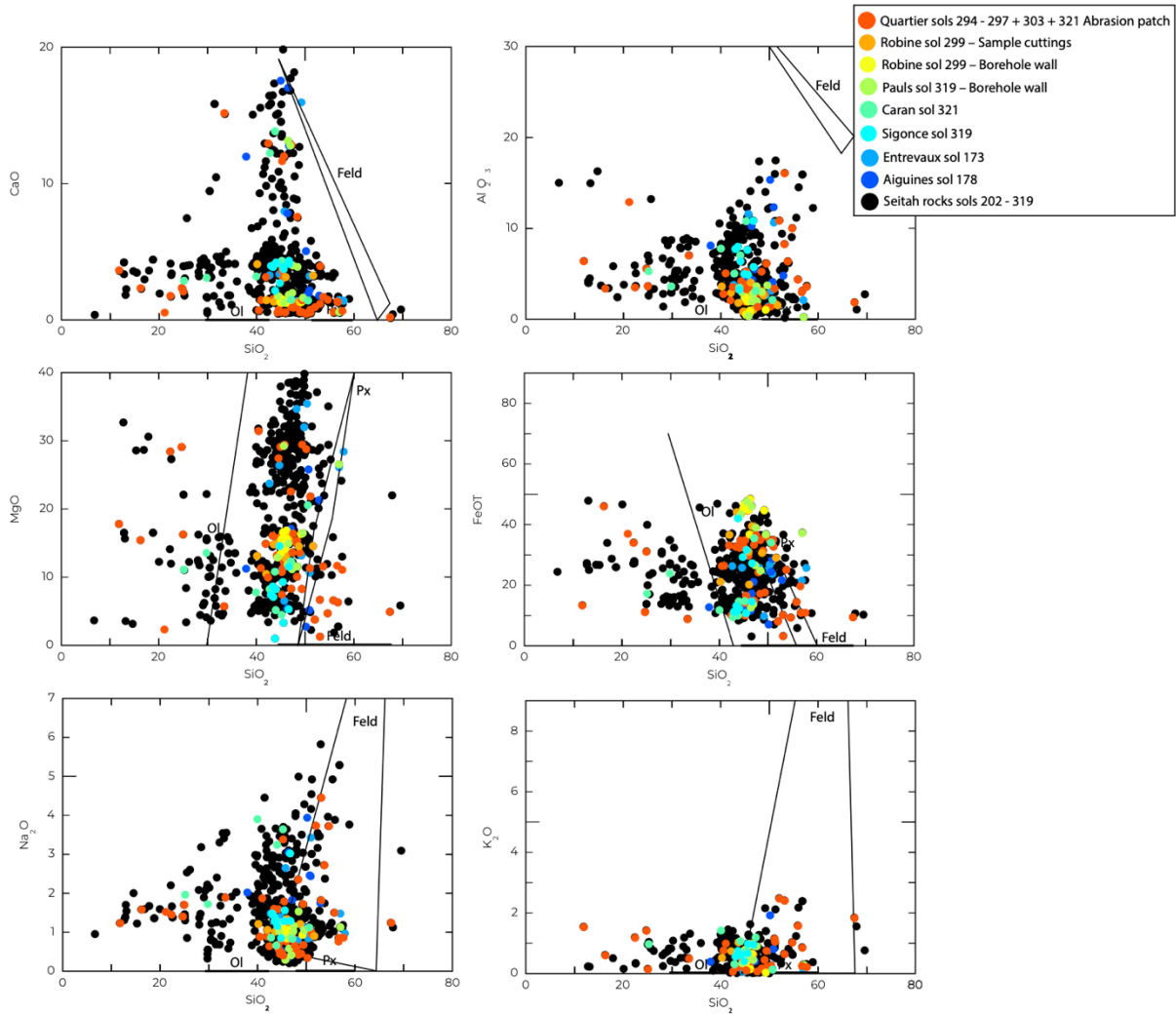
**Figure 19 | TAS plot of SCAM LIBS data on *Séítah* rocks.** Average value of all analyses is shown as a blue circle. Individual *Séítah* analyses, i.e., including those not from the *Issole* outcrop, are plotted as grey points. The LIBS-derived composition of the natural surfaces indicates the presence of grains on a pyroxene to olivine gradient, hydration and distinct coatings enriched in  $\text{Al}_2\text{O}_3$ ,  $\text{TiO}_2$  and  $\text{Na}_2\text{O}+\text{K}_2\text{O}$  compared to the surrounding rock.



Note that the  $\sim 250 \mu\text{m}$  SCAM LIBS spots most commonly interrogate more than one specific mineral. Given that the typical *Quartier* grain size is larger than this size, as described above, many of the trends observed in the diagrams shown in **Figures 19 and 20** can be reasonably attributed to mixing among several mafic minerals, e.g. olivine and pyroxene.

**Figure 21** shows the mean VISIR spectrum of the natural surface of *Issole*, the *Quartier* abrasion patch, and the tailings of the *Quartier* abrasion and *Robine* tailings acquired between sols 294 and 303. The broad slope between  $2.2$  and  $2.5 \mu\text{m}$  in all VISIR data is consistent with the presence of hydrated minerals. The broad absorption between  $0.8$  and  $1.8 \mu\text{m}$  indicates olivine, consistent with PIXL and SHERLOC data on the abraded surface described above. The olivine signal is stronger in the abraded surface than on the natural surface. The absorption near  $2.3 \mu\text{m}$  is consistent with carbonates and/or Fe/Mg-phyllsilicates. The broader single absorption (as in *Quartier* sol 297) is more consistent with carbonate, whereas the narrower  $2.28\text{--}2.29$  and  $2.32 \mu\text{m}$  absorptions (as in *Quartier* sol 303) are more consistent with Fe-phyllsilicate and Mg-phyllsilicates, respectively.

**Figure 20 | Harker oxide diagrams of SCAM data from *Séitah*.** Data relating to the *Issole* outcrop are shown in color. All *Séitah* points, i.e., including those not from the *Issole* outcrop, are shown in black.





depositional origin for *Issole* (e.g., water-lain sediment, pyroclastics, or impactoclastics), compelling observations elsewhere in this document indicate *Seitah* has a cumulate igneous origin.

Further east toward the *Brac* outcrop (*Salette* and *Coulettes* sampling site) the reflectors become less apparent. One possible interpretation of the radargram with the *Bastide Mb* (*Brac* outcrop) capping the *Issole Mb* above an unconformity is shown in the middle and lower panels. In contrast to this interpretation, projection of dip angles from both outcrop and the radargram near *Issole* would indicate that *Issole* lies a few meters above the *Bastide Mb*. If our currently preferred explanation that *Brac* and *Issole* are layers of a single layered igneous body is correct, this distinction is not of great significance.

**Figure 22 | Geological context and RIMFAX-derived subsurface stratigraphy from *Issole* to *Brac*.** a) Location of *Issole* and *Brac* together with selected RIMFAX traverses used. b) Radargram for sols 201 to 202 (yellow traverse in panel a) showing dipping high-amplitude reflectors. The black box denotes the subsurface extension of *Issole* shown in detail in **Figure 23**. c) Radargram along sol 285 and onwards traversing the *Issole* outcrop (blue traverse in panel a) showing the boundary between the *Bastide* and *Issole* members. d) Radargram along sols 280 and 281 (green traverse in panel a) showing the *Brac* outcrop and a possible erosional unconformity at the top of the *Issole* member and base of the *Bastide* member extending SE into the regions shown in panel c.

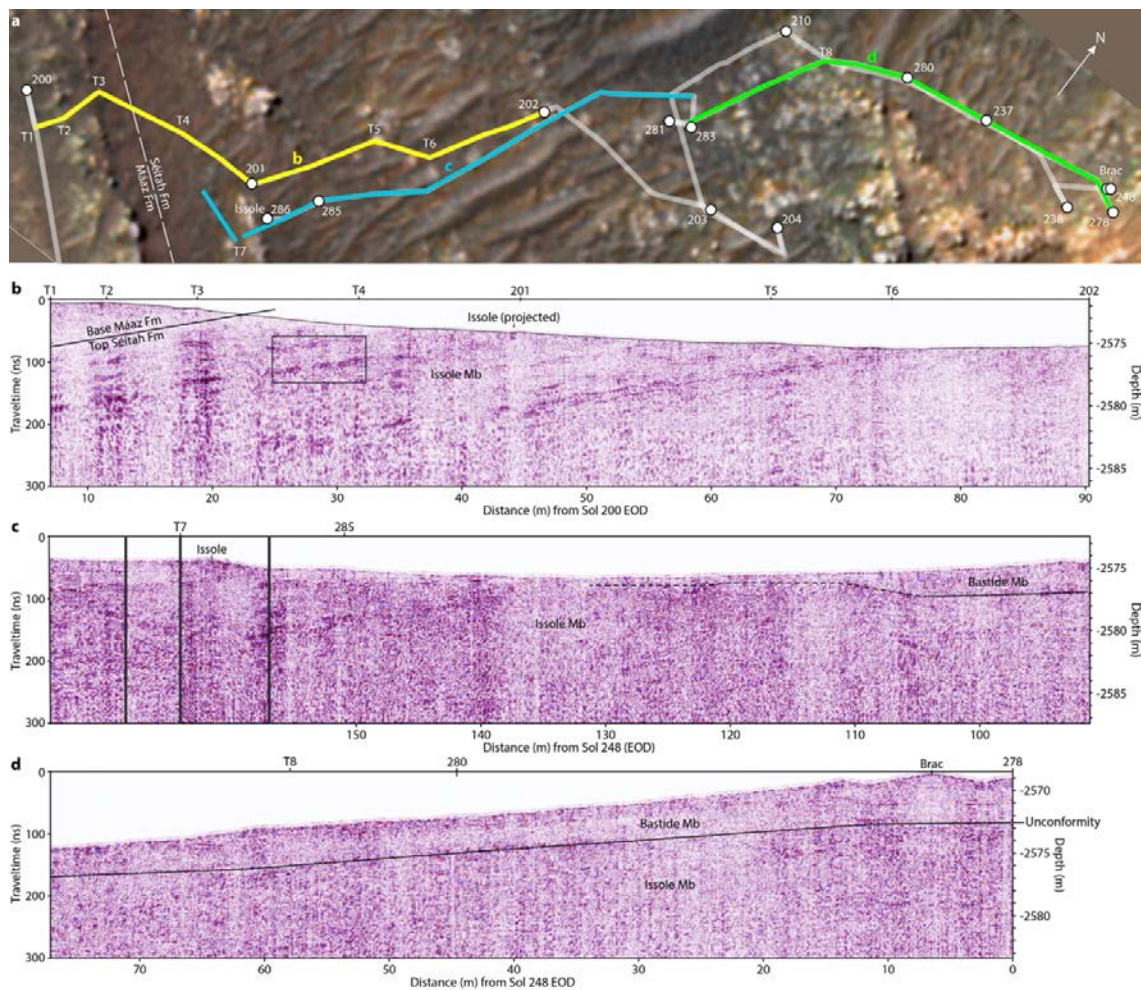
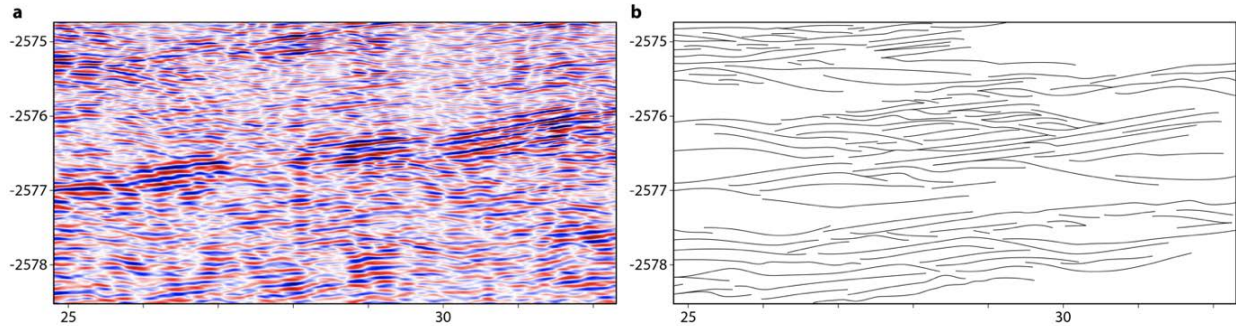


**Figure 23 | Subsurface extension of *Issole* enlarged.** a) Subsurface extension of *Issole* outcrop in sol 201 radargram (location given in **Figure 22**). b) Line tracing of reflector geometries in panel a showing intimate relationship between SW-dipping and antithetic NE-dipping reflectors, as well as crosscutting horizontal surfaces.



### Core orientation

At the time of drilling and 5.9 cm pre-drilling WATSON imaging, the rover, coring drill, WATSON, and coring target (“Robine\_coring.PSC.0.0341”), had the following characteristics:

1. Rover orientation quaternion just after drilling but before unloading the stabilizers (transferring from RMECH to SITE frame): **bQI1** = (0.4283390, 0.0740838, 0.0263520, -0.9001910);
2. Coring Drill orientation quaternion just after drilling but before unloading the stabilizers (transferring from CORING DRILL to RMECH frame): **cdQb** = (0.6646180, 0.1631090, -0.7068370, 0.1790540);
3. Rover orientation quaternion at time of acquisition of WATSON image SIF\_0293\_0692957683\_398FDR\_N0090000SRLC00643\_0000LMJ02: (transferring from RMECH to SITE frame): **bQI2** = (0.428458, 0.0711518, 0.0249948, -0.900409);
4. WATSON orientation quaternion at time of acquisition of WATSON image SIF\_0293\_0692957683\_398FDR\_N0090000SRLC00643\_0000LMJ02: (transferring from WATSON to RMECH frame): **wQb** = (0.666062, 0.167862, -0.704872, 0.177028).

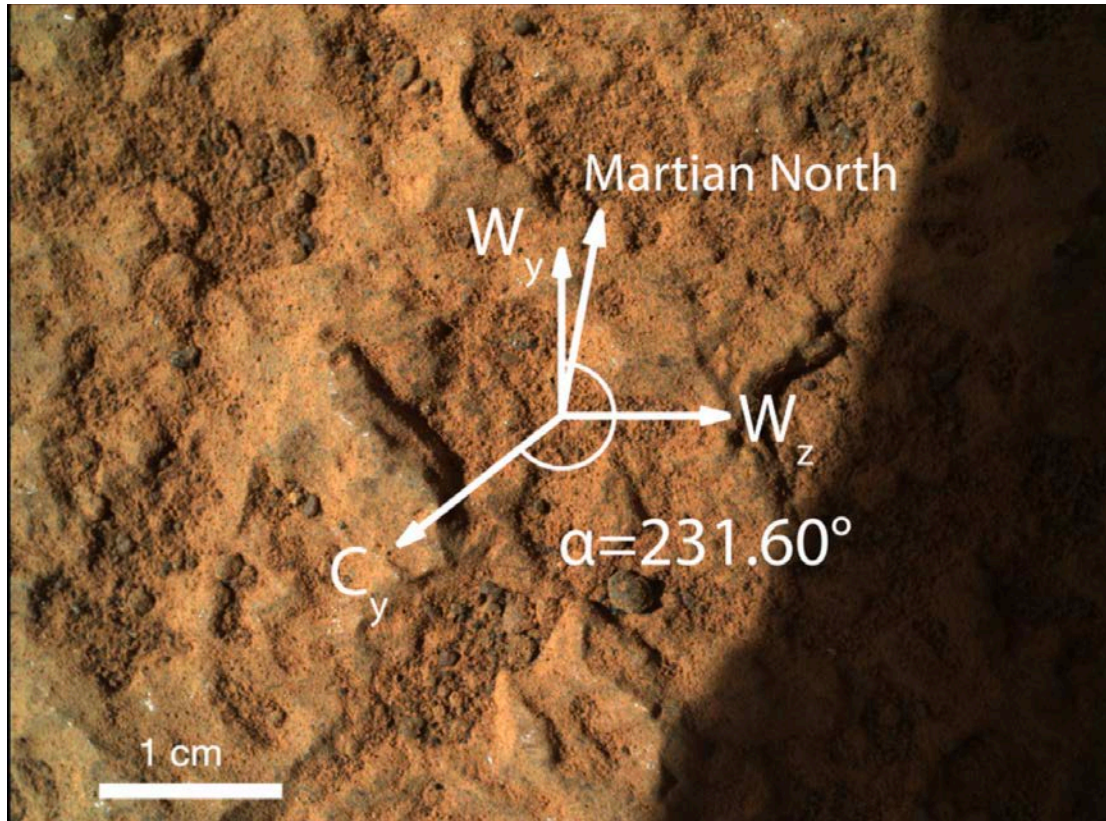
Items 1 and 2 give a coring drill pointing vector estimate of

**hade = 5.36°**  
**azimuth = 225.58°**

Items 3 and 4 give an estimate of the angle between the WATSON y-axis and the up-dip direction in SITE coordinates (**Figure 24**) of

**core roll,  $\alpha$  = 231.60°**

**Figure 24** | 5.9-cm standoff WATSON image of *Robine* core target on sol 295. Image scale is  $28.4 \mu\text{m pixel}^{-1}$ . Orientation compass gives WATSON frame ( $w_x, w_y, w_z$ ). Core roll is clockwise angle of core y-axis,  $c_y$ , from  $w_y$ , given by  $\alpha = 231.60^\circ$ . Projection of Martian geographic north onto WATSON image plane is noted. WATSON image SIF\_0293\_0692957683\_398FDR\_N0090000SRLC00643\_0000LMJ02.



## Preliminary Scientific Assessment

### Synthetic sample description and preliminary interpretation

Sample type: **Olivine cumulate**

#### 1. Relationship with surrounding rocks

- Robine* and *Malay* were obtained from the *Issole* outcrop, which has a stratigraphic position close to, but below, the boundary/contact with the *Máaz* formation.
- Based on its occurrence as part of a NE–SW-trending ridge, concordance with surrounding outcrops, and estimated dip consistent with that of the wider *Séítah* region, *Issole* is confidently interpreted to be an in-place portion of the *Séítah* bedrock.

#### 2. Texture and fabric

- Grain size: <0.1–4 mm
- Rock fabric (natural surface): large olivine crystals exposed on relatively fresh surfaces, but few definitive observations of grains on natural weathered surfaces.

- c. Rock fabric (abrasion patch): some textural heterogeneity, main constituents include <0.1–3 mm pale brown–white sub-angular phases, 0.2–0.8 mm mid-brown sub-angular to angular crystals, 1–4 mm grey–green angular and elongate crystals, <0.1 mm white crystals. Secondary minerals (including a large region of sulfates) are particularly concentrated within the central region of the abrasion patch.

### 3. Mineralogy and chemistry

- a. Minerals present: olivine, pyroxene (augite), Ca/Mg-sulfate, carbonate, Na-rich and K-rich feldspars, Fe-Cr-Ti magnetite, Ca-phosphates; also, aromatic organic materials sometimes associated with secondary mineral phases. Mesostasis consists of Na-rich alkali feldspar, Cr-rich and Ti-rich Fe oxides, and Ca-phosphates. Secondary phases include poorly diffracting (or very fine-grained) silicate(s) with low Fe and Mg, carbonate, and salt minerals (sulfates, perchlorates).
- b. The bulk composition is consistent with a mafic/ultramafic rock modified by limited aqueous alteration. Point analyses by SCAM and PIXL plot mostly within the olivine, microbasalt and basalt regions of the TAS diagram.

### 4. Alteration/secondary characteristics

- a. Interactions with aqueous fluids, alteration, and mineral hydration: evident, but limited.
- b. Secondary mineralogy: see point 3a above.

## Returned Sample Science Considerations

Observations of olivine surrounded by clinopyroxene in a poikilitic texture within the *Dourbes and Quartier* abrasion patches, along with remote observations of the mineralogy, texture, and spectral characteristics of *Brac, Issole* and other *Séitah* outcrops, suggest that the *Robine* and *Malay* samples (as well as the *Salette* and *Coulettes* samples), and much or all of *Séitah*, are best interpreted as an igneous olivine cumulate. As such, the return of these samples is expected to address a number of RSS themes of significance to the Mars 2020 mission:

*Geochronology:* The timing of volcanic rock crystallization can be quantified using laboratory-based, radiometric dating of returned samples. Likewise, assuming cosmogenic nuclide production rates in specific mineral on Mars can be established, quantitative constraints on the sample's surface exposure age and/or erosion rate may also be obtained. Quantifying the timing of crystallization of *Brac* and *Issole* will also constrain the emplacement ages of other crater floor units, given their stratigraphic relationships (e.g. *Séitah* is likely older than Cf-fr from which the *Montdenier* and *Montagnac* samples were collected).

*Paleomagnetism:* The igneous lithologies of the *Salette/Coulettes/Robine/Malay* samples may enable absolute measurements of the paleointensity of the ancient Martian magnetic field at the time of crystallization. The orientations of the samples, combined with paleohorizontal indicators from outcrop foliation, may enable measurements of the absolute paleodirection of the ancient field. Paleomagnetic investigations of secondary ferromagnetic minerals if present could constrain the field at the time of aqueous alteration. Combined with measurements from other samples, these data could test the hypothesis that Martian atmospheric loss was driven by the cessation of an early dynamo, constrain the dynamo's secular variation, and determine if the dynamo exhibited polarity reversals. Paleomagnetic analyses could also test whether *Séitah* rocks have experienced regional or global-scale tectonic tilting

and displacements. Comparison of paleomagnetic directions with *Máaz* rocks (*Montdenier/Montagnac* and *Atsah/Hahonih*) could distinguish between the hypotheses that *Máaz* and *Séitah* form a single layered intrusion versus *Máaz* being an overlying lava flow deposited on *Séitah*.

*Geochemistry:* With a hypothesized origin as an olivine cumulate, understanding the petrogenesis of the *Salette* and *Coulettes* samples will place constraints on the nature of igneous processes on early Mars. These constraints can be applied to the origins of the extensive “Cf-f-1” unit that has been correlated with a regional olivine-bearing unit exposed between Syrtis Major and Nili Fossae. The diverse mineral assemblages of the obtained samples will be valuable for quantifying the conditions and timing of primary, high-temperature crystallization of igneous phases and later-stage alteration events. The bulk chemistry of the rock, as well as trace element and stable and radiogenic isotope geochemistry of the rock and its constituent igneous minerals, will enable comparisons with similar lithologies in the Martian meteorite suite, and insights into magmagenesis and mantle/crustal evolution more generally. The large grains observed in *Brac* may contain melt inclusions that are of sufficient size to track the petrogenesis of this material.

*Water–rock interactions and habitability:* Many hypotheses for the origins of olivine-carbonate rocks involve aqueous alteration of igneous rocks. The interaction of aqueous media with (ultra)mafic rocks produces secondary mineral phases that can be indicative of the temperature, redox state, and fluid chemistry. High resolution mineral identification and stable isotope measurements can place constraints on such aspects of the alteration history and environment and provide insights into the presence, distribution, and nature of water on Mars. Water/rock interactions could have occurred as result of groundwater, possibly associated with Jezero lake, moving through these rocks and may have led to the establishment of microniches with water, energy, pH, nutrients and transition metals essential to life. Although likely a variable component in the history of these samples, the team has noted that low-temperature hydrothermal, serpentinizing and carbonation reactions may have sustained microbial life, particularly chemoautotrophs/chemolithotrophs that have been suggested as likely inhabitants of Martian biotopes. Although the fossil record of igneous rocks is highly variable and generally poor, the biosignature preservation potential of certain alteration phases associated with the *Brac* outcrop is higher, and it is possible that organic materials and/or biosignatures have been preserved within these phases.

The two pairs of cores from the *Séitah* formation (*Brac: Salette* and *Coulettes*, and *Issole: Robine* and *Malay*) are interpreted to be samples of a single olivine cumulate body. However, there are notable differences between them. Compared to *Dourbes* (the abrasion patch for the *Brac* samples), *Quartier* (*Issole* samples) has more Fe and Ca, and less Mg. This appears to arise from a higher ratio of augite to olivine in *Quartier*. In addition, *Quartier* has a lower abundance of Raman detected igneous phases and a higher abundance of alteration products (especially hydrated sulfates and carbonate) compared with *Brac*. One possible interpretation of these differences is that relative to *Brac*, *Issole* is a less-mafic layer of the *Séitah* igneous body that has experienced a greater degree of aqueous alteration.

**References**

Carrier W.D. III, Olhoeft, G.R., Mendell, W. (1991) Physical Properties of the Lunar Surface. Lunar Sourcebook, A User's Guide to the Moon, ISBN 0521334446, Cambridge University Press, 475-594.

Stack, K.M. et al. (2020). Photogeologic Map of the Perseverance Rover Field Site in Jezero Crater Constructed by the Mars 2020 Science Team. Space Science Reviews, 216, 127, doi:10.1007/s11214-020-00739-x.

# INITIAL REPORT

## M2020-337-8 *Malay*

---

**Sample Designation:** M2020-337-8 *Malay*

**Date of Coring:** 30-January-2022

**Mars Time of Sample Core Sealing:** 19:25 LMST, Sol 337, Ls 166.6

**Latitude (N), Longitude (E), Elevation:** 18.43264°, 77.44133, -2574.3 m

**Campaign:** Crater Floor

**Region of Interest:** *Séítah South*

**Lithology:** Medium- to coarse-grained poikilitic olivine cumulate rock. Primary minerals are olivine and pyroxene. Limited secondary aqueous alteration, including carbonate, hydrated sulfate, and other hydrated phases. Organic material is present, at least partially associated with sulfate phase(s).

**Estimated Volume Recovered:** 4.3 cm<sup>3</sup>

**Coring Bit Number:** 2

**Core Orientation:** hade = 2.72°; azimuth = 77.64°; core roll = 274.92°

**Sample Serial Numbers:** Tube SN261; Seal SN53; Ferrule SN062

**ACA Temperature at Time of Sealing:** 40°C

**Estimated Rover-Ambient Pressure and Temperature at Time of Sealing:** 642 Pa, 223 K

**Estimated Amount of Martian Atmosphere Headspace Gas:** 2.7 x10<sup>-6</sup> mol

**Anomalous Behavior:** None

**Abrasion Patch Name and Depth:** *Quartier*, 8 mm

---

January 27, 2022

*K. Hickman-Lewis, K. A. Farley, J. I. Simon, J. R. Johnson, B. Horgan, M. Rice, J. Bell, J. Rice, T. Bosak, L. Mandon, A. Udry, S. VanBommel, McLennan, S.M., Y. Goreva, R. C. Moeller, V. Sun, K.P. Hand, E. L. Berger, F. Calef, A. D. Czaja, C. H. Lee, A.C. Fox E. L. Scheller, S. Sharma, S. Siljeström, H. E. F. Amundsen, L. W. Beegle, B. P. Weiss, D.L. Shuster, C.D.K. Herd, R. C. Wiens, S. Le Mouélic, G. Caravaca, O. Gasnault, S. Maurice and the Mars 2020 Team.*

## Summary Description

This sample is paired with M2020-298-7 *Robine*. Only the core orientation for *Malay* is described below. See the Initial Report for 2020-298-7 *Robine* for sample details.

### **Core orientation**

At the time of drilling and 6 cm pre-drilling WATSON imaging, the rover, coring drill, WATSON, and coring target ("Malay\_337\_snc\_coring"), had the following characteristics:

1. Rover orientation quaternion just after drilling but before unloading the stabilizers (transferring from RMECH to SITE frame): **bQII1** = (0.9452490, 0.0016222, 0.0085824, 0.3262330);
2. Coring Drill orientation quaternion just after drilling but before unloading the stabilizers (transferring from CORING DRILL to RMECH frame): **cdQb** = (0.6986380, 0.1504020, -0.6775800, 0.1736920);
3. Rover orientation quaternion at time of acquisition of WATSON image SIF\_0337\_0696859111\_167FDR\_N0090276SRLC00636\_0000LMJ01: (transferring from RMECH to SITE frame): **bQII2** = (0.945265, 0.00189065, 0.00584646, 0.326245);
4. WATSON orientation quaternion at time of acquisition of WATSON image SIF\_0337\_0696859111\_167FDR\_N0090276SRLC00636\_0000LMJ01: (transferring from WATSON to RMECH frame): **wQb** = (0.700578, 0.153594, -0.675732, 0.17025).

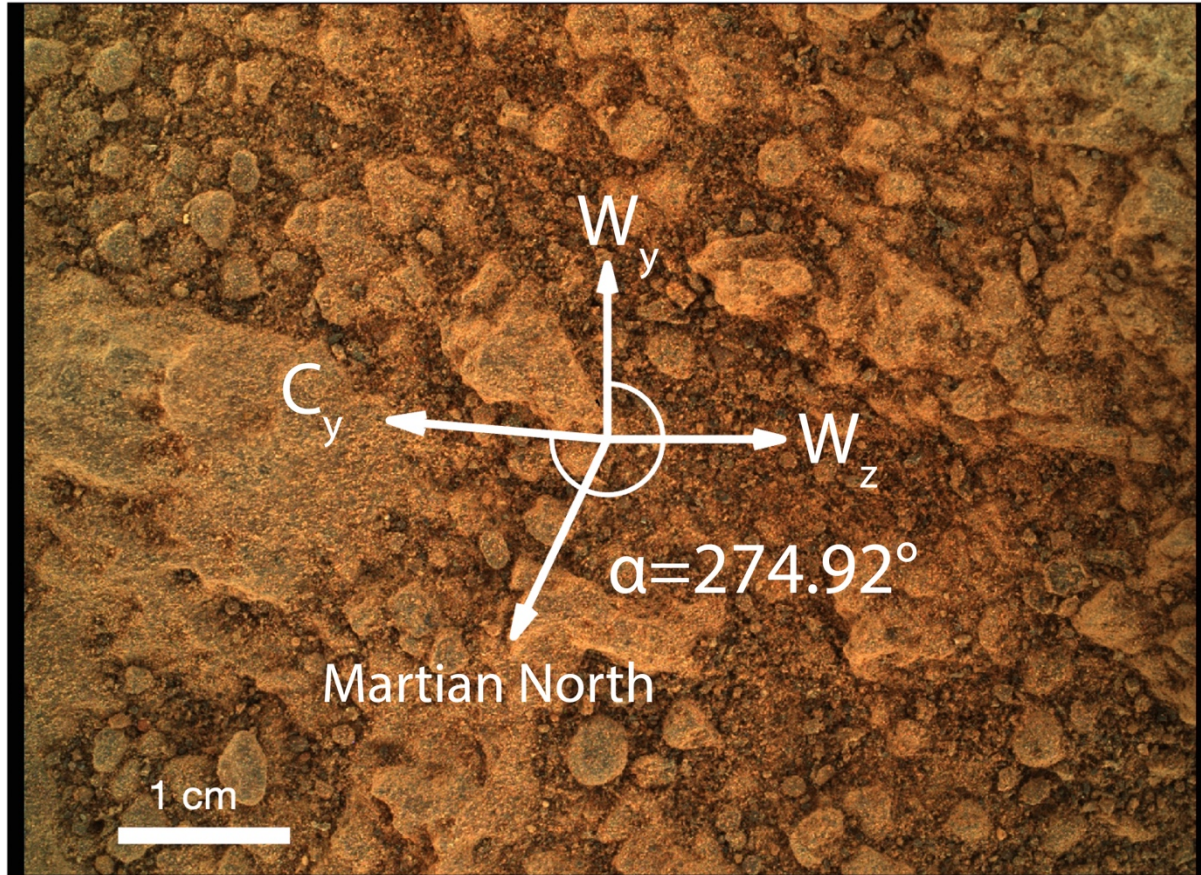
Items 1 and 2 give a coring drill pointing vector estimate of

**hade = 2.72°**  
**azimuth 77.64°**

Items 3 and 4 give an estimate of the angle between the WATSON y-axis and the up-dip direction in SITE coordinates (**Figure 1**) of

**core roll,  $\alpha$  = 274.92°**

**Figure 1.** 6-cm standoff WATSON image of *Malay* core target on sol 337. Image scale is  $28.7 \mu\text{m pixel}^{-1}$ . Orientation compass gives WATSON frame ( $\mathbf{w}_x$ ,  $\mathbf{w}_y$ ,  $\mathbf{w}_z$ ). Core roll is clockwise angle of core y-axis,  $\mathbf{c}_y$ , from  $\mathbf{w}_y$ , given by  $\alpha = 274.92^\circ$ . Projection of Martian geographic north onto WATSON image plane is noted. WATSON image SIF\_0337\_0696859111\_167FDR\_N0090276SRLC00636\_0000LMJ01.



# INITIAL REPORT

## M2020-371-9 Hahonih

---

**Sample Designation:** M2020-371-9 Hahonih

**Date of Coring:** 6-Mar-2022

**Mars Time of Sample Core Sealing:** 19:21:57 LMST, Sol 371, Ls 185.2

**Latitude (N), Longitude (E), Elevation:** 18.44386406, 77.45242176, -2568.357 m

**Campaign:** Crater Floor

**Region of Interest:** *Ch'at* member of *Máaz* formation, east of the Octavia E. Butler landing site

**Lithology:** Likely basaltic andesite. Few mm-size white feldspar laths and pyroxene grains are present, as possibly are olivine and quartz. Limited evidence of secondary alteration includes interstitial iron oxides, carbonate, possible phyllosilicates and chlorite, and hydration. Low concentrations of organic matter were detected.

**Estimated Volume Recovered:** 9.24 cm<sup>3</sup>

**Coring Bit Number:** 3

**Core Orientation:** hade = 21.41°; azimuth = 73.18°; core roll = 126.60°

**Sample Serial Numbers:** Tube SN262, Seal SN172, Ferrule SN129

**ACA Temperature at Time of Sealing:** 40°C

**Estimated Rover-Ambient Pressure and Temperature at Time of Sealing:** 672 Pa, 227 K

**Estimated Amount of Martian Atmosphere Headspace Gas:** 0.98x10<sup>-6</sup> mol

**Anomalous Behavior:** None

**Abrasion Patch Name and Depth:** *Alfalfa*, 9 mm

---

May 8, 2022

B. A. Cohen, H. Amundsen, L. Beegle, J. Bell, E. Berger, T. Bosjak, F. Calef, E. Cardarelli, A. Czaja, V. Debaille, H. Dypvik, K.A. Farley, A. Fox, S.-E. Hamran, C. Herd, B. Horgan, J. R. Johnson, L. Jandura, C. Lee, L. Mandon, E. N. Mansbach, L. E Mayhew, S. M. McLennan, C. Million, M. Rice, E. Scheller, M. E. Schmidt, J. Schroeder, S. Sharma, S. Siljestroem, J. I. Simon, D. L. Shuster, M. St. Clair, A. Udry, S. Van Bommel, B. P. Weiss, R. C. Wiens, M.-P. Zorzano, and the Mars 2020 Team

## **Summary Description**

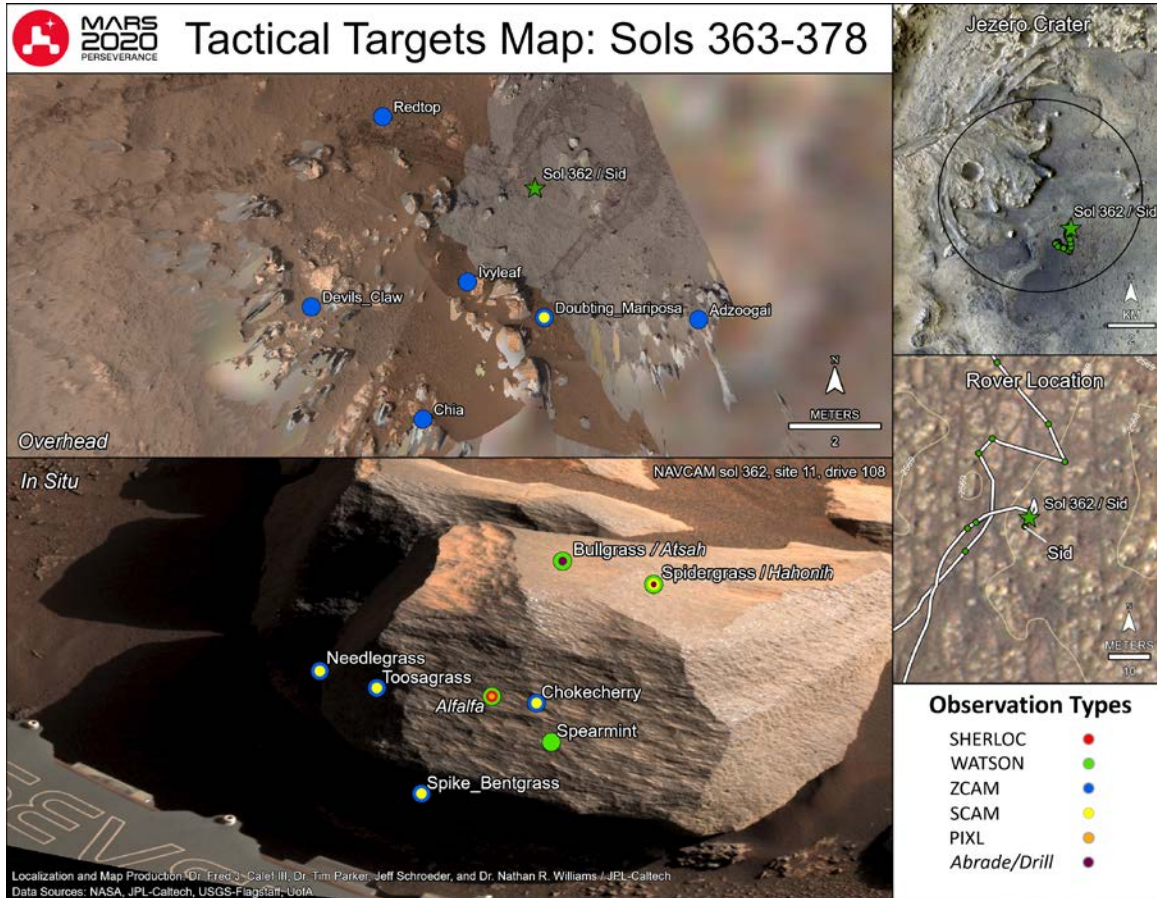
The *Hahonih* and *Atsah* sample cores were collected about 100 m east of the *Perseverance* landing site, as the seventh and eighth rock samples of the mission and the last pair acquired during the Crater Floor Campaign. The *Hahonih* and *Atsah* samples were cored from the top of a boulder named *Sid*, associated with an abrasion patch named *Alfalfa* on the side of the *Sid* rock. The *Hahonih* and *Atsah* samples were selected to represent the *Ch'at* member of the *Máz* formation, the stratigraphically highest *Máz* member, expressed as massive, blocky rocks that appear to cover much of the Jezero crater floor as seen from orbit.

Figure 1 shows the local context of *Perseverance* rover operations leading up to the sampling of *Hahonih* and *Atsah*. *Perseverance* arrived in front of *Sid* on sol 363, abraded the *Alfalfa* target on Sol 367, and collected samples *Hahonih* (Sol 371) and *Atsah* (Sol 374/377; three-sol delay in sample processing due to arm fault between coring and sealing). *Perseverance* also conducted STOP list and opportunistic science observations on *Sid* and other nearby targets (Fig. 1).

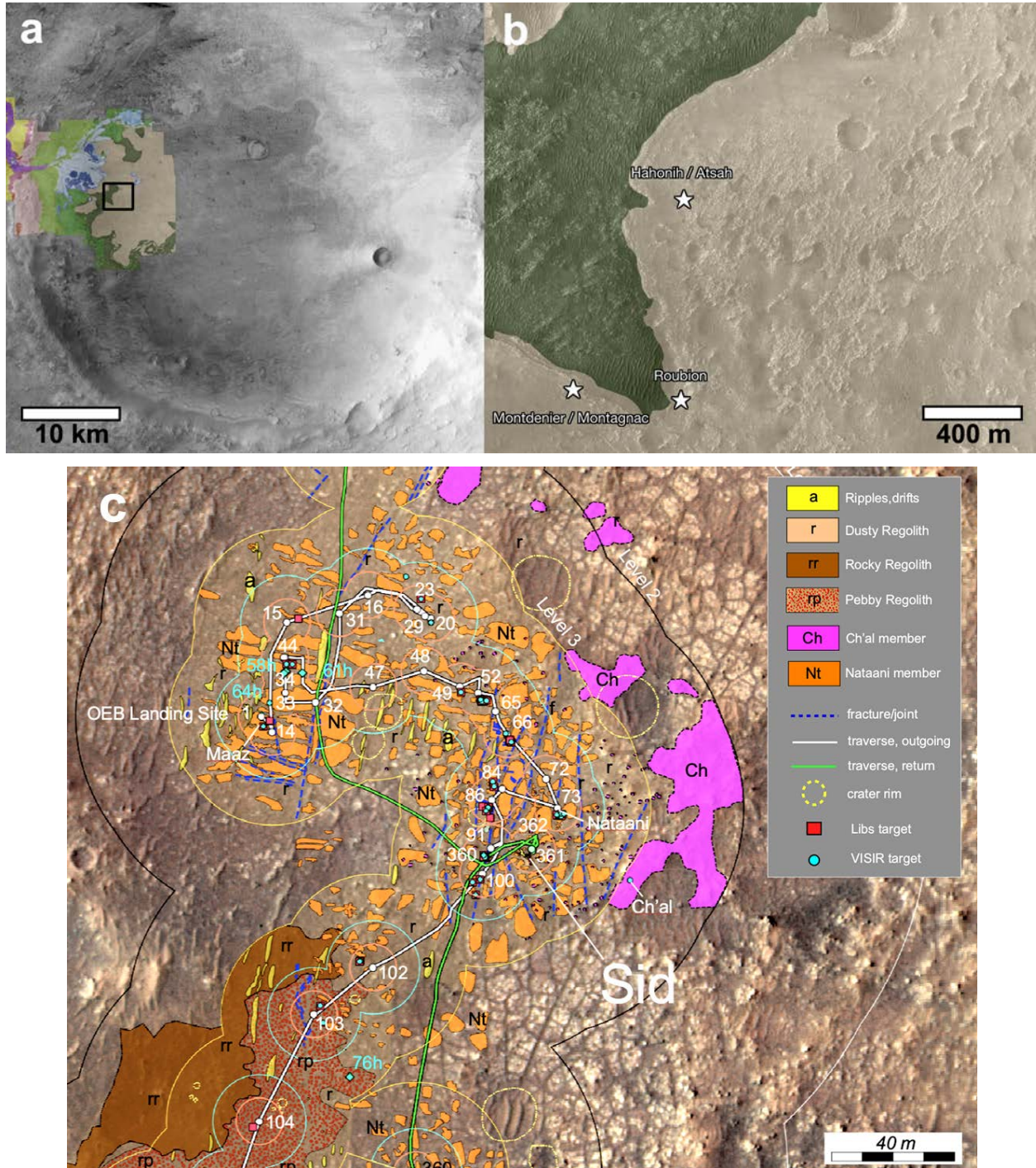
Images of the *Alfalfa* abrasion patch and associated chemistry and mineralogy data reveal interlocking white feldspar laths, pyroxene, possibly olivine, and possibly quartz. Limited evidence of secondary alteration includes interstitial iron oxides, carbonate, possible phyllosilicates and chlorite, and hydration. Low concentrations of organic matter are present in the abrasion patch. Drill parameters during abrasion show that *Sid* is the hardest rock so far abraded by *Perseverance*. The *Hahonih* and *Atsah* cores are believed to be the least altered samples acquired from the Jezero crater floor.

Since the *Hahonih* and *Atsah* samples are the most compellingly in-place cores acquired from the crater-retaining *Máz* formation, radiometric dates of these samples could be compared to crater-density based age models. Radiometric dates could also place constraints on the ages of the apparently overlying delta and the apparently underlying *Séitah* formation. The *Hahonih* and *Atsah* cores are oriented, so the magnetic field present at the time of crystallization could potentially be characterized. As the *Hahonih* and *Atsah* samples are the least altered samples acquired from the *Máz* formation, they could be especially useful in characterizing martian igneous petrology and the geochemical evolution of the mantle or crust. Cosmogenic nuclide measurements could constrain *Máz* formation erosion rates, as well as inform expectations of the impact of galactic cosmic radiation on the preservation and modification of organic molecules in samples from Mars.

**Figure 1 | Local context for the *Hahonih* and *Atsah* sample collection campaign and associated observations.** The green star in the overhead view denotes the location of the rover during sampling, slightly east of the *Sid* rock. *Sid* (approx. 40 cm across) is shown in the lower left panel.



**Figure 2 | Regional context of Perseverance operations.** (a) Geologic map of western Jezero Crater (Stack et al., 2020) over CTX basemap; (b) Zoom of the rectangle in (a) shows the Perseverance Crater Floor campaign area with *Máaz* fm sample locations; dark green is mapped as Cf-F-1 (now *Séítah* fm) and tan is mapped as Cf-fr unit (now *Máaz* fm). *Hahonih* and *Atsah* were chosen to represent the Ch'al member, the extensively-cratered, upper unit that extends east of the landing site. (c) In situ geologic map (Crumpler and others, 2022) showing locations where polygonally-jointed *Nataani* type and massive *Ch'al* type rocks occur near the Perseverance landing site. The labeled *Sid* rock is the source of the *Hahonih* and *Atsah* sample cores.



## **Stratigraphic and Geologic Context**

*Hahonih* and its paired core *Atsah* were collected from the *Sid* outcrop, a representative of the *Ch'at* member (mb), the uppermost unit of the *Máaz* formation (fm). This formation was mapped as crater floor fractured rough (Cf-fr) in Stack et al. (2020) (Fig. 2). The *Máaz* fm has also been referred to as the volcanic floor (Schon et al., 2012; Goudge et al., 2015), the dark-toned floor, and the mafic floor. Orbital detection of olivine and pyroxene in the unit, and the unit's lobate margins and embayment relationships with the basin perimeter and other exposed floor units, have been offered as evidence of a volcanic origin (Goudge et al., 2015; Horgan et al., 2020a; Schon et al., 2012; Shahrzad et al., 2019). Upon landing, the prevalence of loose rocks and boulders with mafic mineralogy and a "pitted" appearance interpreted by some members of the science team as vesicles, provided potential evidence that lava flows were present in the vicinity of the landing site. However, alternative hypotheses, including a volcanoclastic and/or sedimentary origin, were also posited based on the proximity to the Jezero delta, history of water filling the crater, thermal inertia of the crater floor unit, and the apparent absence of volcanic landforms that could have sourced lava flows (Stack et al., 2020).

The *Ch'at* member of the *Máaz* formation is likely the stratigraphically highest member of the formation, lying above the *Nataani*, *Rochette*, *Artuby*, and *Roubion* members. *Ch'at* member outcrops like *Sid* consist of massive rocks that form mounds and ridges east of the Octavia E. Butler landing site and south of the rover's traverse to *Séitah*. The relatively large size of *Sid* and other similar rocks in the area, and their direct contact with the underlying, polygonally jointed, flat rocks of the *Nataani* member, suggest that *Sid* is derived directly from the receding *Ch'at* member and is unlikely to have been moved or rotated significantly after deposition. In many places, dark-toned, ventifacted "nubs" project upward from exposed *Nataani* member outcrops and may be examples of *Ch'at* rocks weathered in place (Fig. 3).

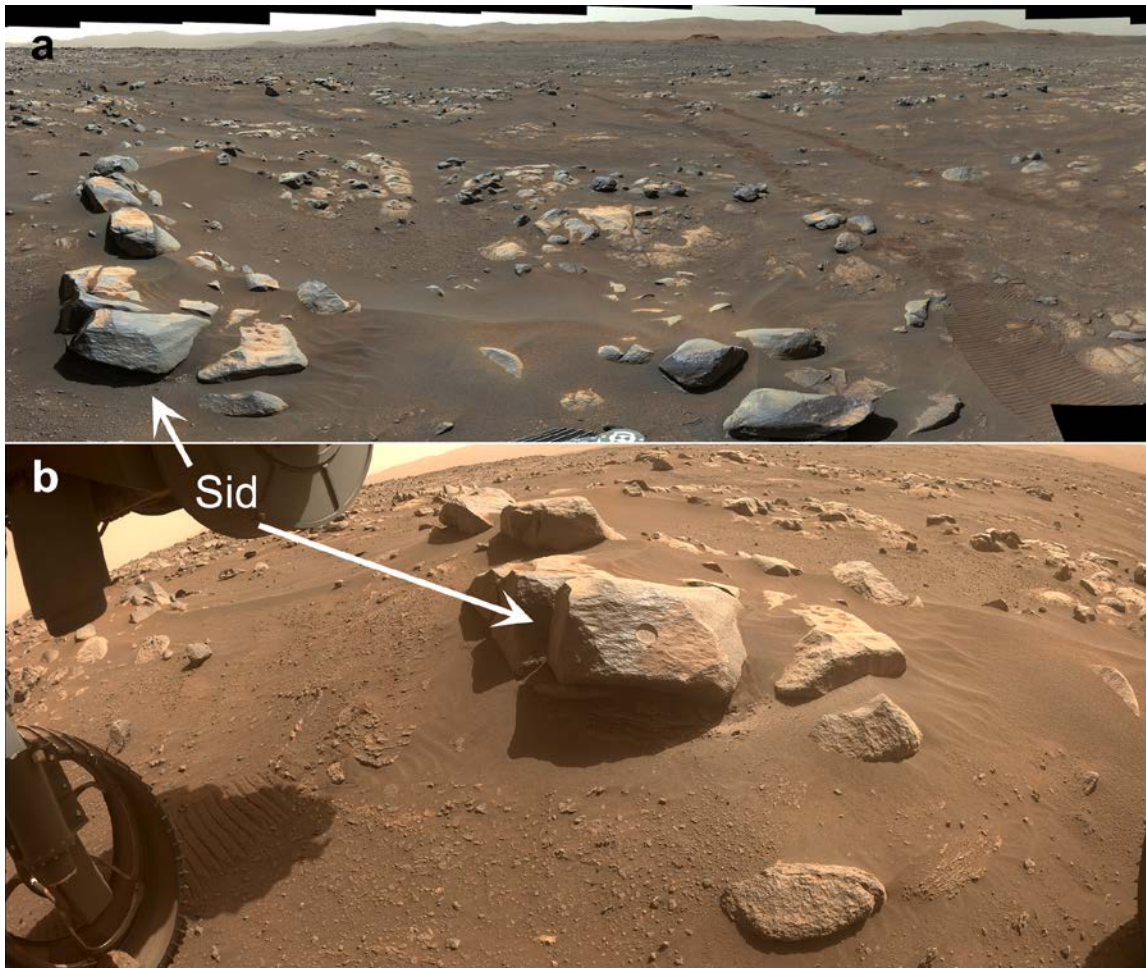
Earlier in the mission, we attempted to collect a sample of one of the low-lying, polygonally jointed members of the *Máaz* fm (*Roubion* member), but that attempt failed when the rock disaggregated such that no core was retained in the sample tube (see *Roubion* IR). Subsequent collection of the *Montdenier* and *Montagnac* cores from the *Rochette* member of *Máaz* was successful. Rover observations indicate that the *Séitah* formation lies below the *Máaz* formation, suggesting that *Séitah* is older. Thus the four *Séitah* formation cores (*Salette*, *Coulettes*, *Robine*, and *Malay*) are likely older than all of the *Máaz* cores. However, if *Séitah* is a younger unit that intruded the *Máaz* formation, the relative age relationship of the samples would be inverted. The crater floor units - *Máaz* and *Séitah* - are interpreted to be stratigraphically below the delta sedimentary rocks, but this interpretation will need to be tested as Perseverance explores the crater floor - delta contact.

Although the lithology and stratigraphy of the crater floor were unknown before landing, the Perseverance team had intended to sample the areally-extensive Cf-fr unit because of the high science value of radiometric ages for constraining the timing of many crater floor units, and for correlation with crater density to provide a comparison with crater-based chronologies (e.g., Beaty et al., 2019; Cohen et al., 2021; Werner, 2019).

## Operations

Because the *Montagnac* and *Montdenier* samples were cored from a rock (*Rochette*) that may be slightly displaced from its original orientation, the Perseverance team had a strong desire to collect a sample of an in-place rock with unambiguous identification as the uppermost member of the *Mááz* fm prior to leaving the crater floor and climbing up the delta. Several locations were considered for sampling as the rover traversed north on the last leg of the Crater Floor Campaign, including examples of the “nubby” outcrops and topographic highs covered with *Ch’at*-type rocks that were inaccessible to the rover. The team ultimately chose to target an easily accessible *Ch’at*-type block close to the rover’s previous traverse. The team prioritized candidates based on their morphologic and topographic similarities to the *Ch’at* member, and evidence that the rock was in place.

**Figure 3 | *Sid* outcrop images.** a) Mastcam-Z merged sol 363-369 enhanced color mosaic of *Sid* and surroundings showing the darker, “bluer” nature of the blocky *Ch’at*-type rocks overlying the paler, tan, polygonally-jointed rocks of the *Nataani* member. b) Sol 367 Front Hazcam image of the workspace; the *Sid* block (with the *Alfalfa* abrasion patch) is ~40 cm across. *Sid* rests on a low mound that appears to be composed of finely-layered material (in shadow) that may represent the *Nataani* member. Images: zcam08394/08386/08401 L0, FLF\_0367\_0699524043\_237RAS\_N0110108FHAZ02008\_OA00LLJ01.IMG.



As the rover passed southeast of the Octavia E. Butler landing site, the team identified several blocks of *Ch'al*-type material in direct contact with underlying *Nataani* rocks, including *Sid* (Fig. 3). The relatively large size of the *Sid* rock and others in the area, and their direct contact with the *Nataani* member, suggest that *Sid* is derived directly from the receding *Ch'al* member and likely was not significantly moved or rotated after deposition. Table 1 provides details of the execution of STOP list observations made on *Sid*.

**Table 1 | STOP list observations for the *Hahonih* and *Atsah* samples.**

Instrument	Rationale	Target	Uplink Sol
ZCAM	Stereo imaging of the workspace, including abrasion and coring targets	<i>Sid</i>	362
WATSON	Pre-and post-abrasion imaging for rock texture documentation	<i>Alfalfa</i> pre-abrasion	366
		<i>Alfalfa</i> post-abrasion	370
SHERLOC	Organic/mineralogical map on abraded patch. SHERLOC scan co-registered with PIXL	<i>Alfalfa</i>	370
PIXL	Overnight elemental chemistry map on abraded patch. PIXL footprint co-registered with WATSON and SHERLOC- for lithology, chemistry, and mineralogy	<i>Alfalfa</i>	369
ZCAM	Multispectral observation of abraded patch for mineralogy and to support SCAM observations	<i>Alfalfa</i>	368
SCAM	SCAM RMI / LIBS / VISIR / RAMAN 3x3 raster on abraded patch for lithology documentation	<i>Alfalfa</i>	370, 375
WATSON	Coring target documentation (pre-drill) at each core site for paired samples	<i>Hahonih</i>	371
		<i>Atsah</i>	373
WATSON	Nighttime image for borehole documentation, only one borehole imaging for paired samples.	<i>Hahonih</i>	373
SCAM	10x1 SCAM RMI / LIBS for chemistry and mineralogy. Only required on one borehole for paired samples.	<i>Hahonih</i>	373
ZCAM	Multispectral image of borehole and tailings for mineralogy. Only required on one borehole for paired samples.	<i>Hahonih</i>	374

## Sample-Related Observations

### *Workspace Images*

*Sid* sits among an accumulation of similar *Ch'al*-type rocks, along with abundant sand and regolith. The surrounding area is characterized by flat-lying, polygonally-jointed bedrock, interpreted to be the *Nataani* member (Fig. 2c). In the bedrock below *Sid*, fine (~5 mm), parallel layers are present, interpreted to represent laminations or exfoliation in the *Nataani* member. The fine laminations below

and around *Sid* do not appear disturbed by the presence of the boulder, and there is no nearby ridge that *Sid* could have fallen from. This strongly suggests that *Sid* represents an in-place remnant of the *Ch'at* member.

The natural surface of *Sid* (Fig. 4, 5) is wind polished and generally dust-free, though dust and wind-blown sediment have accumulated in depressions and in the regions beneath overhangs. *Sid* has patchy coatings which are co-located with modern accumulation of regolith/dust in local topographic lows. Few, if any, individual grains are visible in the WATSON pre-coring natural surface images, but individual grains and pits are observed in the RMIs of relatively fresh/broken surfaces on *Sid* and other nearby targets (Fig. 5). Where individual grains can be identified, an interstitial reddish-white material is present. This phase may represent an interstitial phase and/or surficial dust caught between grains. The few grains/crystals that could be measured ranged in size from 0.2 to 1.5 mm. Distinctive features at the surface of *Sid* were adequate for reconstruction of original core azimuthal orientation, so no additional core orientation marking was performed.

**Figure 4 | Mastcam-Z image of *Sid*.** Note its glossy, fluted exterior texture and the massive character. The yellow rectangle shows the location of the inset WATSON 7 cm standoff image of the *Alfalpa* natural surface texture (lower left) showing ventifact ridges and clinging dust.

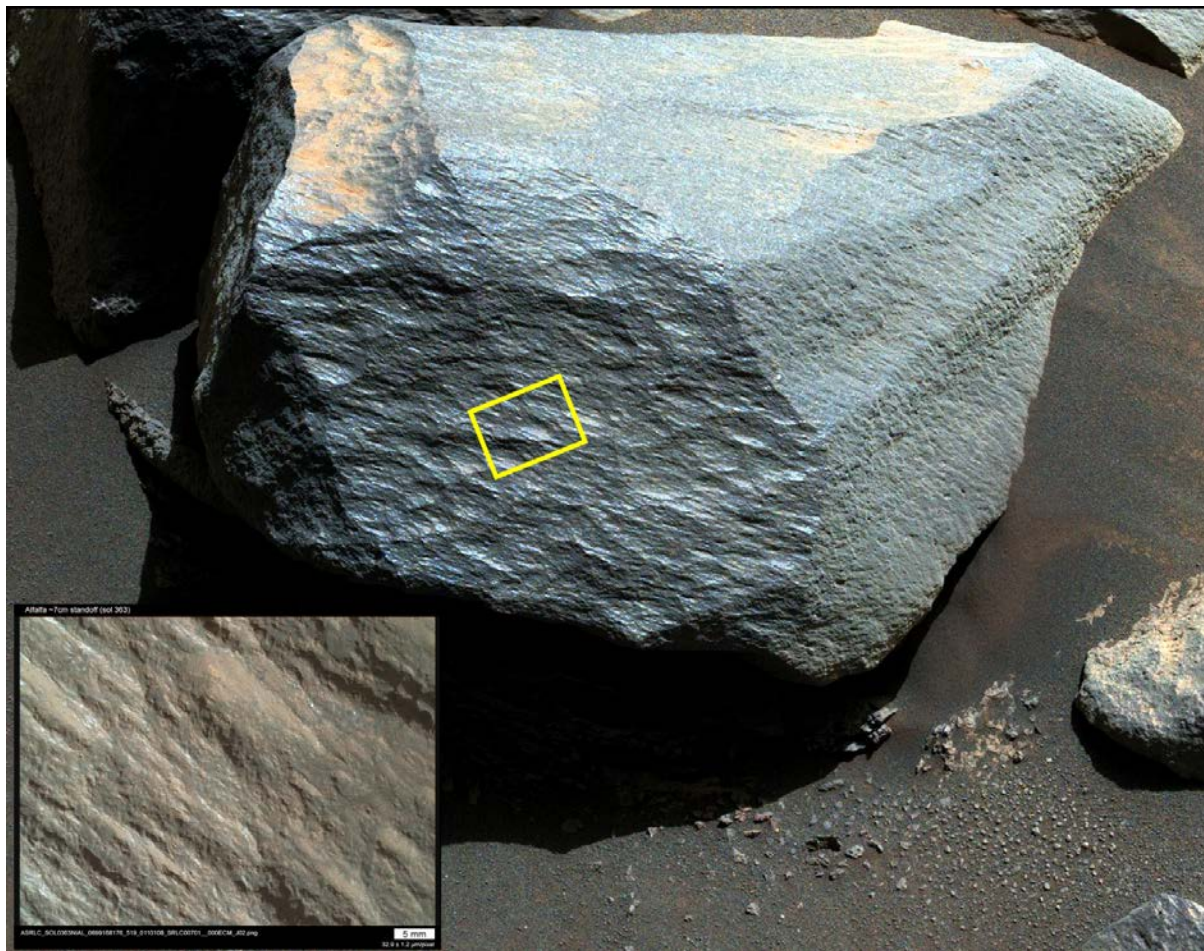
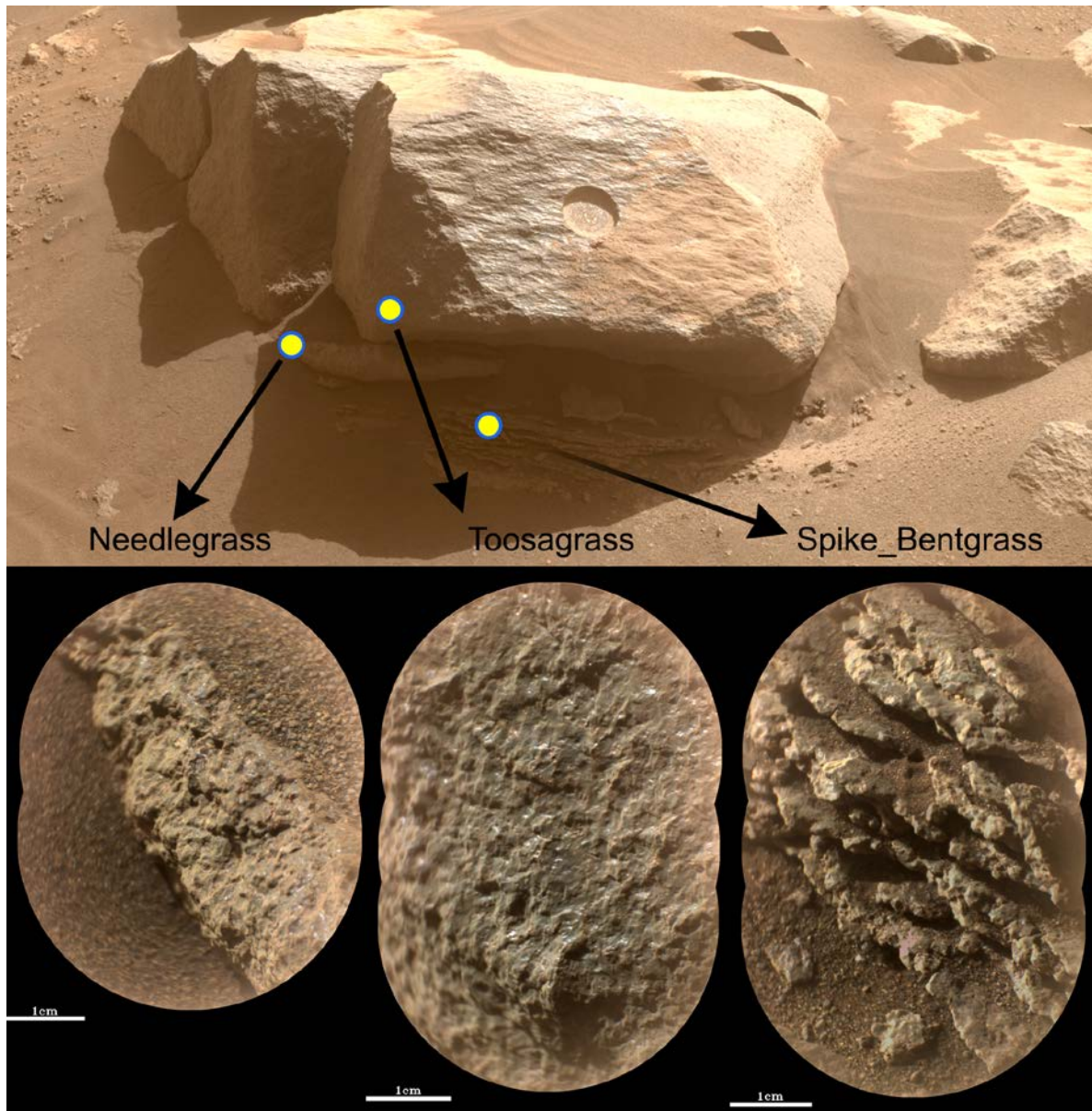


**Figure 5 | Surface textures of Sid.** Stretched Mastcam-Zi mage of the *Sid* block and nearby targets with SCAM RMI images of natural surfaces showing grains and other textures.



### ***Pre and Post Coring/Abrasion Images***

The team evaluated four potential locations for proximity science (abrasion and/or coring). The *Spidergrass* and *Bullgrass* locations on the top of the *Sid* block (Fig. 1) were preferred for coring, in order to sample any internal structure correlated to the gravity vector. The *Alfalfa* target (Fig. 1) was selected for a 9-mm depth abrasion. Drill operation parameters during abrasion suggest that *Sid* was the hardest rock encountered by the mission to date. The abrasion yielded a complete, flat-bottomed disk with a crisp edge. The internal texture of the rock was well exposed, showing a crystalline texture with light-colored lath-like grains, dark grains, and a fair amount of reddish-brown material (Fig. 6). The sample cores *Hahonih* (Navajo for “perseverance”) and *Atsah* (Navajo for “eagle”) were collected from the top of the *Sid* block.

ZCAM multispectral observations of the *Sid* natural surface, *Alfalfa* abrasion patch, and *Hahonih* tailings are shown in Fig. 7. The uncoated wind-polished surface shows a very flat spectrum with a shallow absorption band centered <900 nm. Purple coatings show a similar band shifted to longer wavelengths (~900 nm). The *Sid* natural surface, average abraded patch, and tailings from *Alfalfa* all show a broad band centered near 860 nm. Hematite may be contributing to the position of the band center (some type of iron oxide or oxyhydroxide is supported by the band at ~535 nm), but the broadness is likely due to orthopyroxene. The tailings show a slight flattening or downturn at 1000 nm that could be related to hydration or scattering by fine particles.

The ZCAM multispectral data of *Sid* are consistent with mafic mineralogy (Fig. 8). These observations also show significant internal oxidation in *Sid*, which causes the overall red appearance of the core and tailings. Within the abraded patch, the strong red slopes at short wavelengths that provide the overall red color are associated with hematite, even though little crystalline hematite is detected at Mastcam-Z scales. The abraded patch exhibits bright grains with no clear iron absorptions (likely feldspar) and dark/red grains. The *Hahonih* tailings are redder than the wind-polished rock surface, likely due to liberation of fine-grained hematite from the interior. Similar effects have been observed by the Curiosity rover at Vera Rubin ridge in Gale crater (Horgan et al., 2020b). This is the first sample site for which we have seen this type of reddening in Jezero. For comparison: *Brac* was very magenta (olivine-dominated), *Issole* was very blue (CPX-dominated), *Roubion* was very green (OPX-dominated), and *Rochette* was very magenta (CPX-dominated).

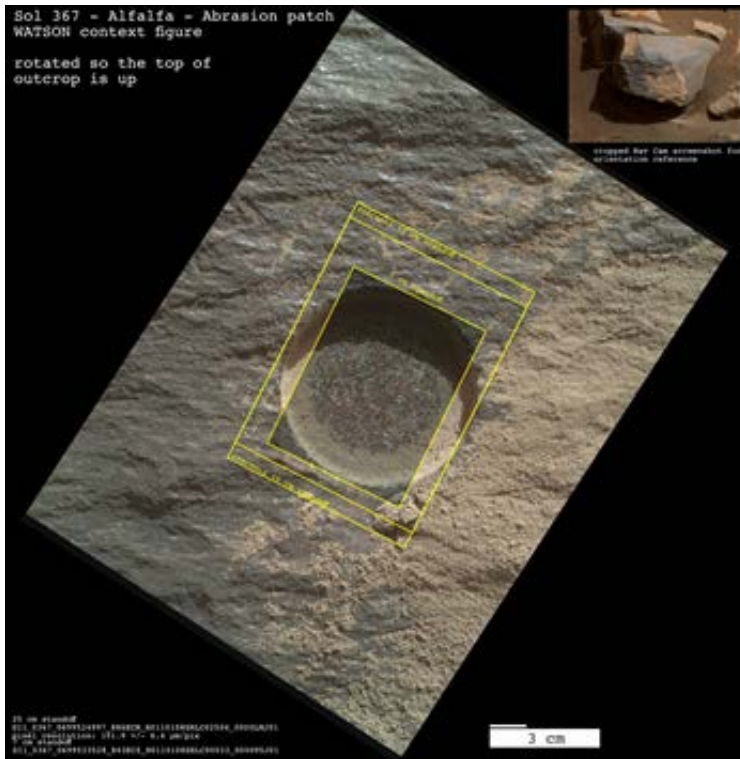


**Figure 6 | The *Alfalfa* abrasion (Left)** Location of the *Alfalfa* abrasion patch in WATSON images (notice the sharp edges and complete abrasion for the 9 mm deep patch). (Bottom) nighttime WATSON image of the *Alfalfa* abrasion patch showing the interlocking, crystalline nature of the rock with large (several mm) white feldspar laths, pyroxene and other mafic minerals in shades of gray, and pervasive, interstitial rusty-brown iron oxides.

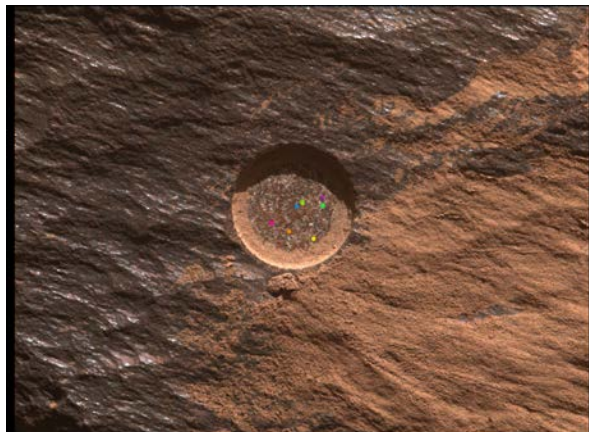
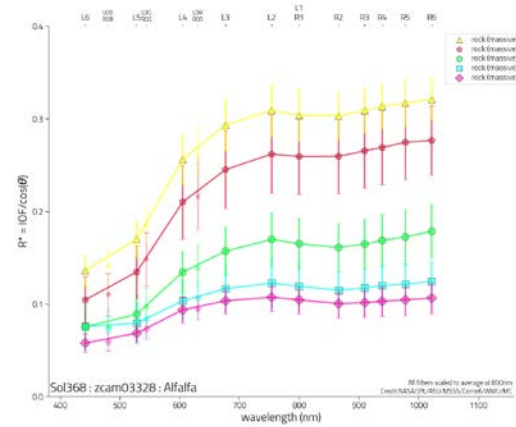
sol 367 - Alfalfa - nighttime - group 2 LEDs on



**Figure 7 | Mastcam-Z multispectral image of *Alfalfa*.** Images on left are approximate natural color with regions of interest for spectra at right indicated by colored boxes. (top) Average spectra of the natural rock surface (cyan/pink), a abrasion tailings (yellow/red), and a braded surface (green), all exhibiting broad and weak absorptions centered near 860-900 nm due to orthopyroxene, hematite, or some combination, with the presence of bands near 525 nm supporting some ferric iron. (bottom) Detailed analysis of the a braded patch showing diversity in individual phenocrysts. Bright white regions (purple/green) show limited absorption due to iron consistent with feldspar, while red regions (magenta, orange, yellow) show broad bands consistent with orthopyroxene, either with Fe<sup>3+</sup> substitutions or mixed with hematite. Dark black regions show limited spectral contrast, possibly due to opaque oxides or fine-grained mafic minerals. Sol 368 Zcam03328 taken at Z110 focal length.



context image right  
Alfalfa, sol 368, seq\_id 03328, rsm 1142  
Credit: NASA/JPL/ASU/MSSS/Cornell/WWU/MC



context image left  
Alfalfa, sol 368, seq\_id 03328, rsm 1142  
Credit: NASA/JPL/ASU/MSSS/Cornell/WWU/MC

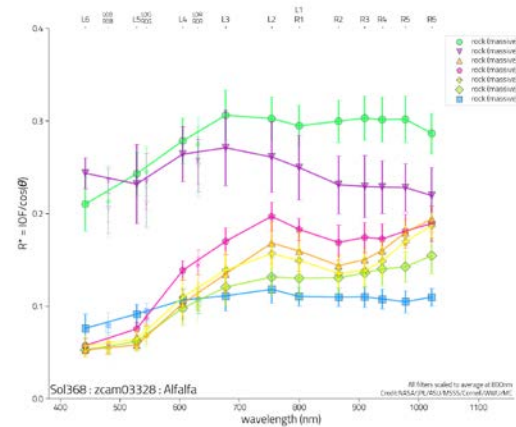
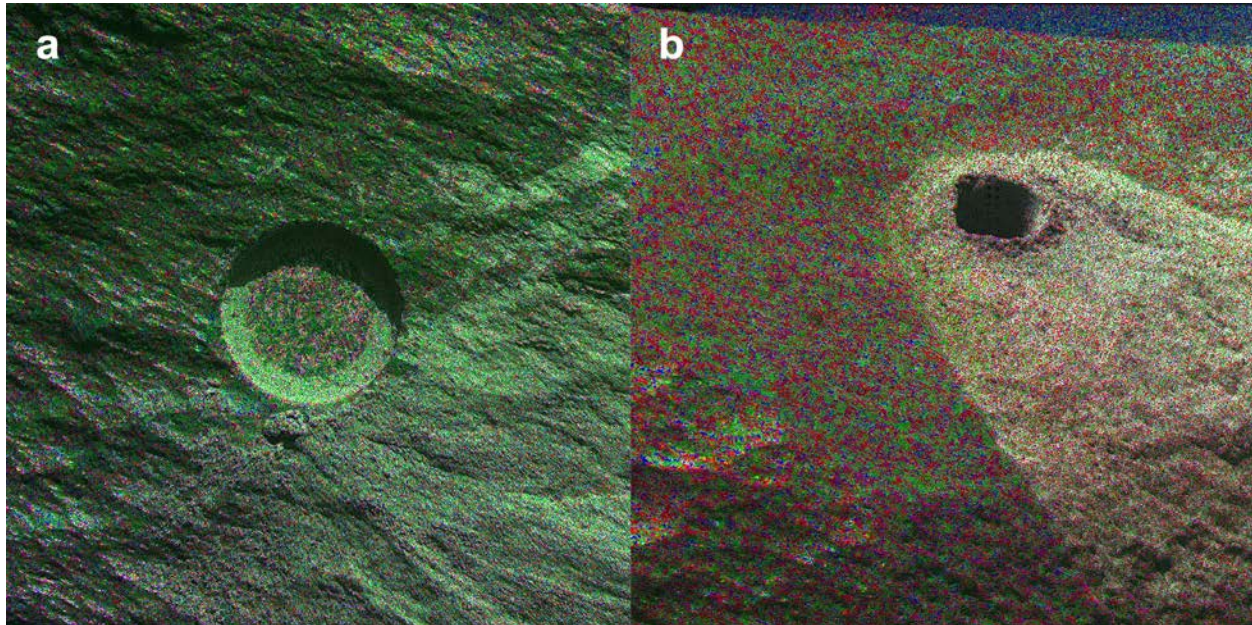


**Figure 8 | ZCAM multispectral mineralogy.** (a) *Sid* natural surface and *Alfalfa* abrasion patch, and (b) *Hahonih* tailings. Red = R0R/R1 (630/800 nm) Green=BD910 (band depth) Blue=R1/R5 (800/978 nm), color over blue Bayer filter grayscale image. Mineral interpretation is magenta= olivine or CPX, blue/green= OPX or CPX, green/black= ferric dust/purple coatings. The *Hahonih* tailings have weaker mafic signatures than the *Sid* rock surface both due to a shallower 910 nm band and a much redder slope.



### **Elemental Geochemistry - PIXL**

Elemental geochemistry for *Sid* from X-ray fluorescence (XRF) mapping by the PIXL instrument on the *Alfalfa* abrasion patch performed on sol 369 is shown in Fig. 9. *Alfalfa* is inferred to be a basaltic igneous rock, likely a ferroan trachyandesite or basaltic trachyandesite (Fig. 10), with large phenocrysts of X-ray-diffracting sodic plagioclase.

The average chemical composition for the sol 369 observations is given in Table 2. These data indicate a silicate rock that is quite rich in ferrous iron compared with terrestrial rocks of comparable SiO<sub>2</sub> contents; its Mg# (molar Mg/(Mg+Fe)) is only 9%. We know of no comparable martian compositions, except for other rocks of the *Mázaz* formation (*Guillaumes*, *Bellegarde*). In addition to the tabulated values, the *Alfalfa* bulk composition contains 650±290 (1σ) ppm Sr, which is consistent with its significant proportion of plagioclase feldspar.

On a total alkali versus silica (TAS) plot (Fig. 10), PIXL analyses for *Alfalfa* are distributed across the fields of basalt, trachybasalt, trachyandesite, and andesite; this range reflects mixing of the abundant plagioclase with mafic materials (augite, K- and Fe-rich mesostasis materials, and their alteration products). The average composition for *Alfalfa* is near the boundary between trachybasalt and trachyandesite classifications. The scattered points at low SiO<sub>2</sub> contents represent igneous Fe-Ti oxide and Ca-phosphate minerals, the Fe-rich mesostasis material, and a small proportion of salt minerals.

**Figure 9 | PIXL placement on *Alfalfa*, sol 369.** PIXL XRF scan, measuring 7x7 mm, on the abrasion patch (~5 cm across). On this image, feldspar is white to greenish, augite pyroxene is dark green, and orthopyroxene and altered material are brown. WATSON image SIF\_0367\_0699544277\_375 FDR N0110108SRLC08029\_0000LMJ01.

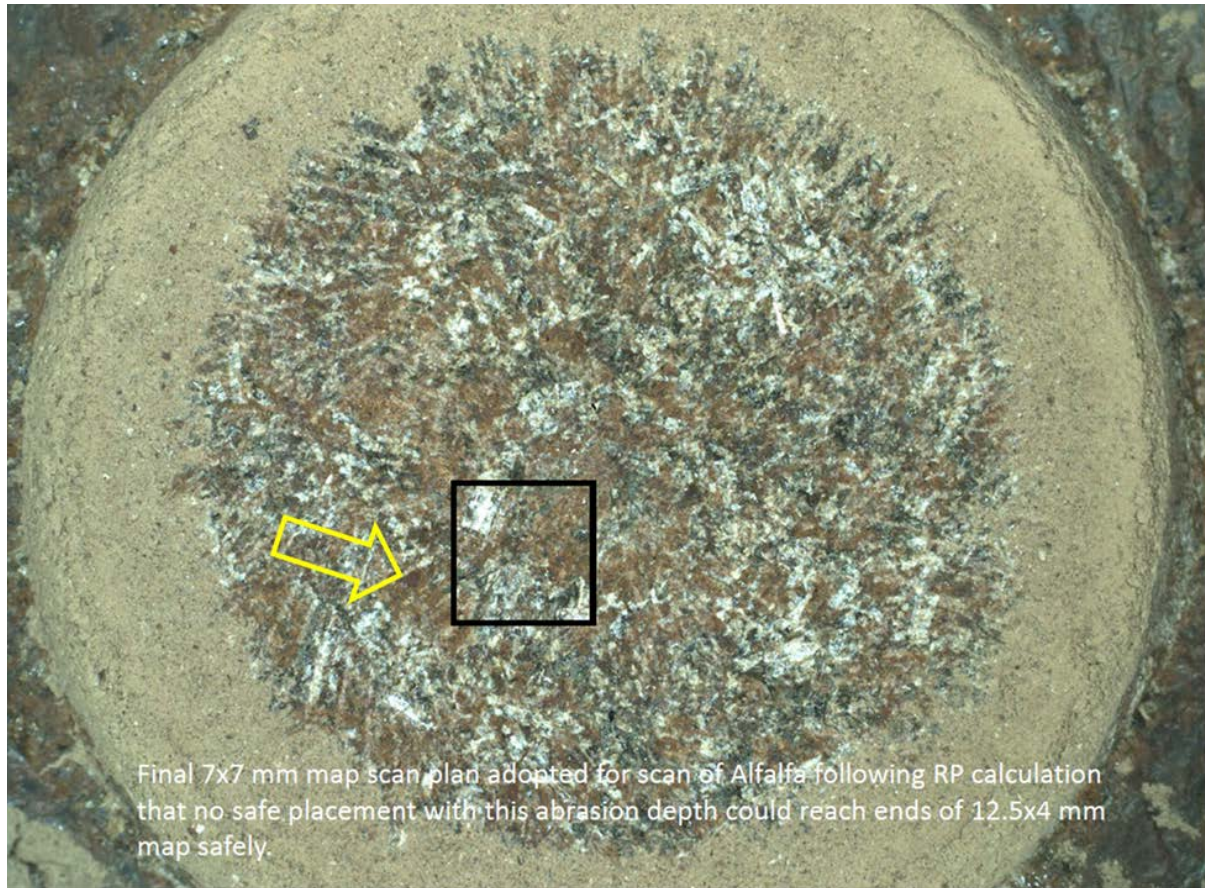
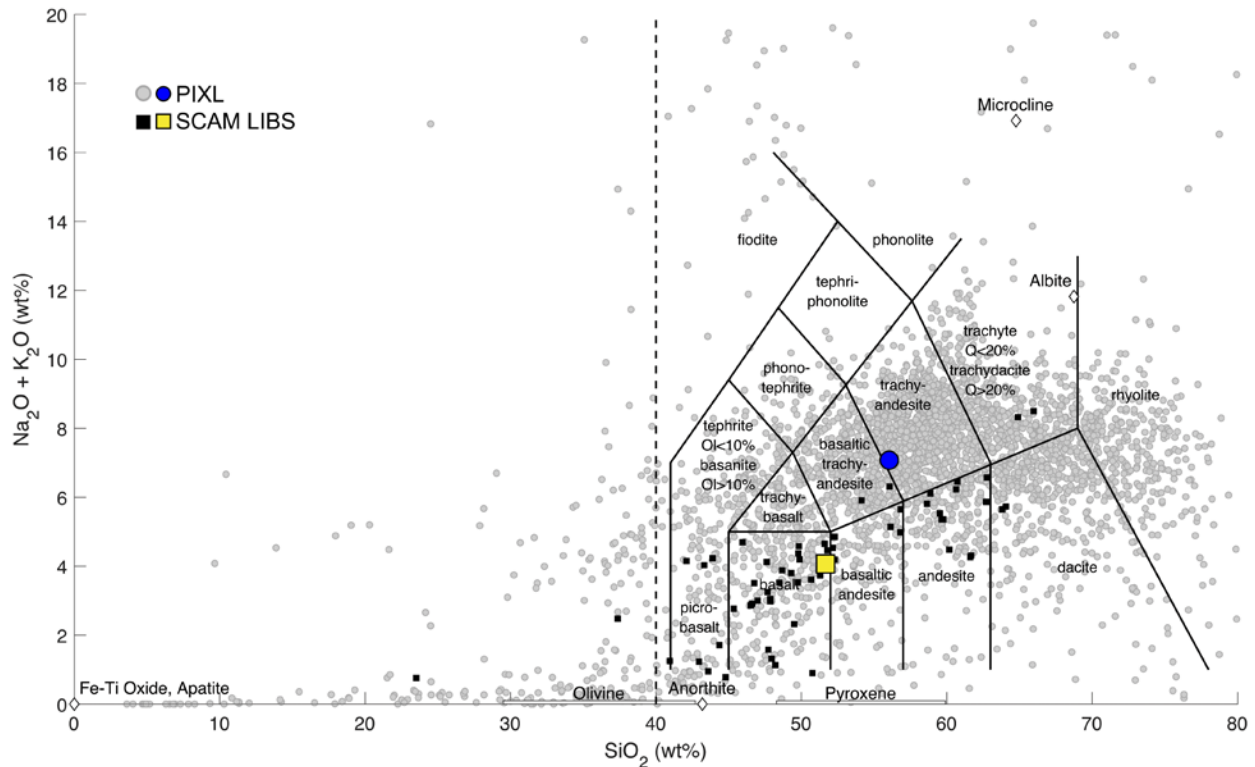


Figure 11 shows a ternary diagram of molar compositions  $\text{Al}_2\text{O}_3 - (\text{CaO} + \text{Na}_2\text{O} + \text{K}_2\text{O}) - (\text{FeOT} + \text{MgO})$  for the average composition and for each individual PIXL spot analysis in the sol 369 observation. Idealized common mineral compositions are also plotted on the diagram. The vast majority of points fall in the triangle defined by typical mafic minerals, and the majority of those project (more or less) near binary mixtures of plagioclase + augite, or plagioclase + an iron and magnesium rich phase. These binary mixtures suggest grains are small enough to permit many PIXL analytical spots to span two grains, but large enough that relatively few spots span three grains. Only a few PIXL analytical points plot above the plagioclase--[FeOT-MgO] line, i.e., are enriched in  $\text{Al}_2\text{O}_3$  relative to typical igneous minerals. Those points are close to a chlorite mineral composition, but could be interpreted as mixtures of the FeOT-MgO-rich material and a small proportion of aluminous clay minerals. Overall, this plot indicates that *Alfalfa* is not intensely weathered.

PIXL multi-element maps of the *Alfalfa* scan area (Fig. 12) show euhedral rectangular crystals of plagioclase and subhedral (partially irregular) augite pyroxene grains in a poorly crystalline (or fine-grained) Fe-rich and K-Al-rich groundmass. Figure 12a emphasizes the plagioclase crystals (light green), and Figure 12b shows that they are chemically zoned. The plagioclase grains show strong diffraction peaks, indicating that they are crystalline. They are commonly surrounded by rinds of

**Figure 10 | Total alkali vs. silica diagram for PIXL analyses of the Alfalfa abrasion patch (gray circles) and SuperCam LIBS observations of Alfalfa, the Sid natural surface, and other nearby similar rocks (black squares).** The relatively large feldspar crystals were of particular interest to the team, so their inclusion in the PIXL scan may bias the bulk composition toward the alkali-rich rock classes. The underlying igneous classification scheme does not apply to the individual data points and simply provides a frame of reference for comparing samples. The weighted mean of the observations (colored symbols) are consistent with *Sid* being a basaltic andesite to trachyandesite.



material poor in Al and K. Among the plagioclase crystals are intergrown augite crystals and K-Al-rich (non-diffracting) mesostasis (purple and dark green respectively in Fig. 12a). Minor igneous minerals include Ca-phosphate (Fig. 12c) and Fe-Ti oxide (Fig. 12d); no Cr-rich oxides were observed (Fig. 12d). The Fe-rich material (red in Figs. 12a & d) does not show X-ray diffractions detectable by PIXL, has analytical total near 100%, and contains Mn but minimal proportions of other elements (alkalis, Ca, S, P, Cr, and Ti). The scan area on *Alfalfa* contains only a small proportion of salt minerals, recognizable as Ca- or Mg- sulfates. Although sulfates in *Alfalfa* are sparse relative to previous samples, chlorine is present at relatively high concentrations in most spots other than the plagioclase crystals. One-quarter of the spot analyzes contain Cl concentrations consistent with moderate levels of Cl-bearing salts, e.g., ~10 wt% of an analytical volume could be a perchlorate salt.

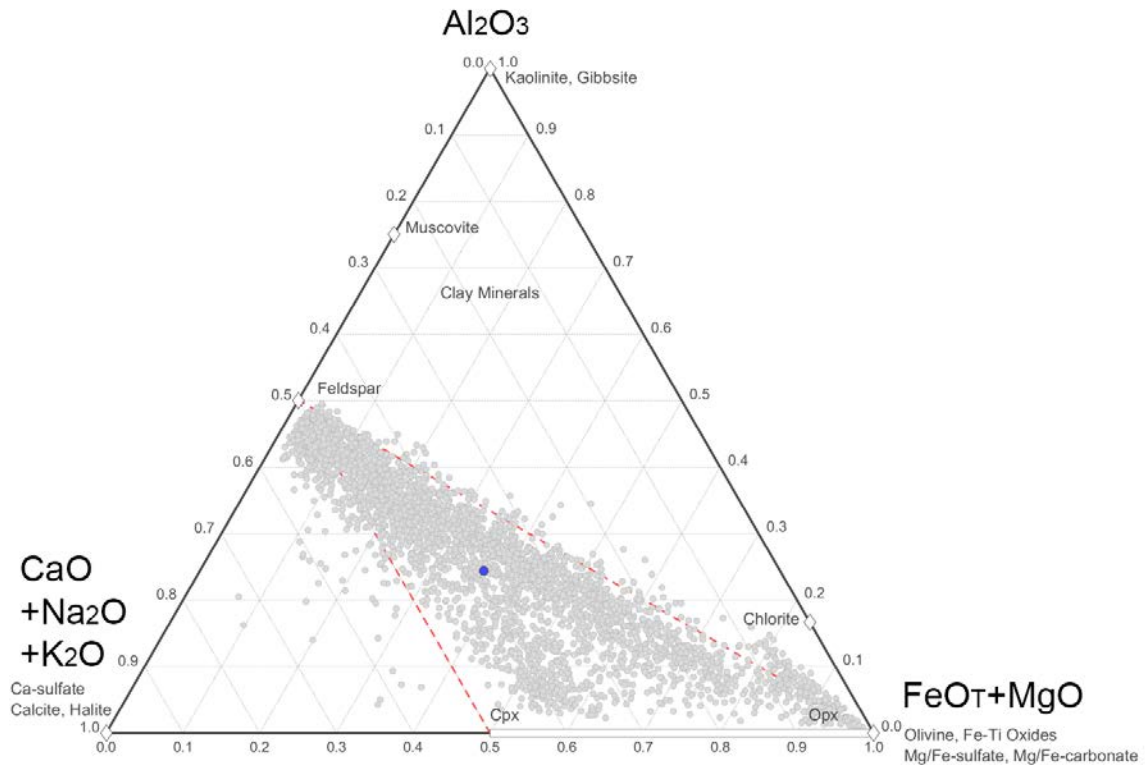
PIXL's Micro-Context Camera (MMC) images of the *Alfalfa* abrasion patch (Fig. 13) show more of the abrasion area than the XRF scans (Fig. 13a), and are used to extrapolate phase proportions from those of the XRF scan areas to nearly the whole abrasion patch. The MMC image of NIR-G-B (Fig. 13b) is analogous to WATSON visible images, and the G/NIR ratio image shows a clear distinction among the phases plagioclase, augite, and mesostasis (Fig. 13c). These visible & qualitative relationships are quantified in a graph of G vs NIR reflectances (Fig. 13d), which allows extraction of the proportions of these phases in the whole MMC image area.

Table 2. Bulk sum (average) chemical compositions by PIXL XRF.

Wt %	Bulk Sum 369		Plagioclase		Augite Salt Free	
	N=3249	Err 1 $\sigma$	N=304	Err 1 $\sigma$	N=46	Err 1 $\sigma$
Na <sub>2</sub> O	4.5	1.0	7.6	0.3	2.3	1.1
MgO	0.73	0.31	0.31	0.02	1.6	0.5
Al <sub>2</sub> O <sub>3</sub>	11.6	0.6	22.1	0.4	4.3	0.4
SiO <sub>2</sub>	57.1	2.8	58.4	0.6	47.9	2.4
P <sub>2</sub> O <sub>5</sub>	0.84	0.24	0.25	0.01	0.5	0.2
SO <sub>3</sub>	1.00	0.23	0.27	0.01	0.0	
Cl	2.08	0.40	0.38	0.04	0.0	
K <sub>2</sub> O	1.90	0.40	0.73	0.04	0.5	0.2
CaO	4.31	0.42	6.70	0.06	14.3	0.7
TiO <sub>2</sub>	0.59	0.18	0.01	0.00	0.7	0.2
Cr <sub>2</sub> O <sub>3</sub>	0.00	0.00	0.00	0.00	0.0	0.0
MnO	0.28	0.15	0.02	0.00	1.1	0.3
FeO-T	13.24	0.78	1.73	0.01	27.4	1.4
Sum %	98.2		98.6		100.6	
Mg#/An	9.		33.		9.	

N are number of analyses averaged. Err is uncertainty (1 $\sigma$ ) from calibration and counting statistics. Mg# is molar Mg/(Mg+Fe), in percent. An for plagioclase is molar Ca/(Ca+Na), in percent.

**Figure 11 | Mineralogical interpretation of the *Alfalfa* abrasion, PIXL observations on sol 369.** Data plotted by pixel and as bulk sum composition (blue circle, Table 1) on ternary diagram of molar abundances of  $\text{Al}_2\text{O}_3$ – $(\text{CaO}+\text{Na}_2\text{O}+\text{K}_2\text{O})$ – $(\text{FeOT}+\text{MgO})$ . Common pure mineral composition are shown (opx = Ca-poor pyroxene, i.e. orthopyroxene; cpx = calcic pyroxene, i.e. augite). Most of the individual PIXL analysis points are consistent with pure minerals (olivine, cpx, Fe-oxide) or binary mixtures of feldspar–cpx, or feldspar– $[\text{FeOT}+\text{MgO}]$ , or ternary mixtures of cpx–feldspar– $[\text{FeOT}+\text{MgO}]$ . Aluminous alteration minerals, like common clay minerals, fall above the upper red dashed line. Several other secondary minerals (e.g., Fe-Mg-Ca-sulfates/carbonates, halite) are also plotted.



**Figure 12 | PIXL X-ray multi-element maps for the *Alfalfa* abrasion patch on sol 369.** (a) Red=FeO, Green=Al<sub>2</sub>O<sub>3</sub>, Blue=CaO. (b) Red=CaO, Green=Na<sub>2</sub>O, Blue=K<sub>2</sub>O. (c) Red=CaO, Green=P<sub>2</sub>O<sub>5</sub>, Blue=SO<sub>3</sub>. (d) Red=FeO, Green=TiO<sub>2</sub>, Blue=Cr<sub>2</sub>O<sub>3</sub>. The rock consists of Na-rich plagioclase crystals (green in frames a & b), augite (purple, frame a), alkali-rich groundmass (blue, frame b), and material of orthopyroxene composition (dark red, frame a; black, frame b). Ca-rich material (red in frames b & c), possibly carbonate, is scattered through the groundmass. Apatite and Ca-sulfate are present but uncommon (frame c) Frame d shows oxide minerals; the brightest red areas are iron-rich with minimal Ti or Cr, and show minimal diffractions, yellow-green is likely ilmenite; the area contains no Cr-rich oxide minerals.

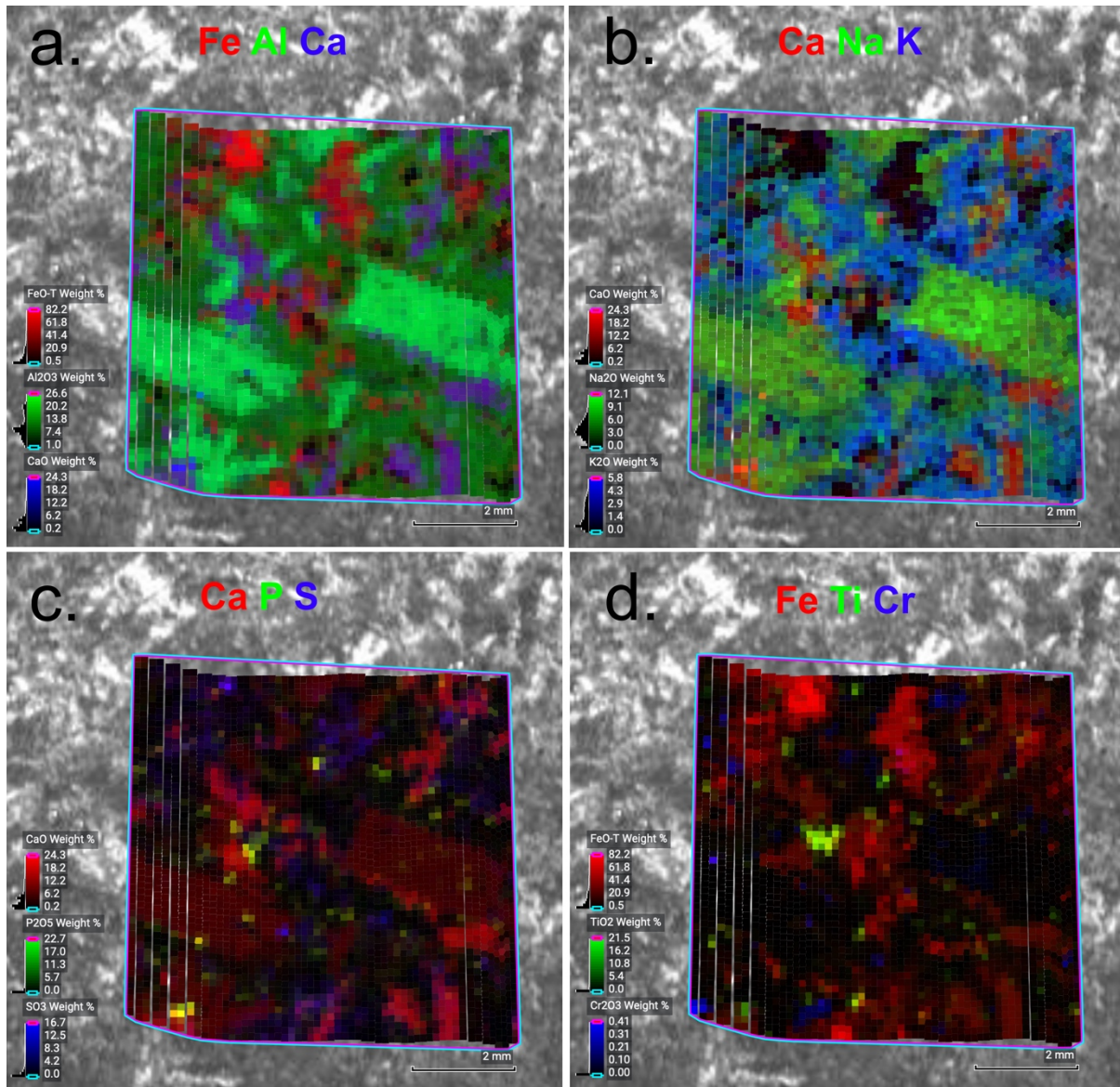
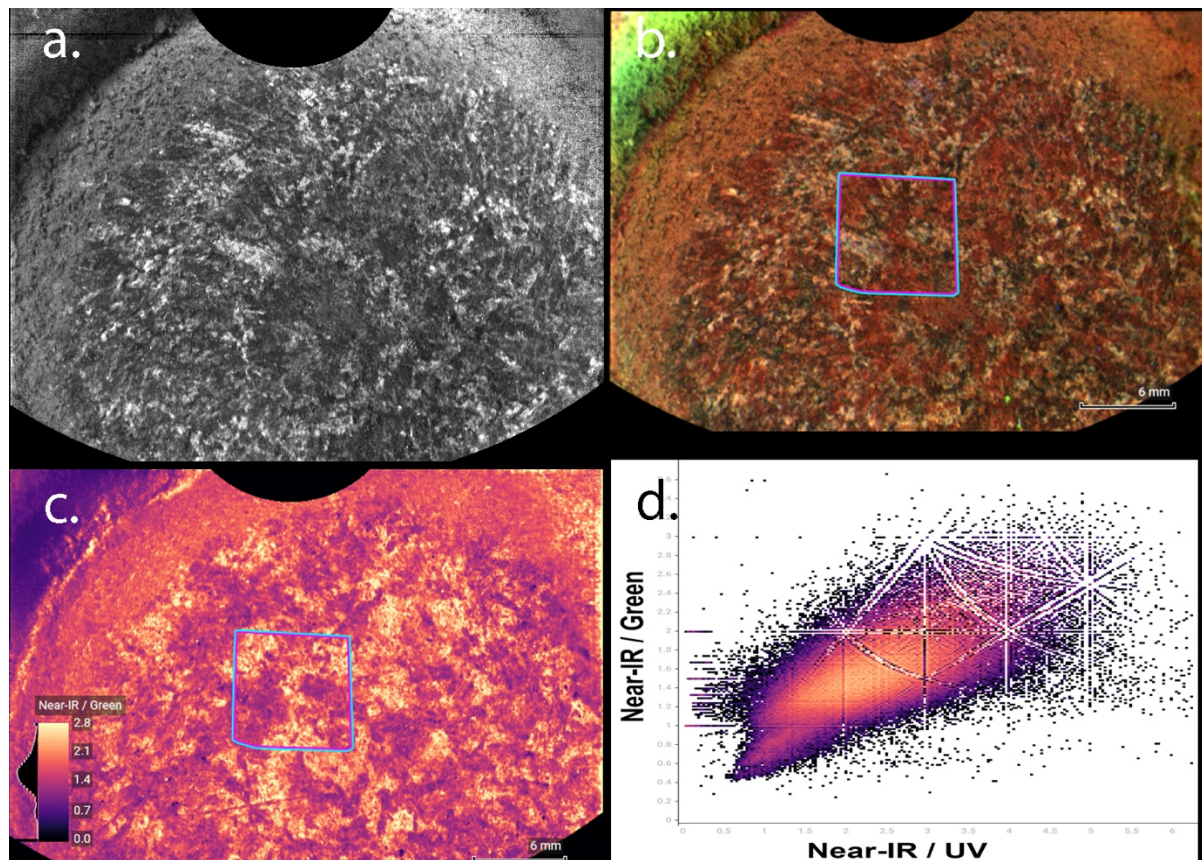


**Figure 13 | PIXL MCC (Micro-context camera) data for the *Alfalpa* abrasion patch, sol 369.** (a) MMC grayscale image, a portion of the *Alfalpa* abrasion. (b) MMC false color of a abrasion area; Red = MMC Near-IR; Green = MMC Green; Blue = MMC Blue. Location of PIXL XRF scans shown. (c) MMC ratio image Near-IR/Green reflectances. Augite is darkest and mesostasis and alteration materials are lightest tone. Location of PIXL XRF scan shown. (d) MMC reflectance ratios.



### ***Mineralogy and Organics-SHERLOC***

SHERLOC observed the *Alfalpa* abrasion patch on sol 370. Spectra were collected with a survey scan (5x5 mm, 1296 points, 144  $\mu\text{m}$  spacing, 15 pulses per point, not shown) and a HDR scan (7x7 mm, 100 points, 780  $\mu\text{m}$  spacing, 500 pulses per point). Results are shown in Fig. 14 and Table 3.

The average Raman spectrum of all 100 points in the scan area shows a broad band assigned to disordered/microcrystalline silicates ( $1000\text{ cm}^{-1}$ ). Peaks in spectra at selected locations are consistent with the presence of carbonate ( $1090\text{ cm}^{-1}$ ) and poly-crystalline carbonate, feldspar ( $515\text{ cm}^{-1}$ ), olivine (low Fo#), and quartz ( $475\text{ cm}^{-1}$ ), though weakness of the possible feldspar and quartz peaks could be due to the fact that they are below the nominal cut-off of the SHERLOC edge filter so only very intense signals would be detectable. The observed fluorescence features (275-280 nm, 330-340 nm) are similar to what has been observed in *Guillaumes* and other targets in the *Máz* fm and are consistent with single and double ring aromatic organic molecules, respectively.

**Figure 14 | Sol 370 SHERLOC fluorescence and Raman spectral results on *Alfalpa*.** A) Colorized ACI image of the abraded patch with a blue rectangle indicating the HDR scan area, and three white circles indicating regions of interest (ROIs) that correlate to the fluorescence data shown in B and C. B) Upper panel is an RGB map showing main regions of organic fluorescence (275-280 and 330-340 nm). The blank lower panel indicates no detection of organic materials by Raman spectroscopy (see Raman data in part D). C) Fluorescence spectra for the whole analysis area (upper) and from selected ROIs (lower) (see A and B). D) Map of the Raman HDR scan (left) and selected spectra (right). In the map, the grid of small red points indicates analysis points, and the large colored circles indicate the locations of mineral detections. In the panel of spectra, the uppermost spectrum is the average spectrum of all 100 points in the scan area. The second spectrum is an average of all the points labeled with blue and light blue on the spectral map. The third spectrum is an average of all the spectra within the two dark green polygons on the map, which enclose two apparent feldspar laths. The lowermost spectrum is from Point 5 (orange circle on map). Each spectrum has been baseline subtracted and offset along the y-axis for clarity. Note in each the presence of a laser artifact near 650  $\text{cm}^{-1}$ . The scale in panel A also applies to the map in panel D.

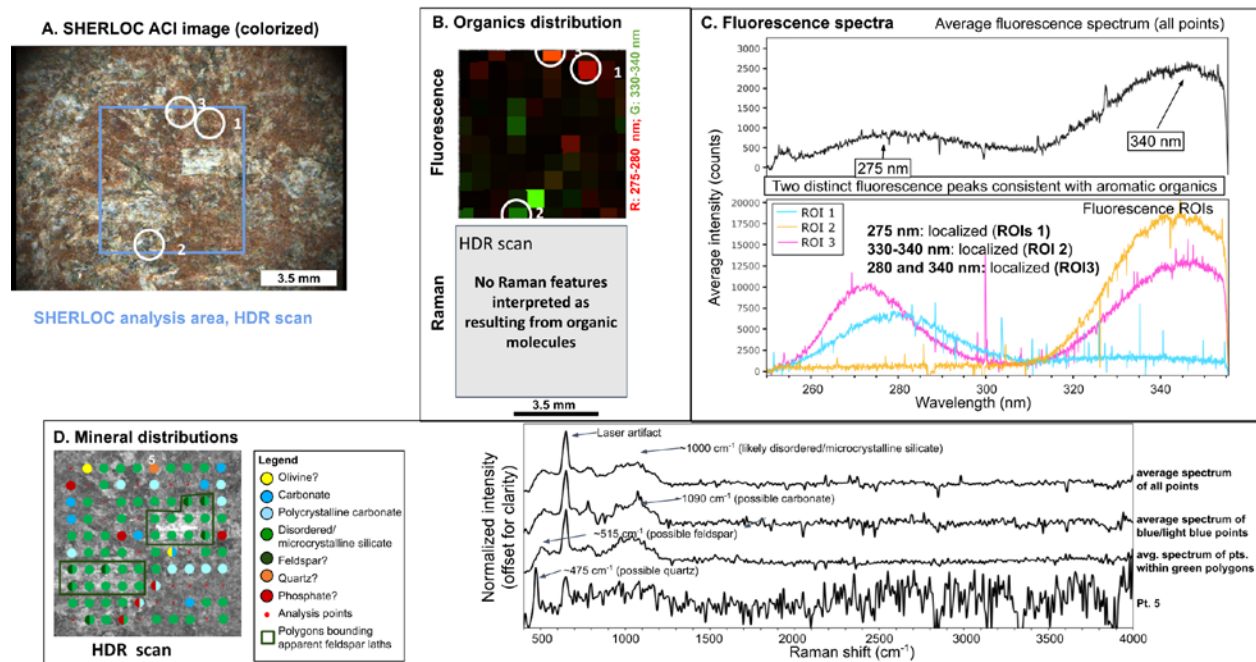


Table 3. SHERLOC Raman spectra mineral ID.

Sample	Certain	Possible (not confirmed)	We looked for these, but cannot find them
Alfalfa	Disordered and/or microcrystalline silicates (widespread throughout)	Olivine (low Fo#) occurs in two spots, but not obviously associated with crystal habit.  Carbonate (could be Mg/Ca/Fe)  Feldspar, difficult to confirm because of weak signal, but largely associated with crystal habit  Quartz, only found in one point spectrum, weak signal	Pyroxene

### ***Elemental Geochemistry and Mineralogy – SuperCam***

The SuperCam LIBS observations for *Sid* and nearby targets (Fig. 15) show that *Ch'at* member rocks are heterogeneous, consistent with being coarse-grained on the scale of RMI images (Fig. 5) and LIBS point spacing (generally a few mm). The overall elemental trends are consistent with the presence of feldspar and pyroxene, with some Ca-pyroxene and the possible presence of olivine and/or Fe-oxide, with additional unrecognized phases. All points show evidence of hydration, some points have evidence for Fe-OH band and possible Al-phyllsilicates (2.2mm band) indicating some degree of aqueous alteration. Generally, the composition of *Sid* and nearby targets is in family with previously encountered *Ch'at*-like rocks (Wiens et al., 2022).

SuperCam VISIR spectra on *Sid* (natural surface, abraded surface and tailings from coring activity; Fig. 12) also reveal an overall mafic mineralogy, where the broad band between 0.7-1.8 microns is due to mafic minerals like olivine, pyroxene, or glass. The SCAM VISIR technique is highly sensitive to hydrated minerals, so the signatures of hydration are present in the spectra even when these minerals are a minor proportion of the rock. Fig. 16 shows the absorption bands that indicate the presence of hydrated minerals in *Sid*. The main signal of hydration is present at 1.94  $\mu\text{m}$ , whereas the absorptions at 2.29  $\mu\text{m}$  coupled with absorptions centered near 1.4, 1.9 and 2.39  $\mu\text{m}$  likely indicate Fe-bearing phyllosilicate minerals. The weak absorption at 2.32  $\mu\text{m}$  in the tailings likely indicates a Mg-OH phase and the 2.46  $\mu\text{m}$  can possibly be explained by the presence of akaganeite. The VISIR spectra are greatly affected by the grain size, contributing to the differences in the tailings and rock spectra.

Figure 15 | SuperCam LIBS major element oxide analyses of *Sid* and all *Máaz* fm natural surface analyses from sols 15–201 and sols 343–379. Solid solution fields for olivine, pyroxene, and feldspar compositions are included.

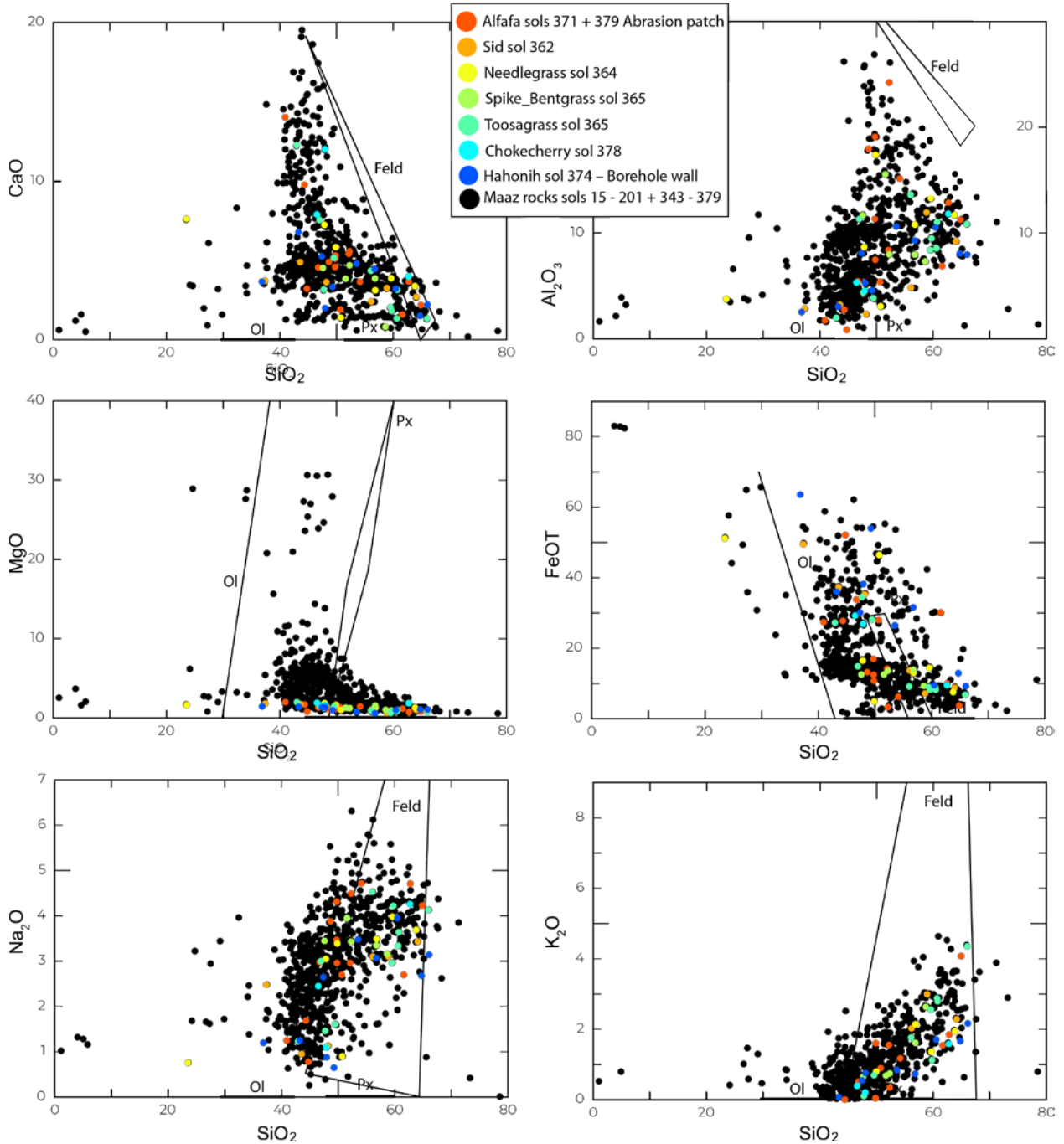
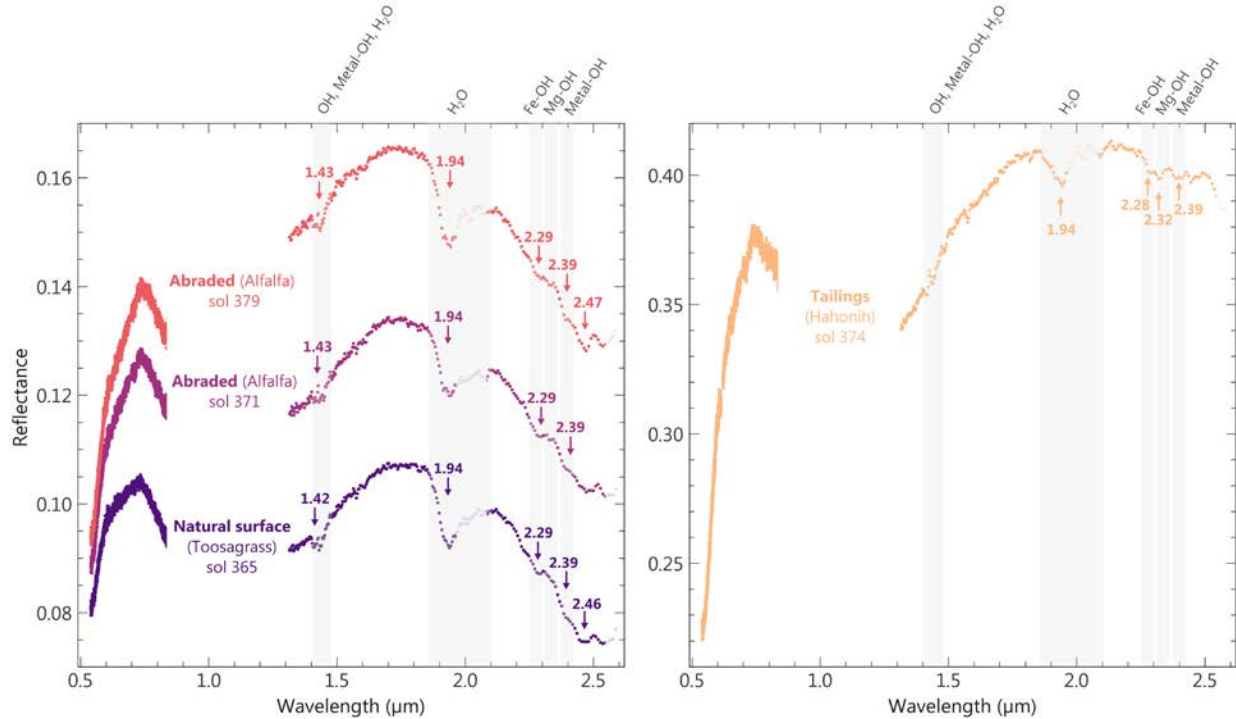


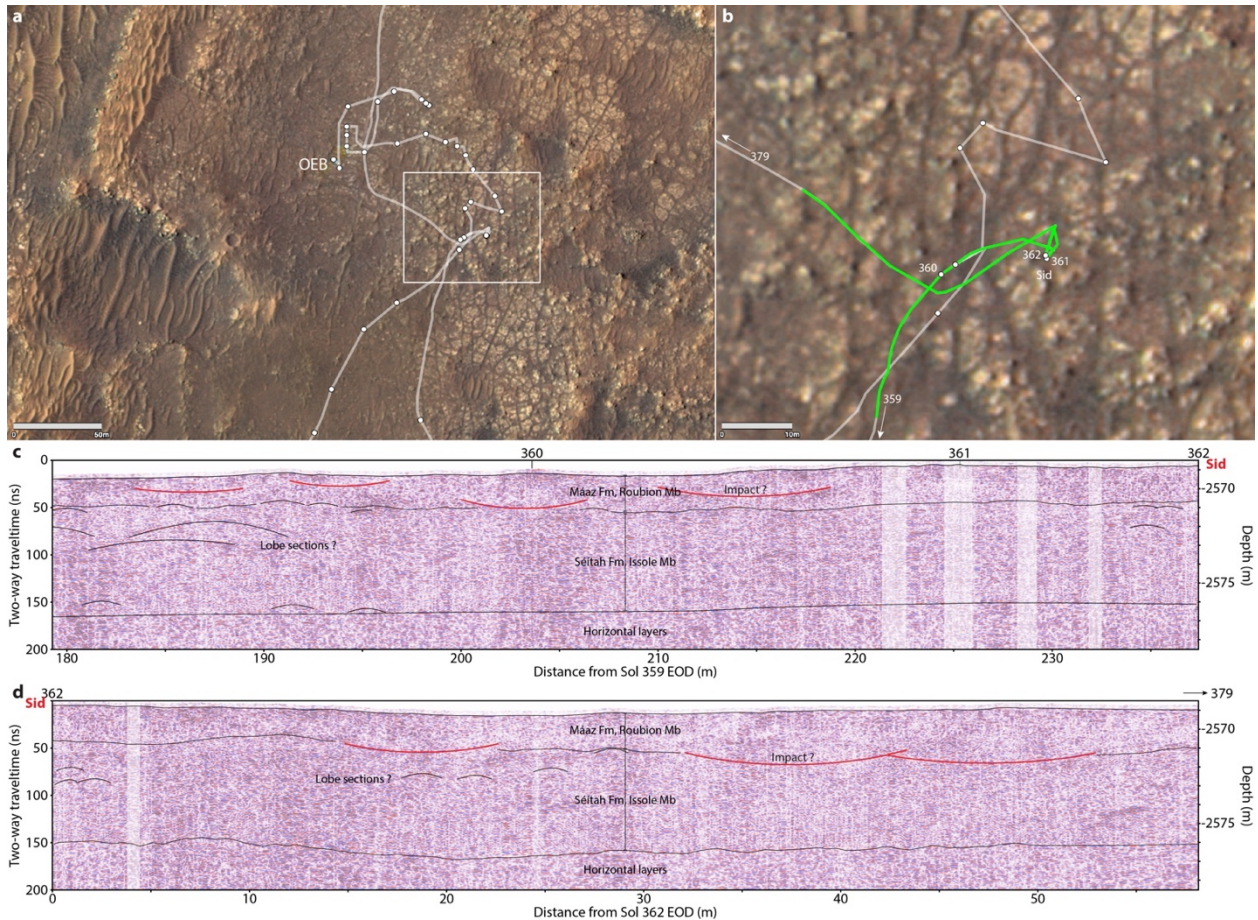
**Figure 16 | Mean reflectance spectra of the SuperCam VISIR observations on *Sid* (natural surface, abraded surface and tailings).** Saturated and shadowed points were excluded from averaging. Lighter dots near  $2\ \mu\text{m}$  indicate the spectral range possibly affected by  $\text{CO}_2$  absorption features that could remain after the atmospheric correction. Note that owing to temperature sensitivities in the IRS instrument, the calibration is still uncertain for wavelength longer than  $\sim 2.5\ \mu\text{m}$ .



### Subsurface Structure

The subsurface structure in the vicinity of the *Sid* outcrop is revealed by RIMFAX radargrams acquired on sols 360–362, inbound to the outcrop, and sol 379, outbound from the outcrop (Fig. 17a and b). *Sid* is a *Ch'at*-type rock that outcrops as blocky material on top of topographic highs overlying recessive polygonal rocks, such as *Nataani* and *Roubion*, that appear to form a coherent layer in the subsurface as seen in RIMFAX radargrams (Fig. 17c and d). In the radargrams, the uppermost  $\sim 2\ \text{m}$  represents the *Máaz* fm, where the deposits are dominated by horizontal layering and polygons visible at the surface. Polygon-bounding fractures are not visible in the radargrams, suggesting that these fractures may be very shallow. Bowl-shaped reflector geometries in the *Máaz* fm are interpreted to represent remnant (eroded) impact structures (Fig. 17c and d). The underlying *Séítah* fm strata occur between  $\sim 2$  and  $7\ \text{m}$  burial depth. The boundary between the base of the *Máaz* fm and the top of the *Séítah* fm is interpreted as an erosional unconformity based in part on the presence of eroded impact structures. To avoid safety hazards, the rover traverse stayed clear of high standing *Ch'at* member outcrops, so this unit was not characterized by radar.

**Figure 17 | Geological context and RIMFAX-derived subsurface stratigraphy of the Sid area.** (a) Location of the Sid area, southeast of the Octavia E. Butler (OEB) landing site. (b) Detailed map of the area around Sid showing rover drive sections (green traverses) used to create radargram sections; (c) Radargram of the inbound traverse toward Sid on sols 360–362 with annotations. (d) Radargram of the outbound traverse away from Sid on sol 379 with annotations. Each radargram covers similar stratigraphy and record a mixture of horizontal, dipping, and bowl-shaped reflector geometries.



### Core orientation

The *Hahonih* core was collected on Sol 371 using nominal operations for drilling and caching. The core broke off cleanly at the base of the borehole with a slight “mushroom” stem (Fig. 18).

Features of the natural surface of the coring targets on *Sid* were used to measure core orientation (Fig. 19). The core roll ( $\alpha$ ) is defined as the angle between the WATSON y-axis and the up-dip direction in SITE coordinates. At the time of drilling and 5.6-cm pre-drilling WATSON imaging, the rover, coring drill, WATSON target, and coring target (called “Hahonih.PSC.0.0729”), had the following characteristics:

- Rover orientation quaternion just after drilling but before unloading the stabilizers (transferring from RMECH to SITE frame):  $\mathbf{bQII1} = (0.1500300, 0.0144798, -0.0209876, -0.9883530)$

- b) Coring Drill orientation quaternion just after drilling but before unloading the stabilizers (transferring from CORING DRILL to RMECH frame):  $\mathbf{cdQb} = (0.5911830, 0.1944370, -0.7818390, 0.0377382)$
- c) Rover orientation quaternion at time of acquisition of WATSON image SIF\_0370\_0699795188\_894RAS\_N0110108SRLC00663\_0000LMJ01: (transferring from RMECH to SITE frame):  $\mathbf{bQII2} = (0.1500950, 0.0115230, -0.0213943, -0.9883730)$
- d) WATSON orientation quaternion at time of acquisition of WATSON image SIF\_0370\_0699795188\_894RAS\_N0110108SRLC00663\_0000LMJ01: (transferring from WATSON to RMECH frame):  $\mathbf{wQb} = (0.5908020, 0.1961150, -0.7817180, 0.0375390)$

**Figure 18 | Hahonih borehole and core images.** (left) SHERLOC WATSON image of the *Hahonih* borehole and (right) cropped CacheCam image of the bottom of the *Hahonih* core. The sample core is 13 mm in diameter.



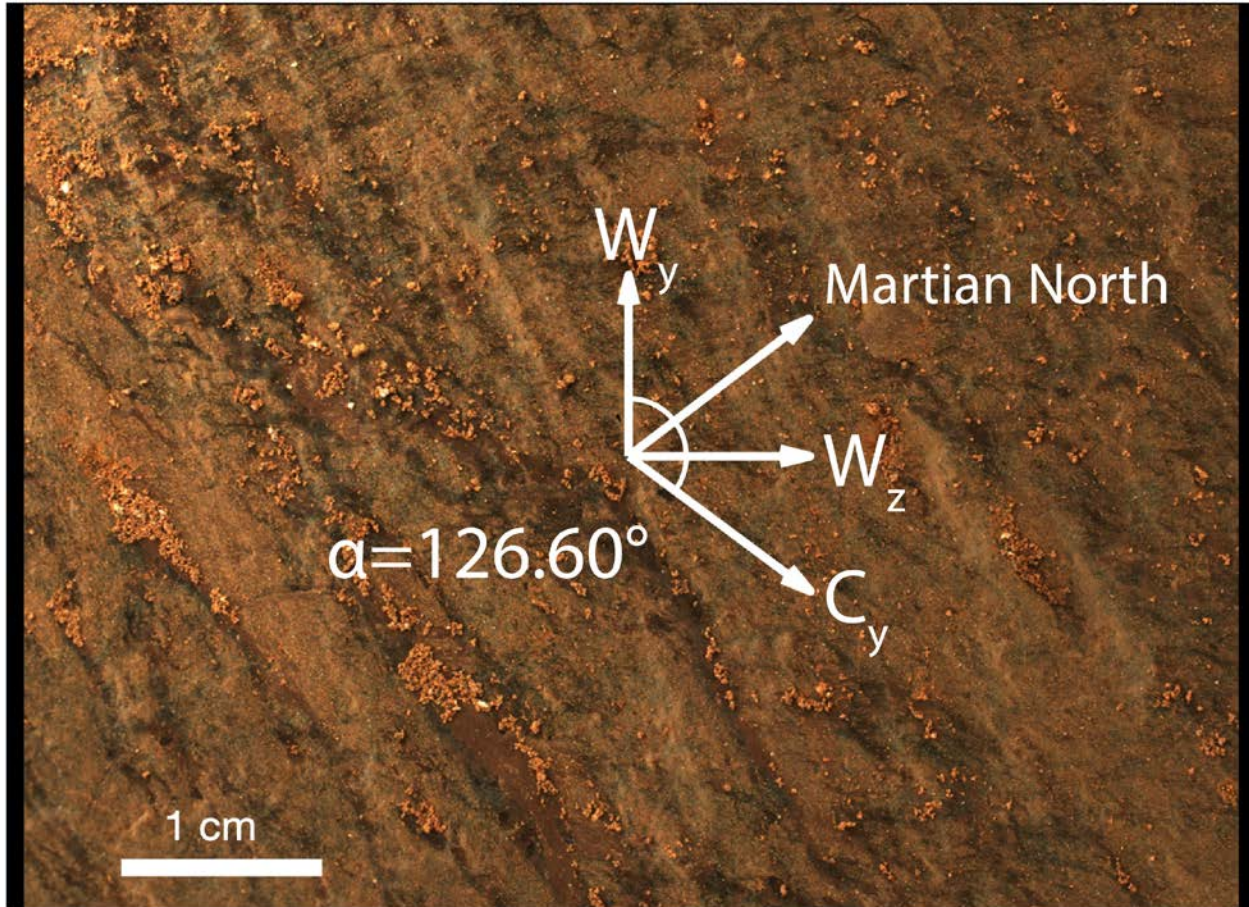
Items 1 and 2 give a coring drill pointing vector estimate of

$$\begin{aligned} \text{hade} &= 21.41^\circ \\ \text{azimuth} &= 73.18^\circ \end{aligned}$$

Items 3 and 4 give an estimate of the angle between the WATSON y-axis and the up-dip direction in SITE coordinates of (Fig. 19):

$$\text{core roll, } \alpha = 126.60^\circ$$

**Figure 19 | Hahonih core orientation.** 5.6-cm standoff WATSON image of *Hahonih* core target on sol 370. Image scale is  $27.3 \mu\text{m pixel}^{-1}$ . Orientation compass gives WATSON frame ( $w_x, w_y, w_z$ ). Core roll is clockwise angle of core y-axis,  $c_y$ , from  $w_y$ , given by  $\alpha = 126.60^\circ$ . Projection of Martian geographic north onto WATSON image plane is noted. WATSON image SIF\_0370\_0699795188\_894RAS\_N0110108SRLC00663\_0000LMJ01.



## Preliminary Scientific Assessment

### Synthetic sample description and preliminary interpretation

**Sample type: Basaltic andesite**

#### **1. Stratigraphic and Geologic Context**

- a. Stratigraphic position: *Hahonih* and *Atsah* represent the *Ch'al* member of the *Máaz* formation. The *Ch'al* member appears to be the stratigraphically highest member of the *Máaz* fm, overlying the recessive rocks of the *Nataani* member.
- b. Source rock: *Hahonih* and *Atsah* are derived from the *Sid* rock. *Sid* is interpreted to be an in-place block of the *Ch'al* member bedrock.

## 2. Texture and fabric

- a. Rock fabric (natural surface): Massive, ventifacted, individual grains or crystals rarely visible
- b. Rock fabric (abrasion patch): Holocrystalline, no compelling evidence of intergranular porosity or cement
- c. Grain Size: Large euhedral feldspar crystals a few mm long; subhedral crystalline ortho- and clinopyroxene  $\leq 1$  mm.

## 3. Petrology, Mineralogy and Elemental composition

- a. Minerals present: Major: feldspar, orthopyroxene, clinopyroxene. Minor: iron oxides, carbonate, salts. Possible: olivine, phyllosilicates, quartz, chlorite.
- b. Bulk composition: Consistent with a basaltic andesite.
- c. Organic molecules: Present, low abundance, probably aromatic ring compounds.
- d. Alteration and hydration: Minimal. Evidence of hydration and some hematite coloration.

## 4. Core orientation

- e. Sample cores were absolutely oriented to  $\sim 1^\circ$  in martian geographic coordinates. Cores were taken from the top of the *Sid* rock.

## Returned Sample Science Considerations

The collection of the *Hahonih* and *Atsah* samples from the *Ch'at* member completes the suite of samples from the *Máaz* fm and the Crater Floor Campaign. The *Hahonih* and *Atsah* samples are currently believed to be the best candidates for the least altered, and possibly most compellingly in-place, samples of the *Máaz* fm.

*Geochronology:* The *Hahonih* and *Atsah* samples appear to have limited alteration relative to other *Máaz* fm samples, which may make them the most robust Crater Floor samples for radiometric dating. The *Ch'at* member's stratigraphic position and the timing of its emplacement will help constrain the age of the other units in Jezero crater, such as the (apparently overlying) delta and (apparently underlying) *Séitah* fm. The *Máaz* formation and especially the *Ch'at* mb can be related to relatively high crater densities observed on the Jezero crater floor (Quantin-Natif and others, 2022), therefore ages determined by radiometric and possibly cosmogenic methods of the *Hahonih* and *Atsah* samples may provide a comparison point with crater chronology age estimates. Published crater retention model ages for the *Máaz* fm range from 1.8 Ga to older than 3 Ga (Goudge et al., 2012; Holm-Alwmark et al., 2021; Marchi, 2021; Shahrzad et al., 2019) with the spread possibly due to erosional exposure of the unit.

In addition, cosmogenic nuclide measurements of these two samples will constrain their integrated duration of exposure to galactic cosmic rays while residing near the martian surface. Cosmic-ray exposure dating may help reveal the erosion rates at the (modern) Martian surface, as the *Ch'at* member is apparently eroding away from the underlying *Nataani* member surface. Such information

would also inform the expected preservation and modification of organic molecules present in these rocks.

*Paleomagnetism:* The igneous lithologies of the *Sid* cores may enable absolute measurements of the paleointensity of the ancient martian magnetic field at the time of crystallization. The orientations of the cores, combined with paleohorizontal indicators from outcrop foliation, may enable measurements of the absolute paleodirection of the ancient field. Paleomagnetic investigations of secondary ferromagnetic minerals could constrain the field at the time of (limited) aqueous alteration. Combined with measurements from other samples, these data could test the hypothesis that Martian atmospheric loss was driven by the cessation of an early dynamo, constrain the dynamo's secular variation, and determine if the dynamo exhibited polarity reversals. Comparison of paleomagnetic directions with *Séitah* rocks (*Salette/Coulletes* and *Malay/Robine*) could distinguish between the hypotheses that *Máaz* and *Séitah* form a single layered intrusion versus *Máaz* being an overlying lava flow.

*Geochemistry:* The geochemical and isotopic composition of the *Sid* cores can be used to characterize the evolution of the martian mantle/crust, and melting processes. The *Hahonih* and *Atsah* samples appear to be slightly altered, in contrast to the more intense aqueous alteration in *Máaz* and *Séitah* fm cores. In tandem with other *Máaz* fm cores, laboratory analysis of the alteration minerals, formation temperatures, and ages will provide a history of aqueous alteration conditions in Jezero crater post-crystallization. A particularly compelling comparison will be between the *Ch'at* member samples and the *Rochette* member samples, which appear to have a similar primary mineralogy, but different extents of alteration. Given that *Hahonih* and *Atsah* represent the least altered igneous rocks from the crater floor and contain only a weak organic signal, laboratory analyses may help establish the background level of reduced carbon in igneous crater floor rocks (including the nature and distribution of such carbon).

*Comparison with other Máaz samples:* Abraded proximity science was conducted on four rocks in the *Máaz* fm: *Roubion*, *Rochette*, *Rimplas*, and *Sid*. *Roubion* is an example of the flat-lying, polygonally jointed material of the *Máaz* fm. The *Guillaumes* abrasion patch revealed that *Roubion* was a fine- to medium-grained mafic rock, composed of plagioclase and pyroxene with minor apatite and FeTi oxides. *Roubion* was pervasively altered, as evidenced by pits and crevices in the abraded surface and abundant secondary minerals including iron oxide (possibly hydrated), sulfates, perchlorate, and possibly phosphate and halite. Both *Rochette* (abraded patch *Bellegarde*) and *Rimplas* were located along the feature named *Artuby Ridge*, a resistant ledge within the *Máaz* fm that can be traced from near the *Roubion* site along the southern edge of the *Séitah* fm contact. Proximity science showed that the *Rochette* and *Rimplas* rocks were similar to each other and broadly mineralogically similar to *Roubion*, being fine-to-medium grained mafic rocks dominated by plagioclase and pyroxene. The *Rochette* and *Rimplas* rocks also contained abundant secondary phases likely resulting from aqueous alteration, including iron oxide, Ca-sulfates (occasionally hydrated), phosphate, and minor carbonate. However, *Rochette* and *Rimplas* appear to be substantially less altered than *Roubion*, from which it was not possible to collect a sample. The *Alfalfa* abrasion patch on the *Sid* rock, a representative of the *Ch'at* member of the *Máaz* fm, appears to be relatively coarser-grained, more alkalic, and less altered than other *Máaz* fm samples. It also contains large feldspar laths that are lacking in the other *Máaz* fm samples. The *Sid* samples appear significantly less altered than all of the other *Máaz* fm samples including the *Rochette* samples *Montdenier* and *Montagnac*.

The *Hahonih* and *Atsah* samples are currently believed to be the best candidates for the least altered, and most compellingly in-place, sample of the *Mázaz* fm. The *Montdenier* and *Montagnac* samples seem to have a similar primary mineralogy, and contain more abundant secondary phases that will better reveal the post-emplacement history of water interaction with the *Mázaz* fm.

*Summary:* the return of the *Ch'af* member samples will directly address several major RSS objectives and markedly improve our understanding of the earliest history of igneous processes on Mars. Returned samples of this unit have particularly high science value for determining the igneous petrogenesis of possible lava flows, the global evolution of Mars (interior and near surface environments), and for understanding the geological setting and relative and absolute chronology of Jezero floor units.

## **References**

- Beatty D. W., Grady M. M., McSween H. Y., Sefton-Nash E., Carrier B. L., Altieri F., Amelin Y., Ammannito E., Anand M., Benning L. G., Bishop J. L., Borg L. E., Boucher D., Brucato J. R., Busemann H., Campbell K. A., Czaja A. D., Debaille V., Des Marais D. J., Dixon M., Ehlmann B. L., Farmer J. D., Fernandez-Remolar D. C., Filiberto J., Fogarty J., Glavin D. P., Goreva Y. S., Hallis L. J., Harrington A. D., Hausrath E. M., Herd C. D. K., Horgan B., Humayun M., Kleine T., Kleinhenz J., Mackelprang R., Mangold N., Mayhew L. E., McCoy J. T., McCubbin F. M., McLennan S. M., Moser D. E., Moynier F., Mustard J. F., Niles P. B., Ori G. G., Raulin F., Rettberg P., Rucker M. A., Schmitz N., Schwenzer S. P., Sephton M. A., Shaheen R., Sharp Z. D., Shuster D. L., Siljeström S., Smith C. L., Spry J. A., Steele A., Swindle T. D., ten Kate I. L., Tosca N. J., Usui T., Van Kranendonk M. J., Wadhwa M., Weiss B. P., Werner S. C., Westall F., Wheeler R. M., Zipfel J., and Zorzano M. P. (2019) The potential science and engineering value of samples delivered to Earth by Mars sample return. *Meteoritics & Planetary Science* **54**, S3-S152.
- Cohen B. A., Young K. E., Zellner N. E. B., Zacny K., Yingst R. A., Watkins R. N., Warwick R., Valencia S. N., Swindle T. D., Robbins S. J., Petro N. E., Nicoletti A., Moriarty III, Dan P., Lynch R., Indyk S. J., Gross J., Grier J. A., Grant J. A., Ginyard A., Fassett C. I., Farley K. A., Farcy B. J., Ehlmann B. L., Dyar M. D., Daelemans G., Curran N. M., van der Bogert C. H., Arevalo Jr, Ricardo D., and Anderson F. S. (2021) In Situ Geochronology for the Next Decade: Mission Designs for the Moon, Mars, and Vesta. *The Planetary Science Journal* **2**, <https://doi.org/10.3847/PSJ/abedbf>.
- Crumpler L. S. and others (2022) In Situ Geologic Context Mapping (GXM) Transect on the Jezero Crater Floor from Mars 2020/Perseverance Rover Observations. *JGR Issue on Jezero Crater Floor*, in preparation.
- Elsila J. E., Callahan M. P., Dworkin J. P., Glavin D. P., McLain H. L., Noble S. K., and Gibson E. K. (2016) The origin of amino acids in lunar regolith samples. *Geochimica et Cosmochimica Acta* **172**, 357-369.
- Farley K. A., Stack K. M., and others (2022) Aqueously altered igneous rocks on the floor of Jezero crater, Mars. *Science*, accepted / in press.
- Fuex A. N. and Baker D. R. (1973) Stable carbon isotopes in selected granitic, mafic, and ultramafic igneous rocks. *Geochimica et Cosmochimica Acta* **37**, 2509-2521.

- Goudge T. A., Mustard J. F., Head J. W., and Fassett C. I. (2012) Constraints on the history of open-basin lakes on Mars from the composition and timing of volcanic resurfacing. *Journal of Geophysical Research: Planets* **117**.
- Goudge T. A., Mustard J. F., Head J. W., Fassett C. I., and Wiseman S. M. (2015) Assessing the mineralogy of the watershed and fan deposits of the Jezero crater paleolake system, Mars. *Journal of Geophysical Research: Planets* **120**, 775-808.
- Horgan B. H. N., Anderson R. B., Dromart G., Amador E. S., and Rice M. S. (2020a) The mineral diversity of Jezero crater: Evidence for possible lacustrine carbonates on Mars. *Icarus* **339**, 113526.
- Horgan B. H. N., Johnson J. R., Fraeman A. A., Rice M. S., Seeger C., Bell III J. F., Bennett K. A., Cloutis E. A., Edgar L. A., Frydenvang J., Grotzinger J. P., L'Haridon J., Jacob S. R., Mangold N., Rampe E. B., Rivera-Hernandez F., Sun V. Z., Thompson L. M., and Wellington D. (2020b) Diagenesis of Vera Rubin Ridge, Gale Crater, Mars, From Mastcam Multispectral Images. *Journal of Geophysical Research: Planets* **125**, e2019JE006322.
- Marchi S. (2021) A New Martian Crater Chronology: Implications for Jezero Crater. *The Astronomical Journal* **161**, 187.
- McSween H. Y., Jr. (2015) Petrology on Mars. *American Mineralogist* **100**, 2380-2395.
- Quantin-Natif C. and others (2022) The Complex Exhumation History of Jezero Crater Floor Unit. *Journal of Geophysical Research*, in preparation.
- Schon S. C., Head J. W., and Fassett C. I. (2012) An overfilled lacustrine system and progradational delta in Jezero crater, Mars: Implications for Noachian climate. *Planetary and Space Science* **67**, 28-45.
- Septon M. A., Wright I. P., Gilmour I., de Leeuw J. W., Grady M. M., and Pillinger C. T. (2002) High molecular weight organic matter in martian meteorites. *Planetary and Space Science* **50**, 711-716.
- Shahrazad S., Kinch K. M., Goudge T. A., Fassett C. I., Needham D. H., Quantin-Nataf C., and Knudsen C. P. (2019) Crater Statistics on the Dark-Toned, Mafic Floor Unit in Jezero Crater, Mars. *Geophysical Research Letters* **46**, 2408-2416.
- Stack K. M., Williams N. R., Calef F., Sun V. Z., Williford K. H., Farley K. A., Eide S., Flannery D., Hughes C., Jacob S. R., Kah L. C., Meyen F., Molina A., Nataf C. Q., Rice M., Russell P., Scheller E., Seeger C. H., Abbey W. J., Adler J. B., Amundsen H., Anderson R. B., Angel S. M., Arana G., Atkins J., Barrington M., Berger T., Borden R., Boring B., Brown A., Carrier B. L., Conrad P., Dypvik H., Fagents S. A., Gallegos Z. E., Garczynski B., Golder K., Gomez F., Goreva Y., Gupta S., Hamran S.-E., Hicks T., Hinterman E. D., Horgan B. N., Hurowitz J., Johnson J. R., Lasue J., Kronyak R. E., Liu Y., Madariaga J. M., Mangold N., McClean J., Miklusicak N., Nunes D., Rojas C., Runyon K., Schmitz N., Scudder N., Shaver E., SooHoo J., Spaulding R., Stanish E., Tamppari L. K., Tice M. M., Turenne N., Willis P. A., and Aileen Yingst R. (2020) Photogeologic Map of the Perseverance Rover Field Site in Jezero Crater Constructed by the Mars 2020 Science Team. *Space Science Reviews* **216**, 127.

Udry A., Howarth G. H., Herd C. D. K., Day J. M. D., Lapen T. J., and Filiberto J. (2020) What Martian Meteorites Reveal About the Interior and Surface of Mars. *Journal of Geophysical Research: Planets* **125**, e2020JE006523.

Werner S. C. (2019) In situ calibration of the Martian cratering chronology. *Meteoritics & Planetary Science* **54**, 1182-1193.

Wiens R. C., Udry A., Beyssac O., Quantin-Nataf C., Mangold N., Cousin A., L. M., Bosak T., Forni O., McLennan S. M., Sautter V., Brown A., Benzerara K., Johnson J. R., Mayhew L., Maurice S., Anderson R. B., Clegg S. M., Crumpler L., Gabriel T. S. J., Gasda P., Hall J., Horgan B. H. N., Kah L., Legett C., Madariaga M. J., Meslin P.-Y., Ollila A. M., Poulet F., Royer C., Sharma S. K., Siljeström S., Simon J. I., Acosta-Maeda T. E., Llamas C. A., Angel S. M., Arana G., Beck P., Bernard S., Bertrand T., Bousquet B., Castro K., Chide B., Clavé E., Cloutis E., Connell S., Dehouck E., Dromart G., Fischer W., Fouchet T., Francis R. T., Frydenvang J., Gasnault O., Gibbons E., Gupta S., Hausrath L., Jacob X., Kalucha H., Kelly E., Knutsen E., Lanza N., Laserna J., Lasue J., Mouélic S. L., Leveille R., Lopez Reyes G., Lorenz R., Manrique J. A., Martinez-Frias J., McConnochie T., Melikechi N., Mimoun D., Montmessin F., Moros J., Murdoch N., Pilleri P., Pilorget C., Pinet P., Rapin W., Rull F., Schröder S., Shuster D. L., Smith R. J., Stott A., Tarnas J., Turenne N., Veneranda M., Vogt D. S., Weiss B. P., Willis P., Stack K. M., Williford K. H., Farley K. A., and the SuperCam Team (2022) Compositionally and density stratified igneous terrain in Jezero Crater, Mars. *Science Advances*, accepted / in press.

# INITIAL REPORT

## M2020-377-10 *Atsah*

---

**Sample Designation:** M2020-377-10 *Atsah*

**Date of Coring:** 9-Mar-22

**Mars Time of Sample Core Sealing:** 21:12:02 LMST, Sol 377, Ls 187

**Latitude (N), Longitude (E), Elevation:** 18.44386406, 77.45242176, -2568.357m

**Campaign:** Crater Floor

**Region of Interest:** *Ch'at* member of *Máaz* formation, east of the Octavia E. Butler landing site

**Lithology:** Likely basaltic andesite. Few mm-size white feldspar laths and pyroxene grains are present, as possibly are olivine and quartz. Limited evidence of secondary alteration includes interstitial iron oxides, carbonate, possible phyllosilicates and chlorite, and hydration. Low concentrations of organic matter were detected.

**Estimated Volume Recovered:** 8.46 cm<sup>3</sup>

**Coring Bit Number:** 4

**Core Orientation:** hade = 18.02°; azimuth = 69.87°; core roll = 110.96°

**Sample Serial Numbers:** Tube SN202, Seal SN168, Ferrule SN074

**ACA Temperature at Time of Sealing:** 40°C

**Estimated Rover-Ambient Pressure and Temperature at Time of Sealing:** 669 Pa, 215 K

**Estimated Amount of Martian Atmosphere Headspace Gas:** 1.3x10<sup>-6</sup> mol

**Anomalous Behavior:** Three sols elapsed between sample coring and sealing.

**Abrasion Patch Name and Depth:** *Alfalfa*, 9 mm

May 8, 2022

B. A. Cohen, H. Amundsen, L. Beegle, J. Bell, E. Berger, T. Bosjak, F. Calef, E. Cardarelli, A. Czaja, V. Debaille, H. Dypvik, K.A. Farley, A. Fox, S.-E. Hamran, C. Herd, B. Horgan, J. R. Johnson, L. Jandura, C. Lee, L. Mandon, E. N. Mansbach, L. E Mayhew, S. M. McLennan, C. Million, M. Rice, E. Scheller, M. E. Schmidt, J. Schroeder, S. Sharma, S. Siljestroem, J. I. Simon, D. L. Shuster, M. St. Clair, A. Udry, S. Van Bommel, B. P. Weiss, R. C. Wiens, M.-P. Zorzano, and the Mars 2020 Team

## Summary Description

This sample is paired with M2020-190-9 *Hahonih*. Only the core orientation for *Atsah* is described below. See the Initial Report for M2020-190-9 *Hahonih* for sample details.

### **Core orientation**

At the time of drilling and 5.7-cm pre-drilling WATSON imaging, the rover, Coring Drill, WATSON, and coring target (called “*Atsah.PSC.0.0687*”), had the following characteristics:

- a) Rover orientation quaternion just after drilling but before unloading the stabilizers (transferring from RMECH to SITE frame): **bQI1** = (0.150025, 0.0148175, -0.020817, -0.988352)
- b) Coring Drill orientation quaternion just after drilling but before unloading the stabilizers (transferring from CORING DRILL to RMECH frame): **cdQb** = (0.58264, 0.235836, -0.76571, 0.136382)
- c) Rover orientation quaternion at time of acquisition of WATSON image SIF\_0373\_0700065505\_402RAS\_N0110108SRLC00657\_0000LMJ01: (transferring from RMECH to SITE frame): **bQI2** = (0.1501010, 0.0114020, -0.0207122, -0.9883880)
- d) WATSON orientation quaternion at time of acquisition of WATSON image SIF\_0373\_0700065505\_402RAS\_N0110108SRLC00657\_0000LMJ01: (transferring from WATSON to RMECH frame): **wQb** = (0.5801300, 0.23807000, -0.7670220, 0.1358290)

Items 1 and 2 give a coring drill pointing vector estimate of

**hade = 18.02°**  
**azimuth = 69.87°**

Items 3 and 4 give an estimate of the angle between the WATSON y-axis and the up-dip direction in SITE coordinates of (Fig. 1):

**core roll,  $\alpha$  = 110.96°**

**Figure 1 | *Atsah* core orientation.** 5.7-cm standoff WATSON image of *Atsah* core target on sol 373. Image scale is  $27.6 \mu\text{m pixel}^{-1}$ . Orientation compass gives WATSON frame ( $\mathbf{w}_x$ ,  $\mathbf{w}_y$ ,  $\mathbf{w}_z$ ). Core roll is clockwise angle of core y-axis,  $\mathbf{c}_y$ , from  $\mathbf{w}_y$ , given by  $\alpha = 110.96^\circ$ . Projection of Martian geographic north onto WATSON image plane is noted. WATSON image SIF\_0373\_0700065505\_402RAS\_N0110108SRLC00657\_0000LMJ01.

